Advanced Coding and Signal Processing Methods for Multiuser MIMO Systems

Darian Pérez Adán

Doctoral Thesis UDC / 2022

Advisors: Luis Castedo Ribas
José P. González Coma

PhD Program in Information Technology and Mobile Network Communication

Métodos Avanzados de Codificación e Procesamento de Sinal para Sistemas MIMO Multiusuario

Darian Pérez Adán

Tese de Doutoramento UDC / 2022

Directores: Luis Castedo Ribas
José P. González Coma

Programa de Doutoramento en Tecnoloxías da Información e das Comunicacións en Redes Móbiles

UNIVERSIDADE DA CORUÑA

Métodos Avanzados de Codificación y Procesamiento de Señales para Sistemas MIMO Multiusuario

Darian Pérez Adán

Tesis Doctoral UDC / 2022

Directores: Luis Castedo Ribas
José P. González Coma

Programa de Doctorado en Tecnologías de la Información y de las Comunicaciones en Redes Móviles

UNIVERSIDADE DA CORUÑA

Darian Pérez Adán

CERTIFICA / *CERTIFICA* / *CERTIFIES*

Que a presente memoria é o resultado do meu propio traballo de investigación e que o traballo doutros autores está citado axeitadamente.

Que la presente memoria es el resultado de mi propio trabajo de investigación y que el trabajo de otros autores está citado apropiadamente.

That the present report is the result of my own research work and that the work done by other authors is appropriately cited.

A Coruña, *novembro de 2022 / noviembre de 2022 / November 2022*

Darian Pérez Adán

Luis Castedo Ribas
José P. González Coma

CERTIFICAN / *CERTIFICAN* / *CERTIFY*

Que a presente tese titulada "Métodos Avanzados de Codificación e Procesamento de Sinal para Sistemas MIMO Multiusuario " foi realizada por Darian Pérez Adán baixo a nosa dirección no Departamento de Enxeñaría de Computadores da Universidade da Coruña e preséntase para obter o grao de Doutor con Mención Internacional.

Que la presente tesis titulada "Métodos Avanzados de Codificación y Procesamiento de Señales para Sistemas MIMO Multiusuario" fue realizada por Darian Pérez Adán bajo nuestra dirección en el Departamento de Ingeniería de Computadores de la Universidade da Coruña y se presenta para obtener el grado de Doctor con Mención Internacional.

That the present thesis titled "Advanced Coding and Signal Processing Methods for Multiuser MIMO Systems" was done by Darian Pérez Adán under our supervision in the Department of Computer Engineering at the University of A Coruña and it is submitted to obtain the Ph.D. degree with International Mention.

Os directores da tese / *Los directores de la tesis* / *The Ph.D. supervisors*.
A Coruña, novembro de 2022 / *noviembre de 2022* / *November 2022*.

Dr. Luis Castedo Ribas
Catedrático de Universidade
Dpto. de Enxeñaría de Computadores
Universidade da Coruña

Full Professor
Dept. of Computer Engineering
University of A Coruña

Dr. José P. González Coma
Prof. Axudante Doutor
Centro Universitario de la Defensa en la Escuela Naval Militar
Universidade de Vigo

Ph.D. Assistant Professor
Defense University Center at the Spanish Naval Academy
University of Vigo

Tese de Doutoramento / *Tesis Doctoral* / *Doctoral Thesis*

Título:	Métodos Avanzados de Codificación e Procesamento de Sinal para Sistemas MIMO Multiusuario
***Título*:**	*Métodos Avanzados de Codificación y Procesamiento de Señales para Sistemas MIMO Multiusuario*
***Title*:**	*Advanced Coding and Signal Processing Methods for Multiuser MIMO Systems*
Autor / *Autor* / *Author*:	Darian Pérez Adán
Directores / *Directores* / *Supervisors*:	Luis Castedo Ribas José P. González Coma
Data / *Fecha* / *Date*:	novembro de 2022 / *noviembre de 2022* / *November 2022*

Tribunal / *Tribunal* / *Evaluation Committee*

Presidente / *Presidente* / *President*:	Francisco Javier López Martínez
Vogal / *Vocal* / *Member*:	Michael Joham
Secretaria / *Secretaria* / *Secretary*:	Paula María Castro Castro

To my family

Acknowledgements

First of all, I would like to thank my supervisor Dr. Luis Castedo for the opportunities he has given me to work on different projects, which have led me to strengthen my knowledge in signal processing and coding for wireless communications. I am particularly grateful to Luis for the trust he placed in me by inviting me to join his prestigious research group GTEC.

I would also like to thank my co-supervisor Jose P. for all his efforts in helping me to prepare this thesis. Thank you for your suggestions and new ideas and for allowing me to put them into practice in the best way possible.

It is impossible to forget a person who has also been essential in the development of this thesis: Óscar Fresnedo. The invaluable and constant support I have received from Óscar has played a crucial role in the development of practical issues related to my thesis.

In general, thanks to the GTEC members and former members who have been here and whom I have had the pleasure of meeting, especially Tomás, for his constant support in different research projects, Pedro for his valuable contribution to the works related to source coding, and thanks to Franc Laport, Marc, Darío, Manuel, Valentín, Angel and José Francisco for making my integration into the laboratory more enjoyable from the beginning. Thanks also to Dariel for helping me with different practical issues related to this thesis. Of course, I am not forgetting the rest of the GTEC members, former members, and professors that I have had the pleasure of meeting: Adriano, Aida, Adriana, Carlos, Fran, Dani, José Juan Lamas, Julio, Miguel, Oscar Blanco, Paula Castro, Paula Fraga, José Antonio, Tiago, and Roberto. Thanks also to Cris for helping me with the bureaucracy of the university.

My sincere thanks to the excellent researchers at the Technical University of Munich, especially to Wolfgang Utschick for integrating me into his prestigious research group and to Michael Joham for his constant technical support during my stay in Germany in 2021.

My most important gratitude goes to my family. They have always been there for me, and I am sure they will continue standing by me. To my beloved mom, Leticia, for raising me in a favorable environment for my personal and intellectual growth. Her dedication and unconditional support have been essential to achieve each of my goals.

To my brother Danyer, my grandparents Tico, Eneida, Oneida, Agustin, my dad Lazaro, and all other family members; thanks for your support.

Finally, I also want to remember my friends, who have accompanied and helped me during all these years, especially Lilly, for her constant support during the last two years of this beautiful journey.

Resumo

Os sistemas de comunicacións sen fíos están a experimentar un crecemento constante nos últimos anos e agárdase que crezan aínda máis nos próximos anos axudados polo uso de novas técnicas de codificación e procesamento de sinal. Os servizos multimedia baseados en datos son cada vez máis demandados para actividades laborais e de socialización, e requiren de novas técnicas de codificación e procesamento do sinal para poderen ser despregados de forma efectiva. Por tanto, é de esperar que estas técnicas acheguen melloras canto á velocidade, a eficiencia enerxética, a fiabilidade, entre outros aspectos.

Nos últimos anos a aplicación das técnicas de codificación avanzadas xogou un papel imprescindible para despregar as redes emerxentes de comunicacións sen fíos. Hoxe en día, a gran maioría dos sistemas de comunicación deséñanse seguindo unha aproximación dixital e de acordo co principio de separación fonte-canle. Con todo, os sistemas de comunicación baseados na optimización conxunta da codificación de fonte e canle (coñecidos pola súa sigla en inglés JSCC) seguen espertando interese nos investigadores, especialmente no caso de transmisión de sinais analóxicos. Os investigadores baséanse en que esta estratexia tamén é capaz de aproximarse aos límites teóricos, ademais de ofrecer vantaxes con respecto aos sistemas dixitais como, por exemplo, unha baixa complexidade e un mínimo retardo.

A aplicación de novas técnicas para procesar o sinal é esencial na implementación das redes emerxentes de comunicacións sen fíos. Especificamente, na banda de ondas milimétricas (ou mmWave), a cal se considera para satisfacer os requisitos das novas xeracións de redes móbiles (5G e B5G), as arquitecturas híbridas foron recentemente propostas como un enfoque innovador que permite aumentar a eficiencia enerxética. Estas arquitecturas baséanse en dividir a precodificación dixital, usada en sistemas que fan uso de múltiples antenas tanto nos transmisores como nos receptores (MIMO, pola súa sigla en inglés), nunha parte analóxica de baixo consumo enerxético e outra dixital. A maioría dos enfoques de codificación e precodificación MIMO están condicionados pola canle de comunicacións sen fíos que, normalmente, segue sendo incontrolable.

Por outra banda, o paradigma de control do medio de propagación vén recibindo moita atención por parte da comunidade científica no ámbito de redes emerxentes sen fíos. Este paradigma foi utilizado anteriormente para aplicacións de radar e satélite mediante o emprego de superficies reflectoras. Porén, non se consideraba para aplicacións móbiles debido á imposibilidade de implementar superficies reflectoras que fixesen fronte ao dinamismo das canles sen fíos por mor da mobilidade dos usuarios presente nestes sistemas. Con todo, os avances acadados na actualidade no estudo dos metamateriais cos que se fabrican estas superficies proporcionan garantías de reconfigurabilidade para habilitar o axuste en tempo real dos cambios de fase nas superficies reflectoras intelixentes (IRSs, pola súa sigla en inglés).

Nesta tese, analizamos e deseñamos novos métodos de codificación de sinais analóxicos baseados no principio de optimización JSCC. Tamén analizamos e implementamos novas técnicas de procesamento do sinal aplicadas ás arquitecturas híbridas na banda de mmWave. Finalmente, desenvolvemos técnicas de procesamento do sinal para establecer un mellor control do medio a través do uso de IRSs.

Resumen

Los sistemas de comunicaciones inalámbricas experimentan un crecimiento sin interrupciones en los últimos años, y se espera que se desarrollen aún más en los próximos años, acompañados en su despliegue por novedosas técnicas de codificación y procesamiento de señales. Los servicios multimedia y basados en datos son cada vez más demandados para actividades laborales y de socialización, y requieren de novedosas técnicas de codificación y procesamiento de señales para su despliegue. Se espera que estas técnicas aporten mejoras en cuanto a la tasa de datos, la eficiencia energética, la fiabilidad, etc.

La aplicación de las técnicas de codificación juega un papel imprescindible en el despliegue de las redes emergentes de comunicaciones inalámbricas. Hoy en día, la gran mayoría de los sistemas de comunicaciones se diseñan siguiendo una aproximación digital y de acuerdo con el principio de separación. Sin embargo, los sistemas de comunicaciones basados en la optimización conjunta de la codificación de fuente y canal (JSCC, por sus siglas en inglés) siguen despertando interés en los investigadores, especialmente para la transmisión de señales analógicas. Los investigadores se basan en que la estrategia JSCC también es capaz de aproximarse a los límites teóricos, además de ofrecer ventajas con respecto a los sistemas digitales como, por ejemplo, baja complejidad y mínimo retardo.

En la actualidad, la aplicación de novedosas técnicas de procesamiento de señales es esencial en la implementación de las redes emergentes de comunicaciones inalámbricas. Específicamente, en la banda de ondas milimétricas (mmWave), la cual ha despertado gran interés para el despliegue de nuevas generaciones móviles (5G y posteriores), las arquitecturas híbridas han ofrecido recientemente un enfoque innovador que permite aumentar la eficiencia energética. Estas arquitecturas están basadas en desacoplar la precodificación digital usada en sistemas de múltiples entradas y múltiples salidas (MIMO, por sus siglas en inglés) en una parte analógica de bajo consumo energético y otra digital. La mayoría de los enfoques de codificación y precodificación MIMO están condicionados por el canal inalámbrico de comunicaciones, el cual normalmente permanece incontrolable.

Afortunadamente, el paradigma de control del medio de propagación está siendo considerado actualmente para redes emergentes de comunicaciones inalámbricas. Este paradigma se había empleado anteriormente para aplicaciones de radares y satélites a través de superficies reflectantes, pero no se consideraba para escenarios con movilidad debido a la incapacidad de implementar superficies reflectantes que hicieran frente al dinamismo de los canales inalámbricos. Sin embargo, los avances obtenidos en la actualidad en el estudio de los metamateriales ofrecen garantías de reconfigurabilidad en tiempo real de las superficies reflectantes inteligentes (IRSs, por sus siglas en inglés).

En esta tesis analizamos e implementamos novedosos métodos de codificación de señales analógicas basados en el principio de optimización JSCC. También analizamos e implementamos novedosas técnicas de procesamiento de señales aplicadas a las arquitecturas híbridas en mmWave y con el objetivo de establecer un mejor control del medio de comunicaciones a través de las IRSs.

Abstract

Wireless communication systems have experienced a non-stopping growth in the last few years and are expected to grow even more in the following years, supported in their deployment by novel coding and signal processing techniques. Multimedia and mobile data-based services are increasingly in demand for online work and socialization purposes, and novel coding and signal processing techniques are required to cope with their implementation. These techniques are expected to accomplish improvements in terms of data rates, energy efficiency, reliability, etc.

The use of encoding techniques plays an essential role in the deployment of emerging wireless communications networks. Nowadays, most communication systems are designed following a digital approach and according to the separation principle. However, communication systems based on the optimization of joint source-channel coding (JSCC) still arouse the interest of researchers, especially in the case of analog signal transmission. The researchers rely on the capability of this strategy to approach theoretical limits and offer advantages over digital systems, e.g., low complexity and minimal delay.

Nowadays, the application of novel signal processing techniques is essential for the implementation of emerging wireless communications networks. Specifically, in the millimeter-wave (mmWave) band—which has received high interest for the deployment of 5G and beyond—hybrid architectures have recently offered an innovative approach to increase the energy efficiency of the systems. These architectures are based on decoupling the digital precoding used in multiple-input multiple-output (MIMO) systems into a low-complexity analog part and a baseband part. Most approaches related to the source coding and the MIMO precoding are conditioned to the wireless channel, which usually remains uncontrollable.

Fortunately, the paradigm of propagation environment control is being considered for emerging wireless communications networks. This paradigm had previously been used for radar and satellite applications by means of reflecting surfaces but it was not considered for mobile communications due to the inability to cope with the dynamic wireless channels because of user mobility. However, currently, the advances obtained in the study of meta-materials provide certain guarantees for reconfigurability by enabling real-time phase shifts in the intelligent reflecting surfaces (IRSs).

In this thesis, we analyze and implement new coding methods for analog signals based on the JSCC optimization principle. We also analyze and implement novel signal processing techniques applied to hybrid architectures in the mmWave band. Finally, we develop signal processing techniques for better control of the propagation environment through the IRSs.

Table of Contents

List of Figures

List of Tables

Chapter I

Introduction

With the popularization of user devices and the Internet of things (IoT), modern societies have experienced a non-stopping growth of wireless communication systems. As a consequence, the efforts to approach challenging network optimization problems to improve wireless network performance in terms of data rate, energy efficiency, and reliability, among others, have also increased. Massive multiple-input multiple-output (MIMO) and millimeter-wave (mmWave) technologies have been incorporated into wireless communications to obtain the demanded data rates or link reliability in the mobile fifth generation (5G) and beyond fifth-generation (B5G) systems. Sophisticated coding and signal processing techniques are indispensable to meet the requirements of the growing number of multimedia and mobile data-based services in cellular networks, wireless machine to machine (M2M) communications (e.g., industrial instrumentation), wireless sensor networks (WSNs), unmanned aerial vehicle (UAV) systems, ultra-reliable and low-latency communications (URLLC) for mission-critical scenarios, etc.

Even though most physical phenomena are described by continuous-time analog signals, most communication systems generally follow digital approaches for both digital and analog sources. Digital approaches require discrete-time discrete-amplitude signals as input, hence the original continuous-time analog signals must be first discretized and later quantized. It is known that the original signal can be reconstructed from a sequence of discrete-time samples, up to the Nyquist limit, by passing the sequence of samples through a reconstruction filter. However, quantization is not an invertible operation and, therefore, the original analog signal cannot be perfectly recovered [1]–[3]. Therefore, for digital systems to perform close to their theoretical limit, high complexity quantization methods such as vector quantization (VQ) should be used [4]. A different approach is the analog transmission of discrete-time continuous-amplitude samples as an appealing alternative to the traditional design of digital systems, especially when analog sources must be transmitted with low latency [5].

Conventional digital communication approaches are based on the separation principle [6] to design the source and the channel encoders. However, this strategy suffers from practical issues due to its high complexity and significant delay by considering large size (n) codewords, as well as the need to optimize the encoders for given channel conditions, which leads to the

requirement of accurately tracking the wireless channel and an adaptive design in time-varying communication scenarios. Joint source-channel coding (JSCC) is an alternative approach where the source and channel encoding are performed jointly in a single step. Most works on analog JSCC focus on zero-delay (codewords of size $n = 1$) mappings due to the difficulty of designing and optimizing these mappings for larger dimensions. This restriction limits the practical applicability of analog JSCC with respect to traditional digital approaches, which consider different encoding block sizes. Therefore, a systematic strategy to design analog JSCC mappings for codewords of arbitrary sizes is fundamental to extend the use of these schemes for emerging wireless communication networks. An appropriate JSCC can be employed to combat the fading suffered by the signals in the wireless channels. For example, in mmWave, which is widely considered the frontier for commercial (high volume consumer) wireless communication systems nowadays [7], indoor wall and surface reflections cause severe fading. Therefore, advanced methods of coding play a crucial role for the practical implementation of the communication systems transmitting in this band.

The propagation in mmWave, formally defined as the spectrum between 30 and 300 GHz, is severely vulnerable to blockage. The main benefit of moving to mmWave carrier frequencies is the larger bandwidth available, which entails higher data rates, a timely circumstance to address for the growth of multimedia and mobile data-based services nowadays. The research activity on wireless transmissions over the mmWave band has been intensive during the last five years. However, the first experiments had been performed many years ago [8]. As mentioned, path loss is one of the major issues when using the mmWave band, together with the blockage of direct links and the high cost and power consumption of the mmWave hardware elements [9]. Such severe path loss can be compensated by the use of beamforming through the deployment of a large number of antennas, i.e., via proper precoding/combining in massive MIMO systems. However, the hardware cost and power consumption of digital beamforming with a massive number of antennas, with a radio frequency (RF) chain per antenna element is, in general, extremely high (see [10, Table I]). In order to achieve a suitable trade-off between the power consumption and the flexibility of fully digital solutions, while providing high beamforming gains, hybrid analog-digital transceiver architectures seem to be the best candidates. These architectures are based on decoupling the signal processing of digital beamforming into analog and baseband domains to reduce the number of RF chains [10], [11]. By deploying hybrid architectures in mmWave, the number of data streams to be simultaneously handled is limited by the number of RF chains available at the transceivers. In multiuser (MU) scenarios, a large number of data streams might come from different users to be served by a common base station (BS). Therefore, sophisticated techniques of scheduling must be adopted to face the reduction of the number of RF chains at the BSs while guaranteeing system reliability.

Although novel signal processing techniques are being developed daily to deal with challenging problems in wireless communications, in the current paradigm of wireless network communications, the radio environment itself remains an uncontrollable factor, and thus it is

usually not accounted for in the optimization problems to improve the communications. In radio environments, the signal propagation typically experiences reflections, diffractions, and scattering before reaching the receiver. Such channel effects become a major limiting factor for the growing wireless communication systems. Consequently, the notion of a smart radio environment, which can be adapted to the communication requirements is being reconsidered nowadays. This paradigm had previously been disregarded for scenarios with mobility due to the inability to cope with the dynamic wireless channels [12]. However, nowadays the advances in metamaterials provide certain guarantees for reconfigurability by enabling real-time phase shifts in intelligent reflecting surfaces (IRSs). Consequently, the IRSs are envisioned as key technology for the B5G mobile communication systems [13]. IRS technologies are labeled in the literature under other names as reconfigurable intelligent surfaces, intelligent walls, software-controlled metasurfaces, etc. The implementation of an IRS-assisted system is similar to the use case of half-duplex relays, with the key difference that an IRS implements passive beamforming [14]–[16], i.e., it reflects the incoming signals without amplification and only phase shifts are introduced to the signals, so that the power consumption of the IRS is minimum. In this regard, the IRS-assisted setups can be employed to enhance system performance by enabling more degrees of freedom through the control of the wireless channel. Moreover, metasurfaces can control the radio environment with low power consumption and do not require either analog/digital converters or power amplifiers.

The notion of smart radio has been analyzed in realistic experiments to verify its ability to enhance transmission performance in different wireless networks. In [17], an active wall (active IRS) has been considered by using a frequency-selective surface to smartly control the wireless environment. The experiments in [18] show that, by deploying an IRS in a building, a significant impact on the interference attenuation and the signal strength at the receiver side can be obtained. The IRSs have also received attention from the industry. In November 2018, the mobile operator NTT DoCoMo and the startup MetaWave experimented with the use of IRS technology to assist wireless communications in the frequency band of 28 GHz [19]. Although the IRSs are recently receiving special attention, some complex scenarios lead to challenging design problems still unexplored.

1.1 Motivation

Analog JSCC has been shown to achieve a near-optimal performance at high rates with low complexity and negligible delay when transmitting Gaussian sources over an additive white Gaussian noise (AWGN) channel [20], [21]. Practical implementations of analog JSCC can be found in [22]–[24]. In the literature, most works related to analog JSCC focus on zero-delay mappings over AWGN channels [25]–[27], while more practical scenarios have not been studied in-depth. For this reason, flexible implementations of analog JSCC mappings with arbitrary block size could help to enhance system performance while keeping low latency requirements

in systems with correlated sources. These challenging implementations constitute an interesting research area with applications in WSNs and URLLC.

On the other hand, hybrid digital-analog transceiver architectures represent an interesting approach for the design of low-complexity mmWave MIMO communication systems with hardware constraints. However, limited works have been considered so far for strongly hardware-constrained wideband MU MIMO scenarios. The authors in [28] and [29] considered MU setups with more than one phase shifter (PS) for each RF chain connection to a single antenna, thus leading to complex hybrid architectures. The authors in [30] developed a projected gradient (PG) algorithm to leverage the common structure of the channel response matrices among different subcarriers in wideband scenarios. All these works assume that the number of RF chains is at least equal to the number of individual data streams to be transmitted, therefore the developed algorithms are not suitable for scenarios, where the number of RF chains is lower than the number of data streams. Moreover, most works do not account for the beam squint effect and its critical impact on the interference cancellation in wideband systems. An exception is [31], where a linear successive allocation (LISA) algorithm is developed by considering this effect. For that, the design of hardware-constrained hybrid transceivers in wideband MU mmWave MIMO systems in the face of beam squint constitutes a challenging and innovative approach for applications in WSNs and cellular networks. In particular, user grouping schemes joined to non-orthogonal analog JSCC mappings could be beneficial to transmit a large number of user streams with a limited number of RF chains.

Although great efforts in the research activity are devoted to the precoding/filtering design to compensate for the channel effects and enhance the performance in the communication systems, the radio channel itself had usually remained uncontrollable. Fortunately, the paradigm of radio communication control via IRSs is receiving special attention nowadays [15], [32]–[35]. The applications of IRSs to reconfigure the wireless channels in different scenarios are immense: device-to-device (D2D) communications, cognitive radio (CR), UAV systems, etc. However, the interest in IRS-aided wireless communication systems is still recent and a large number of use cases remain unexplored. Most works assume narrowband communication systems and do not consider some practical issues as imperfect channel state information (CSI). The use of IRS technology for wideband mmWave communications has not received in-depth treatment in the literature. Therefore, scenarios of wideband MU IRS-aided mmWave MIMO systems under imperfect CSI constitute a timely and interesting approach for a large variety of communication scenarios.

1.2 Contributions

The work presented in this thesis led to the co-authored publications included in Subsection 1.2.1. Although the main work of the thesis is based on the articles in Subsection 1.2.1, the Ph.D. candidate has also contributed to the publications cited in

Subsection 1.2.2. During the development of this thesis, the author collaborated in the research projects included in Subsection 1.2.3 and Subsection 1.2.4.

1.2.1 Publications

JCR Journal Papers

1. Darian Pérez-Adán, Óscar Fresnedo, José P. González-Coma, and Luis Castedo, "**User grouping for the uplink of multiuser hybrid mmWave MIMO**", *IEEE Access*, vol. 8, pp. 55 323–55 341, 2020.
   DOI: 10.1109/ACCESS.2020.2981280.
2. Darian Pérez-Adán, Óscar Fresnedo, José P. González-Coma, and Luis Castedo, "**Wideband user grouping for uplink multiuser mmWave MIMO systems with hybrid combining**", *IEEE Access*, vol. 9, pp. 41 360–41 372, 2021.
   DOI: 10.1109/ACCESS.2021.3065581.
3. Darian Pérez-Adán, Óscar Fresnedo, José P. González-Coma, and Luis Castedo, "**Intelligent reflective surfaces for wireless networks: An overview of applications, approached issues, and open problems**", *Electronics*, vol. 10, no. 19, 2021, ISSN: 2079-9292.
   DOI: 10.3390/electronics10192345. Online access: https://www.mdpi.com/2079-9292/10/19/2345.
4. Darian Pérez-Adán, Michael Joham, Óscar Fresnedo, José P. González-Coma, Luis Castedo, and Wolfgang Utschick, "**An alternating minimization approach for wideband downlink multiuser IRS-aided mmWave MIMO systems**", *In Preparation for IEEE Transactions on Signal Processing*, pp. 1–13, 2022.
5. Pedro Suárez-Casal, Óscar Fresnedo, Darian Pérez-Adán, and Luis Castedo, "**Lattice-based analog mappings for low latency wireless sensor networks**", *Submitted to IEEE Internet of Things Journal*, pp. 1–15, 2022.

International Conference Papers

1. Darian Pérez-Adán, José P. González-Coma, Óscar Fresnedo, and Luis Castedo, "**Hybrid mmWave MIMO transceivers for the uplink of multiple correlated users**", *Proc. of 2019 IEEE 20th International Workshop on Signal Processing Advances in Wireless Communications (SPAWC)*, 2019, pp. 1–5.
   DOI: 10.1109/SPAWC.2019.8815403.
2. Darian Pérez-Adán, José P. González-Coma, Óscar Fresnedo, and Luis Castedo, "**Low-complexity hybrid transceivers for uplink multiuser mmWave MIMO by user clustering**", *Proc. of 2019 27th European Signal Processing Conference (EUSIPCO)*, 2019, pp. 1–5.
   DOI: 10.23919/EUSIPCO.2019.8902982.

3. Pedro Suárez-Casal, Óscar Fresnedo, José P. González-Coma, Darian Pérez-Adán, and Luis Castedo, "**Analog transmission of correlated sources in SIMO MAC using hexagonal lattices**", *Proc. of WSA 2020; 24th International ITG Workshop on Smart Antennas*, 2020, pp. 1–6.
4. Darian Pérez-Adán, Óscar Fresnedo, José P. González-Coma, and Luis Castedo, "**Hybrid combining design for user clustering in mmWave MIMO systems**", *Proc. of 2020 IEEE Workshop on Signal Processing Systems (SiPS)*, 2020, pp. 1–6.
DOI: 10.1109/SiPS50750.2020.9195228.
5. Darian Pérez-Adán, Óscar Fresnedo, José P. González-Coma, and Luis Castedo, "**Alternating minimization algorithm for multiuser RIS-assisted MIMO systems**", *Proc. of 2022 IEEE International Symposium on Broadband Multimedia Systems and Broadcasting (BMSB)*, 2022, pp. 1–6.
DOI: 10.1109/BMSB55706.2022.9828734.
6. Darian Pérez-Adán, Michael Joham, Óscar Fresnedo, José P. González-Coma, Wolfgang Utschick, and Luis Castedo, "**Alternating minimization for the downlink of wideband IRS-aided mmWave MIMO systems**", *Submitted to 2023 International ITG 26th Workshop on Smart Antennas and 13th Conference on Systems, Communications, and Coding*, pp. 1–6.

Note that all the journals appear in the Journal Citation Reports (JCR) in the corresponding publication year. The Journal Impact Factor (JIF), the JIF rank, the JIF quartile, and the JIF percentile are detailed in Table 1.1.

Table 1.1: Rank by JCR of publication journals.

Journal	Year	IF	Category	IF Rank	IF Q.	IF P.
IEEE Access	2020	3.367	ENGINEERING, ELECTRICAL & ELECTRONIC	94/273	2	65.75
IEEE Access	2021	3.476	ENGINEERING, ELECTRICAL & ELECTRONIC	105/276	2	62.14
Electronics	2021	2.690	ENGINEERING, ELECTRICAL & ELECTRONIC	139/276	3	49.82
IEEE Transactions on Signal Processing	2021	4.875	ENGINEERING, ELECTRICAL & ELECTRONIC	66/276	1	76.27
IEEE Internet of Things Journal	2021	10.238	COMPUTER SCIENCE, INFORMATION SYSTEMS	9/164	1	94.82

1.2.2 Publications Beyond the Scope of the Thesis

JCR Journal Papers

1. Dariel Pereira-Ruisánchez, Óscar Fresnedo, Darian Pérez-Adán, and Luis Castedo, "**Deep contextual bandit and reinforcement learning for IRS-assisted MU-MIMO systems**", *Submitted to IEEE Transactions on Vehicular Technology (2nd round of reviews)*, pp. 1–12. Impact factor 2022: 6.239 (IF Q: Q1, IF Rank: 32/276, IF P. 86.41, Category: ENGINEERING, ELECTRICAL & ELECTRONIC).

International Conference Papers

1. Dariel Pereira-Ruisánchez, Óscar Fresnedo, Darian Pérez-Adán, and Luis Castedo, "**Joint optimization of IRS-assisted MU-MIMO communication systems through a DRL-based twin delayed DDPG approach**", *Proc. of 2022 IEEE International Symposium on Broadband Multimedia Systems and Broadcasting (BMSB)*, 2022, pp. 1–6. DOI: 10.1109/BMSB55706.2022.9828652.
2. Dariel Pereira Ruisánchez, Dalila Garrido Mirabal, Ernesto Fontes Pupo, Claudia Carballo González, Darian Pérez-Adán, and Flavia Alvarez Cesar, "**Prediction of signal quality and SFN interference metrics using machine learning models**", *Proc. of 2021 IEEE International Symposium on Broadband Multimedia Systems and Broadcasting (BMSB)*, 2021, pp. 1–6.
   DOI: 10.1109/BMSB53066.2021.9547111.

National Conference Papers

1. Dariel Pereira-Ruisánchez, Darian Pérez-Adán, and Luis Castedo, "**A deep learning-based strategy to predict self-interference in SFN DTT**", *Proc. of The 4th XoveTIC Conference, Engineering Proceedings*, vol. 7, no. 1, pp. 1–4, 2021.
2. Dariel Pereira-Ruisánchez, Óscar Fresnedo, Darian Pérez-Adán, and Luis Castedo, "**Joint optimization of IRS-assisted MIMO communications through a deep contextual bandit approach**", *Proc. of The 5th XoveTIC Conference, Engineering Proceedings*, pp. 1–4, 2022.

1.2.3 Main Research Projects

The work performed in this thesis contributed to the following research projects:

- CARMEN: This project addressed two major trends in wireless networks: radio interfaces with unprecedented high data rates and WSN. The aims were to develop advanced coding and signal processing techniques for emerging wireless communication and sensor networks. CARMEN also carried out the experimental evaluation of coding and signal processing techniques by means of over-the-air (OTA) transmissions and simulations.

  - Reference: TEC2016-75067-C4-1-R.
  - Funding entity: State Research Agency.
  - Funding: €227 359.
  - Duration: 2 years and 6 months.
- ADELE: The mission of this project is twofold. First, it will develop advanced coding and signal processing techniques for wireless communication networks. Furthermore, the project will address long-term objectives and will contribute significantly to (a) coding and information theory for quantum computing and communications, and (b) machine learning (ML) methods and the emerging field of graph signal processing for the analysis and operation of networks that handle massive amounts of data including, but not limited to, wireless communication networks.
  - Reference: PID2019-104958RB-C42.
  - Funding entity: State Research Agency.
  - Funding: €214 775.0.
  - Duration: 2 years and 5 months.

1.2.4 Research Project Beyond the Scope of the Thesis

The Ph.D. candidate also participated for 2 months in the following project related to other issues:

- INRA-CBTC: The project was intended to develop tools for the validation of a Long Term Evolution (LTE) network specially adapted to the railway environment. These tools were destined to evaluate the fulfillment of the communications-based train control (CBTC) requirements by measuring the performance of the deployed network in terms of packet error ratio (PER), delay, and jitter.
  - Funding entity: CAF Signalling S.L. and the CDTI entity of the Spanish Ministry of Science and Innovation.
  - Funding: €262 487.86.
  - Duration: 2 years and 7 months.

1.3 Thesis Overview

Three different research lines can be distinguished in this thesis. Firstly, a study of analog JSCC techniques suitable for wireless communications is performed. Next, the design of hybrid transceivers for narrowband and wideband MU mmWave MIMO systems is addressed, and a user grouping approach leveraging on the features of distributed quantizer linear coding (DQLC) is developed. Finally, the wireless communication paradigm related to the control of the propagation environment through IRSs is approached.

The remainder of this thesis is structured as follows. In Chapter 2, we introduce the general

system model of an analog JSCC wideband MU MIMO system, which is next particularized in the different approaches addressed throughout this thesis. We provide relevant details about MIMO orthogonal frequency-division multiplexing (OFDM) systems, the source correlation model assumed in this thesis, and the multiple access channel (MAC) and broadcast channel (BC) system models. The relationship between the MAC and the BC is explained through the MAC-BC and the BC-MAC dualities. The channel models considered in this thesis are also described.

In Chapter 3, we approach the transmission of correlated sources over fading MU single-input multiple-output (SIMO) MAC systems by implementing analog JSCC mappings based on multidimensional lattices. Different lattice constructions are analyzed, and the impact of the lattice size and thus the delay caused by the encoding process is also addressed, as well as the impact of the lattice density on the overall system performance. At the receiver, the correlation between the user symbols is exploited by jointly decoding the information received from all users with the minimum mean square error (MMSE) estimator. However, the huge computational cost of the decoding operation would make the proposed system impractical, even for a small number of users. Therefore, a sphere decoder is employed to simplify the required search in the lattice space, thus lowering the overall complexity of the system. Comparisons of the system performance by employing the different lattice constructions in different scenarios of encoded correlated sources are performed. It is shown that, by enabling the encoding with different codeword sizes, lattice-based JSCC provides gains with respect to existing zero-delay analog JSCC schemes.

In Chapter 4, by enabling inter-user correlation exploitation, a user grouping approach for the uplink of a narrowband MU hybrid mmWave MIMO system is addressed to handle a high number of sources with a limited number of RF chains with the help of DQLC mappings. The allocation of the users per group and the hybrid design of the filter at the BS to serve the gathered users is also studied. Furthermore, a hybrid MMSE combining design is proposed in order to exploit the spatial correlation between the sources in a conventional uncoded uplink of a mmWave MIMO system. The proposed solution is compared with different state-of-art approaches for hybrid transceivers, and considerable performance gains are obtained. The user grouping approach in Chapter 4 is extended in Chapter 5 to wideband MU mmWave MIMO systems affected by beam squint. In particular, a user grouping and a scheduling strategy for wideband scenarios that considers the beam squint effect and the hybrid transceiver design are proposed.

In Chapter 6, the downlink of a wideband MU IRS-aided mmWave MIMO system under imperfect CSI is approached. This scenario presents some challenging issues as the design of the IRS phase-shift matrix, which is frequency flat and common to all the users, as well as the design of the frequency-dependent precoders at the BS and the receiving filters at the users by considering the estimation error of the CSI. The IRS phase-shift matrix, the filters and the precoders are jointly designed to minimize the mean squared error (MSE) of the estimated

user symbols by considering the statistical of the errors produced in the CSI estimation. The optimization problem is solved by employing the BC-MAC duality and following an alternating PG minimization approach. Substantial gains are achieved with respect to baseline strategies that neglect the imperfect CSI and the inter-user interference control.

Finally, Chapter 7 is devoted to the main conclusions derived from this work and the future research lines.

1.4 Notation

Table 1.2: Symbols and math operators.

Symbol / Operator	Description
$(\bullet)^T$, $(\bullet)^*$, $(\bullet)^\dagger$	Transpose, conjugate transpose, Moore-Penrose pseudoinverse
$\| \bullet \|_2$, $\| \bullet \|_F$	2-norm, Frobenius norm
$\Re(\bullet)$, $\Im(\bullet)$	Real part, imaginary part
$\mathbb{R}$, $\mathbb{C}$	Set of real numbers, set of complex numbers
$\mathbf{I}_N$,$\mathbf{0}_N$	Identity matrix with size N, all zeros matrix with size N
$[\mathbf{A}]_{i,j}$	Entry on the i-th row and the j-th column of $\mathbf{A}$
$[\mathbf{A}]_{i,:}$, $[\mathbf{A}]_{:,j}$	i-th row of $\mathbf{A}$, j-th column of $\mathbf{A}$
$[\mathbf{A}]_{\overline{i:n},:}$	Removing from the i-th row to the n-th row
$\mathrm{span}(\mathbf{A})$	Subspace spanned by the columns of $\mathbf{A}$
$\mathrm{Null}(\mathbf{A})$	Null space of $\mathbf{A}$
blkdiag $(\bullet)$	Construction of a block diagonal matrix from input matrices
tr$(\mathbf{A})$, diag$(\bullet)$	Trace of $\mathbf{A}$, diagonal matrix with the argument in the main diagonal
$\lfloor \bullet \rceil$, $\lfloor \bullet \rfloor$, $\lceil \bullet \rceil$	Element-wise rounding, floor operation, ceiling operation
$\mid a \mid$, $\mid \mathbf{A} \mid$, $\mid \mathcal{A} \mid$	Absolute value of a, determinant of the matrix $\mathbf{A}$, cardinally of the set $\mathcal{A}$
$\mathcal{A} \setminus b$	Exclusion of the element b from the set $\mathcal{A}$
mod $(\mathbf{a}, \mathbf{b})$	Element-wise modulo operation that returns for each vector element
$\mathcal{N}_{\mathbb{C}}(\boldsymbol{\mu}, \mathbf{C})$	Circularly-symmetric complex normal distribution with mean $\boldsymbol{\mu}$ and covariance matrix $\mathbf{C}$
$\circledast$, $\otimes$	Column-wise Khatri-Rao product, Kronecker product
$*$	Convolution
$\mathbb{E}[\bullet]$	Statistical expectation

In this thesis, the following notation is used: upper and lower case italic letters as a and A denote scalars, lower case bold letters, e.g., $\mathbf{a}$, denote vectors, whereas the matrices are denoted by bold uppercase letters such as $\mathbf{A}$. $[\mathbf{A}]_{i,j}$ is the entry on the i-th row and the j-th column of the matrix $\mathbf{A}$, $[\mathbf{A}]_{i,:}$ stands for the i-th row of $\mathbf{A}$, and $[\mathbf{A}]_{:,j}$ represents the j-th column of $\mathbf{A}$. We use the notation $[\mathbf{A}]_{\overline{i:n},:}$ to indicate the resulting matrix after removing from the i-th to the n-th row of $\mathbf{A}$. The operator $\mathrm{span}(\mathbf{A})$ denotes the subspace spanned by the columns of the

matrix $\mathbf{A}$. $\mathrm{Null}(\mathbf{A})$ is an operator that constructs an orthonormal basis for the null space of the input matrix. The operator that constructs a block diagonal matrix from input matrices is denoted as $\mathrm{blkdiag}(\bullet)$. Calligraphic letters such as $\mathcal{A}$ are used to denote sets and sequences, and $\mathcal{A} \setminus b$ represents the exclusion of the element b from $\mathcal{A}$. Finally, a list of the math symbols and operators used in this thesis is summarized in Table 1.2.

Chapter II

Modeling of Wideband Multiuser Wireless Communications

In this chapter, we introduce fundamental concepts about wideband MU wireless communications, including their system model and some assumptions adopted throughout this thesis. The chapter is structured as follows. The main issues and advantages of wideband wireless communication systems are presented in Section 2.1. The source model employed throughout this thesis and the encoding of single-user OFDM-based wideband systems are explained in Section 2.2. Section 2.3 offers the main details about wideband MU MIMO systems by explaining the system models for MAC and BC systems, whereas the MAC-BC and the BC-MAC dualities in terms of MSE are discussed in Section 2.4. Finally, Section 2.5 presents the channel models employed in the different systems considered in this thesis, and Section 2.6 is devoted to the chapter conclusions.

2.1 Introduction

Wireless communications are characterized by the difficulty of predicting the channel behavior [52]. Transmitted radio signals usually propagate through several paths before arriving at the receiver (multipath propagation). Consequently, a superposition of multiple versions of the transmitted signal experiencing different delays and phase shifts due to various effects, such as scattering, reflection, diffraction, or refraction, is received, leading to system performance degradation. These effects have been widely studied in the literature (see [53, Chapter 4] and [54, Chapter 2] for details related to the multipath effects).

In this scenario, the deployment of multiple antennas at both communication ends (i.e., MIMO systems) can be used to increase reliability due to the diversity gain. Furthermore, a MIMO channel can also provide additional gains and degrees of freedom from the spatial dimension allowing the transmission of several independent data streams [53].

A communication system is considered to be wideband when the bandwidth required

to transmit the source message significantly exceeds the channel coherence bandwidth, thus leading to frequency-selective fading [52]–[55]. When considering single-carrier transmission schemes, wideband wireless systems demand time-domain equalization at the receiver to combat the delay spread effects. However, the number of taps required to ensure a good performance in high data rate transmissions is usually large. Therefore, the equalizers become quite complex and can introduce a large delay. Such drawbacks can be overcome by the use of multicarrier modulations such as OFDM [56].

OFDM effectively decomposes a wideband frequency-selective channel into a set of non-interfering flat fading subchannels (each having a bandwidth lower than the coherence bandwidth of the channel) [57]. Therefore, the available bandwidth is split into L orthogonal subcarriers in the frequency domain. Consequently, the overall data stream is divided into L parallel substreams, each modulated into one subcarrier and sent over the corresponding narrowband subchannel. Preceding each OFDM symbol, there is a cyclic prefix longer than the delay spread of the channel, so the inter-symbol interference (ISI) effects are eliminated [58], [59]. Moreover, OFDM is robust against frequency-selectivity without complex equalization filters [53]. The transmission method adopted by the last generation of broadband systems combines OFDM with the MIMO technology (referred to as MIMO-OFDM), thus achieving large spectral efficiencies over frequency-selective channels with low-complexity equalization (see [53, Chapter 9] and [56, Chapter 5] for details).

2.2 Source Model and Encoding

Throughout this thesis, source symbols are modeled as the vector $\mathbf{s}$ of zero-mean circularly symmetric complex Gaussian random variables with covariance matrix $\mathbf{C}_{\mathrm{s}} = \mathbb{E}\left[\mathbf{s}\mathbf{s}^{*}\right]$. The elements $[\mathbf{C}_s]_{i,j} = \rho_{i,j}$ represent the correlation between the i-th and j-th source symbols in $\mathbf{s}$. Without loss of generality (w.l.o.g.), we assume that $\rho_{i,i} = \sigma_{\mathrm{s}}^2, \forall i$. We also consider that source symbols corresponding to different time instants are statistically independent so that only the spatial correlation between different sources is considered. When the wideband model is adopted, we consider the same covariance matrix for the user symbols in the different subcarriers ℓ such that $\mathbf{C}_{\mathrm{s}} = \mathbf{C}_{\mathrm{s}}[\ell], \forall \ell = 1, \ldots, L$.

Throughout this document, we will assume two correlation models

- An equal correlation model where the correlation between any two symbols produced by the different sources is the same, i.e., $[\mathbf{C_s}]_{i,i} = 1 \ \ \forall i = 1, \ldots, K$ and $[\mathbf{C_s}]_{i,j} = \rho \ \ \forall i \neq j$.
- An exponential correlation model where the correlation between the sources is different and the coefficients of the covariance matrix are given by $[\mathbf{C}_{\mathrm{s}}]_{i,j} = \rho^{|i-j|}, \ \forall \ i, j$.

Since the sources are continuous-amplitude and discrete-time, we simplify the transmission model by considering that they are analog encoded. This way we avoid quantization, latency and complexity issues related to source and channel coding. In the following, we describe the encoding of wideband communication systems via analog JSCC over MIMO-OFDM in a single

stream point-to-point system. We assume real-valued source symbols for simplicity. However a real-valued equivalent model can be used for complex-valued symbols (see Appendix A).

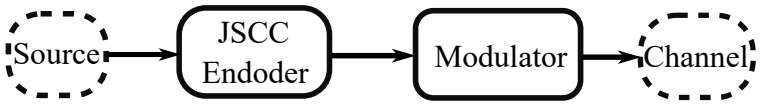

Figure 2.1: Block diagram of a JSCC system.

Analog JSCC represents a set of techniques that combine analog source and channel coding into a single operation (see Figure 2.1) instead of implementing them separately. According to this premise, analog JSCC approaches directly transform continuous-amplitude source symbols into channel symbols to be transmitted, by using continuous mappings [60]. These systems constitute a low-complexity alternative for transmitting analog sources with a negligible delay. Analog JSCC systems also appeal to their robustness against time-varying channel conditions and their capacity to adapt the system as the channel conditions change.

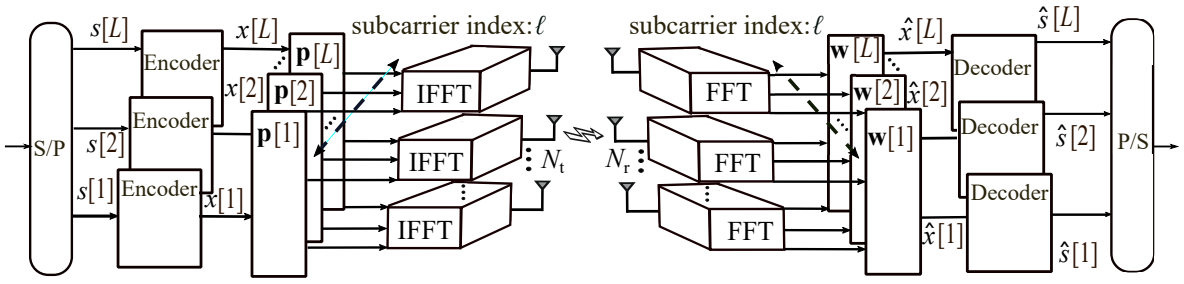

Figure 2.2: Block diagram of the MIMO-OFDM system with analog encoding.

As explained, OFDM splits the wideband channel into a set of non-interfering orthogonal narrowband subchannels. The number of subcarriers L is selected such that each subchannel has a bandwidth smaller than the channel coherence bandwidth. Figure 2.2 shows the block diagram of a point-to-point analog JSCC MIMO-OFDM scheme where the transmitter is equipped with N_t antennas and the receiver deploys N_r antennas. Let $s_t[\ell]$ be the real-valued source symbol transmitted at time instant t over the subcarrier ℓ. Assuming $t = 1, \ldots, n$, $\mathbf{s}[\ell] = [s_1[\ell], \ldots, s_n[\ell]]^T$ is the vector of n consecutive source symbols transmitted over the subcarrier ℓ. The operator $f[\ell](\cdot) : \mathbb{R}^n \to \mathbb{R}^n$ represents the mapping function which produces the vector of encoded symbols $\mathbf{x}[\ell] = f[\ell](\mathbf{s}[\ell])$ such that $\mathbf{x}[\ell] = [x_1[\ell], \ldots, x_n[\ell]]^T$. Note that n stands for the size of the source and encoded symbols block and that $n = 1$ constitutes the particular case of zero-delay mappings [61]. For these cases, the index n is disregarded (see e.g., Figure 2.2).

The received signal at the time instant t over the subcarrier ℓ is given by

$$\mathbf{y}_t[\ell] = \mathbf{H}[\ell]\mathbf{p}[\ell]x_t[\ell] + \boldsymbol{\eta}_t[\ell], \tag{2.1}$$

where $\boldsymbol{\eta}_t[\ell] = \left[\eta_{t1}[\ell], \eta_{t2}[\ell], \ldots, \eta_{tN_\mathrm{r}}[\ell]\right]^T$ stands for the complex-valued AWGN modeled as $\boldsymbol{\eta}[\ell] \sim \mathcal{N}_\mathbb{C}(0, \sigma_\eta^2 \mathbf{I}_{N_\mathrm{r}})$, $\mathbf{H}[\ell] \in \mathbb{C}^{N_\mathrm{r} \times N_\mathrm{t}}$ is the MIMO channel, and $\mathbf{p}[\ell] \in \mathbb{C}^{N_\mathrm{t}}$ is the precoder

employed prior to transmit the symbols at subcarrier ℓ. A power constraint is imposed, i.e., $\| \mathbf{p} \|_F^2 \leq P_{\mathrm{T}}[\ell]$ being $P_{\mathrm{T}}[\ell]$ the power available at subcarrier ℓ. At the receiver, the signal $\mathbf{y}_t[\ell]$ is filtered with $\mathbf{w}[\ell] \in \mathbb{C}^{N_{\mathrm{r}}}$ such that $z_t[\ell] = \mathbf{w}^*[\ell]\mathbf{y}_t[\ell]$. Finally, the estimated symbols are obtained as $\hat{\mathbf{s}}[\ell] = q[\ell](\mathbf{z}[\ell])$, with $\mathbf{z}[\ell] = [z_1[\ell], \ldots, z_n[\ell]]^T$ and $q[\ell](\cdot) : \mathbb{R}^n \rightarrow \mathbb{R}^n$ the decoding function. When considering the transmission of analog sources, MMSE decoding is optimum as it minimizes the observed distortion according to the MSE criterion. The MMSE estimator of the source symbols $\hat{\mathbf{s}}[\ell]$ from the received symbols $\mathbf{z}[\ell]$ is given by [62]

$$\hat{\mathbf{s}}[\ell] = \mathbb{E}[\mathbf{s} \mid \mathbf{z}[\ell]] = \int \mathbf{s}\, p_{\mathrm{s}}(\mathbf{s} \mid \mathbf{z}[\ell])\, d\mathbf{s}. \tag{2.2}$$

2.3 Wideband Multiuser Wireless Communications

As previously explained, MIMO stands for a communication system model in which a multi-antenna node sends/receives information to/from several multi-antenna nodes [63]. The MIMO BC arises when modeling a large number of practical situations in wireless communications, typically in the downlink of cellular systems, where a multi-antenna BS communicates to several multi-antenna receive users. The BC is the dual of the MAC, where several decentralized multi-antenna transmitters (users) send information to a centralized multi-antenna receiver (BS). The MAC is a model that typically arises when considering the uplink in a cellular system and WSNs. Regarding wireless communications, less complex schemes than MU MIMO according to the number of antennas used by the transmitter and the receiver can be found in the literature. When all terminals employ a single antenna, the term single-input-single-output (SISO) is used to label both the BC and the MAC setups. Since the performance is significantly improved if several antennas are deployed, the BSs are usually terminals with larger resources in terms of power supply, computational complexity and antenna array size in practical scenarios. In such a case, the BC is labeled multiple-input single-output (MISO) and the MAC is labeled SIMO.

In the following, the system models for wideband MAC and BC scenarios are described, as well as the sum-MSE concept to measure the performance of analog MU systems. We omit the encoding process explained in Section 2.2 for simplicity and consider multistream schemes.

2.3.1 Mean Squared Error

The MSE of an estimator constitutes a measure of how close the estimator is to the true data. The difference between the true data and the estimator is the error. By considering wideband OFDM (L subcarriers) MU (K users) schemes, the MSE per user at a given subcarrier is formally defined as the average of the squared errors. i.e., $\mathbb{E}\left[|\hat{s}_k[\ell] - s_k[\ell]|^2\right]$, where $s_k[\ell],\ \forall \ell, k$ is the true symbol corresponding to the k-th user at subcarrier ℓ, and $\hat{s}_k[\ell]$ is the estimated data at the receiver. In order to evaluate the overall system performance in practical MU OFDM MIMO

scenarios, the MSE is usually defined in based to the number of realizations, N, as

$$\hat{\xi}_{\text{sum}} = \frac{1}{NLK} \sum_{n=1}^{N} \sum_{\ell=1}^{L} \sum_{i=1}^{K} |s_{n,k}[\ell] - \hat{s}_{n,k}[\ell]|^2. \tag{2.3}$$

The performance of an analog transmission system is commonly measured in terms of the signal-to-distortion ratio (SDR) expressed in dB, i.e

$$\text{SDR (dB)} = 10 \log_{10} \left(\frac{\sigma_{\text{s}}^2}{\hat{\xi}_{\text{sum}}} \right), \tag{2.4}$$

where σ_{s}^2 is the data power and the MSE is used as the performance metric due to the continuous nature of the source information [20].

2.3.2 BC System Model

A BC setup, also commonly named downlink, is a communication system where a single transmitter serves several users, e.g., a WiFi router sending information to different devices, a BS communicating to different users in a cellular system, etc. A downlink wideband MU multistream MIMO OFDM system is shown in Figure 2.3. The wireless channels between the BS and the users $\left(\mathbf{H}_k[\ell] \in \mathbb{C}^{N_{\text{r}} \times N_{\text{t}}}, \forall k\right)$ are assumed to be frequency-selective. An OFDM modulation format is also assumed to have L orthogonal subcarriers and a cyclic prefix long enough to avoid ISI. This way, the frequency-selective channels are decomposed into L parallel narrowband subchannels. The complex-valued symbols vector sent by the BS to the k-th user at subcarrier ℓ is denoted by $\mathbf{s}_k[\ell] \in \mathbb{C}^{N_{\text{s},k}[\ell]}$, where $N_{\text{s},k}[\ell]$ stands for the number of data streams allocated to the k-th user at subcarrier ℓ with $k = 1, \ldots, K$ and $\ell = 1, \ldots, L$. Thus, the total number of streams allocated at subcarrier ℓ is $N_{\text{s}}[\ell] = \sum_{k=1}^{K} N_{\text{s},k}[\ell]$. The symbols sent by the BS are usually linearly precoded prior to be transmitted with $\mathbf{P}_k[\ell] \in \mathbb{C}^{N_{\text{t}} \times N_{\text{s},k}[\ell]}$. These precoders are subject to a per-subcarrier transmit power constraint, i.e., $\sum_{k=1}^{K} \text{tr}\Big(\mathbf{P}_k[\ell]\mathbf{P}_k^*[\ell]\Big) \leq P_{\text{T}}[\ell]$, being $P_{\text{T}}[\ell]$ the available transmit power at subcarrier ℓ.

According to this formulation, the signal received by the k-th user at subcarrier ℓ reads as

$$\mathbf{y}_k[\ell] = \mathbf{H}_k[\ell] \sum_{u=1}^{K} \mathbf{P}_u[\ell]\mathbf{s}_u[\ell] + \boldsymbol{\eta}_k[\ell], \tag{2.5}$$

where $\boldsymbol{\eta}_k[\ell] = \left[\eta_{k1}[\ell], \eta_{k2}[\ell], \ldots, \eta_{kN_{\text{r}}}[\ell]\right]^T$ represents the complex-valued AWGN modeled as $\boldsymbol{\eta}_k[\ell] \sim \mathcal{N}_{\mathbb{C}}(0, \sigma_\eta^2 \mathbf{I}_{N_{\text{r}}})$. Each user estimates its symbols $\hat{\mathbf{s}}_k[\ell]$ at subcarrier ℓ by applying the linear filter $\mathbf{W}_k[\ell] \in \mathbb{C}^{N_{\text{s},k}[\ell] \times N_{\text{r}}}$, that is, $\hat{\mathbf{s}}_k[\ell] = \mathbf{W}_k[\ell]\mathbf{y}_k[\ell]$. In this case, the receive filter that minimizes the MSE between the transmitted symbols to the k-th user and the received symbols is given by [62]

$$\mathbf{W}_{\text{MMSE}_k}[\ell] = \mathbf{P}_k^*[\ell]\mathbf{H}_k^*[\ell] \left(\mathbf{H}_k[\ell]\mathbf{P}_k[\ell]\mathbf{P}_k^*[\ell]\mathbf{H}_k^*[\ell] + \mathbf{Y}_k[\ell]\right)^{-1}, \tag{2.6}$$

where $\mathbf{Y}_k[\ell] \in \mathbb{C}^{N_\mathrm{r} \times N_\mathrm{r}}$ is the interference-plus-noise matrix given by

$$\mathbf{Y}_k[\ell] = \sum_{i \neq k} \mathbf{H}_k[\ell]\mathbf{P}_i[\ell]\mathbf{P}_i^*[\ell]\mathbf{H}_k^*[\ell] + \sigma_\eta^2 \mathbf{I}_{N_\mathrm{r}}.$$

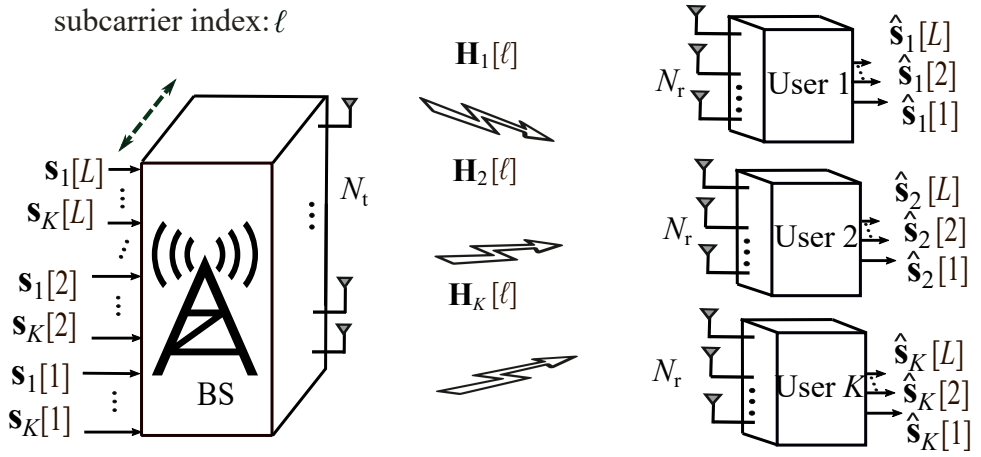

Figure 2.3: Block diagram of the downlink in a wideband MU MIMO-OFDM system with K users and L subcarriers.

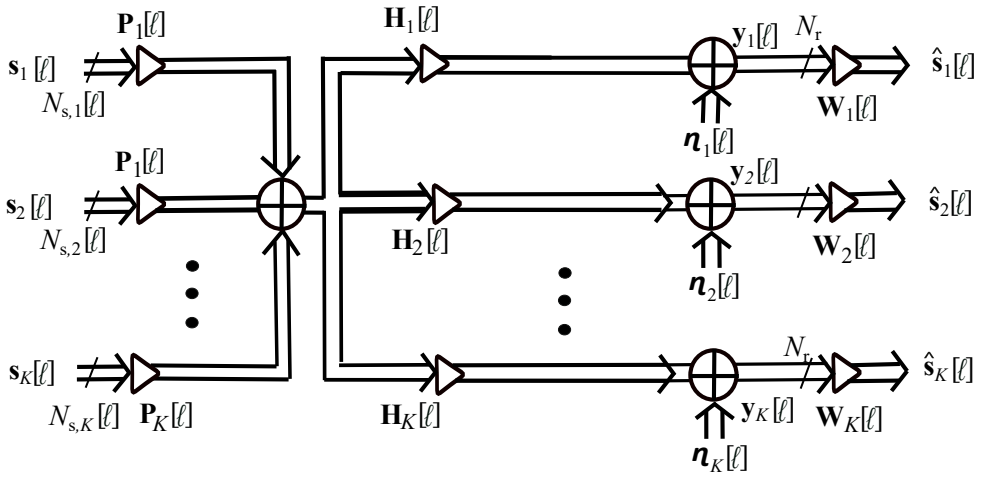

Figure 2.4: Block diagram of the downlink MU MIMO-OFDM system with K users at subcarrier ℓ.

Note that the MU received signal after filtering at the ℓ-th subcarrier can be represented by means of the following compact expression

$$\hat{\mathbf{s}}[\ell] = \mathbf{W}[\ell]\mathbf{H}[\ell]\mathbf{P}[\ell]\mathbf{s}[\ell] + \mathbf{W}[\ell]\boldsymbol{\eta}[\ell], \tag{2.7}$$

where $\hat{\mathbf{s}}[\ell] = \left[\hat{\mathbf{s}}_1^T[\ell], \ldots, \hat{\mathbf{s}}_K^T[\ell]\right]^T \in \mathbb{C}^{N_\mathrm{s}[\ell]}$, $\mathbf{s}[\ell] = \left[\mathbf{s}_1^T[\ell], \ldots, \mathbf{s}_K^T[\ell]\right]^T \in \mathbb{C}^{N_\mathrm{s}[\ell]}$, $\boldsymbol{\eta}[\ell] = \left[\boldsymbol{\eta}_1^T[\ell], \ldots, \boldsymbol{\eta}_K^T[\ell]\right]^T \in \mathbb{C}^{N_\mathrm{r}K}$ and $\mathbf{H}[\ell] = \left[\mathbf{H}_1^T[\ell], \ldots, \mathbf{H}_K^T[\ell]\right]^T \in \mathbb{C}^{N_\mathrm{r}K \times N_\mathrm{t}}$ result from stacking all the estimated user symbols, the source symbols sent to all the users, the overall noise and the channels, respectively, at subcarrier ℓ, whereas $\mathbf{P}[\ell] = [\mathbf{P}_1[\ell], \ldots, \mathbf{P}_K[\ell]] \in \mathbb{C}^{N_\mathrm{t} \times N_\mathrm{s}[\ell]}$ and $\mathbf{W}[\ell] = \mathrm{blkdiag}\left(\mathbf{W}_1[\ell], \ldots, \mathbf{W}_K[\ell]\right) \in \mathbb{C}^{N_\mathrm{s}[\ell] \times N_\mathrm{r}K}$ gather all the BS precoders and the user filters, respectively, at the ℓ-th subcarrier (see Figure 2.4).

2.3.3 MAC System Model

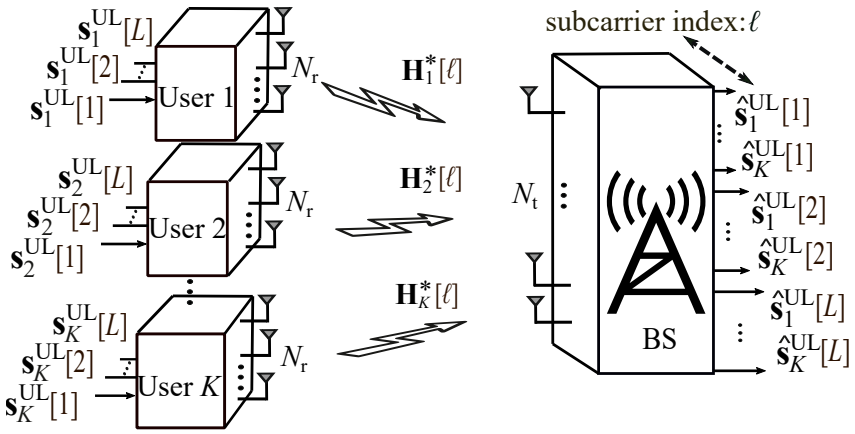

Figure 2.5: Block diagram of the uplink MU MIMO-OFDM system with K users and L subcarriers.

In MAC systems (also referred to as the uplink), multiple users share the same transmission medium to communicate to a centralized receiver node. In this scenario, the users may have one or more antennas while the BS is often equipped with more than one. The data flow is the opposite to that in the BC system shown in Figure 2.3. MAC constitutes the typical scenario in cellular systems when mobile users communicate with the BS. Figure 2.5 shows the uplink of a wideband MU MIMO OFDM system, where the BS is equipped with N_{t} antennas and the users have N_{r} antennas each. Let $\mathbf{s}_k^{\mathrm{UL}}[\ell] \in \mathbb{C}^{N_{\mathrm{s},k}[\ell]}$ be the vector of uplink complex-valued symbols transmitted by the users over subcarrier ℓ in the MAC system. We assume multistream transmission such that $N_{\mathrm{s},k}[\ell]$ is the number of streams transmitted by the user k and the total number of streams allocated at subcarrier ℓ is $N_{\mathrm{s}}[\ell] = \sum_{k=1}^{K} N_{\mathrm{s},k}[\ell]$. The corresponding uplink symbols received at the antennas of the BS will be

$$\mathbf{y}^{\mathrm{UL}}[\ell] = \sum_{k=1}^{K} \mathbf{H}_k^*[\ell]\mathbf{T}_k[\ell]\mathbf{s}_k^{\mathrm{UL}}[\ell] + \mathbf{n}[\ell], \tag{2.8}$$

where $\mathbf{T}_k[\ell] \in \mathbb{C}^{N_{\mathrm{r}} \times N_{\mathrm{s},k}[\ell]}$ and $\mathbf{H}_k^*[\ell] \in \mathbb{C}^{N_{\mathrm{t}} \times N_{\mathrm{r}}}$ are the k-th frequency-selective user precoder and the channel response, respectively, for subcarrier ℓ. The user precoders are subject to a per-subcarrier transmit power constraint, i.e., $\mathrm{tr}\left(\mathbf{T}_k[\ell]\mathbf{T}_k^*[\ell]\right) \leq P_{\mathrm{T}_k}[\ell]$, being $P_{\mathrm{T}_k}[\ell]$ the available transmit power at the k-th user at subcarrier ℓ.

The noise introduced at reception at subcarrier ℓ is represented by $\mathbf{n}[\ell] = [n_1[\ell], \ldots, n_{N_{\mathrm{t}}}[\ell]]^T$ and it is modeled as $\mathbf{n}[\ell] \sim \mathcal{N}_{\mathbb{C}}(0, \sigma_{\mathrm{n}}^2\mathbf{I}_{N_{\mathrm{t}}})$. The matrices $\mathbf{G}_k[\ell] \in \mathbb{C}^{N_{\mathrm{s},k}[\ell] \times N_{\mathrm{t}}}$, $\forall k$ stand for the linear filters used at reception to estimate the incoming uplink symbols from the user k at subcarrier ℓ, i.e.,

$$\hat{\mathbf{s}}_k^{\mathrm{UL}}[\ell] = \mathbf{G}_k[\ell]\mathbf{y}^{\mathrm{UL}}[\ell] = \mathbf{G}_k[\ell] \sum_{i=1}^{K} \mathbf{H}_i^*[\ell]\mathbf{T}_i[\ell]\mathbf{s}_i^{\mathrm{UL}}[\ell] + \mathbf{G}_k[\ell]\mathbf{n}[\ell]. \tag{2.9}$$

In this case, the receive filter that minimizes the of MSE between the sent and the received symbols $\text{MSE}_k^{\text{UL}}[\ell] = \mathbb{E}\left[|\hat{\text{s}}_k^{\text{UL}}[\ell] - \text{s}_k^{\text{UL}}[\ell]|^2\right]$ is given by

$$\mathbf{G}_{\text{MMSE}_k}[\ell] = \mathbf{T}_k^*[\ell]\mathbf{H}_k[\ell]\left(\mathbf{H}^*[\ell]\mathbf{T}[\ell]\mathbf{T}^*[\ell]\mathbf{H}[\ell] + \sigma_{\text{n}}^2\mathbf{I}_{N_{\text{t}}}\right)^{-1},$$

where $\mathbf{H}^*[\ell] = [\mathbf{H}_1^*[\ell], \ldots, \mathbf{H}_K^*[\ell]] \in \mathbb{C}^{N_{\text{t}} \times N_{\text{r}}K}$ and $\mathbf{T}[\ell] = \text{blkdiag}\left(\mathbf{T}_1[\ell], \ldots, \mathbf{T}_K[\ell]\right) \in \mathbb{C}^{N_{\text{r}}K \times N_{\text{s}}[\ell]}$.

That the estimated symbols corresponding to the K users at subcarrier ℓ can be written as

$$\hat{\mathbf{s}}^{\text{UL}}[\ell] = \mathbf{G}[\ell]\mathbf{H}^*[\ell]\mathbf{T}[\ell]\mathbf{s}^{\text{UL}}[\ell] + \mathbf{G}[\ell]\mathbf{n}[\ell], \tag{2.10}$$

where $\mathbf{G}[\ell] = \left[\mathbf{G}_1^T[\ell], \ldots, \mathbf{G}_K^T[\ell]\right]^T \in \mathbb{C}^{N_{\text{s}}[\ell] \times N_{\text{t}}}$ is the receive filter that stacks all the K filters, $\mathbf{G}_k[\ell],\ \forall k$ (see Figure 2.6). In expression (2.10), $\hat{\text{s}}^{\text{UL}}[\ell]$ gathers all the estimated user symbols $(\hat{\text{s}}_k^{\text{UL}}[\ell], \forall k)$, which can also be obtained individually by employing the expression in (2.9). The MMSE receive filter using this compact formulation is given by [62]

$$\mathbf{G}_{\text{MMSE}}[\ell] = \mathbf{T}^*[\ell]\mathbf{H}[\ell]\Big(\mathbf{H}^*[\ell]\mathbf{T}[\ell]\mathbf{T}^*[\ell]\mathbf{H}[\ell] + \sigma_{\text{n}}^2\mathbf{I}_{N_{\text{t}}}\Big)^{-1}.$$

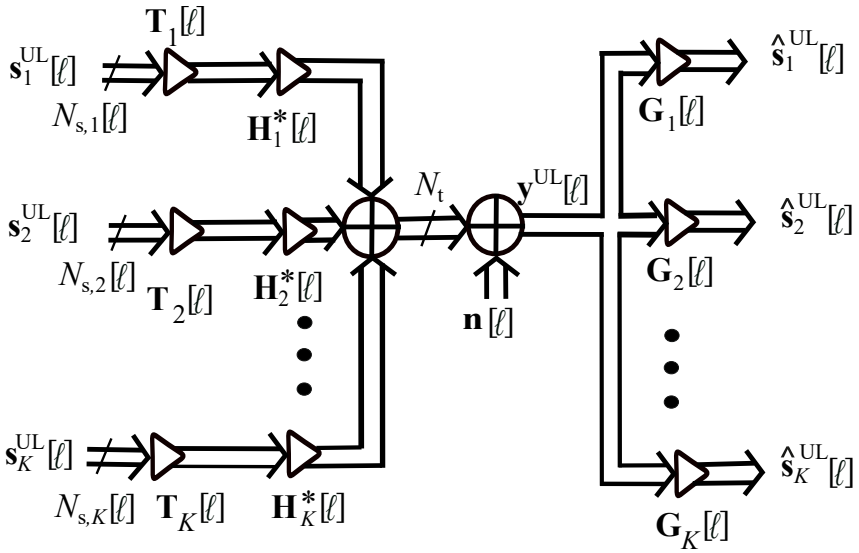

Figure 2.6: Block diagram of the uplink MU MIMO-OFDM system with K users at subcarrier ℓ.

2.4 MAC-BC and BC-MAC Dualities

Some works have employed different dualities between the BC and the MAC systems. These dualities allow for a reformulation of the BC system into the dual MAC and vice versa. These dualities are based on the fact that the figures of some metrics (e.g. MSE, signal-to-interference-plus-noise ratio (SINR)) are equal in both the BC and the dual MAC under certain conditions.

Dualities regarding the SINR [64], achievable rate [65], and MSE [66] have been approached in many works. In particular, we focus on MSE dualities as in [66], where three

kinds of dualities are presented. The first kind preserves both the sum MSE and the total power constraint. For the mentioned second and third kinds, each individual user and stream-wise MSEs remain unchanged, respectively while the same total power is achieved. These dualities are based on the assumption of perfect CSI in both communication ends. Since we are interested in considering systems with imperfect CSI, we also consider the work in [67].

As mentioned, different kinds of dualities have been studied in [66]. For arbitrary filters, the equivalent ones in the dual domain can be derived with different precision levels. For all of them, both the MSE of interest and the total power are preserved.

2.4.1 Sum-MSE Duality

The least restrictive duality is that where the system sum-MSE remains the same, this is called a duality of the first kind. In this case, the filters and precoders in the BC are related to their counterparts in the dual MAC as follows

$$\mathbf{P}[\ell] = \xi[\ell]\mathbf{G}^*[\ell], \tag{2.11}$$

$$\mathbf{W}[\ell] = \xi^{-1}[\ell]\mathbf{T}^*[\ell], \tag{2.12}$$

with $\xi[\ell] \in \mathbb{R}$, given by

$$\xi[\ell] = \sqrt{\frac{P_{\mathrm{T}}[\ell]}{\sum_{k=1}^{K} \|\mathbf{G}_k[\ell]\|_F^2}}, \tag{2.13}$$

and $P_{\mathrm{T}}[\ell]$ the power allocated at subcarrier ℓ. On the other hand, the MAC-BC dual relationship can be established as

$$\mathbf{G}[\ell] = \zeta^{-1}[\ell]\mathbf{P}^*[\ell], \tag{2.14}$$

$$\mathbf{T}[\ell] = \zeta[\ell]\mathbf{W}^*[\ell], \tag{2.15}$$

with $\zeta[\ell] \in \mathbb{R}$ given by the expression

$$\zeta[\ell] = \sqrt{\frac{P_{\mathrm{T}}[\ell]}{\sum_{k=1}^{K} \|\mathbf{W}_k[\ell]\|_F^2}}, \tag{2.16}$$

where the filters/precoders correspond to the BC and MAC system models presented in Section 2.3. Note that the dualities are applied per subcarrier ℓ.

2.4.2 Per-User MSE Duality

If we are interested in keeping the individual MSE for all the users unchanged during the conversion, we need different $\zeta_k[\ell]$ and $\xi_k[\ell]$ parameters for each of them. In these conversions of the second kind, the relationship between the transceivers is given by

$$\mathbf{P}_k[\ell] = \xi_k[\ell]\mathbf{G}_k^*[\ell], \tag{2.17}$$

$$\mathbf{W}_k[\ell] = \xi_k^{-1}[\ell]\mathbf{T}_k^*[\ell], \tag{2.18}$$

with the positive real-valued $\xi_k[\ell], \in \mathbb{R}^+$, given by

$$\left[\xi_1^2[\ell], \ldots, \xi_K^2[\ell]\right]^T = \sigma_{\mathbf{n}}^2 \mathbf{Z}^{-1}[\ell] \left[\| \mathbf{T}_1[\ell] \|_F^2, \ldots, \| \mathbf{T}_K[\ell] \|_F^2\right]^T, \tag{2.19}$$

where $\mathbf{Z}[\ell]$ is a non-singular matrix [66, Section IV] given by

$$[\mathbf{Z}]_{k,j}[\ell] = \begin{cases} \sum_{i \neq k}^{K} \| \mathbf{G}_j[\ell]\mathbf{H}_k^*[\ell]\mathbf{T}_k[\ell] \|_F^2 + \sigma_{\boldsymbol{\eta}}^2 \| \mathbf{G}_k[\ell] \|_F^2 & \text{for } k = j \\ -\| \mathbf{G}_j[\ell]\mathbf{H}_k^*[\ell\mathbf{T}_k[\ell] \|_F^2 & \text{for } k \neq j. \end{cases} \tag{2.20}$$

The MAC-BC dual relationship for this kind of duality is established as

$$\mathbf{G}_k[\ell] = \zeta_k^{-1}[\ell]\mathbf{P}_k^*[\ell], \tag{2.21}$$

$$\mathbf{T}_k[\ell] = \zeta_k[\ell]\mathbf{W}_k^*[\ell], \tag{2.22}$$

with the positive real-valued $\zeta_k[\ell] \in \mathbb{R}^+$ given by

$$\left[\zeta_1^2[\ell], \ldots, \zeta_K^2[\ell]\right]^T = \sigma_{\boldsymbol{\eta}}^2 \mathbf{Y}^{-1}[\ell] \left[\| \mathbf{P}_1[\ell] \|_F^2, \ldots, \| \mathbf{P}_K[\ell] \|_F^2\right]^T, \tag{2.23}$$

with the non-singular matrix $\mathbf{Y}[\ell]$ given by [66, Section V]

$$[\mathbf{Y}]_{k,j}[\ell] = \begin{cases} \sum_{i=1, i \neq k}^{K} \| \mathbf{W}_k[\ell]\mathbf{H}_k[\ell]\mathbf{P}_i[\ell] \|_F^2 + \sigma_{\boldsymbol{\eta}}^2 \| \mathbf{W}_k[\ell] \|_F^2 & \text{for } k = j \\ -\| \mathbf{W}_j[\ell]\mathbf{H}_k[\ell]\mathbf{P}_k[\ell] \|_F^2 & \text{for } k \neq j. \end{cases} \tag{2.24}$$

2.4.3 Per-Stream MSE Duality

When considering MIMO scenarios, multiple streams can be allocated among the users taking advantage of spatial multiplexing. In [66, Section IV, C and Section V, C], another kind of duality is approached when the equivalence between the BC/MAC MSEs has to be fulfilled not only per user but also per stream. The per-stream duality implies that the per-user and the sum-MSE dualities must be fulfilled. The multistream scenario could be seen as a more general case, whereas fewer degrees of freedom are needed for the first and second kinds.

2.5 Channel Models

In the MIMO systems equipped with N_{t} antennas for the transmission and N_{r} receive antennas at the receiver (e.g., a BS), as shown in Figure 2.7, we denote the time-varying channel between the communication ends as

$$\mathbf{H}_{t,\tau} = \begin{pmatrix} h_{1,1_{t,\tau}} & h_{1,2_{t,\tau}} & \cdots & h_{1,N_{\mathrm{t}}t,\tau} \\ h_{2,1_{t,\tau}} & h_{2,2_{t,\tau}} & \cdots & h_{2,N_{\mathrm{t}}t,\tau} \\ \vdots & \vdots & \ddots & \vdots \\ h_{N_{\mathrm{r}},1_{t,\tau}} & h_{N_{\mathrm{r}},2_{t,\tau}} & \cdots & h_{N_{\mathrm{r}},N_{\mathrm{t}}t,\tau} \end{pmatrix} \in \mathbb{C}^{N_{\mathrm{r}} \times N_{\mathrm{t}}}, \tag{2.25}$$

where $h_{i,j_{t,\tau}}$ stands for the equivalent lowpass channel impulse response at the time instant t and the tap τ from the j-th transmit antennas and the i-th receive antenna, whereas η_{j_t} is the AWGN. The receive signal at reception at the j-the antenna can be expressed as

$$y_{j_t} = \sum_{i=1}^{N_\mathrm{t}} h_{j,i_{t,\tau}} * x_{it} + \eta_{j_t}, \tag{2.26}$$

where x_{it} is the transmitted signal from the i-th antenna.

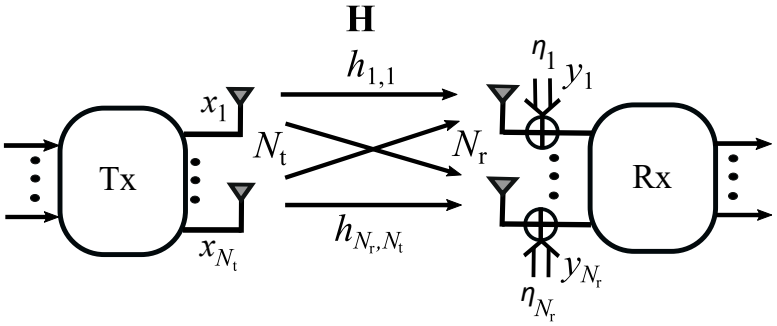

Figure 2.7: Block diagram of a single-user MIMO system.

Note that (2.26) can be rewritten in a compact way to stack the transmitted/received MIMO signals as

$$\mathbf{y}_t = \mathbf{H}_{t,\tau} * \mathbf{x}_t + \boldsymbol{\eta}_t, \tag{2.27}$$

where $\mathbf{x}_t = [x_{1t}, \ldots, x_{N_\mathrm{t}t}]^T \in \mathbb{C}^{N_\mathrm{t}}$, $\mathbf{y}_t = [y_{1t}, \ldots, y_{N_\mathrm{r}t}]^T \in \mathbb{C}^{N_\mathrm{r}}$, $\boldsymbol{\eta}_t = [\eta_{1t}, \ldots, \eta_{N_\mathrm{r}t}]^T$.

By considering flat fading, the parametter τ is removed, and the matrix $\mathbf{H}_{t,\tau}$ in (2.25) is transformed onto [53]

$$\mathbf{H}_t = \begin{pmatrix} h_{1,1_t} & h_{1,2_t} & \cdots & h_{1,N_\mathrm{t}t} \\ h_{2,1t} & h_{2,2t} & \cdots & h_{2,N_\mathrm{t}t} \\ \vdots & \vdots & \ddots & \vdots \\ h_{N_\mathrm{r},1_t} & h_{N_\mathrm{r},2_t} & \cdots & h_{N_\mathrm{r},N_\mathrm{t}t} \end{pmatrix} \in \mathbb{C}^{N_\mathrm{r}\times N_\mathrm{t}}. \tag{2.28}$$

Moreover, if the MIMO channel is assumed to be time-invariant, the parametter t is also removed and the matrix $\mathbf{H}_t$ in (2.28) is reduced to

$$\mathbf{H} = \begin{pmatrix} h_{1,1} & h_{1,2} & \cdots & h_{1,N_\mathrm{t}} \\ h_{2,1} & h_{2,2} & \cdots & h_{2,N_\mathrm{t}} \\ \vdots & \vdots & \ddots & \vdots \\ h_{N_\mathrm{r},1} & h_{N_\mathrm{r},2} & \cdots & h_{N_\mathrm{r},N_\mathrm{t}} \end{pmatrix} \in \mathbb{C}^{N_\mathrm{r}\times N_\mathrm{t}},$$

and the receive signal at reception at the j-the antenna is

$$y_{j_t} = \sum_{i=1}^{N_\mathrm{t}} h_{j,i} x_{it} + \eta_{j_t}, \tag{2.29}$$

and its compact version is

$$\mathbf{y}_t = \mathbf{H}\mathbf{x}_t + \boldsymbol{\eta}_t. \tag{2.30}$$

Different statistical models are assumed in the communication systems by considering diverse propagation aspects. In this thesis, we assume slow fading channel models since user mobility is out of the scope of this work. On the other hand, we will use flat fading and frequency-selective channel models to describe the channel responses in different mmWave scenarios, whereas the sub-6 GHz channles are modeled as statistically independent circularly symmetric random variables.

2.5.1 MmWave Systems

The propagation is unique at mmWave due to the small wavelength, which leads to enormous distance-based path losses and limited spatial selectivity or scattering. The combination of tightly-packed arrays developed for mmWave in sparse scattering environments makes many of the statistical fading distributions used in traditional MIMO analysis inaccurate for the channel modeling of this band. A clustered channel representation is commonly based on the extended Saleh-Valenzuela model [68], [69]. Considering the scattering cluster channel model for mmWave, each channel matrix is assumed to be a sum of the contributions of N_{cl} scattering clusters, each of which contributes N_{ray} paths. Therefore, the frequency-selective and time-invariant mmWave MIMO channel for wideband signals at the m-th delay tap with $m \in \{0, \ldots, L_{\text{D}} - 1\}$, being L_{D} the maximum number of delay taps, can be described by [31], [68]

$$\mathbf{H}_m = \gamma \sum_{i=1}^{N_{\text{ray}}} \sum_{l=1}^{N_{\text{cl}}} \beta_{i,l} p_{\text{rc}}\left(mT_s - \tau_{i,l}\right) \mathbf{a}_{\text{BS}}[\ell](\phi_{i,l}^{\text{BS}}, \theta_{i,l}^{\text{BS}}) \mathbf{a}_{\text{t}}^{*}[\ell](\phi_{i,l}^{\text{t}}, \theta_{i,l}^{\text{t}}), \tag{2.31}$$

where $p_{\text{rc}}(t)$ stands for the raised cosine pulse-shaping filter, $\tau_{i,l}$ is the relative delay for the i-th ray in the l-th cluster, T_s is the sampling period, $\gamma = \sqrt{N_{\text{t}} N_{\text{r}} / N_{\text{cl}} N_{\text{ray}}}$ is a power normalization factor and $\beta_{i,l}$ represents the complex path gain for the i-th ray in the l-th cluster. The term $\phi_{i,l}^{\text{BS}}, (\theta_{i,l}^{\text{BS}})$ stands for the azimuth (elevation) angles of departure (AoD) at the transmitter and $\phi_{i,l}^{\text{t}}, (\theta_{i,l}^{\text{t}})$ are the azimuth (elevation) angles of arrival (AoA) at the BS. The transmit and receive antenna arrays are described by their array steering vectors, $\mathbf{a}_{\text{BS}}[\ell](\phi_{i,l}^{\text{BS}}, \theta_{i,l}^{\text{BS}})$ and $\mathbf{a}_{\text{t}}[\ell](\phi_{i,l}^{\text{t}}, \theta_{i,l}^{\text{t}})$, which are functions of the angular directions.

Although the extended Saleh-Valenzuela model is employed to describe the propagation in mmWave MIMO systems, simulation typically describes the paths as arriving in "clusters", where each cluster has some distribution for the characteristic parameters (delay, power, and central angles of arrival and departure), physically, the path clusters can be approximated to different macro-level paths, and the angle and delay spread within each cluster capture the scattering from diffuse reflections along their paths (see [10] and references therein). Consequently, by considering that the parameters (delay, power, and AoA/AoD) within each cluster are very similar, there is a large number of works in the literature that consider a

simplified multipath channel model. By considering the scattering cluster channel model, an angle spread within each cluster of 10 or 20 degrees is commonly assumed. However, the AoA/AoD for different clusters are assumed to be uniformly distributed over the interval $[0; \pi]$ (see [31, Section IV]). The simplified channel model derived form (2.31) for a mmWave MIMO channel at the m-th delay tap with $m \in \{0, \ldots, L_{\mathrm{D}} - 1\}$, can be described by [31], [68]

$$\mathbf{H}_m = \gamma \sum_{n=1}^{N_{\mathrm{p}}} \beta_n p_{\mathrm{rc}} \left(mT_s \tau_n\right) \mathbf{a}_{\mathrm{BS}}[\ell](\phi_n^{\mathrm{BS}}, \theta_n^{\mathrm{BS}}) \mathbf{a}_{\mathrm{t}}^*[\ell](\phi_n^{\mathrm{t}}, \theta_n^{\mathrm{t}}), \tag{2.32}$$

where $n = 1, \ldots, N_{\mathrm{p}}$ indexes the channel paths. In the frequency domain, the channel response (2.32) for the link between the BS and the users can be represented as [10]

$$\mathbf{H}[\ell] = \sum_{m=0}^{L_{\mathrm{D}}-1} \mathbf{H}_m e^{j2\pi m(\ell-1)/L} = \sum_{n=1}^{N_{\mathrm{p}}} \beta_n[\ell] \mathbf{a}_{\mathrm{BS}}[\ell](\phi_n^{\mathrm{BS}}, \theta_n^{\mathrm{BS}}) \mathbf{a}_{\mathrm{t}}^*[\ell](\phi_n^{\mathrm{t}}, \theta_n^{\mathrm{t}}), \tag{2.33}$$

where $\ell \in \{1, \ldots, L\}$. The path gain $\beta_n[\ell]$ is obtained as $\beta_n[\ell] = \gamma \beta_n \sum_{m=0}^{L_{\mathrm{D}}-1} p_{\mathrm{rc}}(mT_{\mathrm{s}} - \tau_n) e^{j2\pi m(\ell-1)/L}$. The notation $\mathbf{a}_{\mathrm{t}}[\ell](\phi_n^{\mathrm{t}}, \theta_n^{\mathrm{t}})$ and $\mathbf{a}_{\mathrm{BS}}[\ell](\phi_n^{\mathrm{BS}}, \theta_n^{\mathrm{BS}})$ is introduced in (2.31) and (2.33) to highlight that the array response vectors are affected by the beam squint effect present when considering large bandwidths [31], [70], [71].

2.5.1.1 Beam Squint Effect

The large apertures used for wideband mmWave MIMO systems lead to the beam-squint effect [72]. This effect creates a type of spatial frequency-selectivity in the mmWave system (note the frequency dependence of the array response vectors in (2.33)). Consequently, frequency-flat precoders and filters become less optimal due to beam-squint (see [73] for more details about the beam squint).

2.5.1.2 Array Response Vectors

When considering uniform planar arrays (UPAs) at both ends, the array response vectors $\mathbf{a}_{\mathrm{t}}[\ell](\phi^{\mathrm{t}}, \theta^{\mathrm{t}})$ and $\mathbf{a}_{\mathrm{BS}}[\ell](\phi^{\mathrm{BS}}, \theta^{\mathrm{BS}})$ are given by [74], [75]

$$\mathbf{a}_{\mathrm{UPA}}[\ell]\,(\phi, \theta) = \frac{1}{\sqrt{N}} \Big[1, \ldots, e^{j\frac{2\pi}{c} f_\ell \, d \, (\sin\phi \, \sin\theta + n \cos\theta)}, \ldots, e^{j\frac{2\pi}{c} f_\ell \, d((W-1) \, (\sin\phi \, \sin\theta + (H-1) \cos\theta))}\Big]^T, \tag{2.34}$$

where N is the number of antennas in the array, f_ℓ is the frequency at the ℓ-th subcarrier, c is the speed of light, m and n are the indices in an antenna array with size $N = WH$, d is the inter antenna spacing, which is often equal to $\lambda/2$, being $\lambda = \frac{c}{f_{\mathrm{c}}}$ the wavelength and f_{c} the carrier frequency. By considering uniform linear arrays (ULAs) at both ends, the array response vectors $\mathbf{a}_{\mathrm{t}}[\ell](\phi^{\mathrm{t}})$ and $\mathbf{a}_{\mathrm{BS}}[\ell](\phi^{\mathrm{BS}})$ are given by [74], [75]

$$\mathbf{a}_{\mathrm{ULA}}[\ell]\,(\phi) = \frac{1}{\sqrt{N}} \Big[1, e^{j\frac{2\pi f_\ell}{c} \, d \sin\phi}, \ldots, e^{j\frac{2\pi f_\ell}{c} \, d(N-1) \sin\phi}\Big]^T, \tag{2.35}$$

where the response of the array is invariant in the elevation domain. Note that the phases within the steering vectors of the paths in (2.34) and (2.35) are subcarrier dependent due to the beam squint effect.

2.5.1.3 Narrowband Spatial Channel Model

By assuming a narrowband system and no beam squint effect, i.e., a flat fading channel, which is described by a single tap, the expression in (2.33) is reduced to

$$\mathbf{H} = \gamma \sum_{n=1}^{N_{\mathrm{p}}} \beta_n \mathbf{a}_{\mathrm{BS}}(\phi_n^{\mathrm{BS}}, \theta_n^{\mathrm{BS}}) \mathbf{a}_{\mathrm{t}}^*(\phi_n^{\mathrm{t}}, \theta_n^{\mathrm{t}}), \tag{2.36}$$

whereas the scattering cluster channel model in (2.31) reduces to [31], [68]

$$\mathbf{H} = \gamma \sum_{i=1}^{N_{\mathrm{ray}}} \sum_{l=1}^{N_{\mathrm{cl}}} \beta_{i,l} \mathbf{a}_{\mathrm{BS}}(\phi_{i,l}^{\mathrm{BS}}, \theta_{i,l}^{\mathrm{BS}}) \mathbf{a}_{\mathrm{t}}^*(\phi_{i,l}^{\mathrm{t}}, \theta_{i,l}^{\mathrm{t}}). \tag{2.37}$$

2.5.2 Sub-6 GHz Narrowband Systems

In these systems, wireless channels are typically modeled by random processes. In some cases, we assume independent and identically distributed (i.i.d.) complex-valued circularly symmetric Gaussian entries, i.e., a flat Rayleigh fading model. On the other hand, the flat fading Rician narrowband channel models are also considered, such that

$$\mathbf{H} = \sqrt{\frac{\beta}{1+\beta}} \mathbf{H}^{\mathrm{LOS}} + \sqrt{\frac{1}{1+\beta}} \mathbf{H}^{\mathrm{NLOS}}, \tag{2.38}$$

where β is the Rician factor. $\mathbf{H}^{\mathrm{LOS}}$ and $\mathbf{H}^{\mathrm{NLOS}}$ stand for the deterministic line-of-sight (LoS) component and the Rayleigh fading component, respectively.

2.6 Conclusions

In this chapter, some fundamental concepts about wireless communication systems have been introduced for completeness. First, we considered the main issues and advantages of wideband systems. We have briefly described the advantages of MIMO-OFDM systems. The source correlation models employed have also been explained by detailing the two different spatial correlation models assumed in this thesis. A brief description of the analog JSCC encoding in wideband OFDM MIMO systems has also been performed. Then, we have introduced the MU MIMO system model. We have approached the BC-MAC and the MAC-BC dualities in wideband MU MIMO systems. Two different channel models have been introduced in this chapter. In particular, we have studied the flat fading Rician and Rayleigh models for sub-6 GHz narrow band systems and the Saleh-Valenzuela channel model for both narrowband and wideband mmWave systems.

Chapter III

Analog Transmission of Correlated Sources in SIMO MAC using Lattices

Traditional approaches assume the separated design and optimization of the source and the channel encoders. They are based on the well-known separation principle, which was shown to be asymptotically optimal with the encoding block sizes under certain conditions [6]. However, this strategy presents many practical issues related to its high complexity and large delay. In addition, the separation principle constitutes a suboptimal solution when considering the transmission of correlated sources over MAC systems [76]. In such a case, an alternative approach is the implementation of JSCC techniques, where the source and channel encoding are jointly performed in a single step.

In this chapter, we approach the transmission of correlated sources over fading SIMO MAC by means of analog JSCC mappings based on multidimensional lattices. The complex-valued source symbols are individually encoded from the points defined by the generator basis of a multidimensional lattice, and next transmitted to a common receiver equipped with multiple antennas. Different lattice constructions are analyzed. The impact of the lattice size, the lattice density on the system performance and computational complexity is also addressed. At the receiver, source symbols are estimated via an MMSE decoder by considering their correlation. To avoid the huge computational cost of joint MMSE decoding, a sphere decoder is employed to simplify the required search in the lattice space. System performance results show that, by encoding with different codeword sizes, lattice-based JSCC provides a significant gain with respect to baseline analog JSCC schemes.

This chapter is structured as follows. Section 3.1 introduces the chapter. In Section 3.2, we present a brief review of some preliminary concepts corresponding to the lattice theory. In Section 3.3, the considered SIMO MAC system model is detailed. The design of the lattice-based analog JSCC system is addressed in Section 3.4. The derivation of the optimal MMSE estimation combined with a sphere decoder to produce the symbol estimates is also described in this section. The computer experiments to evaluate the system performance and the obtained results are discussed in Section 3.5. Finally, Section 3.6 is devoted to the conclusions.

3.1 Introduction

The transmission of correlated information over fading MACs is a relevant problem in wireless communications that occurs in many practical situations such as WSNs, IoT, or control systems. In this chapter, we particularly focus on MAC communications, where several non-cooperative nodes individually encode and send their data to a common receiver.

We consider analog JSCC techniques to transmit analog correlated information by considering that the sources produce discrete-time continuous-amplitude symbols that are directly transformed into encoded symbols through analog mappings based on geometric curves [60]. These mappings have been shown to closely approach the optimal system performance by considering compression of independent sources in AWGN channels [27], [77], [78], fading channels [79] or even for MU scenarios [80]. In the same sense, interesting results about the optimality of this approach for matched bandwidth can be found for Gaussian channels [5] and multi-node scenarios [81], [82]. Some works have also explored the use of analog mappings for bandwidth expansion, although the results are less promising [83], [84].

In this context, we approach the design of a JSCC SIMO MAC system where non-cooperative nodes transmit their encoded source symbols to a multi-antenna centralized node over a fading channel. The source information is assumed to be spatially correlated at each time instant. In the existing literature, different zero-delay JSCC schemes (codeword size equals to one) have been investigated. One example is [85], where a zero-delay analog JSCC mapping is proposed to transmit multivariate Gaussian sources over an AWGN MAC channel. Modulo-like mappings were also proposed for the orthogonal transmission of correlated sources in a SISO MAC scenario [86], [87]. The approach in [86] can be extended to a SIMO MAC case when the number of receive antennas is significantly larger than the number of users since the receiver has enough degrees of freedom to exploit the source correlation at decoding [20].

Most existing works on analog JSCC focus on zero-delay mappings because of the difficulty of designing and optimizing the mappings for larger dimensions. This limitation, however, significantly reduces the practical utility of analog JSCC with respect to traditional digital approaches, which may consider different encoding block sizes. Therefore, a systematic strategy for the design of analog JSCC mappings with arbitrary codeword lengths is fundamental.

The work in [88] represents a first attempt to construct non-zero delay analog JSCC schemes on the basis of the lattice theory. In particular, [88] considers zero-delay and non-zero delay mappings that use well-known lattices with different dimensions. The encoded symbols are then transmitted over a Rayleigh block fading channel. Specifically, modulo-like mappings (codeword size $n = 1$), the D_4 (codeword size $n = 4$) [89] and the E_8 (codeword size $n = 8$) [89] lattice-based mappings are analyzed. D_4 and E_8 are the densest packing lattices for $n = 4$ and $n = 8$, respectively, and thus adequate candidates for achieving good system performance. However, parameter optimization in [88] is based on an exhaustive search that is infeasible

for large lattice dimensions, and the decoding process is performed by a two-step procedure that first estimates the symbols of uncoded users and next employs such estimates as side information for the remaining users. This strategy is suboptimal as it is not able to jointly exploit the source correlation. Furthermore, [88] just considers lattice dimensions up to $n = 8$.

In any case, the results obtained in [88] provide the intuition that the design of non-zero delay analog JSCC mappings based on n-dimensional lattices is a promising strategy. A comprehensive analysis for the construction of "good" lattices in different dimensions can be found in [89], particularly for the sphere packing problem. The list of the known densest lattices for a large range of dimensions can also be looked up in [90]. An interesting example is the Leech lattice, found in [91], which has been shown to be the unique densest lattice packing of dimension $n = 24$ [92]. Unfortunately, the computational cost of the encoding operation in a lattice-based mapping system exponentially increases with the dimension when using the densest lattices because it is required to find the closest point in the n-dimensional lattice [93]. In that sense, alternative lattice constructions must be considered to balance the system performance and the encoding complexity as the codeword size (dimension) becomes larger.

From this perspective, an interesting type of lattices is the so-called Craig's lattice [94], which is constructed from the ring of integers in a cyclotomic field. The mechanism to construct these polynomial lattices allows to adjust the minimal norm of the resulting lattices and, as a consequence, their density for an arbitrary dimension $n = p - 1$, being p a prime number [89]. Therefore, an alternative approach for the analog encoding of source symbols with an affordable computational cost in large dimensions is given by adjusting the density of the Craig's lattices used to construct the analog mapping. This reduces the computational effort required to find the closest lattice points.

Making use of all these ideas, we address the transmission of spatially correlated information in a fading SIMO MAC scenario using analog JSCC techniques. Blocks of source symbols are individually encoded at each node with an analog JSCC mapping constructed from a suitable lattice. At the receiver, the estimates of the transmitted symbols are jointly computed by means of a decoding approach that exploits the spatial correlation and the use of codeword sizes larger than one (i.e., non-zero delay). The main contributions of the chapter are summarized as follows:

- A multidimensional lattice-based analog JSCC system is designed and optimized for transmitting blocks of symbols with size n larger than that considered in state-of-the-art approaches. This allows analog JSCC techniques to be a real practical alternative to conventional digital schemes for a large number of situations. The proposed design is sufficiently flexible to allow working with different codeword sizes and efficiently exploiting the sources spatial correlation.
- For large codeword sizes, Craig's lattices are considered to reduce the computational cost of the analog JSCC encoding. The possibility of adjusting the lattice density allows us to balance the trade-off between the system performance and the computational complexity.

- A performance evaluation showing the advantages of the proposed system design and the use of Craig's lattices is performed. The performance gains are obtained for scenarios with non-orthogonal configurations or moderate correlations, where zero-delay mappings have significant performance limitations. In addition, the impact of the block size and the lattice density on the system performance is analyzed.

3.2 Fundamentals of Lattices

This section introduces the theoretical fundamentals of lattices that will be used throughout this chapter. An n-dimensional lattice $\mathcal{T}$ is defined as a discrete set of vectors in $\mathbb{R}^n$ that form a group under vector addition. These vectors will be referred to as the lattice points. A lattice $\mathcal{T}$ will be defined by its generator matrix $\mathbf{M} = [\boldsymbol{\nu}_1, \ldots, \boldsymbol{\nu}_n] \in \mathbb{R}^{n \times n}$, where the column vectors $\boldsymbol{\nu}_j,\ j = 1, \ldots, n$ are the basis vectors. Therefore, the i-th lattice point will be generated as $\mathbf{x}_{\mathrm{l}i} = \mathbf{M}\mathbf{l}_i, \forall i = 1, \ldots, M$, where $\mathbf{l}_i \in \mathbb{Z}^n$ is a vector of integers and M is assumed to be large enough. The fundamental region of the lattice is that area in the n-dimensional space which includes only a point of the lattice, and, when considering all the lattice points, the entire space is tiled. The Voronoi region is that fundamental region in which every point of the euclidean space is closer to its corresponding lattice point than to any other lattice point. The different possibilities of partitioning or covering an n-dimensional Euclidean space by using lattices lead to different well-known problems in algebra such as the sphere packing, the covering packing, or the quantization problem [89].

3.2.1 Sphere Packing

Sphere packing seeks to fill the n-dimensional space with non-overlapping equal-sized spheres. Unlike cubic regions, there is always some wasted space when packing spheres. The minimization of such wasted space is a still unsolved problem, which can be stated as follows: determine the largest number of spheres with the same radius r that can be packed into a largely empty n-dimensional region. As observed in Figure 3.1, the wasted space between spheres, also known as deep holes, corresponds to the points whose minimum distance to any point in the lattice r_{t} is larger than the radius of the spheres, i.e., $r_{\mathrm{t}} > r$.

In the sphere packing problem, the lattice points $\mathcal{T} = \{\mathbf{x}_{\mathrm{l}1}, \mathbf{x}_{\mathrm{l}2}, \ldots, \mathbf{x}_{\mathrm{l}M}\}$ correspond to the central points of the spheres. The lattice density is defined as the ratio between the space that is occupied by the spheres and the total volume, i.e.,

$$\Delta = \frac{V_1 p_{\mathrm{r}}^n}{V(\mathcal{T})}, \tag{3.1}$$

where V_1 is the volume of an n-dimensional sphere of radius $r = 1$. $V(\mathcal{T})$ is the volume of the lattice $\mathcal{T}$, which is determined as [89]

$$V(\mathcal{T}) = \det\left(\mathbf{M}\mathbf{M}^T\right)^{1/2}, \tag{3.2}$$

and p_{r} is the packing radius defined as half of the minimal distance between lattice points, i.e., $p_{\mathrm{r}} = \frac{1}{2}\sqrt{\mu(\mathcal{T})}$, where $\mu(\mathcal{T}) = \min_{i \neq j}\{\| \mathbf{x}_{\mathrm{l}i} - \mathbf{x}_{\mathrm{l}j} \|^2\},\ \forall\, \mathbf{x}_{\mathrm{l}i}, \mathbf{x}_{\mathrm{l}j} \in \mathcal{T}$ is the minimum norm of the lattice. Another important parameter is the center density which is defined as

$$\psi = \frac{\Delta}{V_{\mathrm{l}}} = \frac{p_{\mathrm{r}}^n}{V(\mathcal{T})}. \tag{3.3}$$

Note that the center density provides a more intuitive idea of how dense a packing lattice is. For instance, in packings with unitary-radius spheres, the center density directly indicates the number of centers (lattice points) per unit volume.

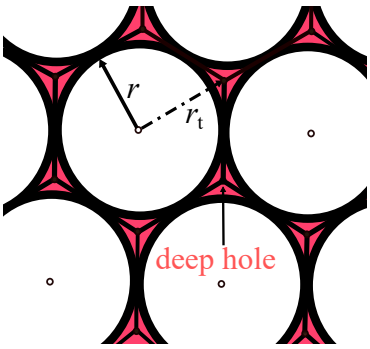

Figure 3.1: Circle packing problem and deep holes.

3.2.2 Lattice-Based Quantization

In general, quantization consists of partitioning an n-dimensional space into M non-overlapping regions each of them represented by a representation point usually termed centroid that will be interpreted as a point in a lattice. Typically, quantization regions are Voronoi regions. This way, each point in the source space is quantized to the closest point in the lattice and the quantization error is minimized.

An n-dimensional lattice-based quantizer comprises a lattice $\mathcal{T} = \{\mathbf{x}_{\mathrm{l}1}, \mathbf{x}_{\mathrm{l}2}, \ldots, \mathbf{x}_{\mathrm{l}M}\} \subset \mathbb{R}^n$, defined via a generator matrix $\mathbf{M}$, and a quantization function $Q_{\mathcal{T}}(\cdot)$ which maps any input vector $\mathbf{s} \in \mathbb{R}^n$ into the closest lattice point $\mathbf{x}_{\mathrm{l}i} \in \mathcal{T}$. The quantization region associated to the i-th lattice point $\mathbf{x}_{\mathrm{l}i} = \mathbf{M}\mathbf{l}_i$, $\forall i = 1, \ldots, M$, will be its Voronoi region defined as

$$\Omega_{\mathcal{T}}\left(\mathbf{x}_{\mathrm{l}i}\right) = \{\mathbf{s} : \|\mathbf{s} - \mathbf{x}_{\mathrm{l}i}\| \leq \|\mathbf{s} - \mathbf{x}_{\mathrm{l}j}\|\},\ \forall i \neq j. \tag{3.4}$$

Therefore, the quantization function is mathematically defined as $Q_{\mathcal{T}}(\mathbf{s}) = \mathbf{x}_{\mathrm{l}i}, \forall\, \mathbf{s} \in \Omega_{\mathcal{T}}\left(\mathbf{x}_{\mathrm{l}i}\right)$.

A possible metric to measure the quantization error, by considering M to be a very large number, is the average MSE, i.e.,

$$\varepsilon = \frac{1}{n} \sum_{i=1}^{M} \int_{\Omega_{\mathcal{T}}(\mathbf{x}_{\mathrm{l}i})} \|\mathbf{s} - \mathbf{x}_{\mathrm{l}i}\|^2\, p(\mathbf{s})\, d\mathbf{s}, \tag{3.5}$$

where the factor $1/n$ is introduced for fair comparison among quantizers of different dimensions.

Although quantization and sphere packing are different lattice design problems, there is an intrinsic relation between them. A "good" packing lattice implies efficiently covering the region of interest with non-overlapping spheres, minimizing the deep holes, and thus minimizing the probability of having points very distant from the lattice points. Therefore, this feature apparently leads to the minimization of the quantization error in (3.5) if those "good" packing lattices were used to solve the quantization problem. In this sense, optimal lattice-based quantizers are only known for low dimensions, while sphere packing is a widely studied problem in multidimensional lattice theory. Indeed, the densest sphere packing lattices have been shown to provide satisfactory performance when used for quantization [89].

On the other hand, quantization with extremely dense lattices leads to a huge computational effort when considering large dimensions. There exist several algorithms in the literature to alleviate this problem but in any case their computational cost exponentially increase with the dimension n and the lattice density. Therefore, there is a trade-off between quantization error minimization and computational complexity that can be balanced through the lattice density factor defined in (3.1).

3.3 System Model

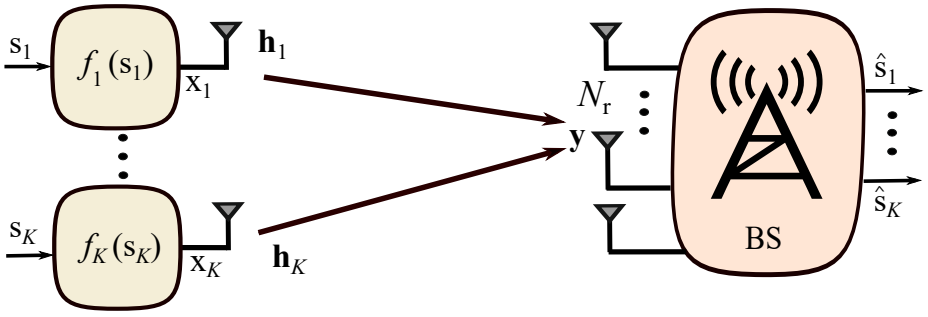

Figure 3.2: Block diagram of the considered SIMO MAC communication system.

Let us consider the uplink of a MU SIMO communication system, as shown in Figure 3.2, where K single-antenna users transmit their source information to a centralized receiver that deploys N_{r} antennas. Henceforth, we will refer to this model as a $K \times N_{\mathrm{r}}$ SIMO MAC system. The complex-valued analog source symbol transmitted by the k-th user at the discrete-time instant t is denoted by $s_{k,t}$. The source symbols transmitted by the K users at the time instant t is represented by the vector $\mathbf{s}_t = [s_{1,t}, \cdots, s_{K,t}]^T \in \mathbb{C}^K$, which is modeled as a multivariate circularly symmetric complex-valued zero-mean Gaussian distribution with covariance matrix $\mathbf{C_s} = \mathbb{E}[\mathbf{s}_t \mathbf{s}_t^*]$. The elements $[\mathbf{C_s}]_{i,j} = \rho_{i,j}$ represent the spatial correlation between the i-th and j-th source symbols of $\mathbf{s}_t$. Without loss of generality, we assume that $\rho_{i,i} = \sigma^2, \forall i$. We also

consider that the source symbols at different time instants t are statistically independent so that we only consider the user spatial correlation. Such spatial correlation is assumed to not depend on the time instant, i.e., remains constant for a sufficiently long period of time. The probability density function (PDF) of $\mathbf{s}_t$ is therefore given by

$$p_{\mathbf{s}_t}(\mathbf{s}) = \frac{1}{\pi^K |\mathbf{C}_\mathbf{s}|} \exp\left(-\mathbf{s}^* \mathbf{C}_\mathbf{s}^{-1} \mathbf{s}\right). \tag{3.6}$$

A block of source symbols is individually encoded at each user prior to its transmission by means of an analog mapping function. We employ lattice-based mappings which transform the continuous-amplitude source symbols into the complex-valued encoded symbols to be transmitted. In particular, a vector of $n/2$ consecutive complex-valued source symbols $\mathbf{s}_k$ corresponding to the k-th user is mapped with the function $f_k(\cdot) : \mathbb{C}^{\frac{n}{2}} \rightarrow \mathbb{C}^{\frac{n}{2}}$ to produce the encoded vector $\mathbf{x}_k = f_k(\mathbf{s}_k), \forall k = 1, \ldots, K$, with $\mathbf{s}_k = [s_{k,1}, s_{k,2}, \ldots, s_{k,\frac{n}{2}}]^T$ and $\mathbf{x}_k = [x_{k,1}, x_{k,2}, \ldots, x_{k,\frac{n}{2}}]^T$. The encoded vectors are next transmitted to the common BS over the fading MAC by using $n/2$ channel uses to produce the received signal vectors $\mathbf{y}_t \in \mathbb{C}^{N_\mathrm{r}}$ as

$$\mathbf{y}_t = \sum_{k=1}^{K} \mathbf{h}_k x_{k,t} + \mathbf{n}_t, \quad \forall t = 1, \ldots, n/2, \tag{3.7}$$

where $\mathbf{h}_k \in \mathbb{C}^{N_\mathrm{r}}$ is the channel response from the k-th user to the BS, and $\mathbf{n}_t = [n_{1,t}, \ldots, n_{N_\mathrm{r},t}]^T \sim \mathcal{N}_\mathbb{C}(\mathbf{0}, \sigma_\mathrm{n}^2 \mathbf{I})$ is the AWGN component. The channel responses are assumed to remain the same at least during the transmission of a block of $n/2$ symbols. Each user is also subject to an individual power constraint such that $\mathbb{E}[|x_{k,t}|^2] \leq P_{\mathrm{T}k}, \forall k = 1, \ldots, K$. The expression in (3.7) can be rewritten in a more compact way as

$$\mathbf{y}_t = \mathbf{H}\mathbf{x}_t + \mathbf{n}_t, \quad \forall t = 1, \ldots, n/2, \tag{3.8}$$

where $\mathbf{H} \in \mathbb{C}^{N_\mathrm{r} \times K}$ stacks all the user channel responses, i.e., $\mathbf{H} = [\mathbf{h}_1, \cdots, \mathbf{h}_K]$, and $\mathbf{x}_t = [x_{1,t}, \ldots, x_{K,t}]^T$ contains all the encoded user symbols at a given time instant t.

At the BS, an estimate of the transmitted user symbols $\hat{\mathbf{s}}_t$ is obtained from the MAC signal $\mathbf{y}_t$ by using an appropriate decoding function that jointly decodes the symbols received during the corresponding $n/2$ channel uses. Since we are considering the analog encoding and transmission of the source information, the user symbols will always be recovered with a certain level of distortion which is measured in terms of the MSE between the source and the estimated symbols, i.e., $\xi_{\text{sum}} = \mathbb{E}[||\hat{\mathbf{s}}_t - \mathbf{s}_t||^2]$. In this case, the MMSE estimator is the optimal decoding strategy. Table 3.1 summarizes the parameters of the system model described in this section.

In the considered system model, the variables corresponding to the source symbols, user channels, and AWGN components are complex-valued with uncorrelated real and imaginary parts (circularly symmetric). However, analog lattice-based mappings work in the real domain, as the lattices are defined as a group in $\mathbb{R}^n$. Our complex-valued model can be converted to a real-valued equivalent model (see Appendix A). Hence, we can obtain the equivalent real-valued channel model $\tilde{\mathbf{H}} \in \mathbb{R}^{2N_\mathrm{r} \times 2K}$. In addition, the source and noise covariance matrices must be adapted such that $\tilde{\mathbf{s}} \sim \mathcal{N}_\mathbb{R}(\mathbf{0}, \mathbf{C}_{\tilde{\mathbf{s}}})$, with $\mathbf{C}_{\tilde{\mathbf{s}}} = \mathbf{C}_\mathbf{s} \otimes \frac{1}{2}\mathbf{I}_2$, and $\tilde{\mathbf{n}} \sim \mathcal{N}_\mathbb{R}(\mathbf{0}, \frac{\sigma_\mathrm{n}^2}{2}\mathbf{I})$.

Table 3.1: SIMO MAC system model parameters.

Description	Parameter
Number of antennas at the BS	N_{r}
Number of users	K
Vector of consecutive symbols of k-th user	$\mathbf{s}_k$
Vector of all the user symbols at time t	$\mathbf{s}_t$
Cross correlation: i-th user and j-th user	$\rho_{i,j}$
Spatial corelation matrix	$\mathbf{C}_{\mathrm{s}}$
Number of complex-valued symbols per block	$\frac{n}{2}$
User-BS channel: k-th user	$\mathbf{h}_k$
Mapping function applied to the k-th user	$f_k(\cdot)$
Power constraint at k-th user	$P_{\mathrm{T}k}$
Vector of AWGN at time instant t	$\mathbf{n}_t$
Received MAC signal by the BS at time instant t	$\mathbf{y}_t$
Estimated user symbols by the BS at time instant t	$\hat{\mathbf{s}}_t$

3.4 Lattice-Based Mappings

Throughout this chapter, we will assume that the users in the $K \times N_{\mathrm{r}}$ SIMO MAC system under consideration use analog JSCC mappings to encode their source symbols individually. As shown in [20], modulo-like mappings provide satisfactory performance when the block size is $n = 1$ (i.e., zero-delay). The symbols encoded with modulo-like mappings are the difference between the source symbols and the central point of their corresponding interval. In the following, this idea is extended to the consideration of an arbitrary dimension $n > 1$.

The parametric definition of the multidimensional lattice-based mapping functions is stated as

$$\tilde{\mathbf{x}}_k = f_k(\tilde{\mathbf{s}}_k) = \delta_k \left(\tilde{\mathbf{s}}_k - Q_{\mathcal{T}}(\tilde{\mathbf{s}}_k)\right) = \delta_k(\tilde{\mathbf{s}}_k - \alpha_k \mathbf{M}\mathbf{l}_k), \tag{3.9}$$

where $\tilde{\mathbf{s}}_k \in \mathbb{R}^n$ and $\tilde{\mathbf{x}}_k \in \mathbb{R}^n$ comprise the real and the imaginary parts of the k-th user source and encoded symbols, respectively. The operator $Q_{\mathcal{T}}(\cdot)$ determines the lattice point (centroid) closest to its argument. Note that this quantization step depends on the considered lattice $\mathcal{T}$ that is generated by the matrix $\mathbf{M}$ and scaled with the parameter α_k. The mapping parameters δ_k and α_k are used to fulfill the power constraint at the users and to adjust the distance between any two lattice points, respectively, whereas $\mathbf{l}_k \in \mathbb{Z}^n$ is the index vector that represents the coordinates of the specific Voronoi region where the vector of source symbols falls into during the encoding process (cf. [43]). It is worth remarking that the same lattice $\mathcal{T}$ is employed for all the K users but with different scaling factors $\{\alpha_k, \delta_k\}, \forall k = 1, \ldots, K$.

The encoded symbols are obtained by determining the difference vector between the source symbols and their corresponding centroid. In this sense, the system performance improves when the difference vectors have the smallest possible norm as long as the correct decoding

of the source symbols is guaranteed. For given power constraints, this fact results in the use of larger power factors at each user, δ_k, and thus minimizes the resulting decoding distortion. Hence, an adequate optimization of the mapping parameters $\{\alpha_k, \delta_k\}$ is essential to ensure the lattice-based system works properly.

The lattice-based mappings for all the K user symbols can be rewritten in a compact way as

$$\tilde{\mathbf{x}}_{\mathrm{c}} = f(\tilde{\mathbf{s}}_{\mathrm{c}}) = \mathbf{D}(\tilde{\mathbf{s}}_{\mathrm{c}} - \mathbf{B}\mathbf{l}), \tag{3.10}$$

where the vector $\tilde{\mathbf{s}}_{\mathrm{c}} \in \mathbb{R}^{nK}$ stacks the real and imaginary parts of the blocks of $n/2$ complex-valued symbols for all the K users, i.e., $\tilde{\mathbf{s}}_{\mathrm{c}} = \left[\tilde{\mathbf{s}}_1^T,\ \tilde{\mathbf{s}}_2^T, \ldots,\ \tilde{\mathbf{s}}_K^T\right]^T$, $\mathbf{D} = \mathrm{diag}\left(\delta_1, \ldots, \delta_K\right) \otimes \mathbf{I}_n$, whereas $\mathbf{B} = \mathbf{U} \otimes \mathbf{M}$ with $\mathbf{U} = \mathrm{diag}\left(\alpha_1, \ldots, \alpha_K\right)$. Note that the vector $\tilde{\mathbf{s}}_{\mathrm{c}}$ comprises all the source symbols for the K users and for the $n/2$ channel uses. In turn, the vector $\mathbf{l} = \left[\mathbf{l}_1^T, \ldots, \mathbf{l}_K^T\right]^T$ such that $\mathbf{l} \in \mathbb{Z}^{nK}$ stacks all the coordinates corresponding to the K Voronoi regions which the K vectors of source symbols fall into.

By considering the discrete nature of the lattices, the compact expression for the mapping function $f(\cdot)$ can be rewritten from its piece-wise formulation given by

$$f_i(\tilde{\mathbf{s}}_{\mathrm{c}}) = \begin{cases} \mathbf{D}(\tilde{\mathbf{s}}_{\mathrm{c}} - \mathbf{B}\mathbf{l}_i) & \text{if } \tilde{\mathbf{s}}_k \in \Omega_{\mathcal{T}}(\mathbf{l}_{k,i})\ \forall k \\ \text{undefined} & \text{otherwise,} \end{cases} \tag{3.11}$$

such that

$$f(\tilde{\mathbf{s}}_{\mathrm{c}}) = \sum_{i=1}^{|\mathcal{L}|} f_i(\tilde{\mathbf{s}}_{\mathrm{c}}). \tag{3.12}$$

Note that the vector $\mathbf{l}_i \in \mathbb{Z}^{nK}$ identifies a particular combination of K Voronoi regions, one for each user, and $\mathcal{L}$ is the set of all the integer-valued vectors of dimension nK which constitutes a feasible combination of K Voronoi regions, i.e., $\mathbf{l}_i \in \mathcal{L}$. As observed in (3.11), the function $f_i(\cdot)$ is actually defined only for the combination of regions corresponding to the K Voronoi regions, $\Omega_{\mathcal{T}}(\mathbf{l}_{k,i})$, which each user symbol vector $\tilde{\mathbf{s}}_k$ falls into. Recall that $\mathbf{l}_{k,i}$ stands for the coordinates vector corresponding to the lattice point closest to $\tilde{\mathbf{s}}_k$ and $\Omega_{\mathcal{T}}(\mathbf{l}_{k,i})$ represents the corresponding Voronoi region.

The blocks of $n/2$ complex-valued encoded symbols at each user are transmitted over the MAC by using $n/2$ channel uses. Accordingly, decoding is applied to the entire block of $n/2$ complex-valued received symbols. For that reason, we extend the compact formulation for the MAC signal in (3.8) to include all the user symbols received during $n/2$ consecutive channel uses and also considering the real-valued equivalent model. Hence, the compact representation of the received symbols is

$$\tilde{\mathbf{y}}_{\mathrm{c}} = \tilde{\mathbf{H}}_{\mathrm{c}}\tilde{\mathbf{x}}_{\mathrm{c}} + \tilde{\mathbf{n}}_{\mathrm{c}}, \tag{3.13}$$

where $\tilde{\mathbf{H}}_{\mathrm{c}} = \tilde{\mathbf{H}} \otimes \mathbf{I}_{\frac{n}{2}}$ such that $\tilde{\mathbf{H}}_{\mathrm{c}} \in \mathbb{R}^{nN_{\mathrm{r}} \times nK}$, $\tilde{\mathbf{x}}_{\mathrm{c}} = \left[\tilde{\mathbf{x}}_1^T, \ldots, \tilde{\mathbf{x}}_K^T\right]^T$ with $\tilde{\mathbf{x}}_{\mathrm{c}} \in \mathbb{R}^{nK}$ stacking all the K blocks of $n/2$ encoded symbols, and $\tilde{\mathbf{n}}_{\mathrm{c}} = \left[\tilde{\mathbf{n}}_1^T, \ldots, \tilde{\mathbf{n}}_n^T\right]^T$ is the noise affecting the

received symbols during the $n/2$ channel uses. Note that $\tilde{\mathbf{x}}_c$ is obtained according to (3.10). The vector of received symbols, $\tilde{\mathbf{y}}_c \in \mathbb{R}^{n \times N_r}$, is employed to produce the estimates of the K blocks of transmitted symbols by using the MMSE-based procedure to be explained in Subsection 3.4.2.

As mentioned, the encoding operation requires finding the closest lattice point for each vector of user symbols $\tilde{\mathbf{s}}_k$. We employ a refined version of the Pohst's algorithm [93], which has been shown to be faster than other known methods like, e.g., Kannan's algorithm [95] or the conventional Pohst's algorithm [96]. This iterative algorithm searches for the optimal lattice point inside a hypersphere in $\mathbb{R}^n$ that should contain such a point. The search implies exploring all the lattice points that fall into the considered n-dimensional hypersphere to determine the one with minimum Euclidean distance. Therefore, their computational complexity not only grows exponentially with the lattice dimension but also with the lattice density since the number of lattice points inside the hypersphere will be larger. In practice, the closest point algorithms are able to deal with the densest packing lattices up to $n \approx 24$, whereas they exhibit a prohibitive complexity for larger dimensions. This issue will be circumvented by using Craig's lattices whose density can be properly adjusted for a given dimension. This fact allows us to increase the encoding lattice dimension at the expense of reducing the lattice density. In the following subsection, we introduce the fundamentals of Craig's lattices.

3.4.1 Craig's Lattices

Craig's lattices are constructed from the ring of integers in a cyclotomic field. Let ζ_p be a primitive p-th root of unity being p an odd prime. The elements of the ring of integers $\mathbb{Z}[\zeta_p]$ in the cyclotomic field $\mathbb{Q}[\zeta_p]$ are represented as

$$\omega = P(\zeta_p) = a\zeta_p^{n-1} + , \ldots , + b\zeta_p + c, \tag{3.14}$$

where the polynomial coefficients are restricted to be integer values. In this case, $n = p - 1$ determines the order of the elements in the ring and the dimension of the resulting lattices.

An n-dimensional Craig's lattice, usually denoted as $A_n^{(m)}$, is generated from the elements of the ideal $(1 - \zeta_p)^m$, with m a positive integer, in the cyclotomic ring of integers $\mathbb{Z}[\zeta_p]$ [97]. Thus, an n-dimensional Craig's lattice is given by the subset of polynomials in the ring of integers $\mathbb{Z}[\zeta_p]$, which are multiples of $(1-\zeta_p)^m$. Alternatively, the lattice points can be obtained as the vector representation of the elements of the ideal generated by $(1 - x)^m$ in the quotient ring $\mathbb{Z}[x]/(x^p - 1)$. Such elements can be obtained as

$$P(x)(1 - x)^m = Q(x)(x^p - 1) + R(x), \tag{3.15}$$

for some polynomial $P(x) \in \mathbb{Z}[x]$. With this formulation, the elements of the ideal generated by $(1 - x)^m$ would be the remainders $R(x)$, and the corresponding lattice points in $A_n^{(m)}$ will be the vectors that contain the coefficients of the polynomials $R(x)$. However, for the encoding

operation, we need to obtain the generator matrix for the Craig's lattice $A_n^{(m)}$. Next, we explain the construction of this matrix.

3.4.1.1 Generator Matrix Construction

The construction for the generator matrix of a Craig's lattice is based on the idea of constructing sub-lattices from the well-known A_n lattice. In that case, given an n-dimensional lattice $\mathcal{T}$, the difference lattice $\mathbf{\Delta}^T\mathcal{T}$ satisfies $\mathbf{\Delta}^T\mathcal{T} \subseteq \mathcal{T}$, where

$$\mathbf{\Delta}^T = \begin{bmatrix} 1 & -1 & 0 & \cdots & 0 & 0 \\ 0 & 1 & -1 & \cdots & 0 & 0 \\ \cdot & \cdot & \cdot & \cdots & \cdot & \cdot \\ 0 & 0 & 0 & \cdots & 1 & -1 \\ 1 & 1 & 1 & \cdots & 1 & 2 \end{bmatrix}$$

is a $n \times n$ matrix. Thereby, the generator matrix of a Craig's lattice $A_n^{(m)}$ can be defined as

$$\mathbf{M}_n^{(m)} = \mathbf{\Delta}^{m-1}\mathbf{M}_n, \quad \forall\, m \leq n/2, \tag{3.16}$$

where $\mathbf{M}_n$ is the generator matrix for the A_n lattice.

In practice, this procedure is equivalent to considering the following polynomial sequence $\{P_1(x) = 1, P_2(x) = x, P_3(x) = x^2, \ldots, P_n(x) = x^{n-1}\}$ in (3.15) to generate the n basis vectors $\{\boldsymbol{\nu}_1, \ldots, \boldsymbol{\nu}_n\}$ corresponding to the n columns of the generator matrix of the Craig's lattice. Because of the polynomial properties, this construction is in turn equivalent to setting the first column of $\mathbf{M}_n^{(m)}$ to $\boldsymbol{\nu}_1 = P_1(x)(1-x)^m$ and the remaining columns to cyclic shifts of this primary vector [89, Ch. 8, Th. 10].

3.4.1.2 Craig's Lattice Parameters

In this subsection, we present important parameters related to the Craig's lattices. The determinant of the Craig's lattice $A_n^{(m)}$ is $\det\left(A_n^{(m)}\right) = (n+1)^{2m-1}$, where $n = p-1$, with p an odd prime, and $m < n/2$ [89, Chapter 8]. The volume can be computed from (3.2) and is hence given by

$$V_{\text{c}} = V\left(A_n^{(m)}\right) = (n+1)^{(m-1)/2}. \tag{3.17}$$

The minimum norm for the Craig's lattice $A_n^{(m)}$ is at least $2m$, i.e., $\mu\left(A_n^{(m)}\right) \geq 2m$. Therefore, the choice of m directly impacts the lattice packing radius, which is given by

$$p_{\text{rc}} = \frac{1}{2}\sqrt{\mu\left(A_n^{(m)}\right)} \geq \sqrt{\frac{m}{2}}. \tag{3.18}$$

Using (3.17) and (3.18), a lower bound for the density of the Craig's lattice is given by

$$\Delta_{\text{c}} = \frac{V_1 p_{\text{rc}}^n}{V_{\text{c}}}. \tag{3.19}$$

Table 3.2: Center density (ψ_{c}) versus m.

Lattice **size** ($\mathbf{n}$)	$m=2$	$m=3$	$m=4$	$m=5$	$m=6$	$m=7$	$m=8$	$m=9$	$m=10$
16	-6.13	-5.54	-6.31	-7.82	-9.80	-12.11	-14.66	-17.38	-20.26
36	-7.81	-2.49	-0.23	0.35	-0.12	-1.33	-3.07	-5.22	-7.70
52	-8.60	0.89	5.95	8.60	9.71	9.76	9.04	7.73	5.95
60	-8.90	2.72	9.24	12.97	14.93	15.67	15.51	14.69	13.32

As observed, we can obtain different lattice densities depending on the parameter m. The lower bound given by (3.19) is maximized for the value $m = m_0$, where

$$m_0 = \left\lfloor \frac{1}{2} \frac{n}{\log_e(n+1)} \right\rceil. \tag{3.20}$$

This is the value of m for which an n-dimensional Craig's lattice achieves its maximum density [89, Chapter 8]. Finally, the center density (number of lattice points per volume unit) is

$$\psi_{\mathrm{c}} = \frac{\Delta_{\mathrm{c}}}{V_1} = \frac{p_{\mathrm{rc}}^n}{V_{\mathrm{c}}}. \tag{3.21}$$

Table 3.2 shows the base 2 logarithm of the center density for Craig's lattices having different values of n and m. For the dimension $n = 16$, the highest value for the center density is obtained when $m = 3$, whereas for the dimensions $n = 36$, $n = 52$ and $n = 60$ the densest Craig's lattices are obtained for $m = 5$, $m = 7$ and $m = 7$, respectively. These values agree with the integers resulting from the formula in (3.20). Notice that the computational cost of the closest point algorithms depends on the number of lattice points in the search region, and the parameter ψ_{c} is an intuitive indicator of this number.

3.4.2 MMSE Decoding

When considering the transmission of analog sources, MMSE decoding is optimum as it minimizes the observed distortion. The MMSE estimator of the source symbols $\tilde{\mathbf{s}}_{\mathrm{c}}$ from the received symbols $\tilde{\mathbf{y}}_{\mathrm{c}}$ is given by

$$\hat{\mathbf{s}}_{\mathrm{c}} = \mathbb{E}[\tilde{\mathbf{s}}_{\mathrm{c}} \mid \tilde{\mathbf{y}}_{\mathrm{c}}] = \int \tilde{\mathbf{s}}_{\mathrm{c}}\, p_{\mathrm{s}}(\tilde{\mathbf{s}}_{\mathrm{c}} \mid \tilde{\mathbf{y}}_{\mathrm{c}})\, d\tilde{\mathbf{s}}_{\mathrm{c}}. \tag{3.22}$$

By employing the piece-wise definition of the mapping function in (3.11) and the compact expression for $\tilde{\mathbf{y}}_{\mathrm{c}}$ in (3.13), the conditional probability $p_{\mathrm{s}}(\tilde{\mathbf{s}}_{\mathrm{c}} \mid \tilde{\mathbf{y}}_{\mathrm{c}})$ can be expressed as

$$p_{\mathrm{s}}(\tilde{\mathbf{s}}_{\mathrm{c}} \mid \tilde{\mathbf{y}}_{\mathrm{c}}) \propto \sum_{i=1}^{|\mathcal{L}|} r_i(\tilde{\mathbf{y}}_{\mathrm{c}}, \tilde{\mathbf{s}}_{\mathrm{c}}), \tag{3.23}$$

where

$$r_i(\tilde{\mathbf{y}}_{\mathrm{c}}, \tilde{\mathbf{s}}_{\mathrm{c}}) \propto \begin{cases} \phi_i\; g(\tilde{\mathbf{s}}_c \mid \boldsymbol{\mu}_i, \Sigma) & \text{if } \tilde{\mathbf{s}}_k \in \Omega_{\mathcal{T}}(\mathbf{l}_{k,i})\ \forall k \\ 0 & \text{otherwise,} \end{cases} \tag{3.24}$$

with

$$g(\tilde{\mathbf{s}}_{\mathrm{c}} \mid \boldsymbol{\mu}_i, \boldsymbol{\Sigma}) = \Big(\big(2\pi\big)^{Kn} |\boldsymbol{\Sigma}| \Big)^{-1/2} \exp\left(-\frac{1}{2} (\tilde{\mathbf{s}}_{\mathrm{c}} - \boldsymbol{\mu}_i)^T \boldsymbol{\Sigma}^{-1} (\tilde{\mathbf{s}}_{\mathrm{c}} - \boldsymbol{\mu}_i) \right), \tag{3.25}$$

$$\phi_i = \exp\left(-\frac{1}{2} \left(\sigma_{\mathrm{n}}^{-2} \parallel \tilde{\mathbf{y}}_{\mathrm{c}} - \tilde{\mathbf{H}}_{\mathrm{c}} \mathbf{D} \mathbf{B} \mathbf{l}_i \parallel^2 - \boldsymbol{\mu}_i^T \boldsymbol{\Sigma}^{-1} \boldsymbol{\mu}_i \right) \right), \tag{3.26}$$

$$\boldsymbol{\mu}_i = \frac{1}{\sigma_{\mathrm{n}}^2} \boldsymbol{\Sigma} \mathbf{D}^T \tilde{\mathbf{H}}_{\mathrm{c}}^T (\tilde{\mathbf{y}}_{\mathrm{c}} + \tilde{\mathbf{H}}_{\mathrm{c}} \mathbf{D} \mathbf{B} \mathbf{l}_i), \tag{3.27}$$

and

$$\boldsymbol{\Sigma} = \left(\frac{1}{\sigma_{\mathrm{n}}^2} \mathbf{D}^T \tilde{\mathbf{H}}_{\mathrm{c}}^T \tilde{\mathbf{H}}_{\mathrm{c}} \mathbf{D} + \mathbf{C}_{\tilde{\mathbf{s}}}^{-1} \right)^{-1}. \tag{3.28}$$

The steps required to obtain this result are similar to those explained in [20, Appendix A] for MMSE estimation using modulo-like functions but considering mapping functions from n-dimensional lattices.

Recall that the MMSE integral in (3.22) is decomposed into a sum of terms weighted by their corresponding factor ϕ_i. An important remark is that the function $g(\tilde{\mathbf{s}}_{\mathrm{c}} \mid \boldsymbol{\mu}_i, \boldsymbol{\Sigma})$ actually represents the PDF of a truncated multivariate Gaussian with mean $\boldsymbol{\mu}_i$ and covariance matrix $\boldsymbol{\Sigma}$, which is restricted to the corresponding Kn-dimensional region given by the aggregate of the K Voronoi regions $\Omega_{\mathcal{T}}(\mathbf{l}_{k,i})$. For simplicity, we will represent this Kn-dimensional region by $\Omega_{\mathcal{T}}(\mathbf{l}_i)$. Therefore, we will compute the MMSE estimates of the user symbols as

$$\hat{\mathbf{s}}_{\mathrm{c}} = \frac{\sum_i \phi_i \Theta\left(\Omega_{\mathcal{T}}(\mathbf{l}_i); \boldsymbol{\Sigma}, \boldsymbol{\mu}_i\right)}{\sum_i \phi_i \Phi(\Omega_{\mathcal{T}}(\mathbf{l}_i); \boldsymbol{\Sigma}, \boldsymbol{\mu}_i)}, \tag{3.29}$$

where $\Theta(\Omega_{\mathcal{T}}(\mathbf{l}_i); \boldsymbol{\Sigma}, \boldsymbol{\mu}_i) = \int_{\Omega_{\mathcal{T}}(\mathbf{l}_i)} \tilde{\mathbf{s}}_{\mathrm{c}}\ g(\tilde{\mathbf{s}}_{\mathrm{c}} \mid \boldsymbol{\mu}_i, \boldsymbol{\Sigma})\ d\tilde{\mathbf{s}}_{\mathrm{c}}$ is the mean of a Kn-dimensional multivariate Gaussian truncated to the region given by $\Omega_{\mathcal{T}}(\mathbf{l}_i)$, and $\Phi(\Omega_{\mathcal{T}}(\mathbf{l}_i); \boldsymbol{\Sigma}, \boldsymbol{\mu}_i) = \int_{\Omega_{\mathcal{T}}(\mathbf{l}_i)} g(\tilde{\mathbf{s}}_{\mathrm{c}} \mid \boldsymbol{\mu}_i, \boldsymbol{\Sigma})\ d\tilde{\mathbf{s}}_{\mathrm{c}}$ represents the cumulative distribution of a multivariate Gaussian variable in the aggregated region $\Omega_{\mathcal{T}}(\mathbf{l}_i)$.

Figure 3.3 shows an illustrative example of a bi-dimensional space that is partitioned into four feasible regions $\Omega_{\mathcal{T}}(\mathbf{l}_i)$ by using lattice-based mappings. For simplicity, we assume rectangular regions but, in the general case, the shape of the truncated regions is given by the corresponding Voronoi regions. The pdf of the truncated Gaussian functions at each region is represented by contour lines with different colors indicating different probabilities. According to (3.24), we have different Gaussian functions (with mean $\boldsymbol{\mu}_i$ and same covariance matrix $\boldsymbol{\Sigma}$) weighted by the factor ϕ_i. As shown, the maximum value of these functions could fall outside the truncated region due to the channel and noise effects. Note also that the size of the truncated regions is given by the parameters α_k within the matrix $\mathbf{B}$.

3.4.2.1 Sphere Decoding with MAP Estimation

The computation of the MMSE estimates with (3.29) requires to determine the integrals of the truncated Gaussian functions over the Kn-dimensional regions defined by $\Omega_{\mathcal{T}}(\mathbf{l}_i)$. This computation leads to two important problems:

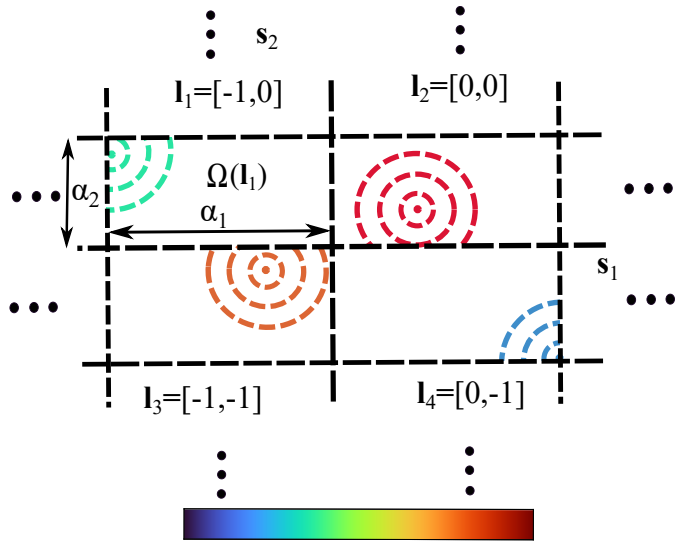

Figure 3.3: Example of the partition of the source space using bi-dimensional truncated Gaussian variables.

- The number of potential combinations of Voronoi regions increases as the lattice dimension becomes larger, i.e., the cardinality of the set $\mathcal{L}$ dramatically grows with n.
- The integration of Gaussian functions over Kn-dimensional regions is an extremely difficult problem with an unaffordable computational complexity, even for small values of K and n, and considering hyperspheres with radius p_{r} as integration regions.

The first problem can be alleviated by considering only those truncated regions $\Omega_{\mathcal{T}}(\mathbf{l}_i)$ with the largest associated weights ϕ_i. In such a case, the problem can be formulated as the search of the candidate vectors $\mathbf{l}_i$ such that their corresponding weight factor ϕ_i exceeds a given threshold T, i.e.,

$$\phi_i(\mathbf{l}_i) = \exp\left(-\frac{1}{2}\left(\sigma_{\mathrm{n}}^2 \parallel \tilde{\mathbf{y}}_{\mathrm{c}} + \tilde{\mathbf{H}}_{\mathrm{c}}\mathbf{D}\mathbf{B}\mathbf{l}_i \parallel^2 - \boldsymbol{\mu}_i^T\boldsymbol{\Sigma}\boldsymbol{\mu}_i\right)\right) > T. \tag{3.30}$$

Hence, the set of relevant candidate vectors is constructed as $\mathcal{L}_d = \{\mathbf{l}_i \in \mathcal{Z}^{Kn} \mid \phi_i(\mathbf{l}_i) > T\}$. This problem was already approached for the case of modulo-like mapping functions with Rayleigh channels in [20]. The proposed solution is based on transforming the Kn-dimensional search space into a "decoding" lattice $\mathcal{T}_{\mathrm{d}}$ whose points correspond to all the possible vectors $\mathbf{l}_i$, and then using a sphere decoder to select those lattice points that fall inside a hypersphere with a particular radius.

Following an approach similar to that explained in [20, Appendix B], we obtain the following Gram matrix for the decoding lattice

$$\mathbf{A}_{\mathrm{d}} = \frac{1}{2}\mathbf{B}^T\mathbf{D}^T\tilde{\mathbf{H}}_{\mathrm{c}}^T\left(\sigma_{\mathrm{n}}^2\mathbf{I} + \tilde{\mathbf{H}}_{\mathrm{c}}\mathbf{D}\mathbf{C}_{\tilde{\mathbf{s}}}\mathbf{D}^T\tilde{\mathbf{H}}_{\mathrm{c}}^T\right)^{-1}\tilde{\mathbf{H}}_{\mathrm{c}}\mathbf{D}\mathbf{B}, \tag{3.31}$$

and the vector $\mathbf{l}_0 = \left(\mathbf{B}^T\mathbf{D}^T\tilde{\mathbf{H}}_{\mathrm{c}}^T\tilde{\mathbf{H}}_{\mathrm{c}}\mathbf{D}\mathbf{B}\right)^{-1}\mathbf{B}^T\mathbf{D}^T\tilde{\mathbf{H}}_{\mathrm{c}}^T\tilde{\mathbf{y}}_{\mathrm{c}}$ for the center of the sphere where the candidate vectors will be searched for. Therefore, the generator matrix for the decoding lattice $\mathcal{T}_{\mathrm{d}}$ is given by $\mathbf{M}_{\mathrm{d}} = \mathbf{A}_{\mathrm{d}}^{1/2}$.

According to this alternative formulation (3.30), the points of the decoding lattices are given by $\mathbf{M}_{\mathrm{d}}\mathbf{l}_i$, and their corresponding ϕ_i will increase as the Euclidean distance with respect to $\mathbf{M}_{\mathrm{d}}\mathbf{l}_0$ decreases. Hence, we can build the set of candidate vectors as

$$\mathcal{L}_d = \{\mathbf{l}_i \in \mathcal{Z}^{Kn} \mid ||\mathbf{M}_{\mathrm{d}}\mathbf{l}_0 - \mathbf{M}_{\mathrm{d}}\mathbf{l}_i)||^2 < R^2\}. \tag{3.32}$$

This idea resembles the so-called integer least-square problem where the sphere decoder has been shown to be an effective solution [98]. In this case, the application of the sphere decoder to construct the set $\mathcal{L}_d$ is the same as in [20] but considering the particular lattice structure of $\mathcal{T}_{\mathrm{d}}$, and using the Gram matrix $\mathbf{A}_{\mathrm{d}}$ and the sphere center $\mathbf{l}_0$.

After obtaining the set of candidate vectors $\mathbf{l}_i$ corresponding to those truncated Gaussian regions with a significant weight, the MMSE estimates are determined as follows

$$\hat{\mathbf{s}}_{\mathrm{c}} = \frac{\sum_{i=1}^{|\mathcal{L}_d|} \phi_i \Theta(\Omega_{\mathcal{T}}(\mathbf{l}_i); \boldsymbol{\Sigma}, \boldsymbol{\mu}_i)}{\sum_{i=1}^{|\mathcal{L}_d|} \phi_i \Phi(\Omega_{\mathcal{T}}(\mathbf{l}_i); \boldsymbol{\Sigma}, \boldsymbol{\mu}_i)}. \tag{3.33}$$

However, this expression still requires the computation of $2|\mathcal{L}_d|$ integrals of Kn-dimensional Gaussian functions over complex truncated regions. To circumvent this problem, we propose to approximate the MMSE integrals in (3.33) by the corresponding maximum a posteriori (MAP) estimates for each region of the candidate vectors in $\mathcal{L}_d$. In this particular case, the MAP and MMSE estimators are not strictly equivalent due to the truncated nature of the conditional posterior probability. However, for an adequate design of the mapping parameters, the MAP estimates will be an accurate approximation since the peak values of the truncated Gaussian functions will mostly fall into the corresponding truncated regions. Hence, we can simplify the expression in (3.33) as $\hat{\mathbf{s}}_{\mathrm{c}} = \sum_{i=1}^{|\mathcal{L}_d|} \phi_i \ \hat{\mathbf{s}}_i^{\mathrm{MAP}}$, where $\hat{\mathbf{s}}_i^{\mathrm{MAP}}$ is the MAP estimation for the region $\Omega_{\mathcal{T}}(\mathbf{l}_i)$, which is the solution to the following maximization problem

$$\hat{\mathbf{s}}_i^{\mathrm{MAP}} = \arg\max_{\tilde{\mathbf{s}}_i} \ p(\tilde{\mathbf{s}}_i \mid \tilde{\mathbf{y}}_{\mathrm{c}}) = \arg\max_{\tilde{\mathbf{s}}_i} \ \frac{p(\tilde{\mathbf{s}}_i \mid \tilde{\mathbf{y}}_{\mathrm{c}})\, p(\tilde{\mathbf{s}}_i)}{p(\tilde{\mathbf{y}}_{\mathrm{c}})}, \tag{3.34}$$

where the a priori probability $p(\tilde{\mathbf{s}}_i)$ is given by (3.6) with a covariance matrix $\mathbf{C}_{\tilde{\mathbf{s}}_c} = \mathbf{C}_{\tilde{\mathbf{s}}} \otimes \mathbf{I}_{\frac{n}{2}}$, the conditional probability is given by

$$p(\tilde{\mathbf{s}}_i \mid \tilde{\mathbf{y}}_{\mathrm{c}}) = \frac{1}{(\pi\sigma_{\mathrm{n}}^2)^{nK}} \exp\left(-\frac{1}{\sigma_{\mathrm{n}}^2}\|\tilde{\mathbf{y}_{\mathrm{c}}} - \tilde{\mathbf{H}}_{\mathrm{c}}\mathbf{D}(\tilde{\mathbf{s}}_i - \mathbf{B}\mathbf{l}_i)\|^2\right), \tag{3.35}$$

and the term $p(\tilde{\mathbf{y}}_{\mathrm{c}})$ can be disregarded as it does not depend on $\tilde{\mathbf{s}}_i$. This maximization problem can be reformulated as the minimization of the arguments of the two exponential functions in (3.34), which correspond to the a priori and the conditional probabilities, respectively. Therefore, the MAP estimates are determined by solving the following optimization problem

$$\begin{aligned} \hat{\mathbf{s}}_i^{\mathrm{MAP}} = \arg\min_{\tilde{\mathbf{s}}_i} \ & \|\tilde{\mathbf{y}}_{\mathrm{c}} - \tilde{\mathbf{H}}_{\mathrm{c}}\mathbf{D}(\tilde{\mathbf{s}}_i - \mathbf{B}\mathbf{l}_i)\|^2 + \frac{\sigma_{\mathrm{n}}^2}{2}\tilde{\mathbf{s}}_i^T\mathbf{C}_{\tilde{\mathbf{s}}_{\mathrm{c}}}^{-1}\tilde{\mathbf{s}}_i \\ \text{s.t.} \ & \|\tilde{\mathbf{s}}_{i,k} - \mathbf{B}\mathbf{l}_{i,k}\|^2 \leq p_{\mathrm{r}}(\alpha_k), \ \forall k, \end{aligned} \tag{3.36}$$

where the K constraints in (3.36) are imposed to ensure that the i-th MAP solution falls into the corresponding truncated region $\Omega_{\mathcal{T}}(\mathbf{l}_i)$. It is important to remark that these constraints aim at approximating the corresponding actual Voronoi regions, which cannot be defined analytically for an arbitrary dimension. As observed, the Euclidean distance between the solution vector for each user $\tilde{\mathbf{s}}_{i,k}$ and the corresponding centroid $\mathbf{Bl}_{i,k}$ must be lower than the packing radius $p_{\mathrm{r}}(\alpha_k)$ of the scaled version of the encoding lattice at user k.

The problem in (3.36) can be rewritten in a quadratic form as

$$\begin{aligned} \hat{\mathbf{s}}_i^{\mathrm{MAP}} = \quad & \arg\min_{\tilde{\mathbf{s}}_i} \frac{1}{2}\tilde{\mathbf{s}}_i^T\mathbf{Q}\tilde{\mathbf{s}}_i - \mathbf{v}_i^T\tilde{\mathbf{s}}_i \\ \text{s.t.} \quad & \|\tilde{\mathbf{s}}_{i,k} - \mathbf{Bl}_{i,k}\|^2 \leq p_{\mathrm{r}}(\alpha_k),\ \forall k, \end{aligned} \tag{3.37}$$

where $\mathbf{Q} = 2\mathbf{D}^T\tilde{\mathbf{H}}_{\mathrm{c}}^T\tilde{\mathbf{H}}_{\mathrm{c}}\mathbf{D} + \sigma_{\mathrm{n}}^2\mathbf{C}_{\tilde{\mathbf{s}}_{\mathrm{c}}}^{-1}$ and $\mathbf{v}_i = 2\mathbf{D}^T\tilde{\mathbf{H}}_{\mathrm{c}}^T\left(\tilde{\mathbf{y}}_{\mathrm{c}} + \tilde{\mathbf{H}}_{\mathrm{c}}\mathbf{DBl}_i\right)$. This problem is a variant of a quadratically constrained quadratic program (QCQP), which can be solved efficiently by convex optimization techniques.

3.4.2.2 Choice of the Sphere Decoder Radius

In sphere decoding, there is a trade-off between decoding complexity and estimation accuracy that can be adjusted by means of the sphere radius R. If R is too large, there will be too many candidates inside the search hypersphere, which leads to an intractable complexity. However, if R is too small, there will be no points inside the sphere. A reasonable guess for R is the covering radius of the lattice, which is the smallest radius of the spheres centered at the lattice points that cover the entire space (without holes). This approach guarantees the existence of at least one point inside the sphere [99]. However, determining the covering radius for a given lattice is itself hard. Therefore, we need to use an alternative strategy to optimize the value of R.

Let $\bar{\mathbf{l}}$ denote the true vector used to encode the source symbols $\tilde{\mathbf{s}}_c$, i.e., $d_l = ||\mathbf{M}_{\mathrm{d}}\mathbf{l}_0 - \mathbf{M}_{\mathrm{d}}\bar{\mathbf{l}}||^2$ follows a chi-square distribution $\mathcal{X}^2$ with Kn degrees of freedom [99], i.e., $d_l \sim \mathcal{X}^2_{Kn}$. Using this result, we can ensure that the optimum lattice point will fall inside the hypersphere with center $\mathbf{l}_0$ and radius R with a probability $1-\epsilon$ as long as

$$R^2 \geq F^{-1}_{\mathcal{X}^2_{Kn}}(1-\epsilon), \tag{3.38}$$

where $F_{\mathcal{X}^2_{Kn}}(\cdot)$ represents the cumulative distribution function of a chi-square variable with Kn degrees of freedom. Therefore, the ϵ parameter should be set to a value close to zero to guarantee that the optimum vector is obtained by the sphere decoder with high probability. We have checked experimentally that the criterion in (3.38) provides a good trade-off for $\epsilon \approx 10^{-5}$.

In any case, the choice of the radius R is not critical in terms of the system performance, since if no candidates are found for a given ϵ, R can be decreased and the sphere decoder is applied again with the new value. Conversely, the value of R does impact the computational cost of the decoding phase. It is thus important to prevent the use of excessively large R values.

3.4.3 Parameter Optimization

The optimization of the mapping parameters $\{\alpha_k, \delta_k\}$ is fundamental to achieve good performance. Recall that α_k determines the distance between the lattice points at the k-th user. Reducing α_k decreases the size of the associated Voronoi regions and thus the norm of the encoded vectors. This in turn impacts the power factors δ_k, which are determined as $\delta_k = \sqrt{P_{\mathrm{T}k}/e_k(\alpha_k)}$, where $e_k(\alpha_k)$ is the resulting k-th user quantization error. Note that $e_k(\alpha_k)$ will decrease when lowering α_k, which will allow larger δ_k values for a given power constraint $P_{\mathrm{T}k}$. Recall that large values of δ_k reduce the symbol distortion at reception since the error covariance matrix $\mathbf{\Sigma}$ in (3.28) inversely depends on $\mathbf{D} = \mathrm{diag}\,(\delta_1, \ldots, \delta_K) \otimes \mathbf{I}_n$. This is clear in the ideal situation where one unique candidate $\mathbf{l}_i$ has a significant weight ϕ_i and no decoding ambiguities occur. However, when using too small α_k values, the fading MAC and the noise will cause decoding ambiguities, which will severely degrade the system performance.

Therefore, when optimizing α_k, an adequate trade-off is essential to minimize the system distortion. The intuitive idea is to use the minimum possible α_k values, which minimize the probability of decoding ambiguities. Recall that the decoding ambiguities are caused by the presence of several candidate vectors $\mathbf{l}_i$ with relevant and similar weights. In the alternative lattice-based formulation, this implies that there are several points in the decoding lattices with a similar distance to the center point given by $\mathbf{l}_0$. Therefore, an adequate criterion for the optimization of α_k is to guarantee that the separation among the points in the decoding lattice $\mathcal{T}_d$ is larger than a certain threshold S, i.e.,

$$||\mathbf{M}_{\mathrm{d}}\mathbf{l}_i - \mathbf{M}_{\mathrm{d}}\mathbf{l}_j||^2 \geq S, \quad \forall\, \mathbf{l}_i \neq \mathbf{l}_j. \tag{3.39}$$

Note that the lattice expression in (3.31) depends on $\mathbf{B}$, which includes the diagonal matrix $\mathbf{U} = \mathrm{diag}\,(\alpha_1, \ldots, \alpha_K)$. This way, we can formulate an iterative procedure, which alternatively updates the values of α_k and δ_k until the criterion in (3.39) is satisfied.

Finally, an appropriate value for the threshold S should be selected. A conservative value is $S = 2R^2$ to ensure that the probability of finding other lattice points at a distance equal or smaller than to the optimum one is negligible. However, we have experimentally observed that this threshold can be reduced to $S \approx R^2$ without causing detrimental decoding ambiguities.

3.5 Simulation Results

In this section, we present the results of simulations carried out to evaluate the performance of the proposed lattice-based analog JSCC system in a $K \times N_{\mathrm{r}}$ SIMO MAC scenario.

At each time instant, the vector of K source symbols is generated from a zero-mean multivariate circularly symmetric Gaussian distribution with covariance matrix $\mathbf{C_s}$. We consider an equal correlation model as explained in Section 2.2 for the user symbols i.e., $[\mathbf{C_s}]_{i,i} = 1\ \forall i = 1, \ldots, K$ and $[\mathbf{C_s}]_{i,j} = \rho,\ \forall i \neq j$. As mentioned, blocks of n source symbols are encoded

at each user via an analog JSCC lattice-based mapping where the parameters are properly optimized as explained in Subsection 3.4.3 to avoid decoding ambiguities. The resulting encoded symbols are sent to the BS over a fading SIMO MAC, where the channel coefficients follow a Rayleigh distribution as explained in Subsection 2.5.2. The fading channel response is assumed to remain constant during the transmission of B_{s} blocks of n source symbols. At the BS, the vector $\tilde{\mathbf{y}}_{\mathrm{c}}$, with all the received symbols corresponding to a block, is employed to estimate the source symbols of all users with the help of the sphere decoder. This simulation procedure is repeated for C_{R} different channel realizations. Table 3.3 summarizes the system model configurations considered in the computer simulations.

Table 3.3: Simulation parameter setting.

Description	Setting
Number of analog sources	$K \in \{4, 10\}$
Antennas at the BS	$N_{\mathrm{r}} \in \{10, 20\}$
Signal-to-noise ratio	SNR (dB) $\in \{0, 5, 10, 15, 20, 25, 30\}$
Correlation model	$[\mathbf{C_s}]_{i,i} = 1,\ \forall i,\ [\mathbf{C_s}]_{i,j} = \rho,\ \forall i \neq j$
Correlation factor	$\rho \in \{0.80, 0.95, 0.99\}$
Channel realizations	$C_{\mathrm{R}} = 1000$
Block size (lattice dimension)	$n \in \{1, 2, 8, 16, 24, 36, 52\}$

Performance is evaluated in terms of the SDR obtained for a given range of signal-to-noise ratio (SNR) values. As explained in Subsection 2.3.1, SDR (dB) $= 10\log_{10}(1/\hat{\xi}_{\mathrm{sum}})$, where

$$\hat{\xi}_{\mathrm{sum}} = \frac{1}{C_{\mathrm{R}} B_{\mathrm{s}} n K} \sum_{l=1}^{C_{\mathrm{R}}} \sum_{j=1}^{B_{\mathrm{s}} n} \sum_{k=1}^{K} |s_{k,j,l} - \hat{s}_{k,j,l}|^2 \tag{3.40}$$

is the average MSE between the source and the estimated symbols. For simplicity, we assume that the available power at the K users is the same, i.e., $P_{\mathrm{T}k} = P_{\mathrm{T}},\ \forall k$, whereas the noise component is $\sigma_{\mathrm{n}}^2 = 1$. Therefore, the system SNR is SNR (dB) $= 10\log_{10}(P_{\mathrm{T}})$.

3.5.1 Performance Evaluation of the Lattice-Based Analog JSCC

The following lattices have been considered in the simulation experiments carried out:

1. Craig's lattices with dimensions $n \in \{16, 36, 52\}$. The parameter m is chosen to obtain the densest possible lattices for each n with an affordable encoding computational cost. For dimensions up to 36 we consider the densest Craig's lattices, i.e., $m = 3$ for $n = 16$ and $m = 5$ for $n = 36$ whereas for $n = 52$, $m = 3$ is considered since the densest lattice in this high dimension leads to impractical computational complexity.
2. The Leech lattice ($n = 24$) [89], [92].
3. The Barnes-Wall (BW_{16}) lattice ($n = 16$) [89].
4. The E_8 lattice ($n = 8$) [88], [89].

5. The bi-dimensional hexagonal lattice ($n = 2$) [43].
6. The modulo-like mappings ($n = 1$) [20], [88].

In addition, two performance bounds were considered as benchmarks. The first one results from uncoded transmission, which provides the best performance achievable assuming a zero-delay linear strategy. In this uncoded transmission, each user source symbol is multiplied by a complex-valued scalar to exploit both the channel information and the user correlation while satisfying the individual power constraints (cf. [100]). The other bound is the optimum performance theoretically attainable (OPTA), which corresponds to the best performance achievable by any communication system designed according to the separation principle. The OPTA is determined by equating the source rate distortion region and the capacity region of the MAC [20, Appendix C].

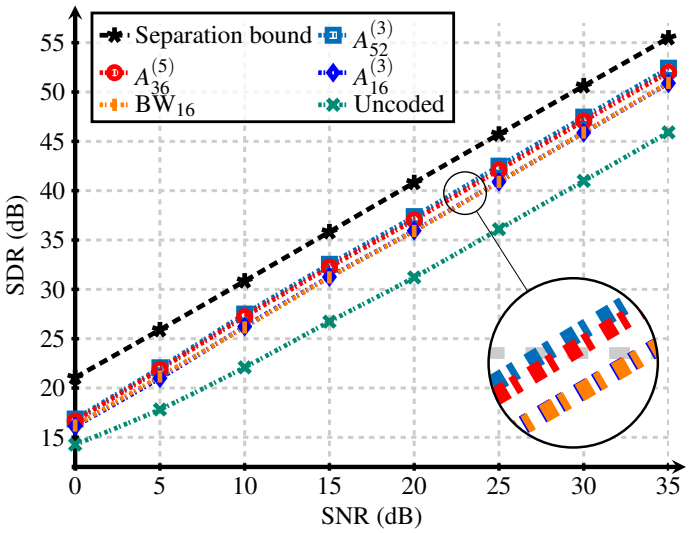

Figure 3.4: SDR (dB) for different sizes of a Craig's lattice-based mapping ($n \in \{16, 36, 52\}$) with $m = 3$ for $n = 16$, $m = 5$ for $n = 36$ and $m = 3$ for $n = 52$, and for the (BW_{16}) lattice in a 4×20 SIMO MAC setup with $\rho = 0.95$.

Figure 3.4 plots the SDR obtained in a 4×20 SIMO MAC with correlated sources ($\rho = 0.95$). This first experiment was set up to analyze the performance obtained with Craig's lattices of increasing block size. Three Craig's lattices with dimensions $n \in \{16, 36, 52\}$ were considered.

According to Table 3.2, the values of m that lead to the densest Craig's lattices are $m \in \{3, 5, 7\}$, respectively. Note that we have taken the optimal values of m for $n = 16$ and $n = 36$ while for $n = 52$, $m = 3$ was selected because is the largest value leading to a reasonable encoding cost. We also remark that the proposed alternative construction makes it possible to perform Craig's lattice encoding for larger values of m when $n = 36$, and for some values of m when $n = 52$.

As observed in Figure 3.4, the best performance is obtained by the Craig's lattice with the largest dimension $n = 52$. This is a very interesting result as it shows that system performance

is improved when increasing the codeword size in spite of not using the best packing lattices. Figure 3.4 also shows that Craig's lattices are a good choice for encoding since the lattice $A_{16}^{(3)}$ approximately provides the same performance as BW_{16}, which is the densest lattice for $n = 16$ [89]. Finally, Craig's lattices allow to reduce the gap of the linear approaches (uncoded transmission) w.r.t. the OPTA from 10 dB to only 2 or 3 dB. Nevertheless, note that OPTA is actually an optimistic upper bound since infinite block length for the source and channel encoders is assumed and the constraints for the individual rates are disregarded.

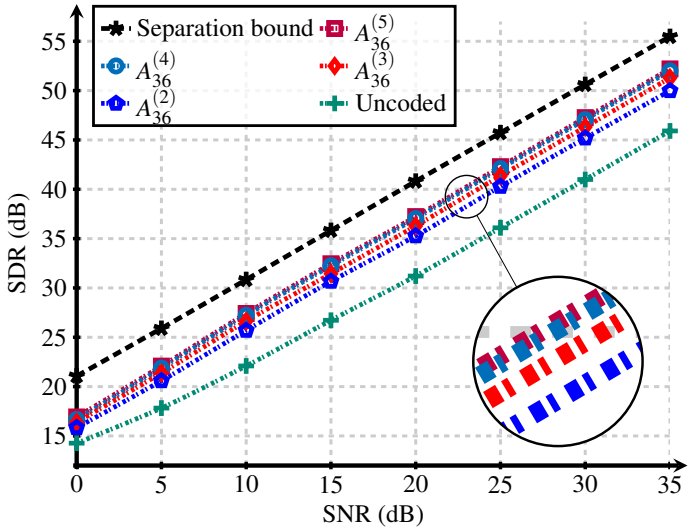

Figure 3.5: SDR (dB) obtained with $m \in \{2, 3, 4, 5\}$ by considering a Craig's lattice-based mapping (with size $n = 36$) in a 4×20 SIMO MAC setup with spatial correlation $\rho = 0.95$.

Table 3.4: SDR (dB) obtained for different analog JSCC mappings for different SNRs and $\rho = 0.95$.

SNR (dB)	**Sep. Bound**	$\mathbf{A_{52}^{(3)}}$	$\mathbf{A_{36}^{(4)}}$	**Leech**	$\mathbf{BW_{16}}$	$\mathbf{E_8}$	**Hex.**	**Mod.**	**Unc.**
0	21.07	16.86	16.66	16.39	16.23	16.06	15.55	15.05	14.26
5	25.90	22.05	21.88	21.42	21.17	20.76	19.97	19.23	17.82
10	30.84	27.50	27.23	26.64	26.15	25.77	24.71	23.95	22.09
15	35.82	32.54	32.25	31.61	31.21	30.76	29.68	28.81	26.72
20	40.82	37.37	37.03	36.33	35.92	35.38	34.24	33.28	31.21
25	45.73	42.49	42.10	41.31	40.89	40.32	39.11	38.21	36.10
30	50.62	47.46	47.07	46.21	45.90	45.24	44.12	43.21	40.99
35	55.48	52.42	52.00	51.25	50.93	50.18	49.06	48.25	45.91

Next, we evaluate the impact of the lattice density on the system performance. Figure 3.5 shows the SDRs achieved in the same communication scenario as before when considering Craig's lattice-based mappings for $n = 36$ and $m \in \{2, 3, 4, 5\}$. As observed, the SDR improves with the lattice density. Indeed, the best performance is achieved for $m = 5$, i.e., the densest $A_{36}^{(5)}$ lattice provides the highest SDR. This result illustrates the importance of

optimizing the lattice density for a given codeword size n. The gain obtained when moving from $m = 4$ to $m = 5$ is minimum because the increase of the lattice density is also relatively small (see Table 3.2). We have also observed that the system performance starts to decrease for m values above the optimal one m_0.

Table 3.4 shows the SDR values obtained with the proposed lattice-based analog JSCC approach when using different block sizes for the encoding of correlated sources with $\rho = 0.95$ in a fading 4×20 SIMO MAC system. We consider the best packing lattices for each dimension until $n = 24$ and two different Craig's lattices for $n = 52$ and $n = 36$, namely $A_{52}^{(3)}$ and $A_{36}^{(4)}$. These Craig's lattices provide an appropriate balance between performance and computational cost.

Figure 3.6 illustrates the system performance for the $A_{52}^{(3)}$ lattice-based mapping, the modulo-like mapping, the uncoded transmission and the OPTA bound. In the figure, we can appreciate SDR gains of about 2 dB by using the optimized modulo-like mappings instead of the uncoded transmission. This gain is due to the non-linearity of the modulo functions which makes them more suitable for the zero-delay transmission of correlated sources [86]. The improvement w.r.t. the modulo-like mappings when using the Craig's lattice $A_{52}^{(3)}$ is significantly larger (around 5 dB at high SNR values) which is due to the utilization of a suitable lattice with considerably larger block size. It is also remarkable that lattice-based analog encoding is able to significantly reduce the gap from the separation bound by assuming practical block sizes, significantly smaller than those normally used for digital encoding. The results in Table 3.4 support these conclusions for all the considered SNRs and block sizes.

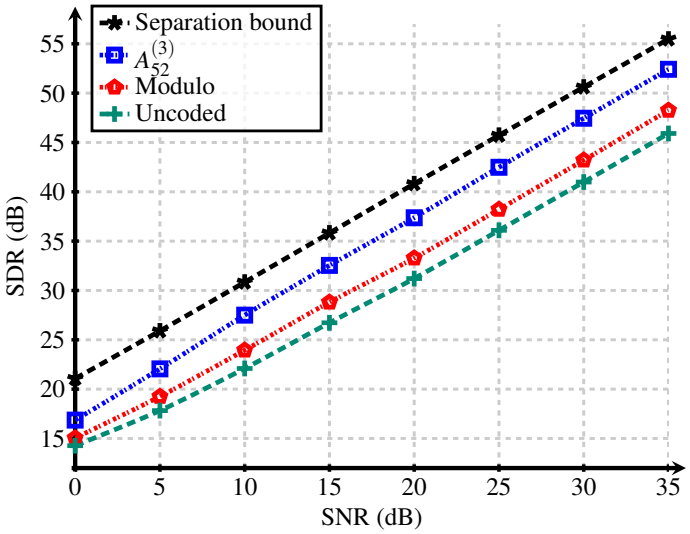

Figure 3.6: SDR (dB) obtained with different JSCCs in a 4×20 SIMO MAC setup with $\rho = 0.95$.

We next analyzed performance for different levels of spatial correlation among users. Figure 3.7 plots the SDR obtained in a fading 4×20 SIMO MAC system with two different correlation values $\rho \in \{0.80, 0.99\}$, and different analog lattice-based mappings. For $\rho = 0.8$,

modulo-like mappings and E_8 lattices provide negligible gain w.r.t. uncoded transmission.

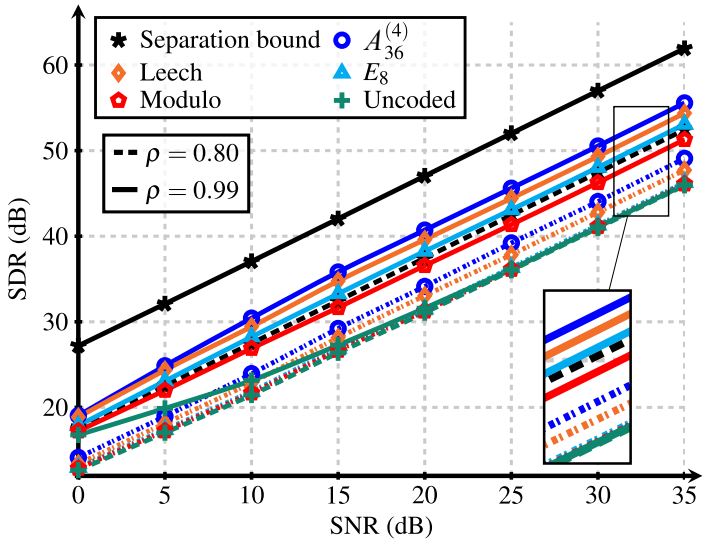

Figure 3.7: SDR (dB) obtained with different JSCCs in a SIMO MAC setup with $N_r = 20$, $K = 4$ and $\rho \in \{0.80, 0.99\}$.

In this case, the use of larger encoding blocks is necessary to exploit the spatial correlation among the sources. For example, the lattice $A_{36}^{(4)}$ already achieves an SDR improvement of about 4 dB. This behavior changes when the correlation factor becomes larger since the SDR gains over uncoded transmission are noticeable even for zero-delay modulo-like mappings. Such gains gradually increase with the block size. On the other hand, the gap of the analog JSCC systems w.r.t. the separation bound apparently increases with the sources correlation level, e.g., with $A_{36}^{(3)}$, the gap goes from 2 dB to 4 dB. This result hence suggests that analog lattice-based JSCC needs even larger block sizes to efficiently exploit high correlation levels in the source symbols.

The communication scenario considered in the previous experiments was favorable for zero-delay modulo-based mappings and uncoded transmissions since the receiver has enough degrees of freedom to handle the inter-user interference. We next analyze the impact of the encoding with larger block sizes on the performance degradation observed for scenarios with higher levels of interference (i.e., less orthogonal).

Figure 3.8 shows the performance obtained for correlated sources with $\rho = 0.95$ and two different MU SIMO setups: 4×20 and 10×20. It is interesting to observe that the system with modulo-like mappings (and uncoded transmission) leads to higher performance for the 4×20 SIMO setup than for the 10×20 configuration. Thus, higher levels of interference prevent the system to efficiently exploit the user correlation, and therefore the performance degrades when there are more users. Conversely, the Craig's lattice-based schemes lead to better performance for the 10×20 SIMO MAC in spite of having fewer degrees of freedom to cancel the MU interference.

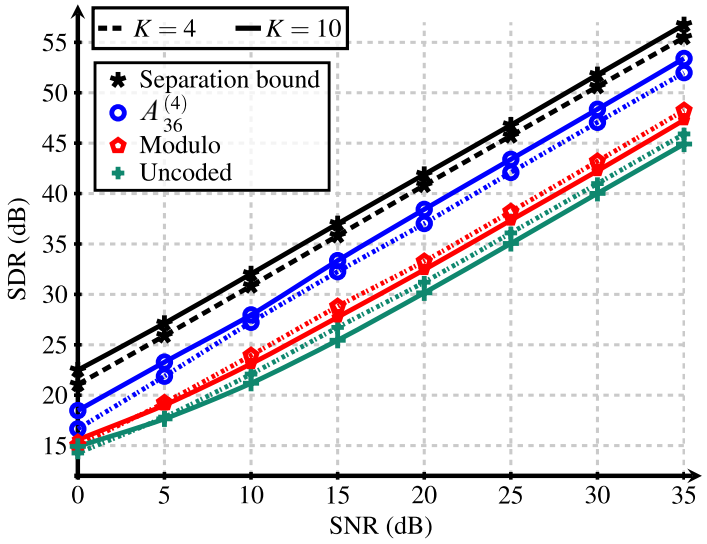

Figure 3.8: SDR (dB) obtained with different JSCCs in a SIMO MAC setup with $N_{\mathrm{r}} = 20$, $K \in \{4, 10\}$ and $\rho = 0.95$.

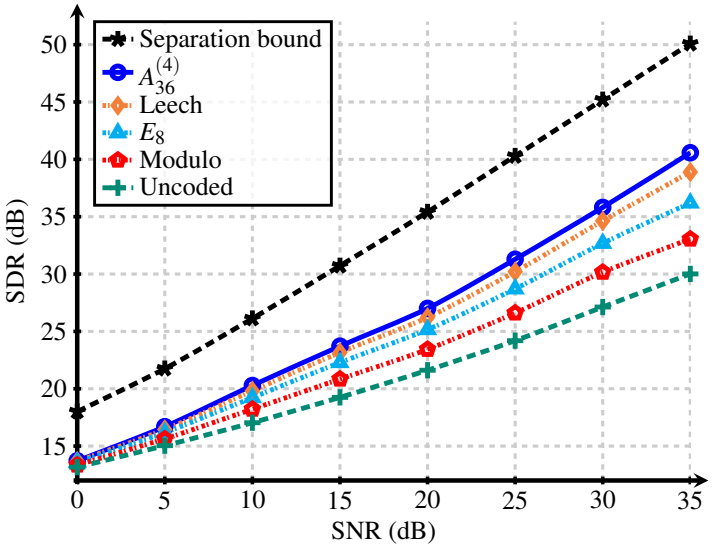

Figure 3.9: SDR (dB) obtained with JSCC in a SIMO MAC setup with $N_{\mathrm{r}} = 10$, $K = 10$ and $\rho = 0.95$.

This behavior is similar to that of the upper bound which suggests that the separation-based schemes are able to deal properly with the MU interference while exploiting the higher overall correlation for the 10×20 configuration if the number of users increases. This is another relevant result as it allows us to circumvent other of the major limitations of the zero-delay mappings and approximate the behavior of conventional digital separation-based systems.

In the ensuing experiment, we aimed at providing more insight into the previous issue. We considered an extreme setup with $K = N_{\mathrm{r}}$, namely a 10×10 SIMO MAC. The $A_{36}^{(4)}$ lattice-based mapping, the Leech lattice-based mapping, the E_8 construction, and the modulo-like mappings were employed to encode correlated sources with $\rho = 0.95$. From the results

in Figure 3.9, we derive two important conclusions: 1) the use of large block sizes provides larger gains w.r.t. zero-delay mappings than in the previous (more orthogonal) configurations, and 2) the gap w.r.t. the OPTA is also larger. The first point becomes clear by comparing the performance of modulo-like mappings to that of the $A_{36}^{(3)}$ lattice in figures 3.8 and 3.9. The gain of using the Craig's lattices goes from 5 dB to 8 dB when considering a 10×10 setup instead of a 10×20 one. The second claim is confirmed by comparing the gap between the SDR curve for the Craig's lattice and the one for the OPTA. This gap goes from 3 dB to almost 10 dB when we move to the 10×10 setup. This analysis supports that the use of larger block sizes helps to mitigate the impact of high levels of MU interference. Still, significantly large block sizes are required to closely approach the OPTA.

3.5.2 Optimization of Lattice-Based Analog JSCC

In this subsection, we address some details about the optimization of the proposed lattice-based analog JSCC approach and the complexity of the decoding operation.

3.5.2.1 Parameter S

As commented in Subsection 3.4.3, the optimization of the mapping parameters is fundamental to achieve an adequate system performance. The trade-off between reducing the symbol distortion and avoiding decoding ambiguities when selecting the α_k parameters is managed by the threshold S. In Subsection 3.4.3, we provide some insight into an adequate choice of S. However, in the following, we experimentally evaluate the accuracy of this choice.

Figure 3.10 shows the SDR versus reasonable values for the parameter S when using the Craig's lattice $A_{36}^{(4)}$ and the Leech lattice in a 4×20 SIMO MAC with $\rho \in \{0.80, 0.95\}$. As observed, the highest system performance is obtained when $S = R^2$ for both lattices, i.e., a proper value for S is to be found in the order of R^2. These results hence confirm our initial hypothesis. Figure 3.10 also shows that the system performance dramatically degrades when $S < R^2$ because the lattice points are too close to each other leading to inevitable decoding ambiguities. This effect is less severe for $S > R^2$, but the resulting system performance is not optimal. At the same time, performance seems more sensitive to the adjustment of S for high levels of source correlation.

3.5.2.2 Parameter R

The sphere decoder radius R is set according to (3.38). The choice of R is less critical than that of S because the sphere decoder can be applied again with a larger R if no candidates are found. However, a proper choice is important to avoid repeating the application of the sphere decoder and to limit the number of candidates falling into the sphere. We have observed from the computer experiments that the criterion in (3.38) is a good choice for R.

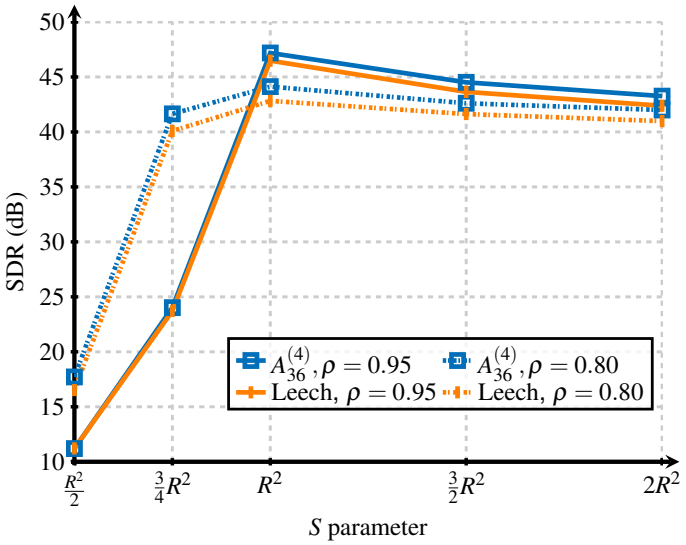

Figure 3.10: SDR (dB) obtained with different values for the parameter S with a Craig's lattice-based mapping $A_{36}^{(4)}$ and the Leech lattice in a SIMO MAC setup with $N_\mathrm{r} = 20$, $K = 4$ and $\rho \in \{0.80, 0.95\}$.

3.5.2.3 Maximum Number of Candidates

The overall computational complexity of lattice-based analog JSCC is determined by the encoding and decoding stages. The operations with the highest computational cost are the search for the closest lattice point given the source vector at the encoder and the search for the candidate vectors in $\mathcal{L}_d$ at the decoder. In this sense, the system was properly designed to get a limited number of candidate vectors with a relevant weight and this, together with the use of MAP estimates, reduces the decoding computational cost. However, the iterative nature of the sphere decoder demands the consideration of large numbers of potential candidates in intermediate iterations, especially for high dimensions. In those cases, we should limit the maximum number of candidate vectors at the end of each iteration in the sphere decoder but minimize the probability of disregarding the optimal vector $\bar{\mathbf{l}}$.

Figure 3.11 plots the SDR obtained when varying the maximum number of candidates considered in the decoding for different lattice-based mappings in a 4×20 SIMO MAC with $\rho = 0.95$. The system performance obtained when using the Craig's lattice $A_{36}^{(4)}$, the Leech lattice, the E_8 construction and the modulo-like mappings are compared for SNR (dB) $\in \{5, 30\}$. As observed, Craig's lattice-based and Leech lattice-based mappings require a higher number of candidates to achieve the best behavior at both SNR levels. This is an expected result because the number of potential combinations of Voronoi regions increases with the lattice dimension n. It is also worth remarking that the impact of excessively limiting the number of considered candidates is less critical in the low SNR regime. The modulo-like mappings are the simplest ones for decoding since they require the smallest number of candidates to reach their best performance. Finally, the E_8 lattice construction leads to a better performance than that obtained with the modulo-like mapping while exhibiting similar decoding complexity.

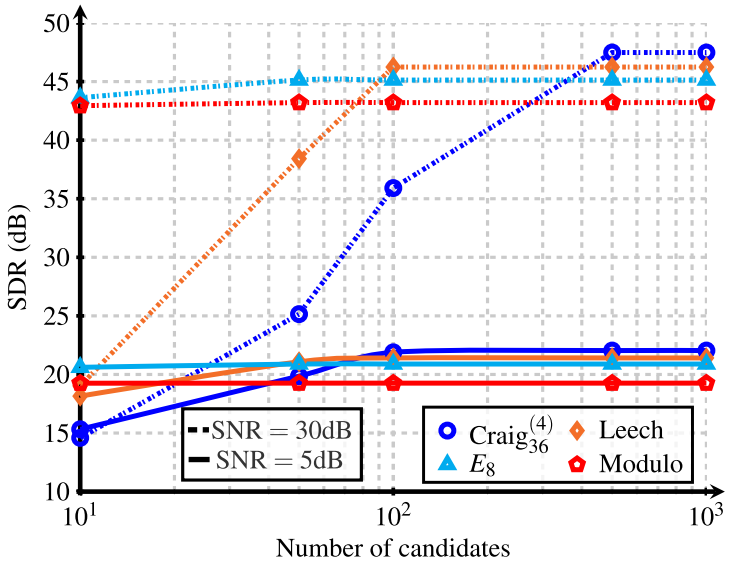

Figure 3.11: SDR (dB) versus maximum number of candidates in the decoding with different analog JSCC mappings in a SIMO MAC setup with $N_r = 20$, $K = 4$, $\rho = 0.95$ and SNR (dB) $\in \{5, 30\}$.

3.6 Conclusions

In this chapter, we have investigated a lattice-based approach to design analog JSCC mappings and encode correlated sources in a fading SIMO MAC system. The proposed system integrates the use of several lattice constructions with different dimensions to encode the user information with variable block sizes. At the receiver, the estimates of the source symbols are computed with the help of a sphere decoder and using MAP estimation to reduce the computational complexity of the decoding operation. This design of the analog JSCC system and an appropriate optimization of the different parameters enable the use of reasonable large block sizes, with a good trade-off between the system performance and the computational cost. In this sense, the Craig's lattices constitute an interesting approach for lattice-based mappings since they allow for balancing the lattice density, which decidedly impacts the system performance, and the computational complexity at the encoding stage.

The results obtained from different computer experiments show that the proposed system is able to reduce the symbol distortion as the codeword size becomes larger. This improvement is especially remarkable for non-orthogonal configurations, where the degrees of freedom of the receiver are more limited to handle the MU interference, and for lower levels of spatial correlation. In these scenarios, zero-delay mappings hardly provided some gains with respect to linear approaches.

Chapter IV

User Grouping for Hybrid mmWave MIMO MAC Systems

MmWave MIMO systems are a promising technology for future wireless communication systems [101]. However, mmWave wireless transmissions suffer from huge path losses. The unfavorable free-space path loss due to the small wavelengths can be compensated with larger gains obtained with antenna arrays having a huge number of elements, i.e., with massive MIMO technologies [102]. A major issue in mmWave massive MIMO is that dedicating one RF chain per antenna leads to inefficient and unaffordable solutions in terms of RF cost and power consumption [7], [10]. This problem is commonly handled by decoupling the fully digital precoder/filter into a baseband part and an analog RF processing part, typically built using a network of variable PSs [103]. This strategy has been extensively considered in the state-of-the-art under the name of hybrid analog-digital architecture and allows for significantly reducing the number of RF chains and, as a consequence, the costs and power consumption, but with reduced flexibility in the precoder/filter design [10], [29], [104]–[106].

In the uplink of MU mmWave MIMO systems, the hardware reduction based on hybrid transceivers is limited by the number of data streams that must be simultaneously decoded by the centralized node. Most works approach hybrid transceiver design by considering more RF chains than data streams, an unrealistic assumption when the number of nodes (or users) is large. Nowadays, applications like WSNs or IoT demand the capability of serving simultaneously a huge amount of nodes. Considering that the number of RF chains must usually be at least equal to the number of transmitted streams, this situation would lead to the need of a tremendous amount of RF chains at the common receiver, $N_{\mathrm{RF}}^{\mathrm{r}}$. These requirements become even more severe when working with critical data, which need to be sent with minimum latency. On the other hand, statistically independent information is conventionally assumed in MU mmWave systems. This assumption does not hold in scenarios like WSNs, where the sources produce correlated information.

In this chapter, by enabling inter-user correlation exploitation, we account for the reduction of the RF chains in mmWave MIMO systems by following a user grouping strategy via non-

orthogonal multiple access (NOMA) JSCC mappings.

The chapter is structured as follows. Section 4.1 introduces the chapter. The system model is detailed in Section 4.2. The analog JSCC, the grouping and the allocation algorithms, as well as the scheduling policy to serve the users, are analyzed in Section 4.3. Novel algorithmic solutions for the hybrid filtering approach with user grouping and for the conventional (without groups) systems with correlated sources are proposed in Section 4.4. Simulation results are presented in Section 4.5, and Section 4.6 is devoted to the conclusions of the chapter.

4.1 Introduction

Hybrid analog-digital schemes for precoding/filtering have proved to be a low-complexity and/or low-power strategy to obtain reasonable beamforming gains in MU mmWave MIMO systems. According to the connectivity level, hybrid mmWave MIMO architectures can be distinguished in two classes [107]: fully-connected structure (FCS) [30], [108], [109], where each antenna is connected to each deployed RF chain, and partially-connected structure (PCS) [110]–[113], which consists on connecting each RF chain only to some antenna groups in order to reduce even more the power consumption to the detriment of the beamforming gain. However, precoding/filtering strategies for both schemes assume at least the same number of RF chains as individual data streams simultaneously handled, i.e., $N_{\text{RF}} \geq K_{\text{s}}$. Specifically, FCS leads to the same performance as that of totally digital beamforming under the condition $N_{\text{RF}} \geq 2K_{\text{s}}$ [114], where N_{RF} is the number of RF chains of the transceiver and K_{s} is the number of data streams to be handled.

MU hybrid precoding/filtering has been investigated in [30], [31], [108], [115]. Although these approaches were developed for the downlink, they can be implemented in the uplink by invoking the MSE duality to transform the filters in the downlink into the precoders in the uplink [116]. In [30], an iterative PG algorithm has been developed to approach the hybrid precoding for wideband MU channels. In [115], a first step is designed to maximize the desired signal power of each user by using the analog precoder, while the inter-user interference is then cancelled in a second step following a zero-forcing (ZF) strategy to design the baseband precoder. The algorithms proposed in [31] and [108] have been developed for multi-stream transmissions in narrowband and wideband scenarios, respectively. These algorithms are based on a greedy approach, where the user data streams are allocated iteratively to the available RF chains by evaluating the impact of allocating the new stream on the overall system performance, according to a specific metric (e.g., sum-rate). In these algorithms, the first step is developed to maximize the desired signal power per user and partially cancel the inter-user interference. Then, the residual interference is cancelled in a second step by adopting a ZF strategy for the baseband precoder. Nevertheless, the hybrid factorization in these works is performed under the assumption $K_{\text{s}} = N_{\text{RF}}^{\text{r}}$.

Nowadays, communication systems demand the capability of serving simultaneously a huge

amount of nodes. By considering the constraint imposed in previous works, where the number of RF chains must be at least equal to the number of transmitted streams, critical scenarios in the practical system deployments would be reached due to the need of a tremendous amount of RF chains at the common receiving node.

In this chapter, we explore a novel strategy for the design of practical mmWave massive MIMO systems, which are able to deal with these requirements in terms of hardware complexity and delay. Specifically, we propose a novel approach, which enables the transmission of a number of streams significantly larger than the number of RF chains available at the receiver with minimum delay. This approach is based on the idea of using some appropriate NOMA technique to ensure that the streams corresponding to several users are effectively superimposed during the transmission, so that the information can then be decoded with an acceptable level of distortion by means of a single RF chain at reception. Since we are mainly interested in applications with minimum latency, an appealing candidate for the encoding operation is the use of DQLC [85], [117]. Another suitable properties of this mapping function are that the encoding and decoding of the user information can be performed with negligible delay and low computational cost. Moreover, it is able to exploit the source correlation between different users (spatial correlation). The latter feature is also important since there exists a large number of scenarios where this premise occurs. Therefore, the proposed DQLC-based scheme provides a suitable solution to reduce the number of required RF chains ($N_{\mathrm{RF}}^{\mathrm{r}}$) in the context of mmWave massive MIMO applications with a large number of potential transmitters and delay constraints. Unfortunately, the design of the DQLC-based scheme poses several challenges in the different parts of the communication link. First, it is required to define some coherent strategy to gather the users to be served by the same RF chain at reception. In addition, digital filters should be designed to cancel inter-group interferences, since the DQLC decoding is quite sensitive to this type of disturbances. Finally, we focus on the common BS filter design and derive a hybrid solution to exploit the intra-group correlation via a MMSE filter, instead of the conventional ZF strategy applied in [31], [108], [115]. The main contributions of this chapter are summarized as follows:

- Proposing a hybrid MMSE filter to exploit the spatial correlation in the uplink of correlated sources in mmWave.
- Proposing a user grouping approach to reduce hardware complexity through the use of DQLC mapping to superimpose user symbols in hybrid MU mmWave MIMO systems.
- Proposing a scheduling algorithm to define the gathered served users and allocate the users per group.
- Proposing a novel approach to face the hybrid filter design for user grouping in mmWave MIMO systems.

4.2 System Model

Figure 4.1 shows the uplink of a MU mmWave system, where K users send data to a common BS. The set $\mathcal{K} = \{1, \ldots, K\}$ contains the subset of active users, $\mathcal{K}_\mathrm{s}$, and the subset of idle users, $\mathcal{K}_\mathrm{I}$, such that $\mathcal{K} = \mathcal{K}_\mathrm{s} \cup \mathcal{K}_\mathrm{I}$. We assume that these users are divided into G groups by using an appropriate scheduling algorithm, subject to a given performance criterion. Accordingly, $\mathcal{G}_i$, $\forall\, i = 1, \ldots, G$, represents the i-th group of users.

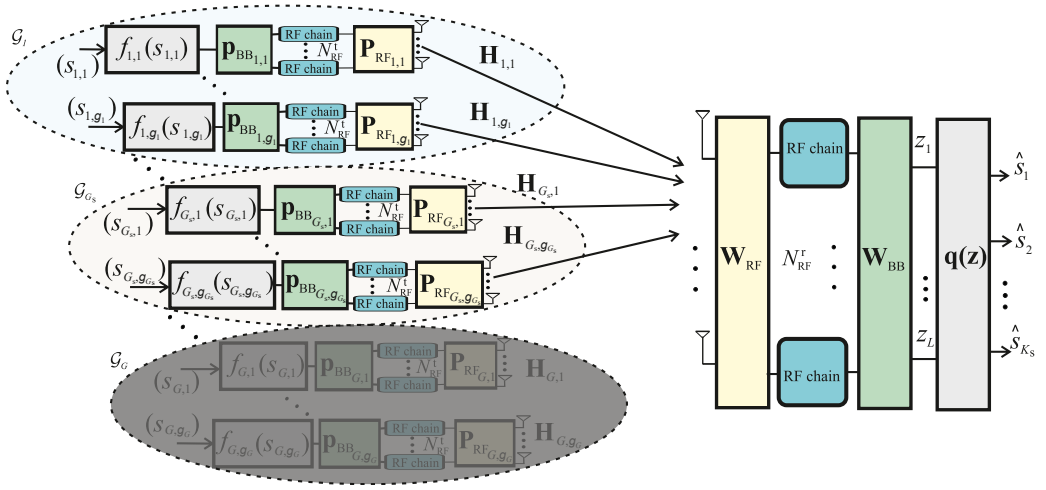

Figure 4.1: Block diagram of the mmWave MIMO MAC setup with G groups that contain g_i users each.

As observed in Figure 4.1, $G_\mathrm{s} \leq G$ groups are simultaneously served, i.e., $\mathcal{K}_\mathrm{s} = \cup_{i=1}^{G_\mathrm{s}} \mathcal{G}_i$. We assume that $G_\mathrm{I} = G - G_\mathrm{s}$ groups of users are idle, leading to $\mathcal{K}_\mathrm{I} = \cup_{i=G_\mathrm{s}+1}^{G} \mathcal{G}_i$, when $G_\mathrm{s} < G$, and $\mathcal{K}_\mathrm{I} = \emptyset$ when $G_\mathrm{s} = G$. We denote the number of active and inactive users by $K_\mathrm{s} = |\mathcal{K}_\mathrm{s}|$ and $K_\mathrm{I} = |\mathcal{K}_\mathrm{I}|$, respectively. Finally, the vector that contains the number of users per group is denoted by $\mathbf{g} = [g_1, \ldots, g_{G_\mathrm{s}}, \ldots, g_G]$, where $g_i = |\mathcal{G}_i|$ is the number of users allocated in the i-th group. Note that the following equality holds $\sum_{i=1}^{G_\mathrm{s}} g_i = K_\mathrm{s}$.

We assume that each user sends a single stream of discrete-time continuous-amplitude symbols to a common receiver with N_r antennas. We also assume that each user is equipped with N_t transmit antennas. The source symbols of the K users are represented by the vector $\mathbf{s} = [s_1, s_2, \ldots, s_K]^T$ which follows a zero-mean spatially correlated multivariate complex-valued Gaussian distribution with covariance matrix $\mathbf{C}_\mathrm{s} = \mathbb{E}[\mathbf{s}\mathbf{s}^*]$, such that $[\mathbf{C}_\mathrm{s}]_{k,k} = 1,\ \forall\ k$, and $[\mathbf{C}_\mathrm{s}]_{i,j} = \rho_{i,j}$, $0 \leq \rho_{i,j} \leq 1,\ \forall\, i, j$ with $i \neq j$.

At each channel use, each active user sends one complex-valued encoded symbol as $f_{i,j}(s_{i,j}), \forall\, i = 1, \ldots, G_\mathrm{s},\ \forall\, j = 1, \ldots, g_i$, where $f_{i,j}(\cdot)$ represents the mapping function that encodes $s_{i,j}$, the source symbol of the j-th user in the i-th group. Note that sub-index i is employed to denote the considered group, whereas sub-index j identifies the j-th user accommodated in the i-th group, i.e., this pair of indices actually represents the user $\mathcal{G}_i(j)$. Therefore, the vector corresponding to all encoded served user symbols per channel use is

represented by

$$\mathbf{f}(\mathbf{s}) = \left[f_{1,1}(s_{1,1}), \ldots, f_{1,g_1}(s_{1,g_1}), \ldots, f_{G_\mathrm{s},g_{G_\mathrm{s}}}(s_{G_\mathrm{s},g_{G_\mathrm{s}}}) \right]^T,$$

where we also assume that the encoded symbols satisfy the condition $\mathbb{E}\left[|f_{i,j}\left(s_{i,j}\right)|^2\right] \leq 1$. After encoding the source information, the resulting encoded symbols are precoded prior to be transmitted over the channel. Hybrid precoding is considered at the users due to the hardware constraints. The hybrid precoder of the j-th user in the i-th group is denoted as $\mathbf{p}_{\mathrm{H}i,j} = \mathbf{P}_{\mathrm{RF}i,j}\mathbf{p}_{\mathrm{BB}i,j}$, and it is implemented by using $N_{\mathrm{RF}}^{\mathrm{t}} = 2$ transmit RF chains. We assume this amount of RF chains per user, which is enough to lead essentially to the performance obtained by the unconstrained precoder implementation, so we focus on the single-stream scenario (see [114, Appendix A]). The baseband precoder is $\mathbf{p}_{\mathrm{BB}i,j} \in \mathbb{C}^{N_{\mathrm{RF}}^{\mathrm{t}}}$ and the analog precoder is $\mathbf{P}_{\mathrm{RF}i,j} \in \mathcal{P}_{\mathrm{RF}}$ such that $\mathcal{P}_{\mathrm{RF}} \subset \mathbb{C}^{N_\mathrm{t} \times N_{\mathrm{RF}}^{\mathrm{t}}}$ is the set of feasible RF precoder matrices with unit modulus entries. An individual power constraint is imposed at each user, such that $\|\mathbf{P}_{\mathrm{RF}i,j}\mathbf{p}_{\mathrm{BB}i,j}\|_F^2 \leq P_{\mathrm{T}i,j},\ \forall\, i,j$.

At the receiver, the K_s served data streams are collected by deploying N_r receive antennas. Therefore, the received signal reads as

$$\mathbf{y} = \sum_{i=1}^{G_\mathrm{s}} \sum_{j=1}^{g_i} \mathbf{H}_{i,j}\mathbf{P}_{\mathrm{RF}i,j}\mathbf{p}_{\mathrm{BB}i,j} f_{i,j}(s_{i,j}) + \mathbf{n}, \tag{4.1}$$

where $\mathbf{H}_{i,j} \in \mathbb{C}^{N_\mathrm{r} \times N_\mathrm{t}}$ describes the mmWave channel response of the j-th user in the i-th group, and the vector $\mathbf{n} = [n_1, n_2, \ldots, n_{N_\mathrm{r}}]^T$ represents the complex-valued AWGN such that $\mathbf{n} \sim \mathcal{N}_{\mathbb{C}}(0, \sigma_\mathrm{n}^2 \mathbf{I}_{N_\mathrm{r}})$. The received signal in (4.1) can also be rewritten in a more compact way as

$$\mathbf{y} = \mathbf{H}\mathbf{P}_\mathrm{H}\mathbf{f}(\mathbf{s}) + \mathbf{n}, \tag{4.2}$$

by considering the stacked channel matrix $\mathbf{H} = \left[\mathbf{H}_{1,1}, \ldots, \mathbf{H}_{G_\mathrm{s},g_{G_\mathrm{s}}}\right] \in \mathbb{C}^{N_\mathrm{r} \times N_\mathrm{t} K_\mathrm{s}}$, whereas the matrix containing all the hybrid precoders of the served users is described by $\mathbf{P}_\mathrm{H} = \mathrm{blkdiag}\left(\mathbf{p}_{\mathrm{H}1,1}, \ldots, \mathbf{p}_{\mathrm{H}G_\mathrm{s},g_{G_\mathrm{s}}}\right) \in \mathbb{C}^{N_\mathrm{t} K_\mathrm{s} \times K_\mathrm{s}}$. For convenience, we define the equivalent channel response for the i-th group as

$$\tilde{\mathbf{H}}_i = \left[\mathbf{H}_{i,1}\mathbf{p}_{\mathrm{H}_{i,1}}, \ldots, \mathbf{H}_{i,g_i}\mathbf{p}_{\mathrm{H}_{i,g_i}}\right], \quad \forall\, i = 1, \ldots, G_\mathrm{s}, \tag{4.3}$$

such that the overall equivalent matrix $\tilde{\mathbf{H}} \in \mathbb{C}^{N_\mathrm{r} \times K_\mathrm{s}}$ can be constructed as

$$\tilde{\mathbf{H}} = \left[\tilde{\mathbf{H}}_1, \ldots, \tilde{\mathbf{H}}_{G_\mathrm{s}}\right]. \tag{4.4}$$

Hence, (4.2) can alternatively be written as

$$\mathbf{y} = \tilde{\mathbf{H}}\mathbf{f}(\mathbf{s}) + \mathbf{n}. \tag{4.5}$$

We assume that the receiver has $N_{\mathrm{RF}}^{\mathrm{r}} \leq K$ available RF chains. Because of this hardware limitation, a hybrid filter $\mathbf{W}_\mathrm{H} = \mathbf{W}_{\mathrm{RF}}\mathbf{W}_{\mathrm{BB}}$ is implemented at the BS to decouple the

superimposed MAC signal before applying the demapping functions to estimate the source symbols.

The signal after this filtering processing can be described as

$$\mathbf{z} = \mathbf{W}_{\mathrm{H}}^{*}\mathbf{y} = \mathbf{W}_{\mathrm{BB}}^{*}\mathbf{W}_{\mathrm{RF}}^{*}\mathbf{y}, \tag{4.6}$$

where $\mathbf{W}_{\mathrm{BB}} \in \mathbb{C}^{N_{\mathrm{RF}}^{\mathrm{r}} \times G_{\mathrm{s}}}$ represents the baseband filter and $\mathbf{W}_{\mathrm{RF}} \in \mathcal{W}_{\mathrm{RF}}$ denotes the RF filter with constant value entry constraints. $\mathcal{W}_{\mathrm{RF}} \subset \mathbb{C}^{N_{\mathrm{r}} \times N_{\mathrm{RF}}^{\mathrm{r}}}$ represents the set of feasible RF filters with that property. It is important to highlight that the hybrid filter actually produces G_{s} channel symbols, which are then processed by the demapping functions $\mathbf{q}(\mathbf{z}) = \left[q_1(z_1), \ldots, q_{G_{\mathrm{s}}}(z_{G_{\mathrm{s}}})\right]^T$ to obtain an estimation of the served user symbols $\hat{\mathbf{s}} = \left[\hat{s}_{1,1}, \ldots, \hat{s}_{G_{\mathrm{s}},g_{G_{\mathrm{s}}}}\right]^T$ by employing just $N_{\mathrm{RF}}^{\mathrm{r}} = G_{\mathrm{s}}$ RF chains. Thus, the demapping function $q_i(z_i) : \mathbb{C} \rightarrow \mathbb{C}^{g_i}$ will provide an estimation for the source symbols transmitted by the g_i users at the i-th group as

$$\hat{\mathbf{s}}_i = q_i(z_i) = \left[\hat{s}_{i,1}, \ldots, \hat{s}_{i,g_i}\right]^T, \quad \forall\, i = 1, \ldots, G_{\mathrm{s}}. \tag{4.7}$$

Since we are considering complex-valued continuous-amplitude source symbols, the information will be recovered with a certain level of distortion. In this chapter, the observed distortion is measured as the MSE between the source symbols and the estimated ones, as explained in Subsection 2.3.1, i.e.,

$$\xi = \frac{1}{K_{\mathrm{s}}} \sum_{i=1}^{G_{\mathrm{s}}} \sum_{j=1}^{g_i} |s_{i,j} - \hat{s}_{i,j}|^2. \tag{4.8}$$

An interesting discussion arises when considering scenarios where the number of total users is significantly larger than the number of available RF chains at reception, i.e., $N_{\mathrm{RF}}^{\mathrm{r}} \ll K$. In this situation, we can opt for two opposite allocation policies. One is to exactly select the same number of active users as the number of available RF chains (i.e., $g_i = 1,\ \forall\, i$ and $G_{\mathrm{s}} = N_{\mathrm{RF}}^{\mathrm{r}}$). In this case, the objective will be to recover the source symbols with the minimum possible distortion although this may imply the number of inactive users to be very large. A different approximation is to gather the users into large groups in order to serve most of the users simultaneously with the available RF chains. In this case, we neglect the impact on the communication reliability. An intermediate solution would be to find a trade-off between the number of served users and the level of distortion obtained after decoding the user symbols. In Section 4.3, we will address the problem of designing the different components of the communication system and the scheduling algorithm to obtain a suitable balance between these two figures of merit: the number of served users and the signal distortion. In addition, the first scenario is considered in Subsection 4.4.2 for completeness. Table 4.1 summarizes the main system model parameters considered in this chapter.

Table 4.1: System model parameters.

Description	Parameter
Number of users	K
Number of antennas per users	N_{t}
Vector of the K user symbols	$\mathbf{s}$
Correlation matrix (user symbols)	$\mathbf{C}_{\mathrm{s}}$
Mapping function: j-th user in the i-th group	$f_{i,j}(\cdot)$
Precoder: j-th user in the i-th group	$\mathbf{p}_{i,j}$
Number of RF chains at the users	$N_{\mathrm{RF}}^{\mathrm{t}}$
Total power constraint per user	$P_{\mathrm{T}i,j}$
Vector of AWGN	$\mathbf{n}$
Subset of active users	$\mathcal{K}_{\mathrm{s}}$
Subset of idle users	$\mathcal{K}_{\mathrm{I}}$
Number of served user groups	G_{s}
Served users	K_{s}
Idled users	K_{I}
i-th group of users	$\mathcal{G}_i$
Vector with the number of users per group	$\mathbf{g}$
Number of antennas at the BS	N_{r}
Number of RF chains at the BS	$N_{\mathrm{RF}}^{\mathrm{r}}$
BS hybrid filter	$\mathbf{W}_{\mathrm{H}}$
Baseband filter	$\mathbf{W}_{\mathrm{BB}}$
RF filter	$\mathbf{W}_{\mathrm{RF}}$
Post-filtering group symbols	$\mathbf{z}$
Decoding functions	$\mathbf{q}(\mathbf{z})$
Estimated served user symbols	$\hat{\mathbf{s}}$

4.3 User Grouping in Hybrid mmWave MIMO MAC

Existing works on hybrid analog-digital MIMO transceivers have mainly focused on the case $K_{\mathrm{s}} \leq N_{\mathrm{RF}}^{\mathrm{r}} < 2K_{\mathrm{s}}$. In order to circumvent this constraint and reduce $N_{\mathrm{RF}}^{\mathrm{r}}$, we consider a design strategy where K users are gathered into G groups, so that the users at each group use a DQLC mapping to encode and superimpose their source symbols. Considering this encoding strategy, the information corresponding to all the users in the same group could be processed using a single RF chain at the receiver by, designing the mapping functions and the different filters in an appropriate way. Note that this approach allows reducing $N_{\mathrm{RF}}^{\mathrm{r}}$ down to the number of served user groups G_{s} ($G_{\mathrm{s}} \leq K_{\mathrm{s}}$). In addition, DQLC encoding presents some additional advantages such as zero-delay and efficient exploitation of the spatial correlation at each user group.

4.3.1 DQLC Implementation

DQLC is a JSCC technique proposed for the non-orthogonal transmission of multivariate Gaussian sources over the MAC [85]. This mapping constitutes a specific case of vector quantizer linear coding (VQLC) by imposing a zero-delay encoding constraint [21]. The conventional implementation of DQLC establishes that $g_i - 1$ users of the i-th group transmit a quantized version of its symbol whereas the symbol of the remaining user is just scaled by a power factor. Thus, it can be placed between two quantization steps of the encoded user symbols. The DQLC mapping function for the i-th group is mathematically defined as

$$f_{i,j}\left(s_{i,j}\right) = \begin{cases} \alpha_{i,j}\left\lfloor \frac{s_{i,j}}{\Delta_{i,j}} - \frac{1}{2} \right\rceil + \frac{1}{2}, & j < g_i \\ \alpha_{i,j} s_{i,j}, & j = g_i \end{cases}, \tag{4.9}$$

where $\alpha_{i,j}$ represents a gain factor and $\Delta_{i,j}$ represents the quantization step employed for the j-th user in the i-th group. A specific DQLC mapping is individually applied into the $G_\mathrm{s} \leq G$ groups containing the users served, and therefore the parameters $\alpha_{i,j}$ and $\Delta_{i,j}$ must be optimized for the g_i users at each group. A detailed description about the DQLC implementation and parameter optimization can be found in [85], [117], [118].

In [118], in-depth treatment about this optimization is provided, where only one group of users is considered. In this chapter, we consider several groups and, as a consequence, the potential inter-group interference has to be taken into account in the parameter design. We follow an alternative approach to [118] by considering the SINR—affected by the inter-group interference due to the hybrid implementation of the filter at the BS—as the metric to optimize the DQLC parameters. In the proposed setup, the symbols at the input of the demapping operation are given by

$$\mathbf{z} = \mathbf{W}_\mathrm{H}^* \mathbf{H} \mathbf{P}_\mathrm{H} \mathbf{f}(\mathbf{s}) + \mathbf{W}_\mathrm{H}^* \mathbf{n} = \mathbf{R}\mathbf{f}(\mathbf{s}) + \tilde{\mathbf{n}}, \tag{4.10}$$

where

$$\mathbf{R} = \mathbf{W}_\mathrm{H}^* \mathbf{H} \mathbf{P}_\mathrm{H} = \mathbf{W}_\mathrm{H}^* \tilde{\mathbf{H}} \tag{4.11}$$

represents the equivalent channel response for the encoded symbols after filtering, and $\tilde{\mathbf{n}} = \mathbf{W}_\mathrm{H}^* \mathbf{n}$ is the equivalent noise. Therefore, the SINR values can directly be computed from the equivalent channel matrix $\mathbf{R}$ and from the noise variance. From the above equation, we can decompose the input signal at the demapping operation into its individual components as

$$z_i = \sum_{j=1}^{K_\mathrm{s}} [\mathbf{R}]_{i,j} f_j(s_j) + \tilde{n}_i, \qquad \forall\, i = 1, \ldots, G_\mathrm{s}, \tag{4.12}$$

which can be rearranged as

$$z_i = \sum_{j=1}^{g_i} [\mathbf{R}]_{i,[l(i)+j]} f_{i,j}(s_{i,j}) \; + \sum_{r \neq i}^{G_\mathrm{s}} \sum_{j}^{g_r} [\mathbf{R}]_{i,[l(r)+j]} f_{r,j}(s_{r,j}) + \tilde{n}_i, \tag{4.13}$$

where the auxiliary indices $l(\cdot)$ determine the first component of the equivalent channel matrix corresponding to the group given by the argument, and they can be computed in a simple way as $l(i) = \sum_{t=1}^{i-1} g_t + 1$. Note that the first term in (4.13) corresponds to the desired signal for the i-th group, the second term represents the interference caused by the signal transmitted by other groups, and the third term is the i-th component of the equivalent noise after filtering.

At the receiver side, different methods have been adopted in order to perform DQLC demapping. One is sequential decoding, where an estimation of the quantized symbols is first computed, and the obtained symbols are then used to estimate the scaled symbol (cf. [21, Section III]). Another is the approximated MMSE estimation with sphere decoding [117, Section III], which in general exhibits a better performance for more than two users per group. Therefore, we will use this latter decoding algorithm since it provides better flexibility (cf. [117] or [118] for details).

4.3.2 Algorithmic Solution for User Grouping

As introduced in the previous sections, the key point to reduce the hardware requirements in the considered mmWave-based massive MIMO system is the grouping of users into disjoint groups and the application of an optimized DQLC scheme to encode the source symbols at each group. Therefore, the design of an adequate allocation policy to define the grouping configuration is essential to achieve a good trade-off between the system performance (i.e., observed distortion) and the number of served users. In this subsection, the proposed user grouping allocation is presented. The scheduling policy involves both the grouping operation, that determines the number of users per group, and the allocation of the specific users that will be accommodated in each group.

The design of the proposed scheduling policy is clearly influenced by some important issues related to the experimental behavior of DQLC mappings over wireless channels. In particular, the following considerations should be taken into account:

- From [25], [118] it is clear that the DQLC mapping is able to improve the system performance by exploiting spatial correlation. Hence, the scheduling approach will be designed to guarantee the exploitation of the inter-user correlation per group. Thus, it is always preferable to allocate users with high levels of correlation in the same group, if possible.
- Another interesting issue related to DQLC performance can be observed from (4.13). As will be seen below, the filter should be designed to cancel the interferences from other groups. Hence, (4.13) boils down to

$$z_i = \sum_{j=1}^{g_i} [\mathbf{R}]_{i,[l(i)+j]} f_{i,j}(s_{i,j}) + \tilde{n}_i, \tag{4.14}$$

  when the inter-group interferences are perfectly cancelled.

As observed in (4.14), each received symbol comprises two different parts: the sum of all encoded symbols in a group weighted by the equivalent channel responses, and the noise component. As shown in [85], [118], the key for an appropriate DQLC decoding is to ensure that the sum of the encoded symbols corresponding to the next users does not cause that the quantized symbol of the considered user crosses to a different quantization interval. Note that DQLC decoding could be interpreted as particular form of successive interference cancellation, where the sum of the symbols for the next users would be the remaining interference, and the decoding would only be possible if such interference did not move the considered quantized symbol to a different interval. In this way, the probability of a crossing event will be lower when SNRs for all the users are large. For this reason, a reasonable scheduling strategy would be to gather in the same group those users whose channel subspaces intersect. Hence, it will be possible to obtain adequate equivalent channel gains for some of them. In this sense, a particular metric is employed to provide a joint measure of the degree of similarity among the user channels and the joint gain of such channels.

- As shown in [117], [118], the performance of DQLC-based systems degrades as the number of users increases in the MAC. This fact inevitably leads to a trade-off between the number of users per group and the system performance. The impact of adding a new user to a group can be determined from the approximation to the sum-MSE for DQLC transmissions considering a single group, which was derived in [118]. From the analysis of this error expression and from the results obtained in [118], it can be seen that the addition of a new user approximately leads to a duplication of the error (for high SNR values). Indeed, the specific increase on the distortion with each new user actually depends on the SNR value, but this increase is similar regardless of the number of users in the group. For instance, the performance loss of adding a new user to a group with 2 users is similar to adding it to a group with 6 users irrespective of the considered SNR value. Moreover, the gain with respect to an uncoded transmission of the source symbols becomes negligible beyond a certain number of users per group (around 7). Considering these two arguments, it is important to prevent oversized groups, which can lead to a performance degradation. In this sense, the maximum number of users per group can explicitly be limited by introducing the parameter $g_{\max} = 7$.
- We have experimentally observed that a balanced configuration of the number of users per group provides better performance than unbalanced ones. This behavior can also be explained from the analysis of the approximation for the sum-MSE expression in [118], since the fact of increasing the group size necessarily implies to increase the size of the quantization intervals employed at the encoding operation, which significantly penalizes the system performance (higher distortions). Hence, considering the sum-MSE as the performance metric and the assumption that each new user implies to double the overall error, it is easy to see that the resulting distortion will be lower when the individual

contributions are balanced.

- Finally and related to the importance of preventing huge distortions caused by the fact that a quantized symbol is erroneously decoded (i.e., if it is detected as a point on an erroneous interval), it is important to ensure that the quantized symbols correspond to those users in the group whose channel matrices have larger singular values [118].

Taking into account all previous issues, we have developed a scheduling procedure that comprises two intertwined parts: the grouping strategy and the allocation policy. The grouping algorithm must determine the group configuration, i.e., the number of groups and the number of users per group, whereas the allocation algorithm is responsible of selecting which users are grouped into each group. The different steps of these two proposed algorithms are described in Algorithm 4.1 and Algorithm 4.2.

As observed, Algorithm 4.1 determines the vector $\mathbf{g}$, which contains the number of users per group, given the set of all available users, $\mathcal{K}$, and the number of available RF chains at reception, N_{RF}^{r}. Basically, the aim of the algorithm is to find a balanced group configuration under the premise that the number of groups, G, should be as close as the number of available RF chains with $G \geq N_{\text{RF}}^{\text{r}}$. This condition is imposed to limit the number of users that can be served simultaneously.

Algorithm 4.1 Grouping

Input: $\mathcal{K}$, N_{RF}^{r}, $g_{\max}$

1: **Initialize:** $i = 0$, $g_i = 0 \; \forall \; i$, $l = N_{\text{RF}}^{\text{r}}$, $K = |\mathcal{K}|$
2: **repeat**
3: $\quad i \leftarrow i + 1$
4: $\quad \hat{g}_i = \min\left(g_{\max}, \left\lceil \frac{K}{l} \right\rceil\right)$
5: $\quad \mathcal{G}_i \leftarrow$ **Algorithm 4.2** with $\hat{g}_i$ and $\mathcal{K}$
6: $\quad g_i \leftarrow |\mathcal{G}_i|$
7: $\quad \mathcal{K} \leftarrow \mathcal{K} \setminus \mathcal{G}_i$
8: $\quad K \leftarrow K - g_i$
9: $\quad$ **if** $g_i \neq \hat{g}_i$ **then**
10: $\quad\quad l \leftarrow \lceil K / g_{\max} \rceil$
11: $\quad$ **else**
12: $\quad\quad l \leftarrow l - 1$
13: **until** $K = 0$

Output: $\mathbf{g} = [g_1, \ldots, g_{Gs}, \ldots, g_G]$, $\{\mathcal{G}_i\}_{i=1}^{G}$

In the first iteration, the size of the first group is determined considering the total number of users and the number of available RF chains (step 4). Note that this size is limited to $g_{\max}$ users. Next, g_1 users will be allocated to the current group by invoking the allocation algorithm (step 5). Note that the actual number of users allocated to the group does not necessarily have to be equal to the size determined a priori for such a group. As we will see later, this situation occurs

when it is not possible to find users with enough source correlation or whose equivalent channel vectors are similar enough. After this step, the sequence and the number of unallocated users are updated (steps 7 and 8), and the counter l for the number of available groups is updated (steps 9 to 12). This counter is initially set to $N_{\mathrm{RF}}^{\mathrm{r}}$ and it is decreased by one at each iteration. However, it may be necessary to occasionally increase it if the available groups are not enough to gather all the remaining users due to the constraint on the maximum group size. This sequence of steps is repeated at each algorithm iteration until all the users are allocated to any group.

4.3.3 Algorithmic Solution for User Allocation

Algorithm 4.2 allocates the users to their corresponding groups. As observed, this algorithm provides the sequence of users $\mathcal{G}_i$ for the i-th group given the set of users that have not been allocated yet, the source correlation matrix, the channel responses, the desirable size for the group and a set of design parameters.

As mentioned in the beginning of this section, two different factors decisively impact into the performance of the DQLC-based systems: the level of correlation between the source symbols corresponding to the users gathered into the same group, and the similarity of their channel matrices (i.e., the ability for aligning their channels). The impact of a high correlation level is in general more positive than that of the similarity, although it depends on the overall correlation in the system. For example, the impact of the first factor is obviously negligible for scenarios with uncorrelated sources. In order to model this behavior, we introduce the factors δ_ρ and δ_{s} which define the weight of the correlation criterion and of the similarity one, respectively, in the proposed metric for selecting users for a same group. In addition, a correlation threshold γ_ρ and a similarity threshold γ_{s} are introduced to discard some users that, even when the constraint of the maximum users per group is fulfilled, could severely degrade the system performance.

In general, the optimization of these design parameters would lead to an exhaustive search in a four-dimension parameter space or to highly non-convex optimization problems involving non-linearities and discontinuities due to the DQLC mapping function. For this reason, we have considered a heuristic approach—based on the insight provided by the issues related to the DQLC behavior—to lower the computational cost for the selection of the parameters. Note also that the thresholds γ_ρ and γ_{s} drive the general behavior of the scheduling procedure: either incorporating as many users as possible by choosing low values for these thresholds, or introducing a smaller number of users but guaranteeing a high level of the received signal quality. Thus, the tuning of these parameters is conducted depending on the overall source correlation and the system requirements.

Algorithm 4.2 summarizes the steps of the proposed allocation strategy. As observed, this algorithm first includes the user with the best channel by evaluating the largest singular value

of the user channels as follows

$$\mathcal{G}(1) = k \;\text{ s.t. }\; \|\mathbf{H}_{\mathcal{K}(k)}\|_2 \geq \|\mathbf{H}_{\mathcal{K}(j)}\|_2,\; \forall\, j \neq k. \tag{4.15}$$

The sequence $\mathcal{G}$ will include the users that are already allocated to the considered group at each iteration. It is worth remarking that we introduce a change in the notation for the allocation algorithm to highlight that the group configuration is not definitively established. Therefore, instead of using index i for the groups and j for the users in the group, we will use $\mathcal{K}(k)$ and $\mathcal{G}(k)$ to refer to the k-th user in the set of unallocated users and the k-th user already allocated to the i-th group, respectively.

Algorithm 4.2 Allocation

Input: $\mathcal{K}$, g, $\mathbf{C}_\text{s}$,$\{\mathbf{H}_k\}_{k=1}^{K}$, γ_ρ, γ_s, δ_ρ, δ_s

$k = \arg\max_{k\in\mathcal{K}} \|\mathbf{H}_{\mathcal{K}(k)}\|_2$
$\mathcal{G}(1) \leftarrow k$
$\mathcal{K} \leftarrow \mathcal{K} \setminus \mathcal{G}(1)$
$\mathbf{H}_\text{c} = \mathbf{H}_k$
$[\mathbf{S}, \mathbf{\Sigma}, \mathbf{D}] \leftarrow \text{svd}(\mathbf{H}_\text{c})$
$\mathbf{p}_1 = [\mathbf{D}]_{:,1}$
for $i = 2 : g$ **do**
  for $k = 1 : |\mathcal{K}|$ **do**
    $\mathcal{G}' = \mathcal{G} \cup \mathcal{K}(k)$
    $\mathbf{H}'_\text{c} = \left[\mathbf{H}_\text{c}^T \;\; \mathbf{H}_{\mathcal{K}(k)}^T\right]^T$
    $[\mathbf{S}, \mathbf{\Sigma}, \mathbf{D}] \leftarrow \text{svd}(\mathbf{H}'_\text{c})$
    $\mathbf{p}' = [\mathbf{D}]_{:,1}$
    $C_{\text{sim}k} \leftarrow$ Compute with (4.18)
    $\tilde{\rho}_k \leftarrow \frac{2!(|\mathcal{G}'|-2)!}{|\mathcal{G}'|!} \sum_{i\in\mathcal{G}'} \sum_{j\in\mathcal{G}', i>j} \rho_{i,j}$
  $\tilde{\mathcal{G}}(i) = \arg\max_{k\in\mathcal{K}} \; |\delta_\rho \tilde{\rho}_k + \delta_\text{s} C_{\text{sim}k}|$
  if $C_{\text{sim}\tilde{\mathcal{G}}(i)} > \gamma_\text{s}$ and $\tilde{\rho}_{\tilde{\mathcal{G}}(i)} > \gamma_\rho$ **then**
    $\mathcal{G}(i) = \tilde{\mathcal{G}}(i)$
    $\mathcal{K} \leftarrow \mathcal{K} \setminus \tilde{\mathcal{G}}(i)$
    $\mathbf{H}_\text{c} = \left[\mathbf{H}_\text{c}^T \;\; \mathbf{H}_{\mathcal{G}(i)}^T\right]^T$
    $[\mathbf{S}, \mathbf{\Sigma}, \mathbf{D}] \leftarrow \text{svd}(\mathbf{H}_\text{c})$
    $\mathbf{p}_i = [\mathbf{D}]_{:,1}$
  else `return`

Output: $\mathcal{G}$

Then, the algorithm iteratively includes the next users by considering the metric

$$m_k = \delta_\rho \tilde{\rho}_k + \delta_\text{s} C_{\text{sim}k}, \tag{4.16}$$

where $\tilde{\rho}_k$ is the mean of the cross-correlation of the users in $\mathcal{G}$ and the candidate user $\mathcal{K}(k)$, whereas the parameter $C_{\text{sim}k}$ measures the convenience of including user $\mathcal{K}(k)$ in $\mathcal{G}$ according to its channel response. As mentioned, this parameter should represent the joint gain of such channels. Following this premise, we define the composite channel for the L users already in the sequence $\mathcal{G}$ as $\mathbf{H}_{\text{c}} = \left[\mathbf{H}_{\mathcal{G}(1)}^T, \mathbf{H}_{\mathcal{G}(2)}^T, \ldots, \mathbf{H}_{\mathcal{G}(L)}^T\right]^T$. Then, the composite channel including the candidate user k reads as

$$\mathbf{H}'_{\text{c}} = \left[\mathbf{H}_{\text{c}}^T \;\; \mathbf{H}_{\mathcal{K}(k)}^T\right]^T. \tag{4.17}$$

We now employ the auxiliary vector $\mathbf{p}_i$ defined as the right singular vector associated with the larger singular value of the decomposition of $\mathbf{H}_{\text{c}}$ and, similarly, $\mathbf{p}'_i$ for $\mathbf{H}'_{\text{c}}$ to compute the parameter $C_{\text{sim}k}$ as

$$C_{\text{sim}k} = \frac{\sum_{z=1}^{L} \|\mathbf{H}_{\mathcal{G}(z)}\mathbf{p}_i\|_2^2}{\sum_{z=1}^{L} \|\mathbf{H}_{\mathcal{G}(z)}\mathbf{p}'_i\|_2^2 + \|\mathbf{H}_{\mathcal{K}(k)}\mathbf{p}'_i\|_2^2}. \tag{4.18}$$

Note that this metric prioritizes users with channels lying in similar subspaces, and takes into account the channel norm to avoid users with low SNRs.

After evaluating the metric in (4.16) for the set of all the unallocated users, the algorithm selects those users with the highest values for this metric as candidates for being included into the considered group. Then, if the value for the measure obtained for $C_{\text{sim}k}$ and the average cross-correlation $\tilde{\rho}_k$ exceed the given thresholds, that user will actually be included in the sequence $\mathcal{G}$.

4.3.3.1 Remarks

As a result of applying the previous grouping and allocation algorithms, we will obtain the sequences $\mathcal{G}_i,\ \forall\ i = 1, \ldots, G$ with the user indices per group, and the vector $\mathbf{g}$ that stacks the number of users per group. Thus, the proposed scheduling procedure provides a suitable grouping configuration with G groups and g_i users for the i-th group. The users in each group are also sorted to ensure that the quantized users correspond to those whose equivalent channel matrices have larger singular values.

Next, $G_{\text{s}} = N_{\text{RF}}^{\text{r}}$ groups of users will be accommodated by considering the hardware constraint at the BS (N_{RF}^{r}). Notice that Algorithm 4.1 provides the groups sorted according to the metric m_k. Hence, only the users corresponding to the first G_{s} groups will be selected to transmit their encoded symbols after the scheduling procedure.

In summary, the proposed scheduling is characterized by:

- Its objective is to serve the maximum number of users but they must be allocated to the groups in a consistent way to minimize the impact on the system performance.
- The grouping configuration must be as balanced as possible according to a consistent user allocation.
- The number of groups must be as small as possible (with $G \geq N_{\text{RF}}^{\text{r}}$).

- The trade-off between the number of served users and the resulting distortion in the decoded symbols can be managed through the thresholds γ_ρ and γ_s. By choosing small values for such thresholds, we allow large groups incorporating some users, which could negatively increase the impact on the observed distortion. Conversely, by choosing large threshold values, only users with minimum impact on the observed distortion are allowed to be incorporated into the served groups. This leads to groups with few users such that the actual number of served users will be small.
- Although the behavior of the scheduling algorithm is fundamentally determined by the above thresholds, an additional constraint is introduced by limiting the maximum size of the groups to g_max. The value of this parameter should be chosen only to prevent oversized groups in scenarios where the number of users is much larger than the number of RF chains, but not to explicitly define the trade-off between served users and system performance.

4.4 Hybrid Filtering for User Grouping

In this section, the design of the user precoders and the receive filter is addressed for the DQLC-based grouped system considered in the previous subsections. Unconstrained fully digital precoding for MIMO systems has been studied for correlated sources [100], [119]. In particular, we choose the PG precoding strategy [100, Section III] in order to exploit the inter-user correlation at each group. On the other hand, the digital filter should be designed to cancel the inter-group interferences in order to avoid penalizing the performance of the DQLC scheme. This strategy hence ensures to split the communication system into non-interfering groups where the users of a group transmit their source symbols using an optimized DQLC scheme, whereas a single RF chain is employed to recover such symbols at the receiver.

The unconstrained digital filter at the receiver, $\mathbf{W}^* \in \mathbb{C}^{G_\mathrm{s} \times N_\mathrm{r}}$, is designed to satisfy the following condition

$$\begin{aligned} &[\mathbf{W}^*]_{l,:}\mathbf{H}_{i,j}\mathbf{p}_{\mathrm{H}i,j} = 0, \\ &\forall\, i \neq l, \text{ with } l, i = 1, \ldots, G_\mathrm{s}, \text{ and } j = 1, \ldots, g_i. \end{aligned} \tag{4.19}$$

Thus, the l-th row of the filter is onto the nullspace of the equivalent channels corresponding to the users of the remaining $G_\mathrm{s} - 1$ groups. Note that the inter-user interference is just cancelled between those users contained in different groups.

In order to exploit the spatial correlation in the groups, while the inter-group interference is cancelled, Algorithm 4.3 has been implemented. As observed, at the l-th iteration, the precoders for the users of the i-th group are computed by means of the gradient-based precoding strategy developed in [100] considering the part of the correlation matrix corresponding to the users of such a group $\mathbf{C}_\mathrm{cl}$.

In a similar way, the i-th row of the filter is also calculated under the premise of satisfying the condition in (4.19). We follow an approach similar to [108] where the filter is computed in two-separate stages, but adapting it to the requirements of the proposed grouped system. First, a projector $\mathbf{T} \in \mathbb{C}^{N_\mathrm{r} \times N_\mathrm{r}}$ is used to project the user channels of the i-th group to the orthogonal subspace of the equivalent channels of the users in the $i-1$ previous groups. This projector is initially defined as $\mathbf{T} = \mathbf{I}_{N_\mathrm{r}}$ and is then updated at each iteration as

$$\mathbf{T} = \mathbf{T} - \mathbf{B}_i \mathbf{B}_i^*, \tag{4.20}$$

where $\mathbf{B}_i$ is the basis for the span of the projected equivalent channels at the i-th group, i.e. $\mathbf{T}\tilde{\mathbf{H}}_i$, with

$$\tilde{\mathbf{H}}_i = \left[\mathbf{H}_{i,1}\mathbf{p}_{\mathrm{H}_{i,1}}, \ldots, \mathbf{H}_{i,g_i}\mathbf{p}_{\mathrm{H}_{i,g_i}}\right]. \tag{4.21}$$

Algorithm 4.3 GSA

Input: $\{\mathbf{H}_k\}_{k=1}^{K_\mathrm{s}}, \mathbf{C}_\mathrm{s}, N_\mathrm{RF}^\mathrm{r}, \mathbf{g}$

Initialize: $\mathbf{P}_\mathrm{H} = [\,], \mathbf{W} = [\,], \mathbf{T} = \mathbf{I}_{N_\mathrm{r}}$, $\mathbf{H}_\text{comp} = [\,], \mathbf{H}_\text{inter} = [\,], l = 0$
repeat
  $l \leftarrow l + 1$
  for $u = 1, \ldots, g_l$ **do**
    $\mathbf{H}_\text{comp} = [\mathbf{H}_\text{comp} \;\; \mathbf{T}\mathbf{H}_{l,u}]$
  $\mathbf{C}_\text{cl} \leftarrow$ Inter-user correlation per group
  $\mathbf{P}_\text{Hcl} = \text{blkdiag}\left(\mathbf{p}_{\mathrm{H}_{l,1}}, \ldots, \mathbf{p}_{\mathrm{H}_{l,g_l}}\right) \leftarrow$ Gradient precoding $(\mathbf{H}_\text{comp}, \mathbf{C}_\text{cl})$ [100]
  $\mathbf{H}_\text{inter} = [\mathbf{H}_\text{inter} \;\; \mathbf{T}\tilde{\mathbf{H}}_i]$
  $\mathbf{B}_i \leftarrow$basis for span$(\mathbf{H}_\text{inter})$
  $\mathbf{T} = \mathbf{T} - \mathbf{B}_i\mathbf{B}_i^*$
  $\mathbf{h}_{\mathcal{G}_l} = \mathbf{T}\sum_{j=1}^{g_l} \mathbf{H}_{l,j}\mathbf{p}_{\mathrm{H}l,j}$
  $\tilde{\mathbf{W}} = [\tilde{\mathbf{W}}, \left(\frac{1}{\sigma_\mathrm{n}^2}\mathbf{I}_{N_\mathrm{r}} + \mathbf{h}_{\mathcal{G}_l}\mathbf{h}_{\mathcal{G}_l}^*\right)^{-1}\mathbf{h}_{\mathcal{G}_l}]$
  $\mathbf{P}_\mathrm{H} = \text{blkdiag}\left(\mathbf{P}_\mathrm{H}, \mathbf{P}_\text{Hcl}\right)$
until $l = N_\mathrm{RF}^\mathrm{r}$
for $l = 1, 2, \ldots, G_\mathrm{s} - 1$ **do**
  $\mathbf{I}_{\mathcal{G}_l} = \left[\tilde{\mathbf{H}}_1, \ldots, \tilde{\mathbf{H}}_{l-1}, \tilde{\mathbf{H}}_{l+1}, \ldots, \tilde{\mathbf{H}}_{G_\mathrm{s}}\right]$
  $\mathbf{N}_l \leftarrow$basis for span $(\mathbf{I}_{\mathcal{G}_l})$
  $[\mathbf{W}]_{:,l} = \left(\mathbf{I} - \mathbf{N}_l\mathbf{N}_l^*\right)[\tilde{\mathbf{W}}]_{:,l}$
$\mathbf{R} = \mathbf{W}^*\mathbf{H}\mathbf{P}_\mathrm{H}$
$\mathbf{W}_\mathrm{H} = \mathbf{W}_\mathrm{RF}\mathbf{W}_\mathrm{BB} \leftarrow$ **Algorithm 4.4** $(\mathbf{H}, \mathbf{P}_\mathrm{H}, \mathbf{W}, \mathbf{R})$

Output: $\mathbf{P}_\mathrm{H}, \mathbf{W}_\mathrm{H}$

Then, each column of $\tilde{\mathbf{W}}$ can be calculated as the conventional MMSE filter taking into

account only the users contained in the group, i.e.,

$$[\tilde{\mathbf{W}}]_{:,i} = \left(\frac{1}{\sigma_{\mathrm{n}}^2}\mathbf{I}_{N_{\mathrm{r}}} + \mathbf{h}_{\mathcal{G}_i}\mathbf{h}_{\mathcal{G}_i}^*\right)^{-1}\mathbf{h}_{\mathcal{G}_i}, \tag{4.22}$$

with $\mathbf{h}_{\mathcal{G}_i} = \mathbf{T}\sum_{j=1}^{g_i}\mathbf{H}_{i,j}\mathbf{p}_{\mathrm{H}i,j}$.

Next, in a second step, the residual interferences can be cancelled by projecting the candidate filter columns onto the nullspace of the equivalent channels of the users scheduled in other groups. Defining $\mathbf{N}_i$ as the basis for the subspace spanned by the columns of the matrix

$$\mathbf{I}_{\mathcal{G}_i} = \left[\tilde{\mathbf{H}}_1, \ldots, \tilde{\mathbf{H}}_{i-1}, \tilde{\mathbf{H}}_{i+1}, \ldots, \tilde{\mathbf{H}}_{G_{\mathrm{s}}}\right],$$

we eventually obtain the columns of the filter as

$$[\mathbf{W}]_{:,i} = \left(\mathbf{I} - \mathbf{N}_i\mathbf{N}_i^*\right)[\tilde{\mathbf{W}}]_{:,i}. \tag{4.23}$$

Hence, the digital filter $\mathbf{W}^*$, yields a MAC signal decoupled and stacked in the vector $\mathbf{z} \in \mathbb{C}^{G_{\mathrm{s}}}$ such that the i-th entry will be

$$z_i = [\mathbf{W}^*]_{i,:}\left(\sum_{j=1}^{g_i}\mathbf{H}_{i,j}\mathbf{p}_{\mathrm{H}_{i,j}}f_{i,j}(s_{i,j}) + \mathbf{n}_i\right),\ \forall\, i = 1, \ldots, G_{\mathrm{s}}, \tag{4.24}$$

and each element z_i contains a weighted sum of the g_i encoded symbols from the i-th group. The individual symbols are then estimated by using the demapping function $q_i(z_i)$.

Note that Algorithm 4.3 employs a matrix factorization algorithm to determine, the hybrid precoders, and the digital and hybrid filters, considering the limited number of RF chains.

4.4.1 Algorithmic Solution for Hybrid Filtering

The functionality of the filter at the BS—which is critical to face the demapping process—can be performed by a hybrid filter. By deploying $N_{\mathrm{RF}}^{\mathrm{r}} \geq 2G_{\mathrm{s}}$ RF chains, we can use the closed-form expression in [114] therefore canceling completely the inter-group interference with the resulting hybrid filter. When $G_{\mathrm{s}} \leq N_{\mathrm{RF}}^{\mathrm{r}} < 2G_{\mathrm{s}}$, a factorization algorithm from [30], [109] or [111] can be employed to decouple the overall digital filter into the baseband and RF components. In this case, a gap in the system performance will be observed because of the inter-group interference cannot be totally cancelled. In Section 4.5 we show that the performance offered by the algorithms in [30], [109], [111] for the grouped system can be considerably exceeded by following a different approach to address the optimization problem when $N_{\mathrm{RF}}^{\mathrm{r}} = G_{\mathrm{s}}$.

The problem of hybrid transceiver design is typically formulated as the solution to the following optimization problem [30], [109], [111]

$$\min_{\mathbf{W}_{\mathrm{BB}},\mathbf{W}_{\mathrm{RF}}} \|\mathbf{W} - \mathbf{W}_{\mathrm{RF}}\mathbf{W}_{\mathrm{BB}}\|_F^2 \tag{4.25}$$
$$\text{s.t. } \mathbf{W}_{\mathrm{RF}} \in \mathcal{W}_{\mathrm{RF}},$$

which represents a non-convex optimization problem due to the constraint on the RF filter. Since the aim of the hybrid filter is also to minimize the inter-group interferences even satisfying the condition in (4.19), we rather focus on preserving the structure of the matrix which integrates the equivalent channel responses of the served users and the unconstrained digital filter, i.e., $\mathbf{R} = \mathbf{W}^{*}\mathbf{H}\mathbf{P}_{\mathrm{H}}$. Note that the approach in (4.25) only guarantees that the hybrid filter is close to the digital one in the Euclidean space, but it does not impose any constraint on the structure of the joint equivalent response.

The desirable structure for the matrix $\mathbf{R} \in \mathbb{C}^{G_{\mathrm{s}} \times K_{\mathrm{s}}}$ is

$$\mathbf{R} = \begin{bmatrix} r_{1,1} & \dots & r_{1,g_1} & 0 & \dots & 0 & 0 & \dots & 0 \\ 0 & \dots & 0 & r_{2,1} & \dots & r_{2,g_2} & 0 & \dots & 0 \\ \vdots & \ddots & \vdots & 0 & \ddots & 0 & \vdots & \ddots & \vdots \\ 0 & \dots & 0 & 0 & \dots & 0 & r_{G_{\mathrm{s}},1} & \dots & r_{G_{\mathrm{s}},g_{G_{\mathrm{s}}}} \end{bmatrix}$$

where the zero entries represents inter-group interference, while the non-zero elements are the desirable post-filtering equivalent channel gains. Following this premise, we state an optimization problem where the cost function aims at minimizing the difference between the joint equivalent response considering the hybrid filter and the above matrix $\mathbf{R}$. Thus, we first define the distortion between the response obtained with the digital filter in (4.23) and the response obtained with the hybrid filter, i.e.,

$$d\left(\mathbf{W}_{\mathrm{RF}}, \mathbf{W}_{\mathrm{BB}}\right) = \left\|\mathbf{R} - \mathbf{W}_{\mathrm{BB}}^{*}\mathbf{W}_{\mathrm{RF}}^{*}\mathbf{H}\mathbf{P}_{\mathrm{H}}\right\|_{F}^{2}. \tag{4.26}$$

Then, the optimization problem can be stated as

$$\begin{aligned} \min_{\mathbf{W}_{\mathrm{BB}}, \mathbf{W}_{\mathrm{RF}}} \ & \left\|\mathbf{R} - \mathbf{W}_{\mathrm{BB}}^{*}\mathbf{W}_{\mathrm{RF}}^{*}\mathbf{H}\mathbf{P}_{\mathrm{H}}\right\|_{F}^{2} \\ \text{s.t. } & \mathbf{W}_{\mathrm{RF}} \in \mathcal{W}_{\mathrm{RF}}. \end{aligned} \tag{4.27}$$

We next propose a PG algorithm to solve the non-convex optimization problem in (4.27) under the assumption $N_{\mathrm{RF}}^{\mathrm{r}} = G_{\mathrm{s}}$. The gradient of the cost function (4.26) is

$$\frac{\partial d}{\partial \mathbf{W}_{\mathrm{RF}}^{*}} = -2\left(\mathbf{W}_{\mathrm{BB}}\mathbf{R}\mathbf{P}_{\mathrm{H}}^{*}\mathbf{H}^{*} - \mathbf{W}_{\mathrm{BB}}\mathbf{W}_{\mathrm{BB}}^{*}\mathbf{W}_{\mathrm{RF}}^{*}\mathbf{H}\mathbf{P}_{\mathrm{H}}\mathbf{P}_{\mathrm{H}}^{*}\mathbf{H}^{*}\right). \tag{4.28}$$

Then, at each iteration of the algorithm, the unconstrained update is given by

$$\tilde{\mathbf{W}}_{\mathrm{RF}}^{*} = \mathbf{W}_{\mathrm{RF}}^{*} - \mu\frac{\partial d}{\partial \mathbf{W}_{\mathrm{RF}}^{*}}, \tag{4.29}$$

which is then projected onto the set of feasible solutions $\mathcal{W}_{\mathrm{RF}}$ according to the aforementioned RF hardware constraints. The initial matrix is given by the projection of the digital filter $\mathbf{W}$ onto the set $\mathcal{W}_{\mathrm{RF}}$, and the step size μ is diminished in order to reach a local optimum. The well-known least squares (LS) solution is employed to update the baseband filter by using the closed-form expression

$$\mathbf{W}_{\mathrm{BB}} = \mathbf{R}(\mathbf{P}_{\mathrm{H}}^{*}\mathbf{H}^{*}\mathbf{W}_{\mathrm{RF}})^{\dagger}. \tag{4.30}$$

Algorithm 4.4 PG

Input: $\mathbf{H} \in \mathbb{C}^{N_\mathrm{r} \times N_\mathrm{t} K_\mathrm{s}}, \mathbf{P}_\mathrm{H} \in \mathbb{C}^{N_\mathrm{t} K_\mathrm{s} \times K_\mathrm{s}}$,
$\mathbf{W} \in \mathbb{C}^{N_\mathrm{r} \times G_\mathrm{s}}, \mathbf{R} \in \mathbb{C}^{G_\mathrm{s} \times K_\mathrm{s}}$, μ_0, δ, ϵ

Initialize: $c \leftarrow 0$
$[\mathbf{W}_\mathrm{RF}^{(0)}]_{m,n} = \frac{1}{\sqrt{N_\mathrm{r}}} \exp\left(j \arg\left([\mathbf{W}]_{m,n}\right)\right), \ \forall\, m, n$
$\mu \leftarrow \mu_0$
repeat
    $c \leftarrow c + 1$
    $\tilde{\mathbf{W}}_\mathrm{RF}^{*} \leftarrow \mathbf{W}_\mathrm{RF}^{*(c-1)} - \mu \frac{\partial d}{\partial \mathbf{W}_\mathrm{RF}^{*}}$
    $[\mathbf{W}_\mathrm{RF}^{(c)}]_{m,n} = \exp\left(j \arg\left([\tilde{\mathbf{W}}_\mathrm{RF}]_{i,j}\right)\right), \ \forall\, m, n$
    $\mathbf{W}_\mathrm{BB}^{(c)} = \mathbf{R}\left(\mathbf{P}_\mathrm{H}^{*} \mathbf{H}^{*} \mathbf{W}_\mathrm{RF}^{(c)}\right)^{\dagger}$
    if $d\left(\mathbf{W}_\mathrm{RF}^{(c-1)}, \mathbf{W}_\mathrm{BB}^{(c-1)}\right) \leq d\left(\mathbf{W}_\mathrm{RF}^{(c)}, \mathbf{W}_\mathrm{BB}^{(c)}\right)$ **then**
        $\mu \leftarrow \mu/2$
until $d\left(\mathbf{W}_\mathrm{RF}^{(c)}, \mathbf{W}_\mathrm{BB}^{(c)}\right) < \delta$ or $c \geq \epsilon$
$\mathbf{W}_\mathrm{H} = \mathbf{W}_\mathrm{RF} \mathbf{W}_\mathrm{BB}$

Output: $\mathbf{W}_\mathrm{H}$

The iterative algorithm stops when the distortion d falls below a certain threshold value δ, or when the maximum number of iterations ϵ is reached. Algorithm 4.4 summarizes the proposed strategy to solve the hybrid factorization problem for the filter at the BS.

4.4.2 Algorithmic Solution for Hybrid Filtering with Correlated Sources

In this subsection, we focus on the scenario where the number of RF chains is assumed to be equal to the number of users, i.e., $N_\mathrm{RF}^\mathrm{r} = K$, and where the user information is correlated. Therefore, we can consider the conventional solution without groups, where all the users simultaneously transmit one source symbol per channel use employing an uncoded scheme, that is, the mapping function applied to each user is just a scale factor to satisfy the power constraints. Note that the scenario approached in this section can be seen as a one-user-per-group system where the equality $N_\mathrm{RF}^\mathrm{r} = K = G_\mathrm{s}$ also holds. In this scenario, we focus on the common hybrid receiver design at the BS, but exploiting the source correlation. Hybrid transceivers for MU has been addressed in various scenarios [108], [115], [120] using ZF strategies. In these schemes, unlike the group-based approach, the inter-user interference must be cancelled for uncorrelated sources, but this strategy would no longer be adequate in the presence of correlation.

We propose a filter design where the conventional cancellation of the inter-user interference using a ZF strategy—which completely ignores the spatial correlation—is replaced with a MMSE filter that exploits the source correlation by incorporating the correlation matrix $\mathbf{C}_\mathrm{s}$.

The user precoders stacked in $\mathbf{P}_{\mathrm{H}}$ are calculated by considering the gradient-based precoding strategy proposed in [100] in order to also exploit the spatial correlation.

In the computation of the hybrid filter, the RF component $\mathbf{W}_{\mathrm{RF}}$ is first obtained by projecting the digital MMSE filter $\mathbf{W}_{\mathrm{MMSE}} \in \mathbb{C}^{N_{\mathrm{r}} \times K_{\mathrm{s}}}$ onto the set of feasible filters—which consists on keeping only the phases of its entries. The baseband component $\mathbf{W}_{\mathrm{BB}} \in \mathbb{C}^{N_{\mathrm{RF}}^{\mathrm{r}} \times K_{\mathrm{s}}}$ is then derived as

$$\mathbf{W}_{\mathrm{BB}} = \left(\mathbf{R}_{\mathrm{RF}}\mathbf{C}_{\mathrm{s}}\mathbf{R}_{\mathrm{RF}}^{*} + \sigma_{\mathrm{n}}^{2}\mathbf{W}_{\mathrm{RF}}^{*}\mathbf{W}_{\mathrm{RF}}\right)^{-1}\mathbf{R}_{\mathrm{RF}}\mathbf{C}_{\mathrm{s}}, \tag{4.31}$$

by using a MMSE-based approach, incorporating the correlation matrix $\mathbf{C}_{\mathrm{s}}$ and employing the equivalent channels comprising the RF filter, i.e.,

$$\mathbf{R}_{\mathrm{RF}} = \mathbf{W}_{\mathrm{RF}}^{*}\tilde{\mathbf{H}}, \tag{4.32}$$

where $\tilde{\mathbf{H}} = \left[\mathbf{H}_1\mathbf{p}_{\mathrm{H}1}, \ldots, \mathbf{H}_{K_{\mathrm{s}}}\mathbf{p}_{\mathrm{H}K_{\mathrm{s}}}\right]$ stacks the equivalent channel vectors for the K_{s} served users in the ungrouped system.

The Algorithm 4.5 summarizes the procedure to compute the hybrid filter which exploits the inter-user correlation for an uncoded system with $K_{\mathrm{s}} = K$ served users and $N_{\mathrm{RF}}^{\mathrm{r}} = K_{\mathrm{s}}$ receive chains at the BS.

Algorithm 4.5 Hybrid MMSE

Input: $\{\mathbf{H}_k\}_{k=1}^{K_{\mathrm{s}}}, \mathbf{C}_{\mathrm{s}}$

$\mathbf{P}_{\mathrm{H}} = \mathrm{blkdiag}\left(\mathbf{p}_{\mathrm{H}1}, \ldots, \mathbf{p}_{\mathrm{H}K_{\mathrm{s}}}\right) \leftarrow$ PG precoding [100]

$\mathbf{W}_{\mathrm{MMSE}} = \left(\mathbf{H}\mathbf{P}_{\mathrm{H}}\mathbf{C}_{\mathrm{s}}\mathbf{P}_{\mathrm{H}}^{*}\mathbf{H}^{*} + \sigma_{\mathrm{n}}^{2}\mathbf{I}_{N_{\mathrm{r}}}\right)^{-1}\mathbf{H}\mathbf{P}_{\mathrm{H}}\mathbf{C}_{\mathrm{s}}$

$[\mathbf{W}_{\mathrm{RF}}]_{m,n} = \frac{1}{\sqrt{N_{\mathrm{r}}}} \exp\left(j \arg\left([\mathbf{W}_{\mathrm{MMSE}}]_{m,n}\right)\right), \ \forall\, m, n$

$\mathbf{R}_{\mathrm{RF}} = \mathbf{W}_{\mathrm{RF}}^{*}\tilde{\mathbf{H}}$

$\mathbf{W}_{\mathrm{BB}} = \left(\mathbf{R}_{\mathrm{RF}}\mathbf{C}_{\mathrm{s}}\mathbf{R}_{\mathrm{RF}}^{*} + \sigma_{\mathrm{n}}^{2}\mathbf{W}_{\mathrm{RF}}^{*}\mathbf{W}_{\mathrm{RF}}\right)^{-1}\mathbf{R}_{\mathrm{RF}}\mathbf{C}_{\mathrm{s}}$

$\mathbf{W}_{\mathrm{H}} = \mathbf{W}_{\mathrm{RF}}\mathbf{W}_{\mathrm{BB}}$

Output: $\mathbf{W}_{\mathrm{H}}$

In [36, Section VI], the computational complexity of algorithms 4.2, 4.3, 4.4 and 4.5 is analyzed.

4.5 Simulation Results

In this section, we evaluate the performance and impact of the proposed solutions by providing numerical results and comparisons to other suitable schemes. We consider the exponential correlation model explained in Section 2.2 for the user symbols. In the computer experiments, we assume that the maximum size of the user groups is limited to $g_{\max} = 4$, since this value provides enough flexibility to the scheduling algorithm while mitigating the potential loss caused by larger groups. A MIMO configuration with $N_{\mathrm{t}} = 16$ antennas per user and

$N_{\mathrm{r}} = 49$ antennas at the BS is considered. We consider the scattering cluster channel model in the expression (2.37) in Subsection 2.5.1. In order to randomly simulate the user channels, the maximum and the minimum number of clusters and rays per user is set to $N_{\mathrm{cl}_{\mathrm{max}}} = 4$, $N_{\mathrm{ray}_{\mathrm{max}}} = 3$ and $N_{\mathrm{cl}_{\mathrm{min}}} = 1$, $N_{\mathrm{ray}_{\mathrm{min}}} = 1$, respectively. Then, the channel response of the j-th user in the i-th group is randomly modeled by assigning $N_{\mathrm{cl}i,j} \in \{N_{\mathrm{cl}_{\mathrm{min}}}, \ldots, N_{\mathrm{cl}_{\mathrm{max}}}\}$ clusters compounded by $N_{\mathrm{ray}_{i,j}} \in \{N_{\mathrm{ray}_{\mathrm{min}}}, \ldots, N_{\mathrm{ray}_{\mathrm{max}}}\}$ rays. The path gain parameter $\beta_{n,m}$ of the n-th ray in the m-th cluster is modelled as a random variable following a standard complex-valued Gaussian distribution, that is, $\beta_{n,m} \sim \mathcal{N}_{\mathbb{C}}(0, 1)$. The angles of departure and arrival (AoA/AoD) follow the Laplacian distribution where the mean angles are uniformly randomly distributed in $[0, 2\pi)$, whereas the angular spread is fixed to 10 degrees like in [111].

The performance of the considered communication systems is assessed in terms of the average SDR (see Subsection 2.3.1), which is computed as

$$\text{SDR (dB)} = 10 \log_{10} \left(\frac{1}{\hat{\xi}_{\mathrm{sum}}} \right), \tag{4.33}$$

where

$$\hat{\xi}_{\mathrm{sum}} = \frac{1}{NK_{\mathrm{s}}} \sum_{n=1}^{N} \sum_{i=1}^{G_{\mathrm{s}}} \sum_{j=1}^{g_i} |s_{n,i,j} - \hat{s}_{n,i,j}|^2 \tag{4.34}$$

represents the average MSE between the source symbols and the estimated ones obtained after the demapping operation. The results reported in this section were computed by averaging the SDR over $N = 1000$ channel realizations.

Table 4.2: Simulation parameter setting.

Description	Setting
Number of users	$K \in \{4, 6, 8, 10, 12, 14, 16\}$
Spatial correlation model	$[\mathbf{C}_{\mathrm{s}}]_{i,j} = \rho^{\lvert i-j \rvert},\ \forall\ i, j$
Correlation factor	$\rho \in \{0, 0.50, 0.75, 0.8, 0.85, 0.95\}$
Number of antennas at the BS	$N_{\mathrm{r}} = 49$
Number of RF chains at the BS	$N_{\mathrm{RF}}^{\mathrm{r}} \in \{2, 4, 8, 10\}$
Number of antennas per user	$N_{\mathrm{t}} = 16$
Channel clusters (minimum)	$N_{\mathrm{cl}_{\mathrm{min}}} = 1$
Channel clusters (maximum)	$N_{\mathrm{cl}_{\mathrm{max}}} = 4$
Channel rays (minimum)	$N_{\mathrm{ray}_{\mathrm{min}}} = 1$
Channel rays (maximum)	$N_{\mathrm{ray}_{\mathrm{max}}} = 3$
AoA's and AoD's (channel model)	$[0, 2\pi)$
Channel gain (channel model)	$\beta_{n,m} \sim \mathcal{N}_{\mathbb{C}}(0, 1)$
Channel realizations	$N = 1000$
Number of iterations (Algorithm 4.4)	$\epsilon = 1000$

Without loss of generality, we assume $\sigma_{\mathrm{n}}^2 = 1$, such that the SNR per user can be defined from its corresponding power constraint, i.e., $\text{SNR (dB)}_{i,j} = 10 \log_{10}(P_{\mathrm{T}i,j}),\ \forall\ i =$

$1, \ldots, G_{\mathrm{s}}$ and $j = 1, \ldots, g_i$. For simplicity, the same power constraint is imposed to all the users such that a single SNR value can be considered for all the users in the simulations. Finally, the parameter ϵ (maximum number of iterations) in Algorithm 4.4 is set to 1000 and the same number of iterations is fixed for the other algorithms of matrix factorization in [30], [109] and [111] as well as for the PG precoding algorithm in [100]. The main parameters considered in the simulations are summarized in Table 4.2.

Several experiments have been carried out to evaluate the performance of the different proposed methods. First, we evaluate the hybrid MMSE-based strategy for uncoded systems developed in Subsection 4.4.2. The performance achieved by the proposed PG algorithm in Subsection 4.4.1 to solve the hybrid filtering for user grouping is compared to the conventional strategies for matrix factorizations derived in [30, Algorithm 1], [109, Algorithm 4] and [111, MO-AltMin Algorithm]. Next, we evaluate the performance gain obtained with the scheduling and the allocation policies presented in Subsection 4.3.2 and Subsection 4.3.3. In this context, we also analyze the impact of the thresholds γ_ρ and γ_{s} as well as the weight factors δ_ρ and δ_{s}. Finally, the performance of DQLC techniques is compared to a conventional NOMA approach—based on the uncoded transmission of the source symbols with power allocation—in the grouped system.

4.5.1 Uncoded Scenario

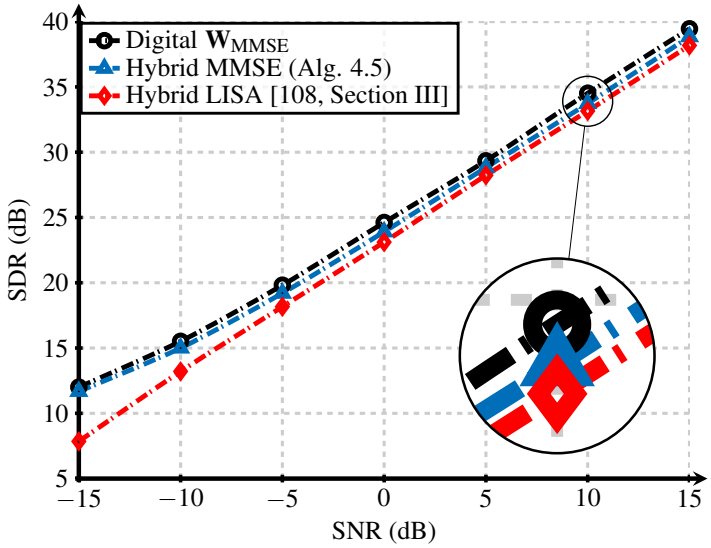

Figure 4.2: SDR (dB) obtained with the different hybrid strategies for the uncoded scenario with $K = 10$ users, $N_{\mathrm{RF}}^{\mathrm{r}} = 10$ and $\rho = 0.80$.

In this subsection, we evaluate the behavior of the proposed hybrid MMSE approach for uncoded correlated sources in Algorithm 4.5. Figure 4.2 shows the SDR obtained by considering different strategies for the design of the hybrid filter in the uncoded scenario with $K = 10$ users, $N_{\mathrm{RF}}^{\mathrm{r}} = 10$ RF chains and correlation factor $\rho = 0.8$. In this setup, all the users are

assumed to transmit their source information simultaneously, i.e., $K_s = K$. The conventional fully digital MMSE filter, the hybrid-linear successive allocation (H-LISA) algorithm and the strategy proposed in Algorithm 4.5 for hybrid implementation are compared. In addition, the PG precoding strategy [100] has jointly been used with the digital MMSE filter and the proposed Hybrid MMSE filter. Notice that the approach H-LISA, inspired on digital LISA for traditional digital precoding, is based on two stages to finally cancel the inter-user interference by applying ZF in the second stage [108, Section III]. The algorithms from [30], [109], [111] present significantly worse performance than H-LISA for the case $N_{RF}^{r} = K_s$, and hence they have not been included in the figure. As expected, the hybrid implementation based on MMSE provides higher performance than that of the hybrid implementation based on the H-LISA algorithm, especially for low SNR values. On the other hand, the loss of the proposed MMSE-based hybrid design with respect to the fully digital MMSE filter is almost negligible for all the range of SNR values. Thus, the impact of the proposed factorization algorithm on the system performance is minimum for the restrictive scenario given by the constraint $N_{RF}^{r} = K$.

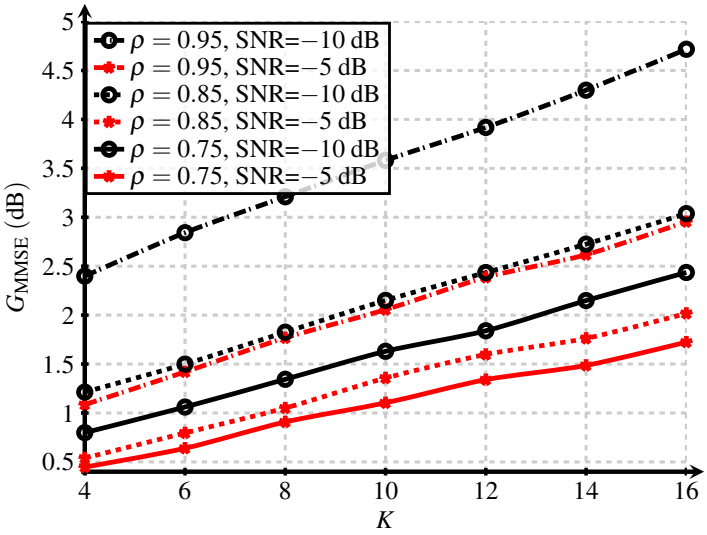

Figure 4.3: Performance gain G_{MMSE} (dB) of the proposed hybrid MMSE algorithm over H-LISA versus number of users for different correlation factors $\rho \in \{0.75, 0.85, 0.95\}$, and SNR (dB) $\in \{-10 \text{ dB}, -5 \text{ dB}\}$.

We now evaluate the performance gain of the proposed hybrid MMSE filter over the H-LISA algorithm. The gain is defined as G_{MMSE} (dB) $=$ SDR$_{\text{H-MMSE}}$ (dB) $-$ SDR$_{\text{HL}}$ (dB), where SDR$_{\text{HL}}$ represents the SDR (dB) obtained by using the H-LISA algorithm and SDR$_{\text{H-MMSE}}$ the one provided by the proposed hybrid MMSE filtering approach. In Figure 4.3, this gain is plotted versus the number of served users, K_s, considering several correlation factors and two particular SNR values, SNR (dB) $\in \{-10 \text{ dB}, -5 \text{ dB}\}$. As expected, the performance gain obtained by using the proposed MMSE solution is higher for the lower SNR levels, since the MMSE exploits the spatial correlation. Figure 4.3 also illustrates that the performance gain increases with the correlation factor and the number of users.

4.5.2 Hybrid Filtering Design

The performance achieved by the proposed PG algorithm in Subsection 4.4.1 to solve the hybrid filtering for user grouping is compared to that of the conventional strategies for matrix factorization derived in [30, Algorithm 1], [109, Algorithm 4] and [111, MO-AltMin Algorithm].

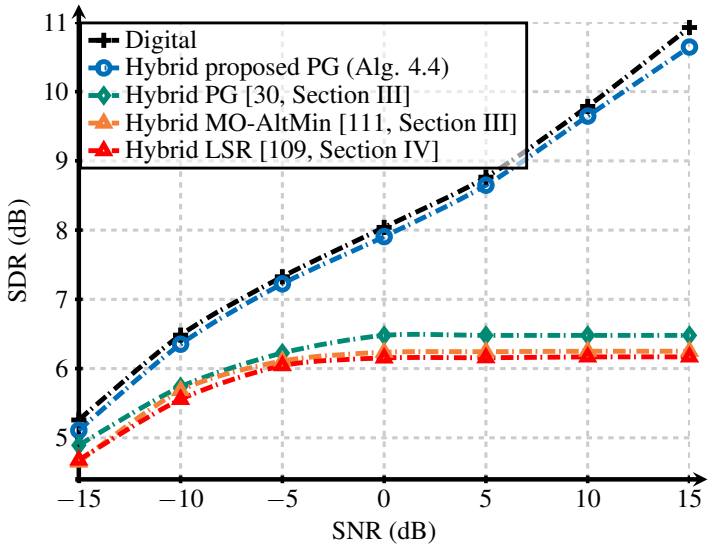

Figure 4.4: SDR (dB) obtained for different strategies of filtering in a scenario with $K = 6$ users, $N_{\text{RF}}^{\text{r}} = 2$, $\rho = 0.80$, and scheduling parameters $\gamma_\rho = 0, \gamma_{\text{s}} = 0, \delta_\rho = 0.2$ and $\delta_{\text{s}} = 0.8$.

Figure 4.4 shows the SDR achieved by considering $K = 6$ users, $N_{\text{RF}}^{\text{r}} = 2$, $\rho = 0.8$ and different strategies for the filtering process. Specifically, the fully digital filter, the strategies of factorization employed in [30], [109], [111], and the proposed hybrid filtering are compared. In this simulation we have considered $\gamma_\rho = 0$ and $\gamma_{\text{s}} = 0$, i.e., $K_{\text{s}} = K$ users are served at each channel realization. We have also considered $\delta_\rho = 0.8$ and $\delta_{\text{s}} = 0.2$ because those values provide good performance for the grouped system in the considered correlation level. Anyways, the same grouping and allocation policies are considered for all the cases. It is shown that the proposed hybrid strategy does not lead to a significant loss in terms of SDR regarding the digital filter (less than 1 dB). Figure 4.4 also illustrates that the proposed hybrid algorithm significantly outperforms the filters based on the factorization of the digital solution in [30], [109] and [111], which saturate in the medium and high SNR regime. This saturation of the system performance when employing the algorithms in [30], [109] and [111] is motivated because the parameter optimization of DQLC is performed according to the SINR of the users per group, which saturates when using these matrix factorization algorithms. Note that these algorithms disregard the desired structure before the demapping functions, and thus the interference between users corresponding to different groups will not be properly cancelled.

4.5.3 Scheduling

We now evaluate the performance gain provided by the scheduling procedure designed in Subsection 4.3.2. We also analyze the impact of the thresholds γ_ρ and γ_s as well as the weight factors δ_ρ and δ_s. Remark that the optimization of these design parameters would lead to an exhaustive search in four-dimension parameter space or to highly non-convex optimization problems involving non-linearities and discontinuities in the DQLC mapping function. We have considered a heuristic approach to choose these parameters, which is based on the insight provided by the issues related to the DQLC behavior presented in Subsection 4.3.2. In this subsection, some numerical results are presented to confirm the validity of the considered approach.

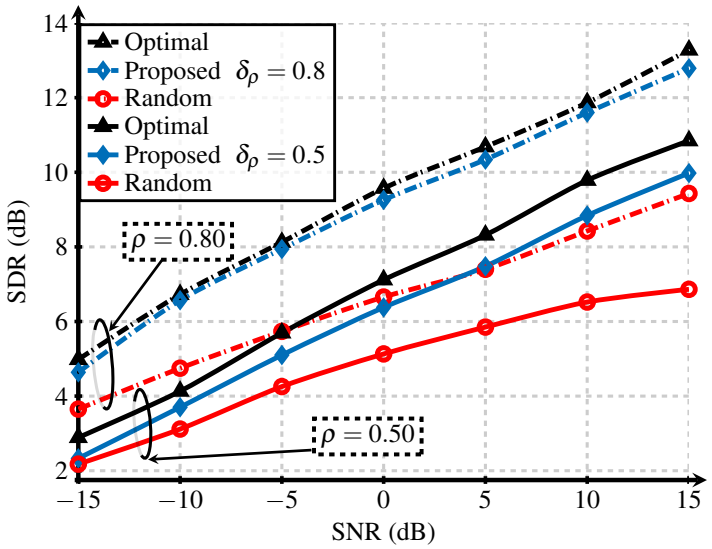

Figure 4.5: SDR (dB) for $K = 5$ users, $N_{\mathrm{RF}}^{\mathrm{r}} = 2$ and $\rho = 0.80$ and different policies of scheduling.

In the first experiment, the proposed scheduling to determine the groups and accommodate the users is evaluated by comparison with two benchmark scenarios. System performance for three scheduling policies are plotted in Figure 4.5: 1) random grouping and allocation, 2) the proposed scheduling following jointly Algorithm 4.1 and Algorithm 4.2, and 3) the optimal combinatorial strategy. We assume a small number of users ($K = 5$) to be served in order to compute the performance of all the grouping and allocation possibilities and select the optimal solution with affordable computational complexity. The proposed PG algorithm is employed to perform the hybrid filtering process.

The performance comparison is carried out for two different correlation factors $\rho \in \{0.50, 0.80\}$, so that the corresponding design parameters of the proposed scheduling should be determined for each case. In particular, such parameters are $\gamma_\rho = 0.5$, $\gamma_\mathrm{s} = 0.35$, $\delta_\rho = 0.8$ and $\delta_\mathrm{s} = 0.2$ for $\rho = 0.80$, whereas we consider $\gamma_\rho = 0.2$, $\gamma_\mathrm{s} = 0.35$, $\delta_\rho = 0.5$ and $\delta_\mathrm{s} = 0.5$ for $\rho = 0.50$. The similarity threshold is the same because the same channel model is used, while the rest of parameters are conveniently adjusted depending on the correlation level. For the sake

of fairness, the same number of served users K_{s} is imposed on each strategy at each channel realization.

Table 4.3: Gap (dB) between the performance obtained by the optimal scheduling and the proposed policies for $\rho = 0.80$.

SNR (dB)	$\delta_\rho = 1$ $\delta_{\mathrm{s}} = 0$	$\delta_\rho = \mathbf{0.8}$ $\delta_{\mathrm{s}} = \mathbf{0.2}$	$\delta_\rho = 0.5$ $\delta_{\mathrm{s}} = 0.5$	$\delta_\rho = 0.3$ $\delta_{\mathrm{s}} = 0.7$
-15	0.68	**0.34**	0.41	0.61
-10	0.69	**0.16**	0.50	1.11
-5	0.69	**0.19**	0.57	1.01
0	0.55	**0.32**	0.69	1.10
5	0.68	**0.34**	0.61	0.90
10	0.95	**0.27**	0.56	0.89
15	0.90	**0.49**	0.74	1.05

As observed in Figure 4.5, the proposed scheduling provides a remarkable performance gain with respect to the random strategy for both correlation factors and in the whole range of SNRs. However, the more interesting conclusion is that the proposed policies closely approach the performance of the optimal combinatorial solution with lower computational cost. These results are especially important since they confirm the suitability of the proposed scheduling procedure for the DQLC-based grouped system, at least for a small number of users. It is not possible to ensure that this behavior holds for scenarios with a larger number of users because of the unaffordable computational complexity. For the considered scenario, the number of grouping possibilities boils down, in general, to two possible configurations, but the number of allocation options is already 30 in the worst case, when $K_{\mathrm{s}} = 3$, since in this case $g_1 = 1$ and $g_2 = 2$, and the number of allocation possibilities is

$$K \times \frac{(K-1)!}{g_2!\,(K-1-g_2)!}, \tag{4.35}$$

i.e., for the first group, we can select one of the $K = 5$ users, and then we have to select $g_2 = 2$ users among the four available ones (combinations without repetition). Note that a combinatorial computation with high complexity is inevitable as the number of users to be allocated increases. For a specific group configuration, the number of allocation possibilities is

$$\prod_{i=1}^{G_{\mathrm{s}}} \frac{(K - \sum_{j=1}^{i-1} g_j)!}{g_i!\,(K - \sum_{j=1}^{i} g_j)!}. \tag{4.36}$$

On the other hand, Table 4.3 and Table 4.4 show the performance loss in dB of the proposed scheduling with respect to the optimal combinatorial solutions for $\rho = 0.80$ and $\rho = 0.50$, respectively. As observed, different parameter configurations are included in these tables showing that the weight factors δ_ρ and δ_{s} depend on the overall correlation of the users. As

expected, it is preferable to lower the weight of the correlation-based metric, δ_ρ, as the overall correlation in the system decreases. Another interesting observation is that the loss of the proposed scheduling with different weight factors is quite stable, and therefore the use of the optimal values for these parameters is not critical.

Table 4.4: Gap (dB) between the performance obtained by the optimal scheduling and the proposed policies for $\rho = 0.50$.

SNR (dB)	$\delta_\rho = 1$ $\delta_\mathrm{s} = 0$	$\delta_\rho = 0.8$ $\delta_\mathrm{s} = 0.2$	$\delta_\rho = \mathbf{0.5}$ $\delta_\mathrm{s} = \mathbf{0.5}$	$\delta_\rho = 0.3$ $\delta_\mathrm{s} = 0.7$
-15	0.60	0.71	**0.56**	0.61
-10	0.67	0.58	**0.43**	0.58
-5	0.64	0.46	**0.41**	0.65
0	0.84	**0.64**	0.74	0.74
5	1.28	0.93	**0.91**	1.02
10	1.01	1.05	**0.95**	0.99
15	1.15	0.97	**0.86**	0.99

Table 4.5: Gap (dB) between the performance obtained by the optimal scheduling and the proposed policies for $\rho = 0$.

SNR (dB)	$\delta_\rho = 1$ $\delta_\mathrm{s} = 0$	$\delta_\rho = 0$ $\delta_\mathrm{s} = 1$	Random
-15	0.88	**0.52**	1.06
-10	0.87	**0.58**	1.32
-5	1.05	**0.77**	1.71
0	1.24	**0.96**	2.25
5	1.89	**0.99**	2.72
10	2.21	**1.14**	3.27
15	2.45	**1.12**	3.66

The extreme situation occurs when the source symbols are uncorrelated, i.e., $\rho = 0$. Table 4.5 shows the performance loss regarding the optimal scheduling as in the previous case but for $\rho = 0$ and considering three different strategies: 1) the proposed scheduling with $\delta_\rho = 1$ and $\delta_\mathrm{s} = 0$; 2) the proposed scheduling with $\delta_\rho = 0$ and $\delta_\mathrm{s} = 1$; and 3) the random scheduling. Note that the first approach would correspond to the case where the grouping configuration is obtained according to Algorithm 4.1. The user allocation, however, is actually random since the users are not correlated. The second approach corresponds to the proposed strategy with grouping and allocation depending on the channel similarity metric. Hence, the difference between both approaches is an interesting measure of the impact of allocating the users with the proposed Algorithm 4.2, even when no correlation is present. As observed, this gain goes from

0.3 dB to 1.3 dB for high SNR values. On the other hand, the difference between the second and fourth columns is a measure of the gain provided by the proposed grouping procedure.

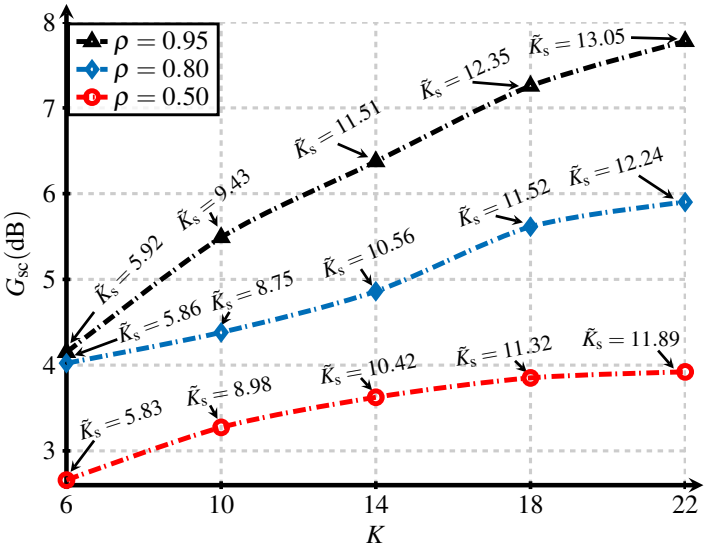

Figure 4.6: G_{sc} (dB) versus K with $N_{\text{RF}}^{\text{r}} = 4$, SNR (dB) $= 10$ dB and $\rho \in \{0.95, 0.80, 0.50\}$.

Table 4.6: Values of the scheduling parameters for the different correlation factors.

Parameter	$\rho = 0.95$	$\rho = 0.8$	$\rho = 0.5$
δ_ρ	0.8	0.8	0.5
δ_{s}	0.2	0.2	0.5
γ_ρ	0.8	0.6	0.3
γ_{s}	0.35	0.35	0.35

In the next experiment, we measure the gain of the proposed scheduling with respect to the random strategy as the number of available users K increases. This gain is defined as

$$G_{\text{sc}}(\text{dB}) = \text{SDR}_{\text{sc}}(\text{dB}) - \text{SDR}_{\text{rm}}(\text{dB}), \tag{4.37}$$

where $\text{SDR}_{\text{sc}}(\text{dB})$ and $\text{SDR}_{\text{rm}}(\text{dB})$ represent the SDR (dB) obtained by the proposed policies and the random policies, respectively. Figure 4.6 plots the gains obtained for $N_{\text{RF}}^{\text{r}} = 4$, $\rho \in \{0.50, 0.80, 0.95\}$ and SNR (dB) = 10 dB, against the number of users K. The thresholds and the weight factors employed in the scheduling procedure are shown in Table 4.6 for the considered correlation factors. The mean number of served users, $\tilde{K}_{\text{s}}$, is also represented at each SNR level. As intuitively expected, the performance gain offered by the proposed algorithms increases with the number of users. On the other hand, the performance of the random scheduling decreases since the probability of grouping low-correlated users with low-capacity channels is higher. Figure 4.6 also shows that the gain $G_{\text{sc}}(\text{dB})$ increases when the correlation becomes higher. This is because the spatial correlation is incorporated in the proposed grouping and allocation policies.

Finally, we evaluate the impact of varying the threshold parameters γ_ρ and γ_s on the number of served users for the grouped system. As commented, we can balance the trade-off between the number of served users and the system performance by adjusting these thresholds conveniently.

Figure 4.7(a) shows the impact of increasing the correlation threshold, γ_ρ, for $K = 16$, $N_{\mathrm{RF}}^{\mathrm{r}} = 4$ and $\rho = 0.9$. The results confirm that a low correlation threshold prioritizes the maximization of the number of served users, whereas a high correlation threshold would preserve the level of signal quality by grouping just the most correlated sources in the same group. The choice of the weight parameters δ_ρ and δ_s also plays an important role in order to decide the grouping and the allocation of the users.

Figure 4.7(a) also shows that increasing the similarity weight factor implies reducing the number of served users, as observed for the setting $\delta_\rho = 0.5, \delta_\mathrm{s} = 0.5$. This is because the ordering of the sets of candidate users to be allocated gives more weight to the channel similarity and, therefore, users with lower correlation levels can be prioritized, although they will then be disregarded when applying the correlation threshold.

A similar effect is shown in Figure 4.7(b) where the mean value of served users, $\tilde{K}_\mathrm{s}$, is plotted versus the similarity threshold, γ_s. It can be observed that increasing γ_s reduces $\tilde{K}_\mathrm{s}$. Conversely, by giving less importance to the channel similarity through the weight factor δ_s, the probability of discarding users increases, because users with low channel similarity can be prioritized in the allocation ordering.

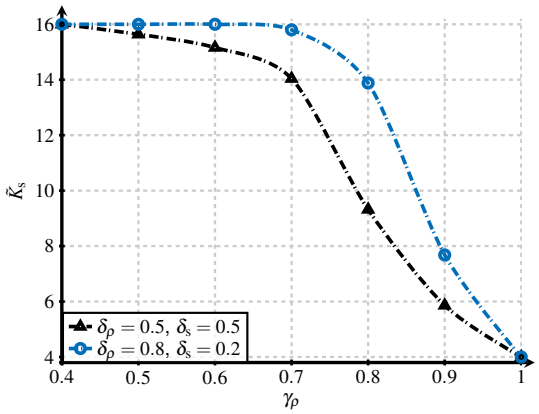

(a) Mean served users $\tilde{K}_\mathrm{s}$ versus the correlation threshold γ_ρ, $K = 16$, $N_{\mathrm{RF}}^{\mathrm{r}} = 4$ and $\rho = 0.9$.

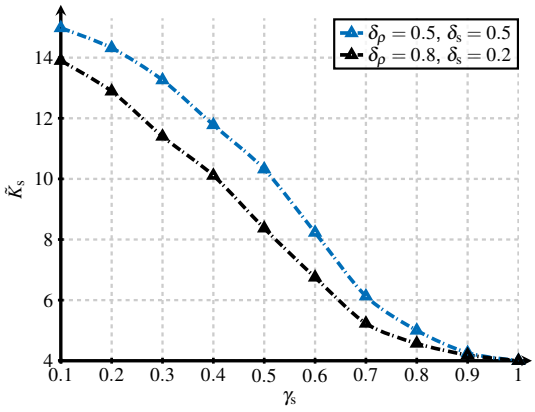

(b) Mean served users $\tilde{K}_\mathrm{s}$ versus the similarity threshold γ_s for $K = 16$, $N_{\mathrm{RF}}^{\mathrm{r}} = 4$ and $\rho = 0.9$.

Figure 4.7: Mean served users by varying the thresholds γ_ρ and γ_s.

4.5.4 NOMA Coding Scheme

We now evaluate the performance of the DQLC-based encoding scheme employed to implement the grouping approach. We specifically compare the performance of the grouped system with DQLC to that of a grouped scheme with a conventional NOMA approach based on the uncoded

transmission of the source symbols with an appropriate power allocation [76], [82]. The same scheduling procedure is applied in both cases to determine the number of groups and users per group. In order to ensure the same number of served users, K_{s}, for both approaches, we set $\gamma_\rho = 0$ and $\gamma_{\mathrm{s}} = 0$, i.e., a conservative strategy is assumed where no users are disregarded in the allocation stage. In addition, the parameters δ_ρ and δ_{s} are equally tuned depending on the correlation factor: $\delta_\rho = 0$ and $\delta_{\mathrm{s}} = 1$ for $\rho = 0$, and $\delta_\rho = 0.8$ and $\delta_{\mathrm{s}} = 0.2$ for $\rho \in \{0.85, 0.95\}$. Finally, the PG algorithm is considered for the hybrid filter at the BS.

Figure 4.8 shows the SDR (dB) achieved for the two NOMA strategies considering $K = 16$, $N_{\mathrm{RF}}^{\mathrm{r}} = 8$ and three different correlation factors $\rho \in \{0, 0.85, 0.95\}$. As observed, the performance of the uncoded scheme is in general higher for the low SNR regime but saturates above some SNR value depending on the correlation. In other words, the uncoded scheme is better than the DQLC scheme just for low SNR values in highly correlated scenarios.

These results match to the theoretical statements derived in [76] for the non-orthogonal transmission over the MAC and the experimental results obtained in [85], [118] for the same scenario. The key point is that the uncoded transmission provides the best performance below a certain SNR threshold, but is no longer optimal above it. Also, this threshold moves to a lower value as the source correlation decreases. This behavior is clearly observed in the results shown in Figure 4.8.

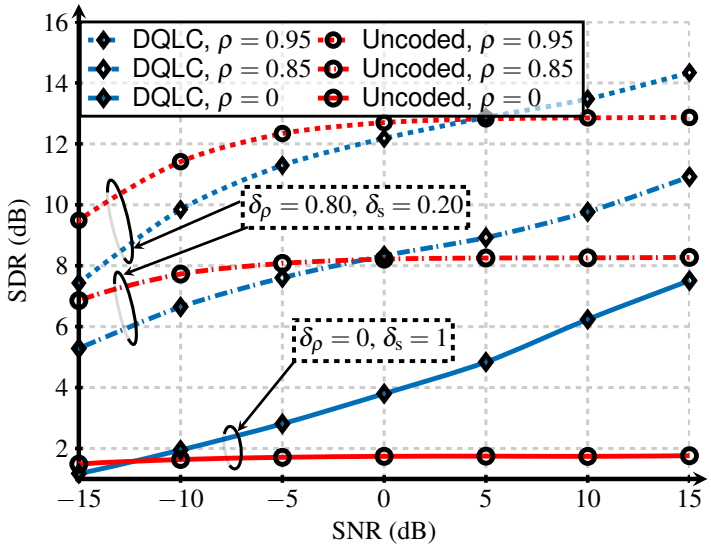

Figure 4.8: SDR (dB) obtained by considering different NOMA strategies for $K = 24$ users, $N_{\mathrm{RF}}^{\mathrm{r}} = 8$, $\gamma_\rho = 0, \gamma_{\mathrm{s}} = 0$ and $\rho \in \{0, 0.85, 0.95\}$.

4.6 Conclusions

This chapter addressed the problem of user grouping for the uplink of MU hybrid mmWave MIMO. A hybrid analog-digital MMSE precoding/filtering approach that exploits the spatial

correlation in the mmWave uplink when $N_{\mathrm{RF}}^{\mathrm{r}} = K_{\mathrm{s}}$ has been derived. User grouping and allocation have been proposed for the case $N_{\mathrm{RF}}^{\mathrm{r}} < K_{\mathrm{s}}$. The proposed scheduling can be easily configured to perform at different points in the trade-off between the number of served users and symbol distortion. Finally, a new approach for the design of the hybrid filter from the fully digital one has been presented. Results show that the proposed scheduling provides reasonable gains compared to a random allocation policy and, in addition, it closely approaches the optimal combinatorial solution. The hybrid design of the BS filter offers large gains over conventional algorithms of matrix factorization. Finally, the results show the feasibility of the grouped system to serve simultaneously a large number of users with a lower number of RF chains.

Chapter V

User Grouping for Wideband Hybrid mmWave MIMO MAC Systems

As already mentioned in previous chapters, the design of the hybrid precoders and filters in MU mmWave MIMO systems is challenging. The main reason is the restrictions imposed by the analog network, typically limited to apply phase-shifts and linear combinations of the digital signal. Furthermore, as explained in Chapter 4, the number of RF chains determines the number of individual streams that a common BS can simultaneously serve. In OFDM wideband scenarios, the design of hybrid precoders and filters to manage the MU interference becomes even more challenging since the common RF filter is frequency flat and, therefore, the analog filter has to be jointly designed for all users and subcarriers. Moreover, the effect of the signal bandwidth over the uniform linear array steering vectors leads to the beam squint [121]. This effect also needs to be considered to effectively remove the MU interference. In this chapter, we extend the work in Chapter 4 by considering all these issues in wideband mmWave MIMO MAC systems.

The chapter is structured as follows. Section 5.1 introduces the chapter. The system model is illustrated in Section 5.2. The analog JSCC, the grouping and the allocation algorithms, as well as the scheduling policy to serve the users, are analyzed in Section 5.3. A novel algorithmic solution for the hybrid filtering approach with user grouping in wideband systems is proposed in Section 5.4. Simulation results are presented in Section 5.5, and Section 5.6 is devoted to the conclusions of the chapter.

5.1 Introduction

Designing hybrid analog-digital schemes is critical for the MU uplinks, where a common filter is employed at the BS to receive all the K_{s} streams. In addition, MU communication systems nowadays demand the feasibility of handling simultaneously a huge amount of nodes (e.g., WSNs or IoT systems) and this would lead to the need of using a large number of RF chains at

the BS ($N_{\mathrm{RF}}^{\mathrm{r}}$), since at least one RF chain is necessary to receive each data stream [10]. For this reason, we have explored in Chapter 4 a new user grouping approach and hybrid system design for practical narrowband mmWave MIMO systems with fewer RF chains than user streams (i.e., $N_{\mathrm{RF}}^{\mathrm{r}} \leq K_{\mathrm{s}}$).

Several works have been developed by assuming single-user schemes in wideband scenarios [72], [122]–[125]. However, in wideband MU scenarios, the design of hybrid precoders and filter to manage the inter-user interference becomes more challenging since the common RF filter is frequency flat and has to be designed for all users and subcarriers. Moreover, the large channel bandwidth leads to the beam direction of the steering vectors (beam squint effect) [121], which also needs to be considered in the system design.

Limited work has been carried out for strongly hardware-constrained hybrid precoding and filtering in wideband MU scenarios [28]–[30], [126], [127]. The authors in [28] and [29] considered MU setups with more than one PS for each RF chain connection to a single antenna, thus leading to more complex architectures. The authors in [30] develop a PG algorithm to leverage the common structure of the channel response matrices among different subcarriers in wideband scenarios. In [126], a hybrid MU equalizer with dynamic subarray antennas for the uplink of single-carrier frequency-division multiple access (SC-FDMA) systems is proposed. The equalizer design is based on two steps by minimizing the MSE: the digital equalizers are iteratively designed on a per-subcarrier basis, whereas the analog equalizer is fixed over the subcarriers and iterations. A dynamic antenna mapping was derived for the analog filter in order to connect the best set of antennas and the PS to each RF chain. The authors in [127] focus on the hybrid precoding design in a downlink mmWave MU scheme. A two-step scheme was developed to cancel the inter-user interference by considering infinite angular resolution and a non-uniformly quantization codebook based on analog precoder with finite angular resolution. Furthermore, the authors proposed a phase compensation operation to alleviate the beam squint effect.

All these works assume that the number of RF chains is at least equal to the number of individual data streams to be collected, i.e., $N_{\mathrm{RF}} \geq K_{\mathrm{s}}$, and therefore the developed algorithms are not suitable for non-orthogonal schemes [128] with user grouping, where $N_{\mathrm{RF}} < K_{\mathrm{s}}$. Moreover, most of these works do not consider the beam squint effect and its critical impact on the cancellation of interferences. In this chapter, we propose a novel wideband hybrid filtering design, with its corresponding user grouping and scheduling scheme, for the uplink of mmWave MIMO systems, where a strong hardware constraint at the BS is considered ($N_{\mathrm{RF}}^{\mathrm{r}} < K_{\mathrm{s}}$). This setup corresponds to a scenario where more streams than available RF chains at the BS could be allocated for each subcarrier. The proposed transmission scheme is specifically designed to deal with the difficulties described above when considering wideband scenarios. In particular, the main contributions of this chapter are the following:

- The design of a novel approach for the interference cancellation at both ends of the communication link considering the hardware constraints imposed by the hybrid

architecture at the BS in wideband scenarios. The proposed algorithm jointly computes the user precoders and the BS hybrid filter to minimize the inter-group interference in the user grouping scheme.

- The development of an extended version of the factorization algorithm proposed in Chapter 4 to design the BS filter which considers the particularities of wideband hybrid mmWave MIMO systems.
- The design of a user grouping and scheduling strategy for wideband scenarios that considers the beam squint effect present in these systems.

5.2 System Model

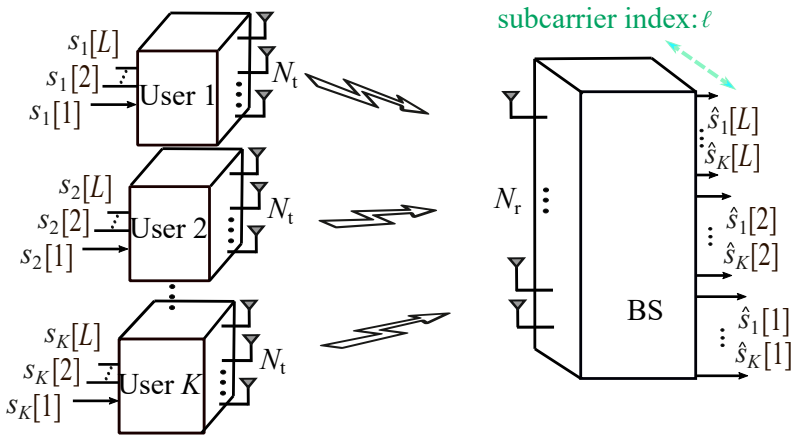

Figure 5.1: System model of a wideband mmWave MIMO MAC system with K users and L subcarriers.

We consider an uplink MU scenario with K users communicating with a common BS equipped with N_{RF}^{r} RF chains and N_{r} antennas as shown in Figure 5.1. To fully exploit the large bandwidths available at mmWave frequencies, users send wideband signals. Consequently, these signals are affected by a frequency-selective channel that is decomposed into L parallel subchannels thanks to the use of the OFDM modulation. The resulting L symbols associated to the L subcarriers are transmitted by considering a cyclic prefix long enough to avoid ISI.

We also consider that the users send a single data stream to the common BS per channel use and subcarrier. At each time instant, $K_{\text{s}}[\ell] < K$ users are served while $K_{\text{I}}[\ell]$ users remain idle at the ℓ-th subcarrier. The set $\mathcal{K}$ contains the subset of active users $\mathcal{K}_{\text{s}}[\ell]$ and the subset of idle users $\mathcal{K}_{\text{I}}[\ell]$ such that $\mathcal{K} = \mathcal{K}_{\text{s}}[\ell] \cup \mathcal{K}_{\text{I}}[\ell],\ \forall\ \ell$. The number of served and idle users is given by the cardinality of the sets, i.e., $K_{\text{s}}[\ell] = |\mathcal{K}_{\text{s}}[\ell]|$ and $K_{\text{I}}[\ell] = |\mathcal{K}_{\text{I}}[\ell]|$, respectively. Finally, the set $\mathcal{K}$ will contain all the available users in the system, i.e., $|\mathcal{K}| = K = K_{\text{s}}[\ell] + K_{\text{I}}[\ell], \forall\ \ell$.

We follow an approximation where the users are gathered in $G[\ell]$ groups by means of an appropriate scheduling algorithm such that $G_{\text{s}} \leq G[\ell]$ groups contain the served users, whereas $G_{\text{I}}[\ell]$ is the number of groups with idle users at the ℓ-th subcarrier. We establish that the number

of served groups is the same for the whole bandwidth, i.e., $G_{\mathrm{s}} = N_{\mathrm{RF}}^{\mathrm{r}}$, whereas the total number of groups $G[\ell]$ is subcarrier dependent and changes according to the considered scheduling algorithm. Denoting $\mathcal{G}_i[\ell]$ as the i-th group at ℓ-th subcarrier, equalities $\mathcal{K}_{\mathrm{s}}[\ell] = \cup_{i=1}^{G_{\mathrm{s}}} \mathcal{G}_i[\ell]$ and $\mathcal{K}_{\mathrm{I}}[\ell] = \cup_{i=G_{\mathrm{s}}+1}^{G[\ell]} \mathcal{G}_i[\ell]$ hold $\forall\ \ell = 1, \ldots, L$, when $G_{\mathrm{s}} < G[\ell]$. Note that for $G_{\mathrm{s}} = G[\ell]$, $\mathcal{K}_{\mathrm{I}}[\ell] = \emptyset$.

For convenience, we also introduce the vector $\mathbf{g}[\ell]$ that contains the number of users per group, where each component $g_i[\ell] = |\mathcal{G}_i[\ell]|$ represents the number of users in the i-th group such that $\sum_{i=1}^{G_{\mathrm{s}}} g_i[\ell] = K_{\mathrm{s}}[\ell]$. Note that, although the number of served groups is fixed throughout the whole bandwidth, the number of collected user symbols per subcarrier at the BS, $K_{\mathrm{s}}[\ell]$, is variable since it depends on the specific composition of the served groups.

We assume that each user has N_{t} antennas to send a single data stream of discrete-time continuous-amplitude symbols to the BS. The vector of the K user symbols at subcarrier ℓ is $\mathbf{s}[\ell] = \left[s_1[\ell], s_2[\ell], \ldots, s_K[\ell]\right]^T$, which follows a zero-mean spatially correlated multivariate complex-valued Gaussian distribution with covariance matrix $\mathbf{C}_{\mathrm{s}} = \mathbb{E}[\mathbf{s}[\ell]\mathbf{s}^*[\ell]]$, such that $[\mathbf{C}_{\mathrm{s}}]_{k,k} = 1,\ \forall\ k$, and $[\mathbf{C}_{\mathrm{s}}]_{i,j} = \rho_{i,j}, 0 \leq \rho_{i,j} \leq 1,\ \forall\ i, j$ with $i \neq j$. Note that we assume the same correlation matrix for all the subcarriers, i.e., $\mathbf{C}_{\mathrm{s}}[\ell] = \mathbf{C}_{\mathrm{s}},\ \forall\ \ell$.

The source symbols corresponding to the served users are individually encoded by means of the mapping functions $f_{i,j}[\ell](s_{i,j}[\ell]),\ \forall\ i = 1, \ldots, G_{\mathrm{s}},\ \forall\ j = 1, \ldots, g_i[\ell],\ \forall\ \ell = 1, \ldots, L$, where $f_{i,j}[\ell](\cdot)$ corresponds to the mapping function applied to the symbols of the j-th user in the i-th group at the ℓ-th subcarrier. We assume that the encoded symbols satisfy the inequality constraint $\mathbb{E}\left[\left|f_{i,j}[\ell]\left(s_{i,j}[\ell]\right)\right|^2\right] \leq 1,\ \forall\ i, j, \ell$. All the encoded users symbols at subcarrier ℓ are stacked in the following vector

$$\mathbf{f}[\ell](\mathbf{s}[\ell]) = \left[f_{1,1}[\ell]\Big(s_{1,1}[\ell]\Big), \ldots, f_{1,g_1[\ell]}[\ell]\Big(s_{1,g_1[\ell]}[\ell]\Big), \ldots, f_{G_{\mathrm{s}},g_{G_{\mathrm{s}}}[\ell]}[\ell]\Big(s_{G_{\mathrm{s}},g_{G_{\mathrm{s}}}[\ell]}[\ell]\Big)\right]^T. \quad (5.1)$$

Next, the encoded symbols are transformed by the linear precoder $\mathbf{p}_{i,j}[\ell] \in \mathbb{C}^{N_{\mathrm{t}} \times 1}$ and then transmitted over the uplink channel. An individual per-subcarrier power constraint is considered at each user as in [30], such that $\|\mathbf{p}_{i,j}[\ell]\|_F^2 \leq P_{\mathrm{T}i,j},\ \forall\ i, j, \ell$ with $P_{\mathrm{T}i,j} = P'_{\mathrm{T}i,j}/L$, being $P'_{\mathrm{T}i,j}$ the total power constraint per user. In this chapter, digital precoding is assumed at the users as in [129]. Therefore, we can consider that the number of RF chains required at the users is equal to the number of transmit antennas, i.e., $N_{\mathrm{t}} = N_{\mathrm{RF}}^{\mathrm{t}}$ since N_{t} is often a small number.

The received signal from the active users at the ℓ-th subcarrier reads as

$$\mathbf{y}[\ell] = \sum_{i=1}^{G_{\mathrm{s}}} \sum_{j=1}^{g_i[\ell]} \mathbf{H}_{i,j}[\ell]\mathbf{p}_{i,j}[\ell] f_{i,j}[\ell]\left(s_{i,j}[\ell]\right) + \mathbf{n}[\ell], \quad (5.2)$$

where $\mathbf{H}_{i,j}[\ell] \in \mathbb{C}^{N_{\mathrm{r}} \times N_{\mathrm{t}}}$ is the mmWave channel response corresponding to subcarrier ℓ of the j-th user in the i-th group, and $\mathbf{n}[\ell] = [n_1[\ell], n_2[\ell], \ldots, n_{N_{\mathrm{r}}}[\ell]]^T$ represents the complex-valued AWGN such that $\mathbf{n}[\ell] \sim \mathcal{N}_{\mathbb{C}}(0, \sigma_{\mathrm{n}}^2 \mathbf{I}_{N_{\mathrm{r}}})$. The received signal at subcarrier ℓ can also be rewritten in a more compact way as

$$\mathbf{y}[\ell] = \mathbf{H}[\ell]\mathbf{P}[\ell]\mathbf{f}[\ell]\left(\mathbf{s}[\ell]\right) + \mathbf{n}[\ell], \quad (5.3)$$

$$\mathbf{H}[\ell] = \left[\mathbf{H}_{1,1}[\ell], \ldots, \mathbf{H}_{G_\mathrm{s}, g_{G_\mathrm{s}}[\ell]}[\ell]\right] \tag{5.4}$$

and

$$\mathbf{P}[\ell] = \text{blkdiag}\left(\mathbf{p}_{1,1}[\ell], \ldots, \mathbf{p}_{G_\mathrm{s}, g_{G_\mathrm{s}}[\ell]}[\ell]\right). \tag{5.5}$$

Table 5.1: System model parameters.

Description	Parameter
Number of users	K
Number of antennas per users	N_t
Number of subcarriers	L
Vector of the K user symbols at subcarrier ℓ	$\mathbf{s}[\ell]$
Correlation matrix	$\mathbf{C}_\mathrm{s}$
Mapping function: j-th user in the i-th group at subcarrier ℓ	$f_{i,j}[\ell](\cdot)$
Precoder: j-th user in the i-th group at subcarrier ℓ	$\mathbf{p}_{i,j}[\ell]$
Number of RF chains at the users	N_RF^t
Total power constraint per user	$P'_{\mathrm{T}i,j}$
Vector of AWGN at subcarrier ℓ	$\mathbf{n}[\ell]$
Subset of active users at subcarrier ℓ	$\mathcal{K}_\mathrm{s}[\ell]$
Subset of idle users at subcarrier ℓ	$\mathcal{K}_\mathrm{I}[\ell]$
Number of served user groups for all the subcarriers	G_s
Number of served users at subcarrier ℓ	$K_\mathrm{s}[\ell]$
Number of idled users at subcarrier ℓ	$K_\mathrm{I}[\ell]$
i-th group of users at ℓ-th subcarrier	$\mathcal{G}_i[\ell]$
Vector with the number of users per group at subcarrier ℓ	$\mathbf{g}^{(\ell)}$
Number of antennas at the BS	N_r
Number of RF chains at the BS	N_RF^r
BS hybrid filter at subcarrier ℓ	$\mathbf{W}_\mathrm{H}[\ell]$
Baseband filter at subcarrier ℓ	$\mathbf{W}_\mathrm{BB}[\ell]$
Frequency-flat RF filter	$\mathbf{W}_\mathrm{RF}$
Vector of post-filtering group symbols at subcarrier ℓ	$\mathbf{z}[\ell]$
Decoding functions at subcarrier ℓ	$\mathbf{q}[\ell](\mathbf{z}[\ell])$
Vector of estimated served user symbols at subcarrier ℓ	$\hat{\mathbf{s}}[\ell]$

At the receiver, a BS hybrid filter $\mathbf{W}_\mathrm{H}[\ell],\ \forall\ \ell = 1, \ldots, L$, is implemented with N_RF^r RF chains to fulfill the task of decoupling the uplink received signal $\mathbf{y}[\ell]$ as

$$\mathbf{z}[\ell] = \mathbf{W}_\mathrm{H}^*[\ell]\mathbf{y}[\ell], \tag{5.6}$$

where $\mathbf{W}_\mathrm{H}^*[\ell] = \mathbf{W}_\mathrm{BB}^*[\ell]\mathbf{W}_\mathrm{RF}^*$, with $\mathbf{W}_\mathrm{BB}[\ell] \in \mathbb{C}^{N_\mathrm{RF}^\mathrm{r} \times G_\mathrm{s}}$ the baseband filter for the ℓ-th subcarrier and $\mathbf{W}_\mathrm{RF} \in \mathcal{W}_\mathrm{RF}$ the frequency-flat RF filter. The term $\mathcal{W}_\mathrm{RF} \in \mathbb{C}^{N_\mathrm{r} \times N_\mathrm{RF}^\mathrm{r}}$ represents the set of feasible RF filters imposing a modulus constraint at each entry. The hybrid filter aims at

canceling the interference between the different user groups such that each entry of the vector $\mathbf{z}[\ell]$ only contains the combination of the symbols transmitted by the users in the corresponding served group. Note that the dimension of the vectors of filtered symbols at each subcarrier is actually $\mathbf{z}[\ell] \in \mathbb{C}^{G_\mathrm{s}},\ \forall\ \ell$. Then, the set of decoding functions

$$\mathbf{q}[\ell](\mathbf{z}[\ell]) = \left[q_1[\ell](z_1[\ell]), \ldots, q_{G_\mathrm{s}}[\ell](z_{G_\mathrm{s}}[\ell])\right]^T$$

provides an estimate of the source symbols for the served users at subcarrier ℓ as

$$\hat{\mathbf{s}}_\mathbf{i}[\ell] = q_i[\ell](z_i[\ell]) = \left[\hat{s}_{i,1}[\ell], \ldots, \hat{s}_{i,g_i[\ell]}[\ell]\right]^T, \quad \forall\ i = 1, \ldots, G_\mathrm{s}.$$

Since we are considering the transmission of analog complex-valued source symbols, the performance of the communication system is measured in terms of the MSE between the source and the estimated symbols. Table 5.1 summarizes the main system model parameters.

5.3 User Grouping in Wideband Hybrid mmWave MIMO MAC

In Chapter 4, we proposed a user grouping scheme based on the use of DQLC mappings, which enables to serve more than one user over the same RF chain for narrowband scenarios. This approach requires the design of an adequate user grouping strategy to balance the trade-off between the system performance and the number of served users. We aim at extending this idea to wideband scenarios, which leads to significant changes in the design of the user precoder and the BS hybrid filter, as well as in the scheduling algorithm.

5.3.1 DQLC Implementation for Wideband Systems

In the following analysis, we assume that non-orthogonal DQLC mappings are individually applied into the $G_\mathrm{s} \leq G[\ell]$ served groups. The implementation of DQLC per group establishes that $g_i[\ell] - 1$ users of the i-th group at the ℓ-th subcarrier transmit a quantized version of their symbols while the symbol of the remaining user is just scaled by a power factor $(\alpha_{i,j}[\ell])$ so that it can be placed between two quantization steps of the encoded user symbols. Therefore, the DQLC mapping function for the i-th group at the ℓ-th subcarrier is mathematically stated as [118]

$$f_{i,j}[\ell]\left(s_{i,j}[\ell]\right) = \begin{cases} \alpha_{i,j}[\ell]\left\lfloor \frac{s_{i,j}[\ell]}{\Delta_{i,j}[\ell]} - \frac{1}{2} \right\rceil + \frac{1}{2}, & j < g_i[\ell] \\ \alpha_{i,j}[\ell] s_{i,j}[\ell], & j = g_i[\ell] \end{cases}, \tag{5.7}$$

where $\alpha_{i,j}[\ell]$ represents the scale factor and $\Delta_{i,j}[\ell]$ represents the quantization step employed by the j-th user in the i-th group at the ℓ-th frequency sub-band. The DQLC parameters are

adjusted according to the SINR in a way similar to the narrowband scenario approached in [36]. Here, we consider that the channel symbols at the BS for the ℓ-th subcarrier are given by

$$\mathbf{z}[\ell] = \mathbf{R}[\ell]\mathbf{f}[\ell](\mathbf{s}[\ell]) + \tilde{\mathbf{n}}[\ell], \tag{5.8}$$

where

$$\mathbf{R}[\ell] = \mathbf{W}_{\mathrm{H}}^{*}[\ell]\mathbf{H}[\ell]\mathbf{P}[\ell] \tag{5.9}$$

represents the equivalent channel response for the encoded symbols after the filtering process and $\tilde{\mathbf{n}}[\ell] = \mathbf{W}_{\mathrm{H}}^{*}[\ell]\mathbf{n}[\ell]$ is the equivalent noise. Note that the SINR corresponding to the ℓ-th subcarrier of the uplink signal can be obtained directly from the equivalent channel matrix $\mathbf{R}[\ell] \in \mathbb{C}^{G_{\mathrm{s}} \times K_{\mathrm{s}}[\ell]}$ and the noise power. The vector of filtered symbols can be decomposed into its individual components as

$$\begin{aligned} z_i[\ell] = &\sum_{j=1}^{g_i[\ell]} [\mathbf{R}]_{i,[b(i)+j]}[\ell] f_{i,j}[\ell](s_{i,j}[\ell]) + \\ &\sum_{r \neq i}^{G_{\mathrm{s}}} \sum_{j}^{g_r[\ell]} [\mathbf{R}_{i,[b(r)+j]}][\ell] f_{r,j}[\ell](s_{r,j}[\ell]) + \tilde{n}_i[\ell], \ \forall\, i = 1, \ldots, G_{\mathrm{s}}, \end{aligned} \tag{5.10}$$

where $b(i) = \sum_{t=1}^{i-1} g_t[\ell] + 1$ is an auxiliary index that determines the first component of the equivalent channel matrix corresponding to the i-th group. The first term in (5.10) is the desired signal for the i-th group, the second term is the inter-group interference, and the third term is the i-th component of the equivalent noise after filtering. It is worth noting that the quality of the DQLC demapping process is determined by the SINR level at the input of the demapping functions assuming that the mapping parameters are properly adjusted according to such a value. In addition, SINR values will be maximum when the second term in (5.10) vanishes, which happens when the equivalent response matrices have the following structure

$$\mathbf{R}[\ell] = \begin{bmatrix} r_{1,1}[\ell] & \ldots & r_{1,g_1[\ell]}[\ell] & 0 & \ldots & 0 & 0 & \ldots & 0 \\ 0 & \ldots & 0 & r_{2,1}[\ell] & \ldots & r[\ell]_{2,g_2[\ell]} & 0 & \ldots & 0 \\ \vdots & \ddots & \vdots & 0 & \ddots & 0 & \vdots & \ddots & \vdots \\ 0 & \ldots & 0 & 0 & \ldots & 0 & r_{G_{\mathrm{s}},1}[\ell] & \ldots & r_{G_{\mathrm{s}},g_{G_{\mathrm{s}}}[\ell]}[\ell] \end{bmatrix}, \forall \ell \tag{5.11}$$

where the zero-valued entries represent the inter-group interference at subcarrier ℓ, while the non-zero elements are the desirable post-filtering equivalent channel gains. This structure can be obtained by implementing a fully digital filter at the BS under the condition

$$[\mathbf{W}^{*}]_{k,:}[\ell]\mathbf{H}_{i,j}[\ell]\mathbf{p}_{i,j}[\ell] = 0, \forall\, i \neq k, \text{ with } k, i = 1, \ldots, G_{\mathrm{s}}, \text{ and } j = 1, \ldots, g_i[\ell]. \tag{5.12}$$

Thus, the fully digital filter is designed in the context of DQLC-based systems to cancel the interference caused by all the users from the other groups. The digital filter implementation that guarantees the fulfilment of the conditions in (5.12) was derived in Section 4.4. This

implementation considers digital maximum ratio transmitter (MRT) precoding in the users and a common digital filter for the BS to cancel the inter-group interference per subcarrier. Throughout this chapter, this strategy will be labeled as DFc-DMRT. The same result can also be reached by considering a digital maximum ratio combining (MRC) at the BS and canceling the inter-group interference with the digital precoders DMRC-DPc. This approach is similar to [100, Section 3] and invokes the MSE duality principle [116].

After the filtering step, the DQLC demapping functions $\mathbf{q}[\ell](\mathbf{z}[\ell])$ produce the estimated symbols $\hat{\mathbf{s}}_i[\ell] \ \forall \ i, \ell$. As previously motioned in Chapter 4, DQLC decoding methods can be found in [117, Section III] and [118].

5.3.2 Algorithmic Solution for User Grouping and Allocation in Wideband

The scheduling procedure aims at determining the number of user groups, the composition of each group and which groups are served at the BS per subcarrier, i.e., it must determine $\mathbf{g}[\ell]$ and $\mathcal{G}_i[\ell], \forall \ i, \ell$. It hence comprises two intertwined steps: the grouping strategy and the allocation policy. Both steps have been approached in Subsection 4.3.2 and Subsection 4.3.3 for a narrowband scenario. For wideband systems, we will follow a strategy that considers the limitations imposed by the use of DQLC mappings but with the novelty of incorporating the intrinsic limitations of working with a common RF filter for all the subcarriers, and considering the per-subcarrier dependent impact of the beam squint effect. As we will discuss the two main factors that determine the performance of the proposed wideband system are the source correlation and the similarity between the user and the subcarrier channels.

As explained in Chapter 4, the performance of DQLC schemes is definitively conditioned by the spatial correlation among the source symbols and the channel similarity for those users in the same group for a specific subcarrier. Therefore, it is essential to consider these two factors, intra-group correlation and intra-group channel similarity, to gather users in the same group. On the other hand, the requirement of canceling inter-group interference with a hybrid filter, where the analog part is common for all subcarriers, leads to a scheduling procedure where it is preferable to select users with similar channels for the same group index through all the subcarriers. For example, the composition of the first user group for the L subcarriers, i.e., $\mathcal{G}_1[\ell], \ \forall \ \ell$, should not only consider the channel similarity among the users individually at each subcarrier, but also the inter-subcarrier channel similarity. Thus, it is desirable that the inter-subcarrier channels for the users in $\mathcal{G}_1[1], \mathcal{G}_1[2], \ldots, \mathcal{G}_1[L]$ are also as similar as possible. A user allocation based on this premise will enable a better overall inter-group interference cancellation by using the common RF filter.

In addition, the channel similarity threshold γ_{s} and the cross-correlation threshold γ_ρ defined in Subsection 4.3.3 are considered to discard users that could degrade the system performance when including them into the groups. As explained in Chapter 4, these thresholds allow us to

manage the system requirements: either incorporating as many users as possible to the detriment of the quality of service, or introducing a smaller number of users while guaranteeing a high level of the received signal quality. We set the maximum number of users per group to $g_{\max} = 7$ and focus on the allocation by also considering the different subcarrier channels.

As mentioned, two important factors must be taken into account when considering DQLC mappings to perform the allocation:

1. The spatial correlation between the users per group (intra-group correlation).
2. The similarity of the user channels per group (intra-group channel similarity).

These two factors are jointly integrated by using the metric

$$m_k = \delta_\rho \tilde{\rho}_k + \delta_\mathrm{s} C_{\mathrm{sim}k}, \tag{5.13}$$

where the factors δ_ρ and δ_s define the weight of the correlation and similarity criteria, respectively, $\tilde{\rho}_k$ is the mean of the users cross-correlation in a group $\mathcal{G}_i$, whereas the parameter $C_{\mathrm{sim}k}$ measures the convenience of including a user in the group $\mathcal{G}_i$ according to its channel response similarity w.r.t. the already allocated users in $\mathcal{G}_i$. Note that this part of the allocation procedure should be incorporated into the new allocation policies for wideband scenarios as it is a consequence of using DQLC mappings.

When considering wideband communications, two different situations can arise. First, in wideband scenarios where the beam squint effect is negligible, the user channels across all the subcarriers have rotated row and column spaces [72], i.e., the channels are very similar, since the actual steering vectors are the same at each subcarrier channel. In these scenarios, an individual allocation per subcarrier following a straightforward approximation of Algorithm 4.2 can be performed.

Nevertheless, when considering larger bandwidths, channel similarity is lost and the per-subcarrier AoA and AoD can be spatially distinguished due to the beam squint effect [72]. For that reason, the design of the user allocation also needs to consider the inter-subcarrier channel similarity. In the following, we describe three possible allocation strategies.

5.3.2.1 Individual Allocation

In this strategy, an individual allocation is performed per subcarrier and thus the user groups, the composition of each group, the served group indexes and the number of served users will be different per subcarrier. This strategy is a straightforward extension of [36, Algorithm 2] and it does not consider the beam squint effect.

5.3.2.2 Common Allocation

In this strategy, the user distribution per group is obtained by considering a similar metric to (5.13), $m_{\mathrm{c}k} = \delta_\rho \tilde{\rho}_k + \delta_\mathrm{s} C_{\mathrm{csim}k}$, and this distribution will be the same for all the subcarriers, i.e., $\mathcal{G}_i[\ell] = \mathcal{G}_i,\ \forall\ \ell$ and thus $K_\mathrm{s}[\ell] = K_\mathrm{s},\ \forall\ \ell$. Therefore, we start including in the group the

user with the best channels i.e., with the largest singular values across the subcarrier channels. Next, we use the metric C_{csim_k} to measure the convenience of including a new user $\mathcal{K}(k)$ in $\mathcal{G}_i$ by jointly computing the channel similarity of all the user channels in $\mathcal{G}_i$ and considering all the subcarriers. With this aim, we define the matrix

$$\mathbf{H}_{\text{c}} = \left[\mathbf{H}^T_{\mathcal{G}_i(1)}[1], \ldots, \mathbf{H}^T_{\mathcal{G}_i(1)}[L], \ldots, \mathbf{H}^T_{\mathcal{G}_i(Z)}[L]\right]^T, \tag{5.14}$$

which includes all the subcarrier channels for the Z users already allocated in the sequence $\mathcal{G}_i$, and the matrix

$$\mathbf{H}'_{\text{c}} = \left[\mathbf{H}^T_{\text{c}}, \mathbf{H}^T_{\mathcal{K}(k)}[1], \ldots, \mathbf{H}^T_{\mathcal{K}(k)}[L]\right]^T, \tag{5.15}$$

which additionally includes the L channels for the candidate user $\mathcal{K}(k)$. We now employ the auxiliary vector $\mathbf{p}_i$, i.e., the right singular vector associated to the largest singular value of $\mathbf{H}_{\text{c}}$, and similarly $\mathbf{p}'_i$ for $\mathbf{H}'_{\text{c}}$, to compute the parameter C_{csim_k} as

$$C_{\text{csim}_k} = \frac{\sum_{\ell=1}^{L}\sum_{z=1}^{Z} \|\mathbf{H}_{\mathcal{G}_i(z)}[\ell]\mathbf{p}_i\|^2}{\sum_{\ell=1}^{L}\sum_{z=1}^{Z} \|\mathbf{H}_{\mathcal{G}_i(z)}[\ell]\mathbf{p}'_i\|^2 + \sum_{\ell=1}^{L} \|\mathbf{H}_{\mathcal{K}(k)}[\ell]\mathbf{p}'_i\|^2}. \tag{5.16}$$

Note that this allocation strategy incorporates the inter-subcarrier channel similarity and is thus especially suitable for large bandwidth schemes where the beam squint effect is present. Indeed, by including all the subcarrier channels corresponding to the allocated users as well as the candidate user, the expression (5.16) will provide an overall similarity across all the frequency band.

5.3.2.3 Sequential Allocation

This strategy sequentially includes the inter-subcarrier channel similarity to form the groups. We aim at designing an allocation strategy to approximately overlap the inter-group interference subspaces across all the subcarriers.

We start by including in the first group the user with the best channel and by considering the inter-subcarrier channel similarity as in the previous common allocation. In this case, however, the users per group are specifically chosen at each subcarrier. This allocation procedure is performed sequentially across the subcarriers, such that we select the user whose channels are more similar considering the previous subcarriers of the users already allocated in the same group index. Thus, the proposed policy performs a sequential allocation where the best user is always selected according to the source correlation, the intra-group user channel similarity, and the inter-subcarrier channel similarity. Therefore, unlike the common allocation, the group composition might be different for different subcarriers.

After selecting the first user for each group $\mathcal{G}_i[\ell]$ in a similar way to Algorithm 4.2, we next define the metric C_{psim_k} to measure the convenience of including a user $\mathcal{K}(k)$ in $\mathcal{G}_i[\ell]$. Such metric jointly considers the channel similarity of all the subcarrier channels for the users in $\mathcal{G}_i[\ell]$ and all the subcarrier channels of the candidate user $\mathcal{K}(k)$. Once the allocation for the first

subcarrier is completed, the group scheduling of the next subcarriers is sequentially determined by taking into account the group composition of the already allocated subcarriers. Therefore, the overall channel similarity for the i-th group at the $\tilde{\ell}$-th subcarrier is defined as

$$C_{\text{psim}_k}[\tilde{\ell}] = \frac{\sum_{\ell=1}^{L}\sum_{z=1}^{Z} \|\mathbf{H}_{\mathcal{G}_i[\tilde{\ell}](z)}[\ell]\mathbf{p}_i\|^2 + \tilde{C}}{\sum_{\ell=1}^{L}\sum_{z=1}^{Z} \|\mathbf{H}_{\mathcal{G}_i[\tilde{\ell}](z)}[\ell]\mathbf{p}'_i\|^2 + \sum_{\ell=1}^{L} \|\mathbf{H}_{\mathcal{K}(k)}[\ell]\mathbf{p}'_i\|^2 + \tilde{D}}, \tag{5.17}$$

with

$$\tilde{C} = \sum_{\ell=1}^{L}\sum_{m=1}^{\tilde{\ell}-1}\sum_{\tilde{z}=1}^{g_i[m]} \|\mathbf{H}_{\mathcal{G}_i[m](\tilde{z})}[\ell]\mathbf{p}_i\|^2 \tag{5.18}$$

and

$$\tilde{D} = \sum_{\ell=1}^{L}\sum_{m=1}^{\tilde{\ell}-1}\sum_{\tilde{z}=1}^{g_i[m])} \|\mathbf{H}_{\mathcal{G}_i[m])(\tilde{z})}[\ell]\mathbf{p}'_i\|^2. \tag{5.19}$$

As observed, Z users are assumed to be already allocated to the i-th group at the current $\tilde{\ell}$-th subcarrier, i.e., in $\mathcal{G}_i[\tilde{\ell}]$. The terms $\tilde{C}$ and $\tilde{D}$ take into account the channels corresponding to the users that have already been allocated in the same group index i but at the previous subcarriers. Similarly to the common allocation, we also use the auxiliary vectors $\mathbf{p}_i$ and $\mathbf{p}'_i$, but here $\mathbf{H}_{\text{c}}$ results from the concatenation of the L sub-channels for the users allocated in the same group index i at the previous subcarriers and for the Z users already allocated for that group at the current $\tilde{\ell}$-th subcarrier.

It is important to recall that the user groups, their composition, and thus the number of served user symbols $K_{\text{s}}[\ell]$ are subcarrier dependent in this allocation algorithm. Note also that, by taking into account the channel similarity of both the users and the subcarriers, this strategy jointly considers the DQLC singularities and the limitations of working with a common RF filter at the BS.

5.4 Hybrid Filtering for User Grouping in Wideband mmWave MIMO MAC

In this section, we derive an algorithm termed group null-space directed SVD (GNU-SVD) for the joint design of the user precoders and the hybrid filter at the BS in the uplink MU mmWave MIMO setting under consideration. This algorithm assumes that the composition of each group, the served groups and the number of served users $K_{\text{s}}[\ell]$ per subcarrier provided by the scheduling are known. The inter-user correlation per group is also calculated to compute the DQLC parameter optimization (step 5, Algorithm 5.1). GNU-SVD is summarized in Algorithm 5.1 and can be divided into two main steps.

Step 1: the SNR is maximized at transmission by means of a MRT precoder per user and at each subcarrier $\tilde{\mathbf{p}}_{i,j}[\ell]$, $\forall\ i, j, \ell$ (step 6, Algorithm 5.1). Then, the ℓ-th digital unconstrained filter $\mathbf{W}[\ell]$ is obtained as in Algorithm 4.3 to cancel the inter-group interference (step 9,

Algorithm 5.1), but using the conditions given in (5.12). Up to this point, fully digital precoders and filters are considered and the inter-user interference is just removed among those users in different groups at each subcarrier. Next, we design the hybrid filter by using Algorithm 5.2 (PG) in the step 17 of Algorithm 5.1 and, consequently, a residual inter-user interference will appear since the constraints of the hybrid implementation make infeasible the full cancellation of the inter-group interference. This residual interference can cause large losses in the system performance because it seriously affects the optimization of the DQLC parameters.

Step 2: the residual inter-group interference is removed by means of the digital precoders at the users and the hybrid filter obtained in the previous step. Notice that the limitations imposed by the hardware, namely the frequency flat response of the analog part of the filter, demands a refinement of the joint precoder and filter design in order to lower the interference down to a level that enables the use of DQLC. Therefore, we define the equivalent channels $\tilde{\mathbf{H}}_i[\ell]$ for the i-th user group at subcarrier ℓ as

$$\tilde{\mathbf{H}}_i[\ell] = \left[\mathbf{H}^*_{i,1}[\ell]\mathbf{W}_{\mathrm{H}}[\ell], \ldots, \mathbf{H}^*_{i,g_i}[\ell]\mathbf{W}_{\mathrm{H}}[\ell]\right]. \tag{5.20}$$

Next, we project each MRT user precoder $\tilde{\mathbf{p}}_{i,j}[\ell]\ \forall\ i,j,\ell$ onto the nullspace of the equivalent channels of the users allocated in different groups (step 23, Algorithm 5.1). We eventually get the user precoders as $\mathbf{p}_{i,j}[\ell] = \left(\mathbf{I} - \mathbf{N}_i[\ell]\mathbf{N}^*_i[\ell]\right)\tilde{\mathbf{p}}_{i,j}[\ell]$, where $\mathbf{N}_i[\ell]$ is the basis for the subspace spanned by the columns of the matrix

$$\mathbf{I}_{\mathcal{G}_i[\ell]} = \left[\tilde{\mathbf{H}}_1[\ell], \ldots, \tilde{\mathbf{H}}_{i-1}[\ell], \tilde{\mathbf{H}}_{i+1}[\ell], \ldots, \tilde{\mathbf{H}}_{G_{\mathrm{s}}}[\ell]\right].$$

Algorithm 5.1 summarizes the GNU-SVD procedure to determine the user precoders and the hybrid filter at the BS.

5.4.1 Algorithmic Solution for Hybrid Filtering in Wideband mmWave MIMO MAC

In this section, we extend the Algorithm 4.4 proposed for hybrid filtering to wideband hybrid mmWave scenarios assuming the condition $N^{\mathrm{r}}_{\mathrm{RF}} = G_{\mathrm{s}} \leq K_{\mathrm{s}}[\ell]\ \forall\ \ell$. In this case, we design a PG algorithm for hybrid filtering considering the structure imposed in (5.12) where the analog part is frequency-flat, as shown in Figure 5.2.

Let us define the matrices $\mathbf{W}^* = [\mathbf{W}^*[1], \ldots, \mathbf{W}^*[L]]$ and $\mathbf{W}^*_{\mathrm{H}} = \mathbf{W}^*_{\mathrm{BB}}(\mathbf{I}_L \otimes \mathbf{W}^*_{\mathrm{RF}}) = [\mathbf{W}^*_{\mathrm{BB}}[1], \ldots, \mathbf{W}^*_{\mathrm{BB}}[L]]\,(\mathbf{I}_L \otimes \mathbf{W}^*_{\mathrm{RF}})$ such that $\mathbf{W}^* \in \mathbb{C}^{G_{\mathrm{s}} \times N_{\mathrm{r}} L}$, $\mathbf{W}^*_{\mathrm{BB}} \in \mathbb{C}^{G_{\mathrm{s}} \times G_{\mathrm{s}} L}$ and $\mathbf{W}_{\mathrm{RF}} \in \mathcal{W}_{\mathrm{RF}}$. We focus on minimizing the distance between the digital filter response and the hybrid filter response, therefore considering the following distortion metric

$$d\left(\mathbf{W}_{\mathrm{RF}}, \mathbf{W}_{\mathrm{BB}}\right) = \|\mathbf{R} - \mathbf{W}^*_{\mathrm{BB}}(\mathbf{I}_L \otimes \mathbf{W}^*_{\mathrm{RF}})\mathbf{H}\mathbf{P}\|^2_F, \tag{5.21}$$

and posing the following minimization problem

$$\min_{\mathbf{W}_{\mathrm{BB}}, \mathbf{W}_{\mathrm{RF}}} d\left(\mathbf{W}_{\mathrm{RF}}, \mathbf{W}_{\mathrm{BB}}\right) \quad \text{s.t.} \quad \mathbf{W}_{\mathrm{RF}} \in \mathcal{W}_{\mathrm{RF}}. \tag{5.22}$$

Algorithm 5.1 GNU-SVD

Input: $\mathbf{H}_k[\ell]\ \forall\ k, l,\ \mathbf{C}_\mathrm{s}, N_\mathrm{RF}^\mathrm{r}, \mathbf{g}$

Initialize: $\tilde{\mathbf{P}} = [\,], \mathbf{W} = [\,], \mathbf{H} = [\,], \mathbf{R} = [\,],$
for $\ell = 1, \ldots, L$ **do**
  repeat
    $i \leftarrow i + 1$
    $\mathbf{C}_i \leftarrow$ Inter-user correlation per group
    $\tilde{\mathbf{P}}_i[\ell] = \text{blkdiag}\left(\tilde{\mathbf{p}}_{i,1}[\ell], \ldots, \tilde{\mathbf{p}}_{i,g_i}[\ell]\right) \leftarrow$ MRT
    $\mathbf{H}_i[\ell] = \left[\mathbf{H}_{i,1}[\ell], \ldots, \mathbf{H}_{i,g_i}[\ell]\right]$
  until $i = N_\mathrm{RF}^\mathrm{r}$
  $\mathbf{W}[\ell] \leftarrow$ Algorithm 4.3 per subcarrier
  $\tilde{\mathbf{P}}[\ell] =$blkdiag$(\tilde{\mathbf{P}}_1[\ell], \ldots, \tilde{\mathbf{P}}_{G_\mathrm{s}}[\ell])$
  $\mathbf{H}[\ell] = \left[\mathbf{H}_1[\ell], \ldots, \mathbf{H}_{G_\mathrm{s}}[\ell]\right]$
  $\mathbf{R}[\ell] = \mathbf{W}^*[\ell]\mathbf{H}[\ell]\tilde{\mathbf{P}}[\ell]$
$\mathbf{W}^* = [\mathbf{W}^*[1], \ldots, \mathbf{W}^*[L]]$
$\tilde{\mathbf{P}} = \text{blkdiag}(\tilde{\mathbf{P}}[1], \ldots, \tilde{\mathbf{P}}[L])$
$\mathbf{H} = \text{blkdiag}(\mathbf{H}[1], \ldots, \mathbf{H}[L])$
$\mathbf{R} = [\mathbf{R}[1], \ldots, \mathbf{R}[L]]$
$\mathbf{W}_\mathrm{H}[\ell] = \mathbf{W}_\mathrm{RF}\mathbf{W}_\mathrm{BB}[\ell] \leftarrow$ Algorithm 5.2 $\left(\mathbf{H}, \tilde{\mathbf{P}}, \mathbf{W}, \mathbf{R}\right)$
for $\ell = 1, \ldots, L$ **do**
  for $i = 1, \ldots, G_\mathrm{s}$ **do**
    $\tilde{\mathbf{H}}_i[\ell] = \left[\mathbf{H}_{i,1}^*[\ell]\mathbf{W}_{\mathrm{H}_i}[\ell], \ldots, \mathbf{H}_{i,g_i}^*[\ell]\mathbf{W}_{\mathrm{H}_i}[\ell]\right].$
    $\mathbf{I}_{\mathcal{G}_i[\ell]} = \left[\tilde{\mathbf{H}}_1[\ell], \ldots, \tilde{\mathbf{H}}_{i-1}[\ell], \tilde{\mathbf{H}}_{i+1}[\ell], \ldots, \tilde{\mathbf{H}}_{G_\mathrm{S}}[\ell]\right]$
    $\mathbf{N}_i[\ell] \leftarrow$basis for the subspace span $\left(\mathbf{I}_{\mathcal{G}_i[\ell]}\right)$
    for $j = 1, \ldots, g_i$ **do**
      $\mathbf{p}_{i,j}[\ell] = \left(\mathbf{I} - \mathbf{N}_i[\ell]\mathbf{N}_i^*[\ell]\right)\tilde{\mathbf{p}}_{i,j}[\ell]$

Output: $\mathbf{P}, \mathbf{W}_\mathrm{H}$

Note that $\mathbf{R} = [\mathbf{R}[1], \ldots, \mathbf{R}[L]]$, $\mathbf{H} = \text{blkdiag}\left(\mathbf{H}[1], \ldots, \mathbf{H}[L]\right)$ and $\mathbf{P} = \text{blkdiag}\left(\mathbf{P}[1], \ldots, \mathbf{P}[L]\right)$. Note that $\mathbf{R} \in \mathbb{C}^{G_\mathrm{s} \times \sum_{l=1}^{L} K_\mathrm{s}[\ell]}$, $\mathbf{W}_\mathrm{BB}^* \in \mathbb{C}^{G_\mathrm{s} \times LG_\mathrm{s}}$, $\mathbf{W}_\mathrm{RF} \in \mathcal{W}_\mathrm{RF}$, $\mathbf{H} \in \mathbb{C}^{N_\mathrm{r}L \times N_\mathrm{t} \sum_{l=1}^{L} K_\mathrm{s}[\ell]}$ and $\mathbf{P} \in \mathbb{C}^{N_\mathrm{t} \sum_{l=1}^{L} K_\mathrm{s}[\ell] \times \sum_{l=1}^{L} K_\mathrm{s}[\ell]}$.

Note that this approach is especially suitable for the DQLC-based system because we are rather interested in preserving the structure of the equivalent channel response $\mathbf{R}$ than in preserving the entries of the digital filter. In the following, we derive a PG algorithm (see Algorithm 5.2) to solve the non-convex optimization problem in (5.22) under the assumption $N_\mathrm{RF}^\mathrm{r} = G_\mathrm{s}$. We start determining the gradient of the cost function (5.21), which leads to

$$\frac{\partial d}{\partial \mathbf{W}_\mathrm{RF}^*} = \sum_{\ell=1}^{L} \mathbf{W}_\mathrm{BB}[\ell]\mathbf{R}[\ell]\mathbf{P}^*[\ell]\mathbf{H}^*[\ell] + \mathbf{W}_\mathrm{BB}[\ell]\mathbf{W}_\mathrm{BB}^*[\ell]\mathbf{W}_\mathrm{RF}^*\mathbf{H}[\ell]\mathbf{P}[\ell]\mathbf{P}^*[\ell]\mathbf{H}^*[\ell]. \tag{5.23}$$

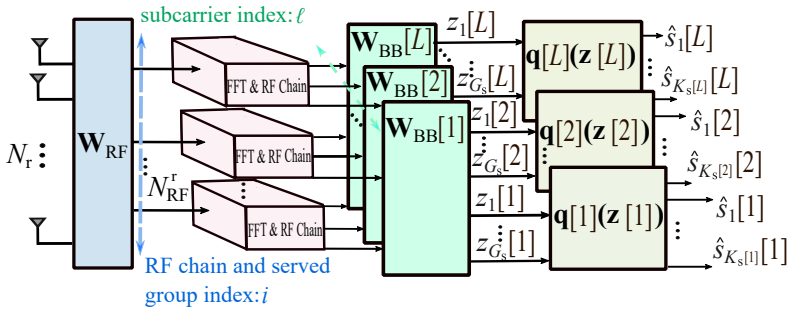

Figure 5.2: Hybrid architecture filter in the wideband mmWave MIMO MAC system with DQLC.

Algorithm 5.2 PG

Input: $\{\mathbf{H}[\ell]\}_{\ell=1}^{L} \in \mathbb{C}^{N_r \times N_t K_s[\ell]}$, $\{\mathbf{P}[\ell]\}_{\ell=1}^{L} \in \mathbb{C}^{N_t K_s[\ell] \times K_s[\ell]}$, $\{\mathbf{W}[\ell]\}_{\ell=1}^{L} \in \mathbb{C}^{N_r \times G_s}$, $\{\mathbf{R}[\ell]\}_{\ell=1}^{L} \in \mathbb{C}^{G_s \times K_s[\ell]}$, μ_0, δ, ϵ

1: **Initialize:** $c \leftarrow 0$
2: $[\mathbf{W}_{RF}{}^{(0)}]_{m,n} = \frac{1}{\sqrt{N_r}} \exp\left(j \arg\left([\mathbf{W}]_{m,n}[L/2]\right)\right), \ \forall\, m, n$
3: $\mu \leftarrow \mu_0$
4: **repeat**
5: $\quad c \leftarrow c + 1$
6: $\quad \tilde{\mathbf{W}}_{RF}^{*} \leftarrow \mathbf{W}_{RF}^{*(c-1)} - \mu \frac{\partial d}{\partial \mathbf{W}_{RF}^{*}}$
7: $\quad [\mathbf{W}_{RF}^{*(c)}]_{m,n} = \frac{1}{\sqrt{N_r}} \exp\left(j \arg\left([\tilde{\mathbf{W}}_{RF}^{*}]_{m,n}\right)\right), \ \forall\, m, n$
8: $\quad \mathbf{W}_{BB}^{*(c)} = \mathbf{R}\left(\mathbf{P}^{*}\mathbf{H}^{*}(\mathbf{I}_L \otimes \mathbf{W}_{RF}^{(c)})\right)^{\dagger}$
9: $\quad \text{error}^{(c)} = d\left(\mathbf{W}_{RF}^{(c)}, \mathbf{W}_{BB}^{(c)}\right)$
10: $\quad$ **if** $\text{error}^{(c)} > \text{error}^{(c-1)}$ **then**
11: $\quad\quad \mu \leftarrow \mu/2$
12: **until** $\text{error}^{(c)} < \delta$ or $c \geq \epsilon$
13: $\mathbf{W}_H[\ell] = \mathbf{W}_{RF}\mathbf{W}_{BB}[\ell], \ \forall\, \ell$

Output: $\{\mathbf{W}_H[\ell]\}_{\ell=1}^{L}$

The analog filter in the first iteration $\left(\mathbf{W}_{RF}{}^{(0)}\right)$ is calculated as the projection of the digital filter corresponding to the central subcarrier onto the set $\mathcal{W}_{RF}$ (step 2, Algorithm 5.2) whereas the step size μ is diminished in order to reach a local optimum. Next, at each algorithm iteration, the unconstrained solution for the analog RF component is given by

$$\tilde{\mathbf{W}}_{RF}^{*} = \mathbf{W}_{RF}^{*} - \mu \frac{\partial d}{\partial \mathbf{W}_{RF}^{*}}, \tag{5.24}$$

which is then projected onto the set of feasible solutions $\mathcal{W}_{RF}$ (step 7, Algorithm 5.2). The LS solution is next employed to update the baseband filter such that $\mathbf{W}_{BB}^{*} = \mathbf{R}(\mathbf{P}^{*}\mathbf{H}^{*}(\mathbf{I}_L \otimes \mathbf{W}_{RF}))^{\dagger}$. Algorithm 5.2 shows the sequence of steps corresponding to the extended PG-based approach to compute the hybrid filter from the digital version. This iterative algorithm is stopped when

the distortion d falls below a certain threshold value or when the maximum number of iterations ϵ is reached.

In [37, Section V], we analyze the computational complexity of the proposed Algorithm 5.2 for hybrid filtering, the proposed Algorithm 5.1 for user precoding and hybrid filtering, and the considered allocation policies: individual, common and sequential.

5.5 Simulation Results

In this section, we evaluate the performance of the proposed algorithms through different computer simulations where several filtering design techniques and scheduling implementations are compared. We consider the exponential correlation model explained in Section 2.2 for the user symbols. Results are averaged over $N = 1000$ channel realizations for each experiment. We consider the simplified multipath channel model in the expression (2.32) in Subsection 2.5.1, which accounts for the beam squint effect. The parameters for the channel model are set to L_{D} = 8 delay taps and $N_{\mathrm{p}_{i,j}} = 3$ channel paths $\forall\ i, j$. The AoAs and the AoDs are assumed to be uniformly distributed over the interval $[0, \pi]$ as in [31]. The relative delays $\tau_{i,j,n}$ are also random and assumed to be uniformly distributed over the interval $\tau_{i,j,n} \in [0, (L_{\mathrm{D}} - 1)T_{\mathrm{s}}]$, with $T_s = 1/f_s$. The complex-valued channel gains are i.i.d. random variables $\beta_{i,j,m} \sim \mathcal{N}_{\mathbb{C}}(0, 1)$. The central carrier frequency is $f_{\mathrm{c}} = 28$ GHz whereas the signal bandwidth varies from 800 MHz to 3200 MHz. The number of subcarriers is set to $L = 32$.

The system performance is assessed in terms of the average SDR defined as

$$\text{SDR (dB)} = 10\ \log_{10}\ \left(1/\hat{\xi}_{\text{sum}}\right), \tag{5.25}$$

where

$$\hat{\xi}_{\text{sum}} = \frac{1}{NL\sum_{l=1}^{L} K_{\mathrm{s}}[\ell]} \sum_{n=1}^{N}\sum_{\ell=1}^{L}\sum_{i=1}^{G_{\mathrm{s}}}\sum_{j=1}^{g_i[\ell]} |s_{n,i,j}[\ell] - \hat{s}_{n,i,j}[\ell]|^2 \tag{5.26}$$

represents the average MSE between the source symbols and the estimated ones obtained after the demapping operation at the BS.

Without loss of generality, we assume $\sigma_{\mathrm{n}}^2 = 1$ and therefore define the SNR per user as

$$\text{SNR (dB)}_{i,j} = 10\ \log_{10}(P'_{\mathrm{T}i,j}),\ \forall\ i = 1, \ldots, G_{\mathrm{s}} \text{ and } j = 1, \ldots, g_i[\ell]. \tag{5.27}$$

For simplicity, the same power constraint is considered for all the users. Finally, the maximum number of iterations ϵ is set to 1000 in Algorithm 5.2 as well as in the other iterative algorithms considered in this section for comparison. The main parameters considered in the simulations are summarized in Table 5.2.

Two experiments have been carried out to evaluate the performance of the different proposed methods. First, we evaluate the behavior of the GNU-SVD algorithm in combination with the extended hybrid PG algorithm, and compare it with other possible system implementations. In the second experiment, we evaluate the performance of the proposed user allocation approaches.

Table 5.2: Simulation parameter setting.

Parameter	Setting
Number of users	$K = 9$
Spatial correlation model	$[\mathbf{C}_{\mathrm{s}}]_{i,j} = \rho^{\lvert i-j \rvert},\ \forall\, i,j$
Number of antennas at the BS	$N_{\mathrm{r}} = 100$
Number of RF chains at the BS	$N_{\mathrm{RF}}^{\mathrm{r}} = 3$
Number of antennas per user	$N_{\mathrm{t}} = 8$
Number of taps (channel model)	$L_{\mathrm{D}} = 8$
Channel paths (channel model)	$N_{\mathrm{p}_{i,j}} = 3,\ \forall\, i,j$
AoA's and AoD's (channel model)	$[0, \pi]$
Relative delay (channel model) $(\tau_{i,j,n})$	$\tau_{i,j,n} \in [0, (L_{\mathrm{D}} - 1)T_{\mathrm{s}}]$
Sampling frequency (channel model)	$f_{\mathrm{s}} = 1760$ MHz
Channel gain (channel model)	$\beta_{i,j,m} \sim \mathcal{N}_{\mathbb{C}}(0,1)$
Carrier frequency (channel model)	$f_{\mathrm{c}} = 28$ GHz
Signal bandwidths	800 MHz $\sim$ 3200 MHz
Number of subcarriers (channel model)	$L = 32$
Channel realizations	$N = 1000$
Number of iterations (PG algorithms)	$\epsilon = 1000$

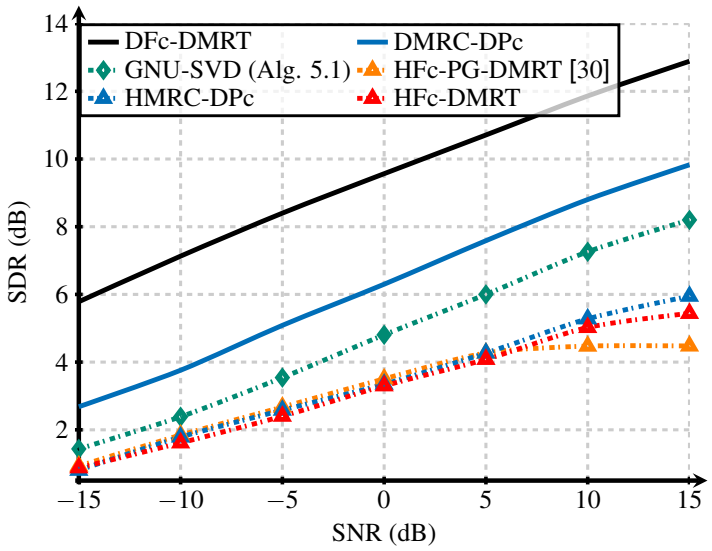

Figure 5.3: SDR (dB) versus SNR (dB) for $K = 9$ users, $N_{\mathrm{RF}}^{\mathrm{r}} = 3$, $B = 3200$ MHz and $\rho = 0.85$.

Figure 5.3 shows the SDR (dB) versus SNR (dB) obtained for $K = 9$ users, $B = 3200$ MHz, $N_{\mathrm{RF}}^{\mathrm{r}} = 3$, $\rho = 0.85$ and different strategies for the design of the user precoding and the BS filter. In particular, we consider the following alternatives: 1) the fully digital filtering cancellation with MRT precoders at the users (DFc-DMRT); 2) a digital precoding cancellation with MRC (DMRC-DPc); 3) a hybrid version of 1) by factorizing the filter with the PG algorithm in [30] labeled as HFc-PG-DMRT; 4) a hybrid version of 1) by factorizing the filter with the proposed

Algorithm 5.2, labeled as HFc-DMRT; 5) a hybrid version of 2) that utilizes the proposed Algorithm 5.2 to factorize the filter and digital precoder cancellation (HMRC-DPc); and 6) the proposed GNU-SVD algorithm. Simulations have considered $\gamma_\rho = 0$ and $\gamma_\mathrm{s} = 0$ to isolate the impact of the group allocation. We have also chosen $\delta_\rho = 0.8$ and $\delta_\mathrm{s} = 0.2$ because those values are a suitable trade-off between the impact of the channel similarity and the correlation for $\rho = 0.85$. As observed, Figure 5.3 shows a gap (around 2.8 dBs) between the two fully digital implementation strategies (DFc-DMRT and DMRC-DPc), which is related to the available degrees of freedom to implement the inter-group interference cancellation. Note that the DMRC-DPc approach performs the cancellation at the user precoders ($\mathbf{p}_{i,j}[\ell] \in \mathbb{C}^{N_\mathrm{t}\times 1},\ \forall\, i,j,\ell$) with $N_\mathrm{t} = 16$ antennas, whereas the DFc-DMRT approach implements the cancellation at the common filter $\mathbf{W}[\ell] \in \mathbb{C}^{N_\mathrm{r}\times G_\mathrm{s}},\ \forall\, \ell$ with $N_\mathrm{r} = 100$ antennas.

In order to compare the hybrid filter implementations, we need to take into account two issues: 1) the structure of the common filter to be factorized, and 2) how the factorization problem is stated. By considering this last issue, we can sense that the factorization algorithm proposed in [30, Section 7] provides the less appropriate strategy to obtain the hybrid filter since that algorithm completely neglects the desired structures $\mathbf{R}[\ell]$ in (5.11). Therefore it is reasonable that the HFc-PG-DMRT strategy exhibits the worst performance, especially for high SNR values. As observed, the implementation strategies HMRC-DPc and HFc (Alg. 5.2)-DMRT provide a similar behavior. Although the digital precoding interference cancellation implemented in the HMRC-DPc is performed with less degrees of freedom, the hybrid factorization of the MRCs is more feasible for wideband scenarios than the one performed over the digital filter implemented according to Algorithm 4.3. This is because this approach destroys the relationship between the column spaces at the different subcarriers [30]. Finally, by implementing the user precoder cancellation in a second refinement step, the proposed GNU-SVD approach provides the best performance among all the hybrid implementations, and also offers a suitable trade-off between hardware-complexity and system performance. Note that in all these hybrid strategies we are able to handle 9 user symbols per sub-band ($L = 32$) with only three RF chains ($N_\mathrm{RF}^\mathrm{r} = 3$).

Figure 5.4 shows the evaluation results for four different user allocation algorithms that determine the user groups: 1) sequential allocation, 2) common allocation per subcarrier, 3) individual allocation per subcarrier neglecting the beam squint effect, and 4) random allocation. We consider $K = 9$ users, $N_\mathrm{RF}^\mathrm{r} = 3$, and $\rho = 0.85$. The proposed GNU-SVD cancellation algorithm is employed to configure the user precoders and the hybrid filter. The comparison is performed for two different bandwidths, i.e., $B \in \{800\ \text{MHz}, 3200\ \text{MHz}\}$. The beam squint effect is more apparent for $B = 3200$ MHz, where the subcarrier offsets $\zeta[\ell] = ((\ell-1) - \frac{L-1}{2})\frac{B}{L},\ \forall\, \ell$ are larger, while this effect practically vanishes when considering $B = 800$ MHz [31]. As observed in Figure 5.4, the random allocation provides the worst performance for both bandwidths since it neglects the main factors (cross-correlation and channel similarity) to define an appropriate allocation policy. Figure 5.4 also shows that, when

$B = 800$ MHz, the remaining allocation strategies present a similar behavior. In this case, the sequential and the common allocation approximately offer the same system performance as the individual allocation because the inter-subcarrier channel similarity does not impact on the allocation. However, the sequential allocation presents a small gain w.r.t. the other strategies because the design of the digital filters takes into account the channel similarity of both the users and the subcarriers, and therefore reduces the losses of working with a frequency-flat analog filter.

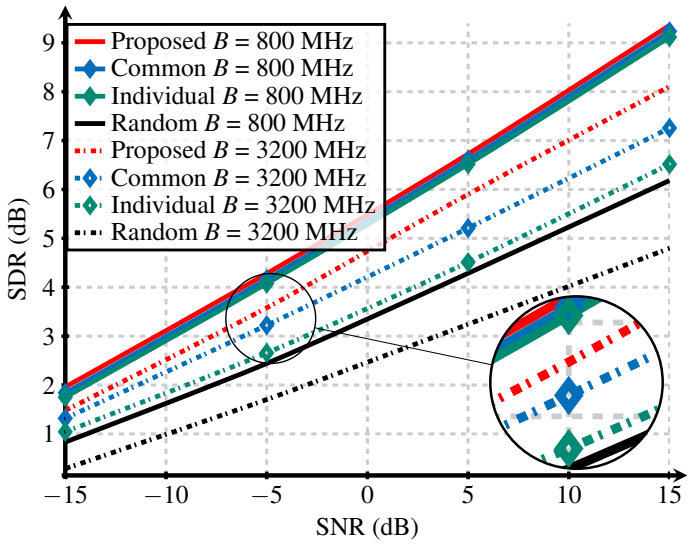

Figure 5.4: SDR (dB) versus SNR (dB) for $K = 9$ users, $N_{\text{RF}}^{\text{r}} = 3$, $B \in \{800 \text{ MHz}, 3200 \text{ MHz}\}$ and $\rho = 0.85$.

A different behavior is observed when $B = 3200$ MHz due to the beam squint effect. Figure 5.4 shows that the sequential and common allocation strategies achieve a higher performance than the individual one since they incorporate the inter-subcarrier channel similarity. Moreover, the sequential allocation strategy provides additional performance gains by considering the limitations of working with a common RF filter at the BS.

Figure 5.5 shows the SDR (dB) versus the signal bandwidth (B) for the four considered user allocation strategies: 1) sequential allocation, 2) common allocation per subcarrier, 3) individual allocation per subcarrier, and 4) random allocation. We consider $K = 9$ users, $N_{\text{RF}}^{\text{r}} = 3$ RF chains, $\rho = 0.85$ and a particular SNR value, namely, SNR $= 5$ dB. The proposed GNU-SVD cancellation algorithm is employed to define the user precoders and the hybrid filter. The beam squint is practically negligible when considering $B = 800$ MHz but its effect starts to be more apparent while the bandwidth increases because the subcarrier offsets become larger. Figure 5.5 clearly illustrates the behavior of the different user allocation strategies under the beam squint effect. Note how the random allocation strategy provides the worst performance in the whole range of bandwidths because it neglects the correlation and the channel similarity factor to determine the allocation. The performance of random allocation also worsens as

the bandwidth increases because the probability of gathering users with significantly different channels is higher. Figure 5.5 also shows that the remaining allocation policies (sequential, common, and individual) present a similar behavior when $B = 800$ MHz since, under a negligible beam squint effect, the inter-subcarrier channel similarity—which is incorporated in the common and the sequential allocation—does not impact on the user allocation. However, their behavior is different as the bandwidth increases because the sequential and the common allocation, by considering the inter-subcarrier channel similarity, offer superior performance than the individual allocation.

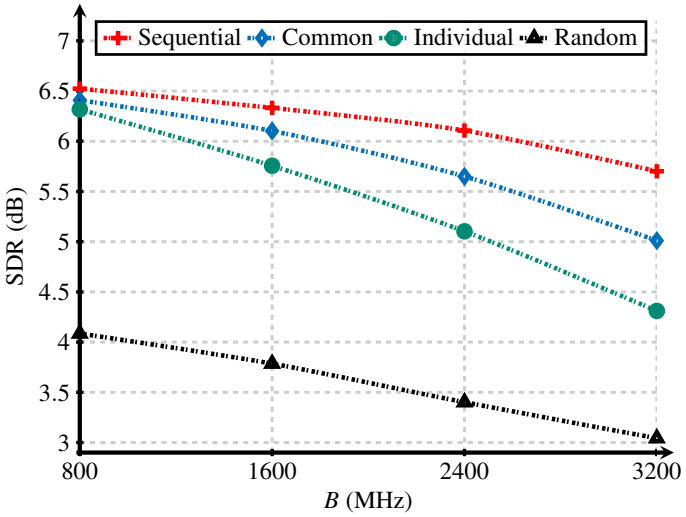

Figure 5.5: SDR (dB) performance for $K = 9$ users, $N_{\text{RF}}^{\text{r}} = 3$, SNR $= 5$ dB and $\rho = 0.85$.

5.6 Conclusions

This chapter has focused on the design of appropriate strategies for user grouping and hybrid filtering in the uplink of wideband MU mmWave MIMO systems. A both-ends interference cancellation procedure has been proposed to deal with the hardware constraints of the system and serve the user groups in a DQLC-based scheme. The proposed hybrid design for the BS filter leads to large gains over conventional algorithms based on matrix factorization for wideband scenarios. A novel sequential allocation approach that considers the effects derived from beam squint in wideband mmWave systems has also been developed. The proposed sequential scheduling procedure provides gains of about 25% compared to the straightforward extension of the scheduling strategy developed for narrowband scenarios, and significant gains over the random allocation policy. Finally, the obtained results show the benefits of the user grouping strategies for wideband scenarios, which allows serving a number of streams per subcarrier larger than the number of available RF chains.

Chapter VI

Intelligent Reflecting Surfaces for Wideband Multiuser mmWave MIMO Systems

Conventional wireless communication systems consist of a transmitter sending information to a receiver via an uncontrollable propagation environment. By considering the growing interest on accomplishing real-time reconfigurable propagation environments for B5G technologies and future wireless communication systems, the IRSs constitute a promising candidate [130]–[133]. An IRS is a real-time reconfigurable reflectarray deployed to smartly reconfigure the wireless propagation environment through the use of massive low-cost passive elements.

The idea of controlling the environment in mmWave and Terahertz (THz) setups has been introduced in [17], [130], [134] by employing software-controlled metamaterials. Although this idea of passive reflecting surfaces has been employed for a number of applications in radar systems, remote sensing, and satellite communications, they were not considered for mobile communication because the traditional reflecting surfaces with fixed PSs were unable to cope with the dynamic wireless channels due to user mobility. Nowadays, the advances in metamaterials (e.g., metasurfaces) represent a certain guarantee for the reconfigurability of reflecting surfaces by enabling the real-time adjustment of the surface PSs [135], [136].

There are some overview papers about IRSs in the literature. In [133], the authors present a survey of the use of IRSs for smart environments. Therein, the main applications, the advantages over existing technologies, the hardware architecture and the signal model for IRS-aided systems are considered. In [137], a short review is provided with the aim of covering IRS implementations, future research directions for IRSs and their role in B5G communications. In [138], the authors emphasize on the potential applications of ML to IRS challenges. In contrast, the authors in [12] mainly focus on the key issues of the design and implementation of IRS-assisted communication systems. In [38], we have presented a comprehensive overview including the theoretical basis of the IRSs, their most recent applications and an up-to-date

review of the papers related to the IRS technology. This analysis includes the performance metrics employed for the system design, their main results, and contributions, as well as the different considered setups (see [38, Tables 1-6]).

In this chapter, we briefly describe some preliminary concepts of the IRS technology and then focus on an unexplored use case of IRS-aided system design. The remainder of this chapter is structured as follows. Section 6.1 introduces the chapter. The main elements about the theory and the design of the IRS technology are described in Section 6.2. A wideband MU multi-stream mmWave MIMO system model under imperfect CSI is described in Section 6.3. A MMSE approach for the design of the frequency-flat IRS phase-shift matrix, the wideband precoders and user filters is explained in Section 6.5, where an alternating minimization algorithm is described to exploit the statistical of the estimation error. We present simulation results and comparisons in Section 6.6 and finally, the Section 6.7 is devoted to the conclusions of the chapter.

6.1 Introduction

Some use cases for IRS-aided wireless communication systems have already been considered in the literature. In [15], a single-user SISO system with a direct channel available between both communication ends is considered. In this specific case, the optimal IRS phase-shift matrix is the one that aligns the reflected rays to the direct path between the transmitter and the receiver. However, this solution is not applicable to MU MIMO systems where a common IRS response must be designed for all users.

In [34], the rank improvement of a downlink IRS-aided MIMO system is exploited to obtain capacity gains in a single-user scenario. The authors in [35] have studied the asymptotic achievable rate of a downlink MU IRS-aided MISO system. The setup considers a scheme with multiple IRSs where some users are supported by the IRSs and others directly communicate to the BS. The authors propose a modulation scheme suitable for a downlink IRS-aided system which provides achievable sum-rate values larger than those obtained in non-IRS-aided schemes. In [33], a MU IRS-aided NOMA MISO downlink system—which enables the communication over both the IRS-aided and the direct channel between each user and the BS—is addressed. The approach considers the joint optimization of the BS precoders and the IRS phase-shift matrix to minimize the total transmission power. The authors in [32] consider a MU MISO IRS-aided system with an on/off modulation at the reflecting elements.

Still, the interest in IRS-aided wireless communication systems is recent and some use cases remain unexplored. For instance, none of the works in [15], [32]–[35] consider MU MIMO setups. They do not consider wideband either, a relevant feature when considering IRS technology for mmWave communications. In this case, the design of the IRS-aided wireless systems is significantly more challenging because it is necessary to consider the frequency-flat nature of the IRS phase shift matrix and wideband communication effects. Regarding CSI,

most works consider perfect knowledge of the channel responses, disregarding the errors in the channel estimations. Only limited works address this effect and propose more robust IRS-aided systems. An example is the work in [139], where the authors considered an MMSE-optimal beamforming in a narrowband single-user MISO system. Another attempt to implement robust design algorithms for IRS-aided systems is the work in [140], where a narrowband MU MISO IRS-aided system under imperfect CSI is approached. However, in this work, the cascaded channel is estimated in two steps, i.e., the BS-IRS channel and the IRS-user channels are independently estimated. This is difficult to achieve since active elements should be installed at the IRS.

In this chapter, we consider that CSI is imperfect in the wideband MU MIMO IRS-aided system. This makes a difference with respect to the previous works on IRS-aided systems [15], [32]–[35], where the authors assume perfect knowledge of the CSI at both ends and works like [139] and [140], where simpler scenarios (narrowband single-user MISO and narrowband MU MISO, respectively) are considered.

We consider a more general scenario than [15], [32]–[35], namely a wideband MU IRS-aided mmWave MIMO system under imperfect CSI. We address the joint optimization of the precoders and the filters for all the subcarriers and the IRS phase-shift matrix, which is assumed to be frequency flat, assuming imperfect CSI at the receivers and the transmitter. To this end, we develop an alternating PG approach that minimizes the MSE between the transmitted and estimated symbols by exploiting the BC-MAC duality. In particular, the main contributions of this chapter are the following:

- The joint design of the frequency-dependent precoders/filters and the frequency-flat IRS phase-shift matrix in the downlink of a wideband MU multi-stream IRS-aided mmWave MIMO system by means of the BC-MAC duality is performed.
- The development of an alternating PG minimization method to design the wideband precoders/filters and the frequency-flat IRS phase-shift matrix in imperfect CSI setups.

6.2 Theory and Design of IRSs

In this section, we provide some details about the theory and the practical implementation of IRSs. The hardware implementation of the IRSs is based on the concept of metasurface, i.e., a controllable two-dimensional metamaterial [135], [141]. The metasurface consists of a planar array with a large number of meta-atoms with a sub-wavelength electrical thickness, which is designed according to the operating frequency. The meta-atoms are metals or dielectrics able to transform the impinging electromagnetic waves. The properties of these elements and the structural arrangement in the array determine the transformations on the incident waves. The physical structure of the metasurface defines the electromagnetic properties and thus the behavior at the specific frequency [142], [143]. The tunable chips inserted in the metasurface to interact with the scattering element and communicate with an IRS controller are implemented

through positive-intrinsic negative (PIN) diodes [144], [145], ferro-electric devices, or varactor diodes [146]–[148]. A typical architecture of IRSs is shown in Figure 6.1. This consists of three layers and a smart controller. In the outer layer, a large number of metallic patches (meta-atoms) are printed on a dielectric substrate to directly interact with the impinging signals (see Figure 6.2(a)). Behind this layer, a copper plate is used to avoid the signal energy leakage. Finally, a control circuit board is also deployed for adjusting the phase shift of each element, triggered by a smart controller attached to the IRS [12].

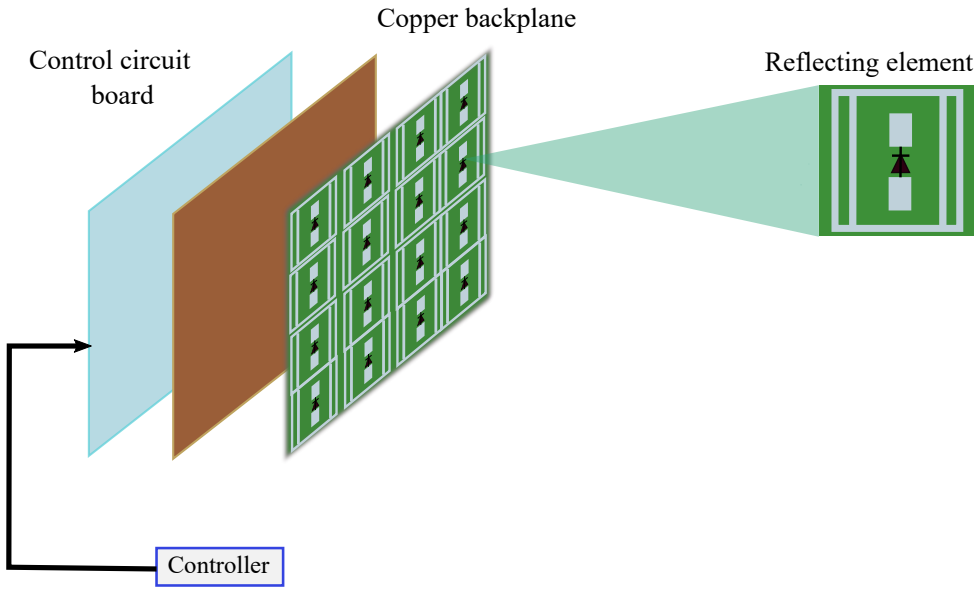

Figure 6.1: IRS architecture.

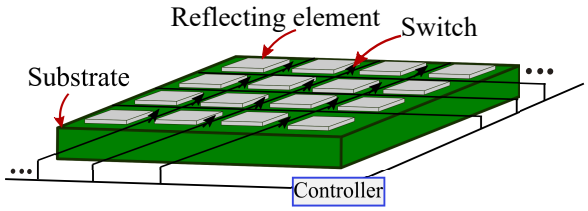

(a) Metasurface composed by an array of passive reflecting elements.

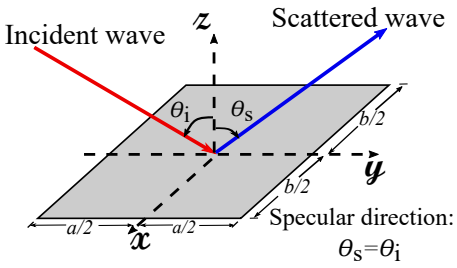

(b) The scattered wave by the $a \times b$ metal plate is strongest for the specular direction, i.e., $\theta_i = \theta_s$.

Figure 6.2: Elements of a metasurface.

Generally, the approaches in the literature related to the design of metasurfaces are based on Snell's law [149]. The strongest scattered signal is obtained in the specular direction, i.e., being θ_i the angle of the incident wave, the strongest reflected signal is obtained for an angular direction θ_s, such that $\theta_s = \theta_i$ (as shown in Figure 6.2(b)). There are a few papers that focus on the theoretical basis, physics and classification of the metasurfaces [150], [151]. In [150], the authors discuss the theoretical basis to characterize metasurfaces and comment on

their application as well as how metasurfaces are distinguished from conventional frequency-selective surfaces. In [151], the physical properties and future applications of the metasurfaces are analyzed.

6.2.1 IRS Controller

The IRS controller is devoted to receiving and communicating the reconfiguration requests, and then distributing the phase shift decisions to all the tunable IRS elements. This controller might be implemented by employing a field programmable gate array (FPGA) [144], [152], a direct current source [153], or a microcontroller [147], [154]. In [155], a metasurface composed of reconfigurable metamaterial strips arranged in a grid has been designed. Specifically, a set of four metamaterial strips is configured via a controller switch. The work in [156] also considers a reduced number of controller chips to serve the full IRS array.

6.3 System Model

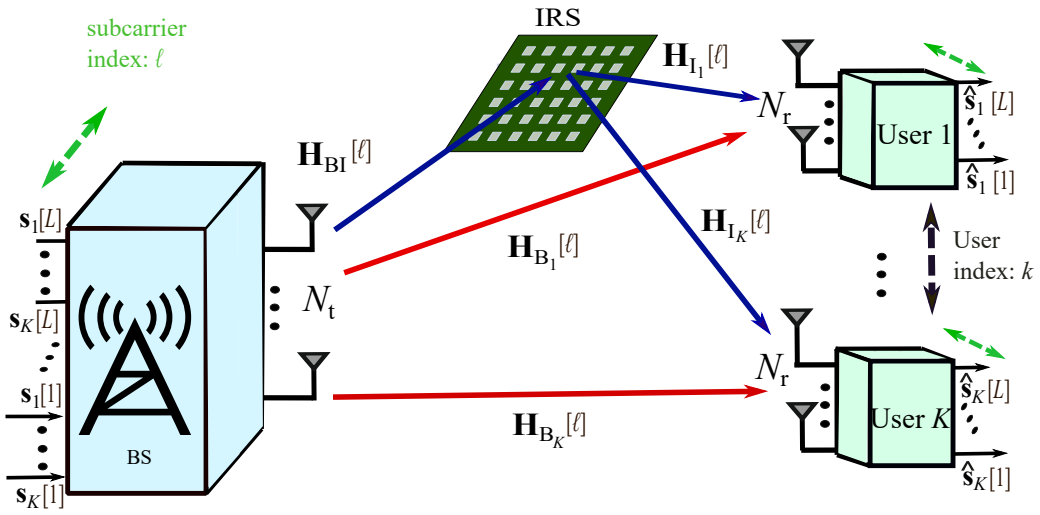

Figure 6.3: Block diagram of the wideband multi-stream IRS-aided mmWave MIMO BC system.

In this chapter, we consider the downlink of a wideband MU mmWave MIMO system shown in Figure 6.3, where a common BS with N_t antennas communicates with K users with N_r antennas each. The BS sends wideband OFDM symbols to fully exploit the large bandwidths available in mmWave. The wireless channels between the BS and the users are assumed to be frequency selective. The OFDM modulation is considered, together with a cyclic prefix long enough to avoid ISI. This way, the frequency selective channels are decomposed into L parallel narrowband subchannels, each experiencing a different channel response.

We also consider multi-stream transmissions such that the BS allocates $N_{\mathrm{s},k}[\ell]$ streams at subcarrier $\ell = 1, \ldots, L$ to be transmitted to user $k = 1, \ldots, K$. Thus, the total number

of streams allocated at subcarrier ℓ is $N_{\mathrm{s}}[\ell] = \sum_{k=1}^{K} N_{\mathrm{s},k}[\ell]$. The vector of $N_{\mathrm{s},k}[\ell]$ symbols transmitted by the BS to the k-th user at subcarrier ℓ is $\mathbf{s}_k[\ell] = \left[s_{k_1}[\ell], s_{k_2}[\ell], \ldots, s_{k_{N_{\mathrm{s},k}[\ell]}}[\ell]\right]^T$. The total number of allocated data streams, by considering the K users and the L subcarriers, is $N_{\mathrm{s}} = \sum_{\ell=1}^{L} N_{\mathrm{s}}[\ell]$. We assume there is no total blockage between the BS and the users, i.e., there is a direct channel between the BS and the k-th user whose response at subcarrier ℓ is $\mathbf{H}_{\mathrm{B}_k}[\ell] \in \mathbb{C}^{N_{\mathrm{r}} \times N_{\mathrm{t}}}$.

In addition, an IRS is deployed to assist the communication, which conforms an additional cascaded BS-IRS-User link. The channel responses at subcarrier ℓ from the IRS to the k-th user and from the BS to the IRS will be termed $\mathbf{H}_{\mathrm{I}_k}[\ell] \in \mathbb{C}^{N_{\mathrm{r}} \times N}$ and $\mathbf{H}_{\mathrm{BI}}[\ell] \in \mathbb{C}^{N \times N_{\mathrm{t}}}$, respectively. The deployed IRS is assumed to have N passive elements. Thus, the IRS phase-shift matrix is represented by a diagonal matrix $\mathbf{\Theta} = \mathrm{diag}(\boldsymbol{\nu}) \in \mathcal{D}$, where $\boldsymbol{\nu} = [\nu_1, \ldots, \nu_N]^T = \left[e^{j\theta_1}, \ldots, e^{j\theta_N}\right]^T$ and $\theta_n \in [0, 2\pi)$ represents the phase shift introduced by the n-th IRS element. $\mathcal{D} \in \mathbb{C}^{N \times N}$ is the set of feasible IRS matrices, i.e., the set of diagonal matrices with unit magnitude entries. The cascaded BS-IRS-user channel response at subcarrier ℓ is given by $\mathbf{H}_{\mathrm{c}_k}[\ell] = \mathbf{H}_{\mathrm{I}_k}[\ell]\mathbf{\Theta}\mathbf{H}_{\mathrm{BI}}[\ell] = \sum_{n=1}^{N} \nu_n \left[\mathbf{H}_{\mathrm{I}_k}\right]_{:,n}[\ell] \left[\mathbf{H}_{\mathrm{BI}}\right]_{n,:}[\ell]$. We highlight that the frequency response of the IRS is nominally flat and thus common to all the subcarriers and users. As explained later, this circumstance significantly complicates the design of the IRS-aided communication system.

The BS employs the linear precoder $\mathbf{P}_k[\ell] \in \mathbb{C}^{N_{\mathrm{t}} \times N_{\mathrm{s},k}[\ell]}$ to communicate with the k-th user at subcarrier ℓ. These precoders are subject to a per-subcarrier transmission power constraint, as in [30], [37], i.e., $\sum_{k=1}^{K} \mathrm{tr}(\mathbf{P}_k[\ell]\mathbf{P}_k^*[\ell]) \leq P_{\mathrm{T}}[\ell]$, being $P_{\mathrm{T}}[\ell]$ the available transmission power at subcarrier ℓ such that $P_{\mathrm{T}}[\ell] = \frac{P_{\mathrm{T}}}{L}$, where P_{T} is the total power available at transmission.

According to this system model, the signal received by the k-th user at subcarrier ℓ reads as

$$\mathbf{y}_k[\ell] = \left(\underbrace{\mathbf{H}_{\mathrm{B}_k}[\ell]}_{\text{Direct link}} + \underbrace{\mathbf{H}_{\mathrm{I}_k}[\ell]\mathbf{\Theta}\mathbf{H}_{\mathrm{BI}}[\ell]}_{\text{IRS-aided link}} \right) \sum_{u=1}^{K} \mathbf{P}_u[\ell]\mathbf{s}_u[\ell] + \boldsymbol{\eta}_k[\ell], \tag{6.1}$$

where $\boldsymbol{\eta}_k[\ell] = \left[\eta_{k_1}[\ell], \eta_{k_2}[\ell], \ldots, \eta_{k_{N_{\mathrm{r}}}}[\ell]\right]^T$ represents the complex-valued AWGN modeled as $\boldsymbol{\eta} \sim \mathcal{N}_{\mathbb{C}}(0, \mathbf{C}_{\eta_k})$ with $\mathbf{C}_{\eta_k} = \sigma_{\eta k}^2 \mathbf{I}_{N_{\mathrm{r}}}$. Finally, the equivalent channel response corresponding to the k-th user at subcarrier ℓ is defined as

$$\mathbf{H}_{\mathrm{e}_k}[\ell] = \mathbf{H}_{\mathrm{B}_k}[\ell] + \mathbf{H}_{\mathrm{I}_k}[\ell]\mathbf{\Theta}\mathbf{H}_{\mathrm{BI}}[\ell] = \mathbf{H}_{\mathrm{B}_k}[\ell] + \sum_{n=1}^{N} \nu_n \left[\mathbf{H}_{\mathrm{I}_k}\right]_{:,n}[\ell] \left[\mathbf{H}_{\mathrm{BI}}\right]_{n,:}[\ell], \tag{6.2}$$

where $n = 1, \ldots, N$ stands for the index of each channel path modified by the IRS by introducing the phase shift corresponding to the element ν_n. At reception, the user k estimates its symbols $\hat{\mathbf{s}}_k[\ell]$ at subcarrier ℓ by applying the linear filter $\mathbf{W}_k[\ell] \in \mathbb{C}^{N_{\mathrm{s},k}[\ell] \times N_{\mathrm{r}}}$, that is, $\hat{\mathbf{s}}_k[\ell] = \mathbf{W}_k[\ell]\mathbf{y}_k[\ell]$.

6.3.1 Channel Estimation

To carry out channel estimation, pilot symbols without precoding are transmitted by the BS during N_{p} channel uses. The matrix $\mathbf{X}_k[\ell] \in \mathbb{C}^{N_{\mathrm{t}} \times N_{\mathrm{p}}}$ stacks all the pilots transmitted to estimate the channel response for the k-th user at subcarrier ℓ. Each column vector in $\mathbf{X}_k[\ell]$ represents the pilots transmitted in a channel use. The symbols received by user k at subcarrier ℓ when transmitting the pilots are stacked in the matrix $\mathbf{Y}'_k[\ell] \in \mathbb{C}^{N_{\mathrm{r}} \times N_{\mathrm{p}}}$, which is given by

$$\mathbf{Y}'_k[\ell] = \left(\underbrace{\mathbf{H}_{\mathrm{B}_k}[\ell]}_{\text{Direct link}} + \underbrace{\mathbf{H}_{\mathrm{I}_k}[\ell] \boldsymbol{\Theta} \mathbf{H}_{\mathrm{BI}}[\ell]}_{\text{IRS-aided link}} \right) \sum_{u=1}^{K} \mathbf{X}_u[\ell] + \mathbf{N}'_k[\ell]. \tag{6.3}$$

Vectorizing $\mathbf{Y}'_k[\ell]$ given by (6.3) we get (cf. [157, Theorem 3.13])

$$\mathbf{y}'_k[\ell] = \left(\sum_{u=1}^{K} \mathbf{X}_u^*[\ell] \otimes \mathbf{I}_{N_{\mathrm{r}}} \right) \mathbf{H}_k[\ell] \boldsymbol{\nu}' + \boldsymbol{\eta}'_k[\ell], \tag{6.4}$$

where

$$\boldsymbol{\nu}' = \left[1, \boldsymbol{\nu}^T\right]^T \in \mathbb{C}^{N+1},$$
$$\mathbf{H}_k[\ell] = \left[\mathbf{h}_{\mathrm{B}_k}[\ell], \mathbf{H}_{\mathrm{IB}}^T[\ell] \circledast \mathbf{H}_{\mathrm{I}_k}[\ell]\right] \in \mathbb{C}^{N_{\mathrm{r}} N_{\mathrm{t}} \times N+1}$$

stacks both the vectorized versions of the direct channel ($\mathbf{h}_{\mathrm{B}_k}[\ell]$) and the cascaded channel, and $\boldsymbol{\eta}'_k \sim \mathcal{N}_{\mathbb{C}}\left(0, \mathbf{I}_{N_{\mathrm{t}}} \otimes \mathbf{C}_{\eta_k}\right)$. Assuming N_ν different phase allocations during the estimation process to modify the paths of the whole channel, we have [158]

$$\mathbf{V} = \left[\boldsymbol{\nu}'_1, \ldots, \boldsymbol{\nu}'_{N_\nu}\right] \in \mathbb{C}^{N+1 \times N_\nu}. \tag{6.5}$$

We next assume that the same pilot matrix $\mathbf{X}_u^*[\ell]$ is transmitted over the N_ν different phase allocations and that the corresponding received symbols are stacked in the following matrix

$$\mathbf{Y}_k[\ell] = \left(\sum_{u=1}^{K} \mathbf{X}_u^*[\ell] \otimes \mathbf{I} \right) \mathbf{H}_k[\ell] \mathbf{V} + \mathbf{N}_k[\ell] \in \mathbb{C}^{N_{\mathrm{r}} N_{\mathrm{p}} \times N_\nu}. \tag{6.6}$$

Note now that the channel response $\mathbf{H}_k[\ell]$ for the k-th user can be estimated following a LS approach. Indeed, following [158], the LS estimation of the channel response is given by

$$\hat{\mathbf{H}}_{\mathrm{LS}_k}[\ell] = \left(\sum_{u=1}^{K} \mathbf{X}_u^*[\ell] \otimes \mathbf{I} \right)^{\dagger} \mathbf{Y}_k[\ell] \mathbf{V}^{\dagger} \in \mathbb{C}^{N_{\mathrm{r}} N_{\mathrm{t}} \times N+1}, \tag{6.7}$$

and the LS estimation error is given by the following matrix

$$\mathbf{N}_{\mathrm{LS}_k}[\ell] = \left(\sum_{u=1}^{K} \mathbf{X}_u^*[\ell] \otimes \mathbf{I} \right)^{\dagger} \mathbf{N}[\ell] \mathbf{V}^* \in \mathbb{C}^{N_{\mathrm{r}} N_{\mathrm{t}} \times N+1}, \tag{6.8}$$

whose column vectors have the distribution $[\mathbf{N}_{\mathrm{LS}_k}]_{:,i}[\ell] \sim \mathcal{N}_{\mathbb{C}}\left(0, \mathbf{C}_{\mathrm{LS}_k}\right)$ with the following covariance matrix

$$\mathbf{C}_{\mathrm{LS}_k} = \Big(\left(\mathbf{X}_k[\ell] \mathbf{X}_k^*[\ell]\right)^{-1} \otimes \mathbf{C}_{\eta_k} \Big) \mathrm{tr}\Big(\left(\mathbf{V}^* \mathbf{V}\right)^{-1} \Big) \mathbb{C}^{N_{\mathrm{r}} N_{\mathrm{t}} \times N_{\mathrm{r}} N_{\mathrm{t}}}. \tag{6.9}$$

where $\mathbf{C}_{\eta_k} \in \mathbb{C}^{N_\mathrm{r} \times N_\mathrm{r}}$ is the receiving noise covariance matrix. Assuming the training sequence is unitary, the LS estimation error covariance matrix $\mathbf{C}_{\mathrm{LS}_k}[\ell]$ is simplified such that $[\mathbf{N}_{\mathrm{LS}_k}]_{:,i}[\ell] \sim \mathcal{N}_{\mathbb{C}}(0, \mathbf{I}_{N_\mathrm{t}} \otimes \mathbf{C}_{\eta_k})$.

By considering the analysis in Subsection 6.3.1, the channel uncertainty can be modeled as a statistical error. Therefore, channel realizations in the downlink can be decomposed as follows

$$\mathbf{H}_{\mathrm{B}_k}[\ell] = \hat{\mathbf{H}}_{\mathrm{B}_k}[\ell] + \mathbf{E}_{\mathrm{B}_k}[\ell]$$

for the direct channels and

$$\mathbf{H}_{\mathrm{I}_k}[\ell]\boldsymbol{\Theta}\mathbf{H}_{\mathrm{BI}}[\ell] = \sum_{n=1}^{N} \nu_n \left(\hat{\mathbf{H}}_{\mathrm{com}_{kn}}[\ell] + \mathbf{E}_{\mathrm{c}_{kn}}[\ell] \right),$$

for the cascaded channels such that

$$\hat{\mathbf{H}}_{\mathrm{com}_{kn}}[\ell] = \widehat{[\mathbf{H}_{\mathrm{I}_k}]_{:,n}[\ell]\,[\mathbf{H}_{\mathrm{BI}}]_{n,:}[\ell]}, \forall n = 1, \ldots, N.$$

Here $\mathbf{H}_{\mathrm{I}_k}[\ell]$, $\mathbf{H}_{\mathrm{BI}}[\ell]$ and $\mathbf{H}_{\mathrm{B}_k}[\ell]$ are the true channels at subcarrier ℓ of user k whereas $\hat{\mathbf{H}}_{\mathrm{com}_k}[\ell]$, and $\hat{\mathbf{H}}_{\mathrm{B}_k}[\ell]$ stand for the estimated channels at subcarrier ℓ of user k.

Recall that the estimations of the channels $\mathbf{H}_{\mathrm{I}_k}[\ell]$ and $\mathbf{H}_{\mathrm{BI}}[\ell]$ are performed jointly due to the passive nature of the IRS. The entries of $\mathbf{E}_{\mathrm{B}_k}[\ell]$ and $\mathbf{E}_{\mathrm{c}_{kn}}[\ell]$ are the estimation errors of the direct and cascaded channels, respectively. Such errors are zero-mean Gaussian distributed with a covariance matrix $\mathbb{E}\left[\mathbf{e}_{\mathrm{B}_k}[\ell]\mathbf{e}^*_{\mathrm{B}_k}[\ell]\right] = \mathbf{I}_{N_\mathrm{t}} \otimes \mathbf{C}_{\eta_k}, \forall \ell$ and $\mathbb{E}\left[\mathbf{e}_{\mathrm{c}_{kn}}[\ell]\mathbf{e}^*_{\mathrm{c}_{kn}}[\ell]\right] = \mathbf{I}_{N_\mathrm{t}} \otimes \mathbf{C}_{\eta_k}, \forall \ell, n$, respectively, where $\mathbf{e}_{\mathrm{B}_k}[\ell]$ and $\mathbf{e}_{\mathrm{c}_{kn}}[\ell]$ are the vectorized versions of $\mathbf{E}_{\mathrm{B}_k}[\ell], \forall\ k, \ell$ and $\mathbf{E}_{\mathrm{c}_{kn}}[\ell], \forall\ k, n, \ell$, respectively. They correspond to the first and the n-th column of $\mathbf{N}_{\mathrm{LS}_k}[\ell]$, respectively. Note that a similar approach can be followed for the dual uplink and we can define a dual covariance error matrix $\mathbf{C}'_{\mathrm{n}k} \in \mathbb{C}^{N_\mathrm{t} \times N_\mathrm{t}}$ for the estimation performed in the dual uplink [159]. According to this error model, the next equivalence can be stated

$$\mathbf{H}_{\mathrm{e}_k}[\ell] = \hat{\mathbf{H}}_{\mathrm{e}_k}[\ell] + \mathbf{E}_{\mathrm{B}_{kn}}[\ell] + \sum_{n=1}^{N} \nu_n \mathbf{E}_{\mathrm{c}_{kn}}[\ell], \tag{6.10}$$

where

$$\hat{\mathbf{H}}_{\mathrm{e}_k}[\ell] = \hat{\mathbf{H}}_{\mathrm{B}_k}[\ell] + \sum_{n=1}^{N} \nu_n \hat{\mathbf{H}}_{\mathrm{com}_{kn}}[\ell] = \hat{\mathbf{H}}_{\mathrm{B}_k}[\ell] + (\boldsymbol{\nu} \otimes \mathbf{I}_{N\mathrm{r}})^T \hat{\mathbf{H}}_{\mathrm{com}_k}[\ell], \tag{6.11}$$

with $\hat{\mathbf{H}}_{\mathrm{com}_k} = \left[\hat{\mathbf{H}}^T_{\mathrm{com}_{k_1}}, \ldots, \hat{\mathbf{H}}^T_{\mathrm{com}_{k_N}}\right]^T$. Note that considering the channel estimation errors, the received symbols given by (6.1) can be expressed as follows

$$\mathbf{y}_k[\ell] = \left(\hat{\mathbf{H}}_{\mathrm{e}_k}[\ell] + \mathbf{E}_{\mathrm{B}_{kn}}[\ell] + \sum_{n=1}^{N} \nu_n \mathbf{E}_{\mathrm{c}_{kn}}[\ell] \right) \sum_{u=1}^{K} \mathbf{P}_u[\ell]\mathbf{s}_u[\ell] + \boldsymbol{\eta}_k[\ell]. \tag{6.12}$$

At reception, the user k estimates its symbols $\hat{\mathbf{s}}_k[\ell]$ at subcarrier ℓ by applying the linear filter $\mathbf{W}_k[\ell] \in \mathbb{C}^{N_{\mathrm{s},k}[\ell] \times N_\mathrm{r}}$, that is, $\hat{\mathbf{s}}_k[\ell] = \mathbf{W}_k[\ell]\mathbf{y}_k[\ell]$.

Table 6.1 summarizes the main system model parameters and variables considered in this downlink wideband MU multi-stream IRS-aided mmWave MIMO system. We model the wideband mmWave channels by following the expression (2.32) in Subsection 2.5.1.

Table 6.1: BC system model parameters.

Description	Parameter
Number of antennas at the BS	N_{t}
Number of users	K
Number of antennas per users	N_{r}
Number of subcarriers	L
Number of streams per user at subcarrier ℓ	$N_{\mathrm{s},k}[\ell]$
Vector of the $N_{\mathrm{s},k}[\ell]$ symbols at subcarrier ℓ	$\mathbf{s}_k[\ell]$
Precoder: k-th BS precoder at subcarrier ℓ	$\mathbf{P}_k[\ell]$
Power available at subcarrier ℓ	$P_{\mathrm{T}}[\ell]$
BS-User direct channel: k-th user at subcarrier ℓ	$\mathbf{H}_{\mathrm{B}k}[\ell]$
BS-IRS channel subcarrier ℓ	$\mathbf{H}_{\mathrm{BI}}[\ell]$
IRS-User channel: k-th user at subcarrier ℓ	$\mathbf{H}_{\mathrm{I}_k}[\ell]$
Frequency-flat IRS phase shift matrix	$\boldsymbol{\Theta}$
Main diagonal of IRS phase shift matrix	$\boldsymbol{\nu}$
Vector of AWGN at the k-th user at subcarrier ℓ	$\boldsymbol{\eta}_k[\ell]$
Filter: k-th user filter at subcarrier ℓ	$\mathbf{W}_k[\ell]$
Vector of the $N_{\mathrm{s},k}[\ell]$ estimated symbols at subcarrier ℓ	$\hat{\mathbf{s}}_k[\ell]$
Number of streams at subcarrier ℓ	$N_{\mathrm{s}}[\ell]$
Total number of data streams	N_{s}
Covariance matrices of the errors in the downlink	$\mathbf{C}_{\mathrm{n}k}$

6.4 Determination of the IRS Phase-Shift Matrix, the Precoders, and the Filters

Considering the described scenario and the corresponding channel model, we aim at determining the precoders $\mathbf{P}_k[\ell], \forall k, \ell$, the receiving linear filters $\mathbf{W}_k[\ell], \forall k, \ell$ and the IRS phase shift matrix $\boldsymbol{\Theta}$ such that the achievable sum rate, given by

$$R_{\text{sum}} = \frac{1}{L}\sum_{k=1}^{K}\sum_{\ell=1}^{L}\log_2\left|\left(\mathbf{I}_{N_{\mathrm{s},k}[\ell]} + \mathbf{X}_k^{-1}[\ell]\mathbf{W}_k[\ell]\mathbf{H}_{\mathrm{e}_k}[\ell]\mathbf{P}_k[\ell]\mathbf{P}_k^*[\ell]\mathbf{H}_{\mathrm{e}_k}^*[\ell]\mathbf{W}_k^*[\ell]\right)\right|, \tag{6.13}$$

with

$$\mathbf{X}_k[\ell] = \sum_{i\neq k}\mathbf{W}_k[\ell]\mathbf{H}_{\mathrm{e}_k}\mathbf{P}_i[\ell]\mathbf{P}_i^*[\ell]\mathbf{H}_{\mathrm{e}_k}^*[\ell]\mathbf{W}_k^*[\ell] + \sigma_{\eta_k}^2\mathbf{W}_k[\ell]\mathbf{W}_k^*[\ell] \tag{6.14}$$

and

$$\mathbf{H}_{\mathrm{e}_k}[\ell] = \mathbf{H}_{\mathrm{B}_k}[\ell] + \mathbf{H}_{\mathrm{I}_k}[\ell]\boldsymbol{\Theta}\mathbf{H}_{\mathrm{BI}}[\ell], \tag{6.15}$$

is maximized while fulfilling the overall power constraint (P_{T}). Note that $\mathbf{H}_{\mathrm{e}_k}[\ell]$ represents the equivalent BS-IRS-User channel for the k-th user at subcarrier ℓ. Therefore, we can state the

following optimization problem

$$\begin{aligned} &\underset{\boldsymbol{\Theta},\mathbf{P}_k[\ell],\mathbf{W}_k[\ell],\forall k,\ell}{\arg\ \max} \quad R_{\text{sum}} \\ &\text{s.t.} \sum_{k=1}^{K} \text{tr}\Big(\mathbf{P}_k[\ell]\mathbf{P}_k^*[\ell]\Big) \leq P_{\text{T}}[\ell], \forall \ell,\ \boldsymbol{\Theta} \in \mathcal{D}. \end{aligned} \tag{6.16}$$

The solution of (6.16) is computationally intractable mainly because of the non-convexity nature of the cost function and the non-convex constraints on the IRS matrix, i.e., unit magnitude for each element in the main diagonal entries. Furthermore, the IRS phase shift matrix is common to all the users and subcarriers, which makes the solution of (6.16) even more difficult, since the common IRS must be designed to simultaneously modify all the user channels at the L subcarriers.

6.5 MMSE Approach

In order to maximize the achievable sum-rate given by (6.13), we reformulate the optimization problem in (6.16) as a MSE minimization problem since minimizing the system sum-MSE maximizes a lower bound of the system capacity [160].

6.5.1 BC-MAC and MAC-BC Dualities for Wideband IRS-Aided Systems

We elaborate the signal model for the symbols corresponding to the k-th user and ℓ-th subcarrier after the linear filtering at reception, i.e.,

$$\hat{\mathbf{s}}_k[\ell] = \mathbf{W}_k[\ell] \left(\hat{\mathbf{H}}_{\text{e}_k}[\ell] + \mathbf{E}_{\text{B}_{kn}}[\ell] + \sum_{n=1}^{N} \nu_n \mathbf{E}_{\text{c}_{kn}}[\ell] \right) \sum_{u=1}^{K} \mathbf{P}_u[\ell]\mathbf{s}_u[\ell] + \mathbf{W}_k[\ell]\boldsymbol{\eta}_k[\ell]. \tag{6.17}$$

The downlink MSE for the k-th user at subcarrier ℓ is

$$\begin{aligned} &\text{MSE}_k^{\text{DL}}[\ell] = \mathbb{E}\left[\|\mathbf{s}_k[\ell] - \hat{\mathbf{s}}_k[\ell]\|_2^2\right] = \mathbb{E}\Big[\text{tr}\Big(\left(\mathbf{s}_k[\ell] - \hat{\mathbf{s}}_k[\ell]\right) \left(\mathbf{s}_k[\ell] - \hat{\mathbf{s}}_k[\ell]\right)^* \Big)\Big] \\ &= \text{tr}\Bigg(\mathbf{W}_k[\ell] \Bigg\{ \hat{\mathbf{H}}_{\text{e}_k}[\ell] \left[\sum_{i=1}^{K} \mathbf{P}_i[\ell]\mathbf{P}_i^*[\ell] \right] \hat{\mathbf{H}}_{\text{e}_k}^*[\ell] + \sigma_{\eta_k}^2 \mathbf{I}_{N_{\text{r}}} \Bigg\} \mathbf{W}_k^*[\ell] \\ &+ \mathbb{E}\left[\mathbf{W}_k[\ell] \Bigg\{ \mathbf{E}_{\text{B}_k}[\ell] \left[\sum_{i=1}^{K} \mathbf{P}_i[\ell]\mathbf{P}_i^*[\ell] \right] \mathbf{E}_{\text{B}_k}^*[\ell] \Bigg\} \mathbf{W}_k^*[\ell] \right] \\ &+ \mathbb{E}\left[\mathbf{W}_k[\ell] \Bigg\{ \sum_{n=1}^{N} \mathbf{E}_{\text{c}_{kn}}[\ell]\nu_n \left[\sum_{i=1}^{K} \mathbf{P}_i[\ell]\mathbf{P}_i^*[\ell] \right] \sum_{l'=1}^{N} \mathbf{E}_{\text{c}_{kn'}}^*[\ell]\nu_{n'}^* \Bigg\} \mathbf{W}_k^*[\ell] \right] \\ &- \mathbf{W}_k[\ell]\hat{\mathbf{H}}_{\text{e}_k}[\ell]\mathbf{P}_k[\ell] - \mathbf{P}_k^*[\ell]\hat{\mathbf{H}}_{\text{e}_k}^*[\ell]\mathbf{W}_k^*[\ell] + \mathbf{I}_{N_{\text{s},k}}[\ell] \Bigg). \end{aligned} \tag{6.18}$$

This expression for the downlink MSE in terms of the precoders $\mathbf{P}_k[\ell]$, the filters $\mathbf{W}_k[\ell]$ the estimated channels $\hat{\mathbf{H}}^*_{\mathrm{e}_k}[\ell]$ and the errors $\mathbf{E}_{\mathrm{B}_k}[\ell]$, $\mathbf{E}_{\mathrm{c}_k n}[\ell], \forall n, k$ can be rewritten as follows

$$\begin{aligned}\mathrm{MSE}_k^{\mathrm{DL}}[\ell] &= \mathrm{tr}\left(\mathbf{W}_k[\ell]\left\{\hat{\mathbf{H}}_{\mathrm{e}_k}[\ell]\left[\sum_{i=1}^{K}\mathbf{P}_i[\ell]\mathbf{P}_i^*[\ell]\right]\hat{\mathbf{H}}^*_{\mathrm{e}_k}[\ell] + \sigma^2_{\eta_k}\mathbf{I}_{N_{\mathrm{r}}}\right\}\mathbf{W}_k^*[\ell]\right)\\ &+ \mathrm{tr}\left(\sum_{i=1}^{K}\mathbf{P}_i[\ell]\mathbf{P}_i^*[\ell]\right)\mathrm{tr}\left(\mathbf{W}_k[\ell]\mathbf{C}_{\mathrm{n}k}\mathbf{W}_k^*[\ell]\right) + \boldsymbol{\nu}^*\mathrm{tr}\left(\sum_{i=1}^{K}\mathbf{P}_i[\ell]\mathbf{P}_i^*[\ell]\right)\mathrm{tr}\left(\mathbf{W}_k[\ell]\mathbf{C}_{\mathrm{n}k}\mathbf{W}_k^*[\ell]\right)\boldsymbol{\nu}\\ &- \mathrm{tr}\left(\mathbf{W}_k[\ell]\hat{\mathbf{H}}_{\mathrm{e}_k}[\ell]\mathbf{P}_k[\ell] - \mathbf{P}_k^*[\ell]\hat{\mathbf{H}}^*_{\mathrm{e}_k}[\ell]\mathbf{W}_k^*[\ell] + \mathbf{I}_{N_{\mathrm{s},k}}[\ell]\right).\end{aligned} \tag{6.19}$$

Note that

$$\begin{aligned}&\mathbb{E}\left[\mathrm{tr}\left(\mathbf{W}_k[\ell]\left\{\mathbf{E}_{\mathrm{B}_k}[\ell]\left[\sum_{i=1}^{K}\mathbf{P}_i[\ell]\mathbf{P}_i^*[\ell]\right]\mathbf{E}^*_{\mathrm{B}_k}[\ell]\right\}\mathbf{W}_k^*[\ell]\right)\right]\\ &= \mathrm{tr}\left(\left\{\sum_{i=1}^{K}\mathbf{P}_i[\ell]\mathbf{P}_i^*[\ell]\right\}\right)\mathrm{tr}\left(\mathbf{W}_k[\ell]\mathbf{C}_{\mathrm{n}k}\mathbf{W}_k^*[\ell]\right)\end{aligned} \tag{6.20}$$

and

$$\begin{aligned}&\mathbb{E}\left[\mathrm{tr}\left(\mathbf{W}_k[\ell]\left\{\sum_{n=1}^{N}\mathbf{E}_{\mathrm{c}_k n}[\ell]\nu_n\left[\sum_{i=1}^{K}\mathbf{P}_i[\ell]\mathbf{P}_i^*[\ell]\right]\sum_{l'=1}^{N}\mathbf{E}^*_{\mathrm{c}_k l'}[\ell]\boldsymbol{\nu}^*_{l'}\right\}\mathbf{W}_k^*[\ell]\right)\right]\\ &= \boldsymbol{\nu}^*\mathrm{tr}\left(\left[\sum_{i=1}^{K}\mathbf{P}_i[\ell]\mathbf{P}_i^*[\ell]\right]\right)\mathrm{tr}\left(\mathbf{W}_k[\ell]\mathbf{C}_{\mathrm{n}k}\mathbf{W}_k^*[\ell]\right)\boldsymbol{\nu}.\end{aligned} \tag{6.21}$$

For given precoder $\mathbf{P}_k[\ell]$ and IRS phase shift matrix $\boldsymbol{\Theta}$, the k-th user MMSE receiving filter is readily determined as follows

$$\mathbf{W}_{\mathrm{MMSE}_k}[\ell] = \mathbf{P}_k^*[\ell]\hat{\mathbf{H}}^*_{\mathrm{e}_k}[\ell]\left(\hat{\mathbf{H}}_{\mathrm{e}_k}[\ell]\mathbf{P}_k[\ell]\mathbf{P}_k^*[\ell]\hat{\mathbf{H}}^*_{\mathrm{e}_k}[\ell] + \mathbf{Y}_k[\ell]\right)^{-1}, \tag{6.22}$$

where $\mathbf{Y}_k[\ell] \in \mathbb{C}^{N_{\mathrm{r}}\times N_{\mathrm{r}}}$ is the interference-plus-noise matrix given by

$$\mathbf{Y}_k[\ell] = \sum_{i\neq k}\hat{\mathbf{H}}_{\mathrm{e}_k}[\ell]\mathbf{P}_i[\ell]\mathbf{P}_i^*[\ell]\hat{\mathbf{H}}^*_{\mathrm{e}_k}[\ell] + \sigma^2_{\eta_k}\mathbf{I}_{N_{\mathrm{r}}} + (\|\boldsymbol{\nu}\|_2^2 + 1)\sum_{i=1}^{K}\mathrm{tr}\left(\mathbf{P}_i[\ell]\mathbf{P}_i^*[\ell]\right)\mathbf{C}_{\mathrm{n}_k}. \tag{6.23}$$

Substituting (6.22) into (6.17) leads to the following expression for the downlink MSE

$$\mathrm{MSE}_k^{\mathrm{DL}}[\ell] = \mathrm{tr}\left(\mathbf{I}_{N_{\mathrm{s},k}}[\ell] + \mathbf{P}_k^*[\ell]\hat{\mathbf{H}}^*_{\mathrm{e}_k}[\ell]\mathbf{Y}_k^{-1}[\ell]\hat{\mathbf{H}}_{\mathrm{e}_k}[\ell]\mathbf{P}_k[\ell]\right)^{-1}. \tag{6.24}$$

Note that the received symbols for all the users at the ℓ-th subcarrier can be represented by means of the following compact expression (cf. Figure 6.4)

$$\hat{\mathbf{s}}[\ell] = \mathbf{W}[\ell]\mathbf{H}_{\mathrm{e}}[\ell]\mathbf{P}[\ell]\mathbf{s}[\ell] + \mathbf{W}[\ell]\boldsymbol{\eta}[\ell], \tag{6.25}$$

where $\hat{\mathbf{s}}[\ell] = \left[\hat{\mathbf{s}}_1^T[\ell], \ldots, \hat{\mathbf{s}}_K^T[\ell]\right]^T \in \mathbb{C}^{N_\mathrm{s}[\ell]}$, $\mathbf{s}[\ell] = \left[\mathbf{s}_1^T[\ell], \ldots, \mathbf{s}_K^T[\ell]\right]^T \in \mathbb{C}^{N_\mathrm{s}[\ell]}$, $\boldsymbol{\eta}[\ell] = \left[\boldsymbol{\eta}_1^T[\ell], \ldots, \boldsymbol{\eta}_K^T[\ell]\right]^T \in \mathbb{C}^{N_\mathrm{r}K}$ and $\mathbf{H}_\mathrm{e}[\ell] = \left[\mathbf{H}_{\mathrm{e}_1}^*[\ell], \ldots, \mathbf{H}_{\mathrm{e}_K}^*[\ell]\right]^* \in \mathbb{C}^{N_\mathrm{r}K \times N_\mathrm{t}}$ result from stacking all the estimated user symbols, the original symbols sent to all the users, the overall noise and the user channels, respectively, at subcarrier ℓ, whereas $\mathbf{P}[\ell] = \left[\mathbf{P}_1[\ell], \ldots, \mathbf{P}_K[\ell]\right] \in \mathbb{C}^{N_\mathrm{t} \times N_\mathrm{s}[\ell]}$ and $\mathbf{W}[\ell] = \mathrm{blkdiag}\left(\mathbf{W}_1[\ell], \ldots, \mathbf{W}_K[\ell]\right) \in \mathbb{C}^{N_\mathrm{s}[\ell] \times N_\mathrm{r}K}$ collect all the BS precoders and the user filters, respectively, at the ℓ-th subcarrier.

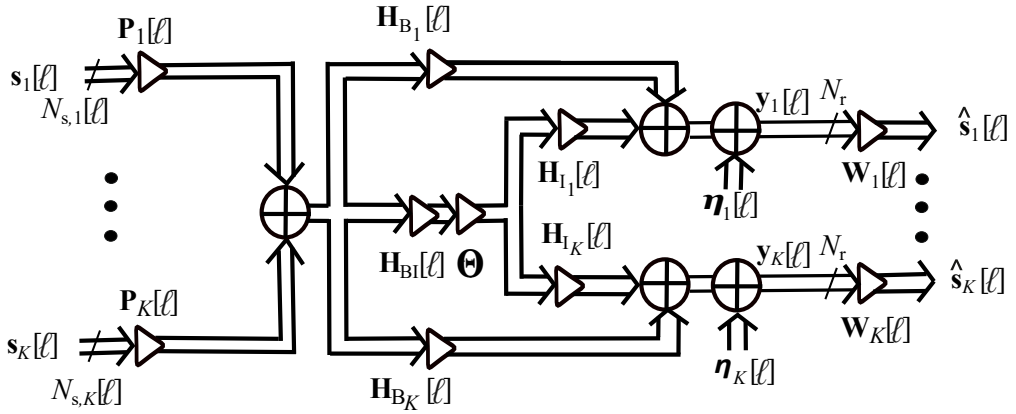

Figure 6.4: Wideband multi-stream mmWave MIMO BC IRS-aided system at subcarrier ℓ.

The overall downlink MSE at subcarrier ℓ, namely $\mathrm{MSE}^{\mathrm{DL}}[\ell] = \sum_{k=1}^{K} \mathrm{MSE}_k^{\mathrm{DL}}[\ell]$ can also be represented in a compact expression as follows

$$\mathrm{MSE}^{\mathrm{DL}}[\ell] = \mathrm{tr}\left(\mathbf{I}_{N_\mathrm{s}}[\ell] + \mathbf{P}^*[\ell]\hat{\mathbf{H}}_\mathrm{e}^*[\ell]\mathbf{Y}^{-1}[\ell]\hat{\mathbf{H}}_\mathrm{e}[\ell]\mathbf{P}[\ell]\right)^{-1}, \tag{6.26}$$

where $\mathbf{I}_{N_\mathrm{s}[\ell]} \in \mathbb{C}^{N_\mathrm{s}[\ell] \times N_\mathrm{s}[\ell]}$ and

$$\mathbf{Y}^{-1}[\ell] = \mathrm{blkdiag}\left(\mathbf{Y}_1^{-1}[\ell], \ldots, \mathbf{Y}_K^{-1}[\ell]\right) \in \mathbb{C}^{N_\mathrm{r}K \times N_\mathrm{r}K}.$$

Finally, in order to determine the wideband precoders and the frequency-flat IRS phase-shift matrix in our downlink wideband multi-stream MU IRS-aided mmWave MIMO system with imperfect CSI, we formulate the following downlink MSE minimization problem

$$\begin{aligned} &\underset{\boldsymbol{\Theta}, \mathbf{P}_k[\ell], \forall k, \ell}{\arg\min} \sum_{\ell=1}^{L} \sum_{k=1}^{K} \mathrm{MSE}_k^{\mathrm{DL}}[\ell] \\ &\text{s.t.} \sum_{k=1}^{K} \mathrm{tr}(\mathbf{P}_k[\ell]\mathbf{P}_k^*[\ell]) \leq P_\mathrm{T}[\ell], \forall \ell, \ \boldsymbol{\Theta} \in \mathcal{D}. \end{aligned} \tag{6.27}$$

Note that $\mathbf{P}_k[\ell]$ appears both in (6.24) and inside $\mathbf{Y}_k[\ell]$. This optimization problem can be formulated in the dual MAC and we will get a reduction of the computational complexity by obtaining a better mathematical structure of the MSE.

We exploit the BC-MAC duality explained in Section 2.4 to solve (6.27). We start defining the virtual dual MAC model for the considered scenario. Let $\mathbf{s}_k^{\mathrm{UL}}[\ell]$ be the vector of uplink

symbols transmitted by the users over subcarrier ℓ in the dual MAC system. The corresponding uplink symbols received at the antennas of the BS will be

$$\mathbf{y}^{\mathrm{UL}}[\ell] = \sum_{k=1}^{K} \mathbf{H}^{*}_{\mathrm{e}_k}[\ell]\mathbf{T}_k[\ell]\mathbf{s}^{\mathrm{UL}}_k[\ell] + \mathbf{n}[\ell], \tag{6.28}$$

where $\mathbf{T}_k[\ell] \in \mathbb{C}^{N_{\mathrm{r}} \times N_{\mathrm{s},k}[\ell]}$ and $\mathbf{H}^{*}_{\mathrm{e}_k}[\ell]$ are the k-th user precoder and the equivalent channel response in the dual MAC, respectively, for subcarrier ℓ. The noise at subcarrier ℓ introduced at reception is represented by $\mathbf{n}[\ell] \sim \mathcal{N}_{\mathbb{C}}(0, \sigma^2_{\mathrm{n}}\mathbf{I}_{N_{\mathrm{t}}})$. Recall that the channel $\mathbf{H}^{*}_{\mathrm{e}_k}[\ell] = \mathbf{H}^{*}_{\mathrm{BI}}[\ell]\boldsymbol{\Theta}^{*}\mathbf{H}^{*}_{\mathrm{I}_k}[\ell] + \mathbf{H}^{*}_{\mathrm{B}_k}[\ell]$ is the conjugate transpose of the joint cascaded and direct channel matrices for the k-th user at subcarrier ℓ given by (6.15).

We now introduce $\mathbf{G}_k[\ell] \in \mathbb{C}^{N_{\mathrm{s},k}[\ell] \times N_{\mathrm{t}}}$, $\forall k$, which are the linear filters used at reception in the dual MAC to estimate the incoming uplink symbols for user k and subcarrier ℓ, i.e.,

$$\hat{\mathbf{s}}^{\mathrm{UL}}_k[\ell] = \mathbf{G}_k[\ell]\mathbf{y}^{\mathrm{UL}}[\ell] = \mathbf{G}_k[\ell]\sum_{i=1}^{K} \mathbf{H}^{*}_{\mathrm{e}_i}[\ell]\mathbf{T}_i[\ell]\mathbf{s}^{\mathrm{UL}}_i[\ell] + \mathbf{G}_k[\ell]\mathbf{n}[\ell]. \tag{6.29}$$

By considering imperfect CSI and a similar approach to that in Subsection 6.3.1, the uplinks symbol expression (6.29) can be rewritten as

$$\hat{\mathbf{s}}^{\mathrm{UL}}_k[\ell] = \mathbf{G}_k[\ell]\sum_{i=1}^{K}\left(\hat{\mathbf{H}}^{*}_{\mathrm{e}_i}[\ell] + \mathbf{E}^{*}_{\mathrm{B}_i}[\ell] + \sum_{n=1}^{N}\mathbf{E}^{*}_{\mathrm{c}_{kn}}[\ell]\nu^{*}_n\right)\mathbf{T}^{*}_i[\ell]\mathbf{s}^{\mathrm{UL}}_i[\ell] + \mathbf{G}_k[\ell]\mathbf{n}[\ell]. \tag{6.30}$$

We next determine the uplink MSE between the sent and the estimated symbols, i.e., $\mathrm{MSE}^{\mathrm{UL}}_k[\ell] = \mathbb{E}\left[\|\mathbf{s}^{\mathrm{UL}}_k[\ell] - \hat{\mathbf{s}}^{\mathrm{UL}}_k[\ell]\|^2_2\right]$. This MSE per user in the dual uplink at subcarrier ℓ when considering imperfect CSI is given by

$$\begin{aligned}
\mathrm{MSE}^{\mathrm{UL}}_k[\ell] = {} & \mathrm{tr}\left(\mathbf{G}_k[\ell]\left\{\left[\sum_{i=1}^{K}\hat{\mathbf{H}}^{*}_{\mathrm{e}_i}[\ell]\mathbf{T}_i[\ell]\mathbf{T}^{*}_i[\ell]\hat{\mathbf{H}}_{\mathrm{e}_i}[\ell]\right] + \sigma^2_{\mathrm{n}}\mathbf{I}_{N_{\mathrm{t}}}\right\}\mathbf{G}^{*}_k[\ell]\right) \\
& + \sum_{i=1}^{K}\mathrm{tr}\left(\mathbf{C}_{\mathrm{n}_i}\mathbf{T}_i[\ell]\mathbf{T}^{*}_i[\ell]\right)\mathrm{tr}\left(\mathbf{G}_k[\ell]\mathbf{G}^{*}_k[\ell]\right) + \boldsymbol{\nu}^{*}\sum_{i=1}^{K}\mathrm{tr}\left(\mathbf{C}_{\mathrm{n}_i}\mathbf{T}_i[\ell]\mathbf{T}^{*}_i[\ell]\right)\mathrm{tr}\left(\mathbf{G}_k[\ell]\mathbf{G}^{*}_k[\ell]\right)\boldsymbol{\nu} \\
& - \mathrm{tr}\left(\mathbf{G}_k[\ell]\hat{\mathbf{H}}^{*}_{\mathrm{e}_k}[\ell]\mathbf{T}_k[\ell] - \mathbf{T}^{*}_k[\ell]\hat{\mathbf{H}}_{\mathrm{e}_k}[\ell]\mathbf{G}^{*}_k[\ell] + \mathbf{I}_{N_{\mathrm{s},k}[\ell]}\right).
\end{aligned} \tag{6.31}$$

The MMSE filter in the uplink is given by

$$\begin{aligned}
\mathbf{G}_{\mathrm{MMSE}_k}[\ell] = {} & \mathbf{T}^{*}_k[\ell]\hat{\mathbf{H}}_{\mathrm{e}_k}[\ell]\Big(\hat{\mathbf{H}}^{*}_{\mathrm{e}}[\ell]\mathbf{T}[\ell]\mathbf{T}^{*}[\ell]\hat{\mathbf{H}}_{\mathrm{e}}[\ell] + \sigma^2_{\mathrm{n}}\mathbf{I}_{N_{\mathrm{t}}} \\
& + (1 + \|\boldsymbol{\nu}\|^2_2)\sum_{i=1}^{K}\mathrm{tr}\Big(\mathbf{C}_{\mathrm{n}_i}\mathbf{T}_i[\ell]\mathbf{T}^{*}_i[\ell]\Big)\mathbf{I}_{N_{\mathrm{t}}}\Big)^{-1},
\end{aligned} \tag{6.32}$$

and the MSE per user achieved at subcarrier ℓ when employing this MMSE receiving filter is

$$\mathrm{MSE}_k^{\mathrm{UL}}[\ell] = \mathrm{tr}\Bigg(\Bigg(\mathbf{I}_{N_{\mathrm{s},k}[\ell]} + \mathbf{T}_k^*[\ell]\hat{\mathbf{H}}_{\mathrm{e}_k}[\ell]\Bigg(\sum_{i\neq k}^{K}\hat{\mathbf{H}}_{\mathrm{e}_i}^*[\ell]\mathbf{T}_i[\ell]\mathbf{T}_i^*[\ell]\hat{\mathbf{H}}_{\mathrm{e}_i}[\ell] + \sigma_{\mathrm{n}}^2\mathbf{I}_{N_{\mathrm{t}}} + (1+\|\boldsymbol{\nu}\|_2^2)\sum_{i=1}^{K}\mathrm{tr}\Big(\mathbf{C}_{\mathrm{n}_i}\mathbf{T}_i[\ell]\mathbf{T}_i^*[\ell]\Big)\mathbf{I}_{N_{\mathrm{t}}}\Bigg)^{-1}\hat{\mathbf{H}}_{\mathrm{e}_k}^*[\ell]\mathbf{T}_k[\ell]\Bigg)^{-1}\Bigg), \tag{6.33}$$

where $\mathbf{T}[\ell] = \mathrm{blkdiag}\left(\mathbf{T}_1[\ell],\ldots,\mathbf{T}_K[\ell]\right)$ is a block diagonal matrix that stacks all the dual uplink user precoders, and $\hat{\mathbf{H}}_{\mathrm{e}}^*[\ell] = \left[\hat{\mathbf{H}}_{\mathrm{e}_1}^*[\ell],\ldots,\hat{\mathbf{H}}_{\mathrm{e}_K}^*[\ell]\right]$ stacks all the equivalent channel response matrices. Note that this expression only depends on the uplink wideband precoders in the dual MAC, $\mathbf{T}_k[\ell]$, and the frequency-flat IRS phase-shift matrix $\boldsymbol{\Theta}$.

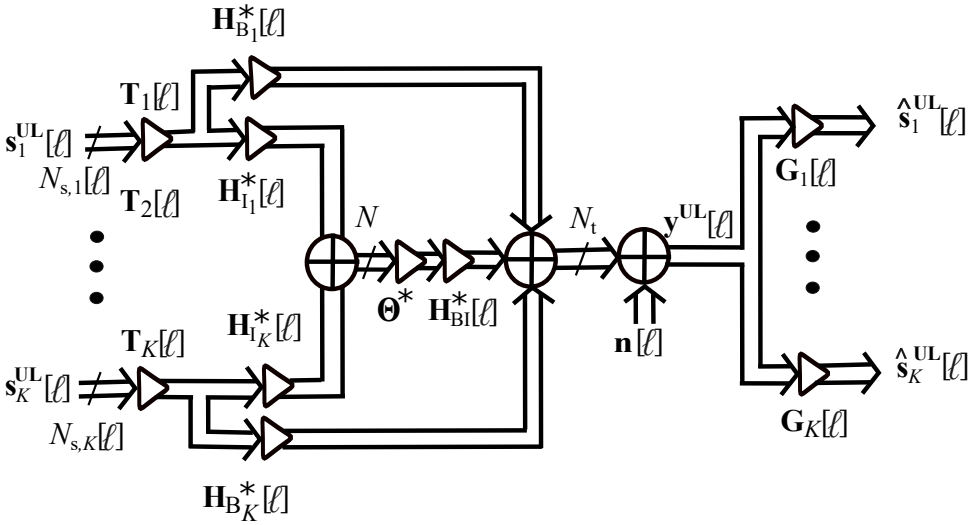

Figure 6.5: Dual MAC of the wideband MU multi-stream IRS-aided mmWave MIMO system model at subcarrier ℓ.

We next rewrite the received uplink symbols at subcarrier ℓ given by (6.28) by means of the following more compact expression (cf. Figure 6.5)

$$\mathbf{y}^{\mathrm{UL}}[\ell] = \mathbf{H}_{\mathrm{e}}^*[\ell]\mathbf{T}[\ell]\mathbf{s}^{\mathrm{UL}}[\ell] + \mathbf{n}[\ell], \tag{6.34}$$

where $\mathbf{s}^{\mathrm{UL}}[\ell] = \left[\mathbf{s}_1^{\mathrm{UL}^T}[\ell],\ldots,\mathbf{s}_K^{\mathrm{UL}^T}[\ell]\right]^T$ is a vector that gathers all the uplink user symbols sent over the ℓ-th subcarrier. According to (6.15), this latter matrix is related to the different channel responses in the signal model as follows

$$\mathbf{H}_{\mathrm{e}}^*[\ell] = \left(\mathbf{H}_{\mathrm{BI}}^*[\ell]\boldsymbol{\Theta}^*\mathbf{H}_{\mathrm{I}}^*[\ell] + \mathbf{H}_{\mathrm{B}}^*[\ell]\right) \in \mathbb{C}^{N_{\mathrm{t}}\times N_{\mathrm{r}}K}, \tag{6.35}$$

where $\mathbf{H}_{\mathrm{I}}^*[\ell] = \left[\mathbf{H}_{\mathrm{I}_1}^*[\ell],\ldots,\mathbf{H}_{\mathrm{I}_K}^*[\ell]\right] \in \mathbb{C}^{N\times N_{\mathrm{r}}K}$, and $\mathbf{H}_{\mathrm{B}}^*[\ell] = \left[\mathbf{H}_{\mathrm{B}_1}^*[\ell],\ldots,\mathbf{H}_{\mathrm{B}_K}^*[\ell]\right] \in \mathbb{C}^{N_{\mathrm{t}}\times N_{\mathrm{r}}K}$.

Substituting the frequency selective equivalent channel responses given by (6.35) into (6.34) leads to

$$\mathbf{y}^{\mathrm{UL}}[\ell] = \left(\mathbf{H}_{\mathrm{BI}}^*[\ell]\boldsymbol{\Theta}^*\mathbf{H}_{\mathrm{I}}^*[\ell] + \mathbf{H}_{\mathrm{B}}^*[\ell]\right)\mathbf{T}[\ell]\mathbf{s}^{\mathrm{UL}}[\ell] + \mathbf{n}[\ell]. \tag{6.36}$$

Note that $\mathbf{T}[\ell] \in \mathbb{C}^{N_\mathrm{r}K \times N_\mathrm{s}[\ell]}$ and $\mathbf{s}^{\mathrm{UL}}[\ell] \in \mathbb{C}^{N_\mathrm{s}[\ell]}$ with $N_\mathrm{s}[\ell] = \sum_{k=1}^{K} N_{\mathrm{s},k}[\ell]$, i.e., their dimensions depend on the number of served data streams per user.

The estimated uplink data symbols corresponding to the K users at subcarrier ℓ in the dual MAC signal model can hence be defined as

$$\hat{\mathbf{s}}^{\mathrm{UL}}[\ell] = \mathbf{G}\left(\mathbf{H}^*_{\mathrm{BI}}[\ell]\boldsymbol{\Theta}\mathbf{H}^*_{\mathrm{I}}[\ell] + \mathbf{H}^*_{\mathrm{B}}[\ell]\right)\mathbf{T}[\ell]\mathbf{s}^{\mathrm{UL}}[\ell] + \mathbf{G}[\ell]\mathbf{n}[\ell], \tag{6.37}$$

where $\mathbf{G}^*[\ell] = [\mathbf{G}^*_1[\ell], \ldots, \mathbf{G}^*_K[\ell]]^*$ is the receiving filter that stacks the filters $\mathbf{G}_k[\ell],\ \forall k$ which estimate all the uplink symbols at subcarrier ℓ. Note that $\hat{\mathbf{s}}^{\mathrm{UL}}[\ell]$ collects all the estimated user symbols $\hat{\mathbf{s}}^{\mathrm{UL}}_k[\ell], \forall k$, which can also be obtained through (6.29). Considering imperfect CSI, the estimated uplink user symbols $\hat{\mathbf{s}}^{\mathrm{UL}}[\ell]$ can be represented as follows

$$\hat{\mathbf{s}}^{\mathrm{UL}}[\ell] = \mathbf{G}[\ell]\left(\hat{\mathbf{H}}^*_{\mathrm{B}}[\ell] + \mathbf{E}^*_{\mathrm{B}}[\ell] + \sum_{n=1}^{N}\left(\hat{\mathbf{H}}^*_{\mathrm{com}_n}[\ell] + \mathbf{E}^*_{\mathrm{c}_n}[\ell]\right)\nu^*_n\right)\mathbf{T}[\ell]\mathbf{s}^{\mathrm{UL}}[\ell] + \mathbf{G}[\ell]\mathbf{n}[\ell], \tag{6.38}$$

with $\mathbf{E}^*_{\mathrm{B}}[\ell] = \left[\mathbf{E}^*_{\mathrm{B}_1}[\ell], \ldots, \mathbf{E}^*_{\mathrm{B}_K}[\ell]\right] \in \mathbb{C}^{N_\mathrm{t} \times N_\mathrm{r}K}$ and $\mathbf{E}^*_{\mathrm{c}_n}[\ell] = [\mathbf{E}_{\mathrm{c}_{1\,n}}[\ell], \ldots, \mathbf{E}_{\mathrm{c}_{K\,n}}[\ell]] \in \mathbb{C}^{N_\mathrm{t} \times N_\mathrm{r}K}$, $\hat{\mathbf{H}}^*_{\mathrm{com}_n}[\ell] = \left[\hat{\mathbf{H}}^*_{\mathrm{com}_{1n}}[\ell], \ldots, \hat{\mathbf{H}}^*_{\mathrm{com}_{Kn}}[\ell]\right] \in \mathbb{C}^{N_\mathrm{t} \times N_\mathrm{r}K}, \forall n$. The MMSE receiving filter using this compact formulation is given by

$$\begin{aligned}\mathbf{G}_{\mathrm{MMSE}}[\ell] =& \mathbf{T}^*[\ell]\hat{\mathbf{H}}_{\mathrm{e}_k}\Big(\hat{\mathbf{H}}^*_{\mathrm{e}}[\ell]\mathbf{T}[\ell]\mathbf{T}^*[\ell]\hat{\mathbf{H}}_{\mathrm{e}}[\ell] \\ &+ \sigma^2_{\mathrm{n}}\mathbf{I}_{N_\mathrm{t}} + (1 + \|\boldsymbol{\nu}\|^2_2)\sum_{i=1}^{K}\mathrm{tr}\Big(\mathbf{C}_{\mathrm{n}_i}\mathbf{T}_i[\ell]\mathbf{T}^*_i[\ell]\Big)\mathbf{I}_{N_\mathrm{t}}\Big)^{-1},\end{aligned} \tag{6.39}$$

and the overall uplink MSE achieved at subcarrier ℓ when employing this MMSE receiving filter is

$$\begin{aligned}\mathrm{MSE}^{\mathrm{UL}}[\ell] = \mathrm{tr}\Bigg(\Bigg(&\mathbf{I}_{N_\mathrm{s}[\ell]} + \mathbf{T}^*[\ell]\hat{\mathbf{H}}_{\mathrm{e}}[\ell] \\ \times\Bigg(&\sigma^2_{\mathrm{n}}\mathbf{I}_{N_\mathrm{t}} + (1 + \|\boldsymbol{\nu}\|^2_2)\sum_{i=1}^{K}\mathrm{tr}\Big(\mathbf{C}_{\mathrm{n}_i}\mathbf{T}_i[\ell]\mathbf{T}^*_i[\ell]\Big)\mathbf{I}_{N_\mathrm{t}}\Bigg)^{-1}\hat{\mathbf{H}}^*_{\mathrm{e}}[\ell]\mathbf{T}[\ell]\Bigg)^{-1}\Bigg).\end{aligned} \tag{6.40}$$

According to [67], [159], the filters and precoders in the downlink are related to their counterparts in the dual MAC as follows:

$$\mathbf{P}[\ell] = \xi[\ell]\mathbf{G}^*[\ell], \tag{6.41}$$

$$\mathbf{W}[\ell] = \xi^*[\ell]\mathbf{T}^*[\ell], \tag{6.42}$$

with $\xi[\ell] \in \mathbb{R}$, given by

$$\xi[\ell] = \sqrt{\frac{P_\mathrm{T}[\ell]}{\sum_{k=1}^{K}\|\mathbf{G}_k[\ell]\|^2_F}}. \tag{6.43}$$

On the other hand, the MAC-BC duality is established as

$$\mathbf{G}[\ell] = \zeta^{-1}[\ell]\mathbf{P}^*[\ell], \tag{6.44}$$

$$\mathbf{T}[\ell] = \zeta[\ell]\mathbf{W}^*[\ell], \tag{6.45}$$

with $\zeta[\ell] \in \mathbb{R}$ given by

$$\zeta[\ell] = \sqrt{\frac{P_{\mathrm{T}}[\ell]}{\sum_{k=1}^{K} \|\mathbf{W}_k[\ell]\|_F^2}}. \tag{6.46}$$

Table 6.2: Dual MAC system model parameters.

Description	Parameter
Precoder: k-th user at subcarrier ℓ	$\mathbf{T}_k[\ell]$
Dual (BC-MAC) frequency flat IRS phase shift matrix	$\boldsymbol{\Theta}^*$
Dual user-BS direct channel: k-th user at subcarrier ℓ	$\mathbf{H}^*_{\mathrm{B}_k}[\ell]$
BS-IRS channel at subcarrier ℓ	$\mathbf{H}^*_{\mathrm{BI}}[\ell]$
IRS-User channel: k-th user at subcarrier ℓ	$\mathbf{H}^*_{\mathrm{I}_k}[\ell]$
Vector of AWGN at subcarrier ℓ	$\mathbf{n}[\ell]$
Filter: k-th BS filter at subcarrier ℓ	$\mathbf{G}_k[\ell]$
Vector of $N_{\mathrm{s},k}[\ell]$ estimated user symbols at subcarrier ℓ	$\hat{\mathbf{s}}^{\mathrm{UL}}_k[\ell]$

By means of duality, the same MSE is achieved in the downlink when using (6.41) and (6.42) to obtain the wideband precoders and filters for the downlink from the wideband filters and precoders in the uplink. Table 6.2 summarizes the main system model parameters and variables for the dual MAC system.

Once the uplink MSE corresponding to all the K users for a particular subcarrier has been determined, we can similarly define $\mathrm{MSE}^{\mathrm{UL}} = \sum_{\ell=1}^{L} \mathrm{MSE}^{\mathrm{UL}}[\ell] = \sum_{k=1}^{K}\sum_{\ell=1}^{L} \mathrm{MSE}^{\mathrm{UL}}_k[\ell]$ which is the overall system MSE in the dual uplink which considers the symbols transmitted by all the users over all the subcarriers. This uplink MSE can be represented in a compact form as follows

$$\begin{aligned}\mathrm{MSE}^{\mathrm{UL}} =& \mathrm{tr}\Bigg(\Bigg(\mathbf{I}_{N_{\mathrm{s}}L} + \mathbf{T}^*\hat{\mathbf{H}}_{\mathrm{e}}\Bigg(\sigma^2_{\mathrm{n}}\mathbf{I}_L \otimes \mathbf{I}_{N_{\mathrm{t}}} + (1+\|\boldsymbol{\nu}\|_2^2) \\ &\times \sum_{i=1}^{K} \mathrm{tr}\Big(\mathbf{I}_L \otimes \mathbf{C}_{\mathrm{n}_i}\mathbf{T}_i\mathbf{T}_i^*\Big)\mathbf{I}_{N_{\mathrm{t}}L}\Bigg)^{-1}\hat{\mathbf{H}}^*_{\mathrm{e}}\mathbf{T}\Bigg)^{-1}\Bigg),\end{aligned} \tag{6.47}$$

with

$$\hat{\mathbf{H}}_{\mathbf{e}} = \hat{\mathbf{H}}_{\mathrm{B}} + \sum_{n=1}^{NL} \tilde{\nu}_n \hat{\mathbf{H}}_{\mathrm{com}_n} = \hat{\mathbf{H}}_{\mathrm{B}} + (\tilde{\boldsymbol{\nu}} \otimes \mathbf{I}_{N\mathrm{t}})^T \hat{\mathbf{H}}_{\mathrm{com}}, \tag{6.48}$$

where $\tilde{\boldsymbol{\nu}}$ is the main diagonal of the resulting matrix after applying $\tilde{\boldsymbol{\Theta}} = \mathbf{I}_L \otimes \boldsymbol{\Theta}$, $\hat{\mathbf{H}}^*_{\text{com}} = \left[\hat{\mathbf{H}}_{\text{com}_1}, \ldots, \hat{\mathbf{H}}_{\text{com}_N}\right]^*$ and

$$\begin{aligned}
&\mathbf{T}^* = \text{blkdiag}\left(\mathbf{T}^*[1], \ldots, \mathbf{T}^*[L]\right), \\
&\mathbf{H}^*_{\text{B}} = \text{blkdiag}\left(\mathbf{H}^*_{\text{B}}[1], \ldots, \hat{\mathbf{H}}_{\text{B}}[L]^*\right), \\
&\mathbf{E}^*_{\text{B}} = \text{blkdiag}\left(\mathbf{E}^*_{\text{B}}[1], \ldots, \mathbf{E}^*_{\text{B}}[L]\right), \\
&\mathbf{E}^*_{\text{c}\,n} = \text{blkdiag}\left(\mathbf{E}^*_{\text{c}_n}[1], \ldots, \mathbf{E}^*_{\text{c}_n}[L]\right), \forall n = 1, \ldots, N, \\
&\hat{\mathbf{H}}^*_{\text{com}_n} = \text{blkdiag}\left(\hat{\mathbf{H}}^*_{\text{com}_n}[1], \ldots, \hat{\mathbf{H}}^*_{\text{com}_n}[L]\right), \forall n = 1, \ldots, N
\end{aligned}$$

are block diagonal matrices that stack all the precoders, the inverse of the noise covariance matrices and the channels corresponding to the K users at the L subcarriers, such that $\mathbf{T} \in \mathbb{C}^{N_{\text{r}}KL \times N_{\text{s}}}$, $\hat{\mathbf{H}}^*_{\text{com}_n} \in \mathbb{C}^{N_{\text{r}}KL \times N_{\text{t}}L}$, $\mathbf{H}^*_{\text{B}} \in \mathbb{C}^{N_{\text{r}}KL \times N_{\text{t}}L}$, $\mathbf{E}^*_{\text{B}} \in \mathbb{C}^{N_{\text{r}}KL \times N_{\text{t}}L}$ and $\mathbf{E}^*_{\text{c}_n} \in \mathbb{C}^{N_{\text{r}}KL \times N_{\text{t}}L}$.

Using the previous compact notation, the MMSE optimization problem for the virtual uplink can be formulated as follows

$$\begin{aligned}
&\underset{\boldsymbol{\Theta}, \mathbf{T}_k[\ell], \forall k, \ell}{\arg \min} \ \text{MSE}^{\text{UL}}(\mathbf{T}, \boldsymbol{\Theta}) \\
&\text{s.t.} \ \sum_{k=1}^{K} \text{tr}(\mathbf{T}_k[\ell]\mathbf{T}^*_k[\ell]) \leq P_{\text{T}}[\ell], \forall \ell, \ \boldsymbol{\Theta} \in \mathcal{D}.
\end{aligned} \tag{6.49}$$

Note that after obtaining the precoders $\mathbf{T}_k[\ell] \ \forall k, \ell$ and the receiving filters $\mathbf{G}_{\text{MMSE}_k}[\ell] \ \forall k, \ell$ in the dual uplink, we readily determine $\mathbf{P}_k[\ell] \ \forall k, \ell$ and $\mathbf{W}_{\text{MMSE}_k}[\ell] \ \forall k, \ell$ in the downlink by through (6.41) and the MMSE expression in (6.22), respectively.

6.5.2 Algorithmic Solution for the Design of the Wideband IRS-Aided System

In this subsection, we develop an alternating algorithm to solve the MSE minimization problem (6.49). The frequency-flat IRS phase-shift matrix $\boldsymbol{\Theta}$ and the frequency-dependent filters/precoders in the uplink and their downlink counterparts are alternately calculated until the MSE reduction at iteration i is not higher than a threshold δ or until a maximum number of iterations ϵ is reached.

Algorithm 6.1 summarizes the steps of the proposed alternating minimization approach. Algorithm 6.1 starts determining the filters and downlink precoders, which are next used to determine the filters and precoders in the dual uplink by using the relationship given by (6.45) and the MMSE expression in (6.39). Then, the IRS phase shift matrix $\boldsymbol{\Theta} = \text{diag}(\boldsymbol{\nu})$ is determined with the following iterative projected gradient algorithm such that

$$\boldsymbol{\nu}^{(i)} = d\left(\boldsymbol{\nu}^{(i-1)} - \mu_{\boldsymbol{\nu}} \nabla_{\boldsymbol{\nu}} \ \text{MSE}^{\text{UL}}(\mathbf{T}, \boldsymbol{\nu})\right). \tag{6.50}$$

The operator $d(\cdot)$ is a projector which enforces $\nu_n, \forall n$ to be an unitary modulus element and, thus, $\boldsymbol{\Theta}$ belongs to the set of feasible solutions $\mathcal{D}$.

Algorithm 6.1 Alternating MSE Minimization PG

Input: $\mathbf{C}_{\mathrm{n}k}, \forall k, P_{\mathrm{T}},\ \mu_1, \delta, \epsilon, \hat{\mathbf{H}}_{\mathrm{B}}^{*} \in \mathbb{C}^{LN_{\mathrm{r}}K \times LN_{\mathrm{t}}}, \hat{\mathbf{H}}_{\mathrm{com}_n}^{*} \in \mathbb{C}^{LN_{\mathrm{r}}K \times LN_{\mathrm{t}}}, \forall n$

1: **Initialize:** $i \leftarrow 0$
2: $\theta_n \in [0, 2\pi),\ \forall\ n$
3: $\boldsymbol{\Theta}^{(0)} = \mathrm{diag}(e^{j\theta_1}, \ldots, e^{j\theta_N}),\ \forall\ n$
4: **for** $\ell = 1 : L$ **do**
5: $\quad \mathbf{P}^{(0)}[\ell] = \left[\mathbf{P}_1^{(0)}[\ell], \ldots, \mathbf{P}_K^{(0)}[\ell]\right] \leftarrow$ MRT precoders
6: $\quad \mathbf{W}_{\mathrm{MMSE}}^{(0)}[\ell] = \mathrm{blkdiag}\Big(\mathbf{W}_{\mathrm{MMSE}_1}^{(0)}[\ell], \ldots,\ \mathbf{W}_{\mathrm{MMSE}_K}^{(0)}[\ell]\ \Big) \leftarrow$ (6.22)
7: $\quad \mathbf{T}^{(0)}[\ell] = \mathrm{blkdiag}\Big(\mathbf{T}_1^{(0)}[\ell], \ldots, \mathbf{T}_K^{(0)}[\ell]\Big) \leftarrow$ (6.45)
8: $\quad \mathbf{G}_{\mathrm{MMSE}}^{(0)}[\ell] = \left[\mathbf{G}_{\mathrm{MMSE}_1}^{*(0)}[\ell], \ldots, \mathbf{G}_{\mathrm{MMSE}_K}^{*(0)}[\ell]\right]^{*} \leftarrow$ (6.39)
9: $\mu_{\boldsymbol{\Theta}} \leftarrow \mu_1$
10: **repeat**
11: $\quad i \leftarrow i + 1$
12: $\quad$ **for** $\ell = 1 : L$ **do**
13: $\quad\quad \mathbf{P}^{(i)}[\ell] = \left[\mathbf{P}_1^{(i)}[\ell], \ldots, \mathbf{P}_K^{(i)}[\ell]\right] \leftarrow$ (6.41) and $\mathbf{G}_k^{(i-1)}[\ell]$
14: $\quad\quad \mathbf{W}_{\mathrm{MMSE}}^{(i)}[\ell] = \mathrm{blkdiag}\Big(\mathbf{W}_{\mathrm{MMSE}_1}^{(i)}[\ell], \ldots, \mathbf{W}_{\mathrm{MMSE}_K}^{(i)}[\ell]\Big) \leftarrow$ (6.22)
15: $\quad\quad \mathbf{T}^{(i)}[\ell] = \mathrm{blkdiag}\Big(\mathbf{T}_1^{(i)}[\ell], \ldots, \mathbf{T}_K^{(i)}[\ell]\Big) \leftarrow$ (6.45)
16: $\quad\quad \mathbf{G}_{\mathrm{MMSE}}^{(i)}[\ell] = \left[\mathbf{G}_{\mathrm{MMSE}_1}^{*(i)}[\ell], \ldots, \mathbf{G}_{\mathrm{MMSE}_K}^{*(i)}[\ell]\right]^{*} \leftarrow$ (6.39)
17: $\quad \boldsymbol{\nu}^{(i)} = d(\boldsymbol{\nu}^{(i-1)} - \mu_{\boldsymbol{\nu}}\, \nabla_{\boldsymbol{\nu}}\, \mathrm{MSE}^{\mathrm{UL}}(\mathbf{T}, \boldsymbol{\nu}))$
18: $\quad$ **while** $\mathrm{MSE}^{\mathrm{UL}}\left(\mathbf{T}^{(i-1)}, \boldsymbol{\nu}^{(i-1)}\right) \leq \mathrm{MSE}^{\mathrm{UL}}\left(\mathbf{T}^{(i)}, \boldsymbol{\nu}^{(i)}\right)$ **do**
19: $\quad\quad \mu_{\boldsymbol{\nu}} \leftarrow \mu_{\boldsymbol{\nu}}/2$
20: $\quad\quad \boldsymbol{\nu}^{(i)} = d(\boldsymbol{\nu}^{(i-1)} - \mu_{\boldsymbol{\nu}}\, \nabla_{\boldsymbol{\nu}}\, \mathrm{MSE}^{\mathrm{UL}}(\mathbf{T}, \nu))$
21: **until** $\mathrm{MSE}^{\mathrm{UL}}\left(\mathbf{T}^{(i-1)}, \boldsymbol{\nu}^{(i-1)}\right) - \mathrm{MSE}^{\mathrm{UL}}\left(\mathbf{T}^{(i)}, \boldsymbol{\nu}^{(i)}\right) < \delta$ or $i \geq \epsilon$

Output: $\mathbf{P}_k[\ell], \mathbf{W}_{\mathrm{MMSE}k}[\ell], \forall k, \ell, \boldsymbol{\Theta} \in \mathcal{D}$

Next, the MAC-BC duality expression in (6.41) and the MMSE filter expression in (6.22) are used to compute the precoders and filters in the downlink, i.e., $\mathbf{P}_k[\ell]\ \forall k, \ell$ and $\mathbf{W}_{\mathrm{MMSE}_k}[\ell]\ \forall k, \ell$. By invoking the MAC-BC duality in both directions, this alternating procedure is repeated until achieving the stopping criterion.

The initial IRS phase-shift matrix $\boldsymbol{\Theta}^{(0)}$ is set to a diagonal matrix whose non-zero entries have unit magnitude and a random phase from the interval $[0, 2\pi)$ (step 3, Algorithm 6.1). The initial block diagonal precoding matrix in the downlink $\mathbf{P}^{(0)}$ is constructed with the MRT precoders for each user at each subcarrier (step 5, Algorithm 6.1) assuming $P_{\mathrm{T}_k}[\ell] = \frac{P_{\mathrm{T}}}{KL}\ \forall k, \ell$. Notice that Algorithm 6.1 also updates at each iteration the power allocation per user and per subcarrier. Finally, the gradient $\nabla_{\nu_n}\, \mathrm{MSE}^{\mathrm{UL}}(\mathbf{T}, \boldsymbol{\Theta})$ used in (6.50) is given by

$$\nabla_{\nu_n} \text{MSE}^{\text{UL}}(\mathbf{T}, \nu_{\mathbf{n}}) = \sum_{\ell=1}^{L} -\Bigg(\text{tr}\Big(\mathbf{A}_7[\ell]\mathbf{T}^*[\ell]\Big) - \Big(\text{tr}\left(\mathbf{A}_8[\ell]\mathbf{T}^*[\ell]\mathbf{A}_0[\ell]\mathbf{A}_6[\ell]\mathbf{A}^*[\ell]\mathbf{T}[\ell]\mathbf{T}^*[\ell]\right) + \text{tr}\left(\mathbf{A}_7[\ell]\mathbf{T}^*[\ell]\mathbf{A}_0[\ell]\mathbf{A}_3[\ell]\mathbf{A}^*[\ell]\mathbf{T}[\ell]\mathbf{T}^*[\ell]\right) + \text{tr}\left(\mathbf{A}_8[\ell]\mathbf{T}^*[\ell]\right)\Bigg), \quad (6.51)$$

where

$$\mathbf{A}_0[\ell] = \mathbf{C}_{N_{\text{r}}K} \sum_{n=1}^{N} \nu_n \hat{\mathbf{H}}_{\text{com}_n}[\ell],$$

$$\mathbf{A}_1[\ell] = \mathbf{A}_0^*[\ell]\mathbf{T}[\ell]\mathbf{T}^*[\ell]\mathbf{A}_0[\ell],$$

$$\mathbf{A}_2[\ell] = (N+1) \sum_{i=1}^{K} \text{tr}\Big(\mathbf{C}_{\text{n}_i}\mathbf{T}_i[\ell]\mathbf{T}_i[\ell]^*\Big)\mathbf{I}_{N_{\text{t}}}\Big),$$

$$\mathbf{A}_3[\ell] = \left(\left(\sigma_{\text{n}}^2\mathbf{I}_{N_{\text{t}}} + \mathbf{A}_1[\ell]\right)^* + \mathbf{A}_2[\ell]\right)^{-1},$$

$$\mathbf{A}_4[\ell] = \mathbf{T}^*[\ell]\mathbf{A}_0[\ell],$$

$$\mathbf{A}_5[\ell] = \left(\mathbf{I}_{N_{\text{s}}[\ell]} + \mathbf{A}_4[\ell]\mathbf{A}_3[\ell]\mathbf{A}_0^*[\ell]\mathbf{T}[\ell]\right)^{-1},$$

$$\mathbf{A}_6[\ell] = \left(\left(\sigma_{\text{n}}^2\mathbf{I}_{N_{\text{t}}} + \mathbf{A}_2[\ell]\right)^* + \mathbf{A}_1[\ell]\right)^{-1},$$

$$\mathbf{A}_7[\ell] = \hat{\mathbf{H}}_{\text{com}_n}[\ell]\mathbf{A}_3[\ell]\mathbf{A}_0^*[\ell]\mathbf{T}[\ell]\mathbf{A}_5[\ell]\mathbf{A}_5[\ell],$$

$$\mathbf{A}_8[\ell] = \hat{\mathbf{H}}_{\text{com}_n}[\ell]\mathbf{A}_6[\ell]\mathbf{A}_0^*[\ell]\mathbf{T}[\ell]\mathbf{A}_5[\ell]\mathbf{A}_5[\ell].$$

6.6 Simulation Results

In this section, we present the results of computer simulations carried out to assess the performance of the wideband IRS-aided MU MIMO systems designed with the alternating MSE minimization algorithm proposed in Subsection 6.5.2. We consider an IRS-aided MU-MIMO system with $K = 3$ users having $N_{\text{r}} = 4$ antennas each, a BS with $N_{\text{t}} = 9$ antennas, which allocates 2 data streams per user at subcarrier ℓ, i.e., $N_{\text{s},k}[\ell] = 2\ \forall k, \ell$, and an IRS with different number of elements $N \in \{9, 16, 25, 36, 49\}$. The error covariance matrix is $\mathbf{C}_{\text{n}k} = \mathbf{C}_{\text{n}}$, $\forall k$ in the downlink with $\mathbf{C}_{\text{n}} = {\sigma_{\text{e}}}^2\mathbf{I}_{N_{\text{r}}}$. Although some authors assume that the error level in the receivers is lower or even negligible, our approach is more general and can be adapted to those cases. We consider the simplified multipath channel model for wideband systems in the expression (2.32) in Subsection 2.5.1. The parameters for the mmWave channel model are set to L_{D} = 8 delay taps and $N_{\text{p}} = 4$ channel paths. The AoAs and the AoDs are assumed to be random and uniformly distributed over the interval $[0, \pi]$ as in [31]. The relative delays τ_n are also random and uniformly distributed over the range $\tau_n \in [0, (L_{\text{D}} - 1)T_{\text{s}}]$, with $T_s = 1/f_s$ and $f_s = 1760$ MHz. The complex-valued channel gains for the m-th path is i.i.d. standard Gaussian random variables, i.e., $\beta_m \sim \mathcal{N}_{\mathbb{C}}(0, 1)$. The central carrier frequency is assumed to be $f_{\text{c}} = 28$ GHz and the signal bandwidth is set to 400 MHz (a negligible beam squint effect is given with this bandwidth). The number of subcarriers is $L = 32$.

Table 6.3: Simulation parameter setting.

Description	Setting
Number of users	$K = 3$
Antennas per users	$N_{\mathrm{r}} = 4$
Antennas at the BS	$N_{\mathrm{t}} = 16$
Number of subcarriers	$L = 32$
Number of data streams per user	$N_{\mathrm{s},k}[\ell] = 2, \forall k, \ell$
Number of IRS elements	$N \in \{9, 16, 25, 36, 49\}$
Channel propagation paths	$N_{\mathrm{p}} = 4$
Channel delay paths	$L_{\mathrm{D}} = 8$
Central carrier frequency	$f_{\mathrm{c}} = 28$ GHz
Covariance of estimation error (downlink)	$\mathbf{C}_{\mathrm{n}k} = \mathbf{C}_{\mathrm{n}}, \forall k$
Variance of the errors in the estimation	σ_{e}^2
Channel realizations	$C_{\mathrm{R}} = 1000$
Max. number of iterations (Algorithm 6.1)	$\epsilon = 100$

All the reported results are obtained after averaging $C_{\mathrm{R}} = 1000$ channel realizations. Performance is evaluated in terms of the downlink achievable sum-rate (6.13) and the MSE (6.26). We assume that noise variance is $\sigma_{\eta_k}^2 = \sigma_{\eta}^2 = 1\ \forall k$, and therefore the per subcarrier SNR is SNR (dB) $= 10\ \log_{10}(P_{\mathrm{T}}/L)$. Finally, the maximum number of iterations in Algorithm 6.1 ϵ is set to 100. Table 6.3 summarizes the configuration considered in the computer simulations.

In the first simulation experiment, we compare the performance of the system designed according to Algorithm 6.1 with the following five baseline approaches. Perfect CSI is considered, i.e., $\sigma_{\mathrm{e}}^2 = 0$.

1. The maximum achievable sum capacity obtained with dirty paper coding (DPC). This approach constitutes an upper bound on the sum rate and has been designed following the power iterative waterfilling proposed in [161, Algorithm 2].
2. Amplify-and-forward with optimized precoders (AF O-Ps). The precoders and the IRS matrix are optimized through Algorithm 6.1 but the IRS matrix is assumed to be unconstrained, i.e., the magnitude of the diagonal entries of the phase-shift matrix is not constrained to be 1, and thus the IRS is able to modify both the amplitude and phase of the impinging signals. For the sake of fairness we assume that $\|\mathbf{\Theta}\|_F^2 = N$.
3. Random IRS with optimized precoders (R-IRS O-Ps). The precoders are optimized via the MAC-BC and the BC-MAC dualities in Algorithm 6.1 while the phases of the diagonal IRS phase-shift matrix are random uniform variables over $[0, 2\pi]$, i.e., there is no control of the IRS phase-shift matrix.
4. Optimized IRS with MRT precoders (O-IRS MRT-Ps). The precoders are designed as MRT precoders while the IRS phase-shift matrix is optimized via Algorithm 6.1.
5. No IRS with MRT precoders (No-IRS MRT-Ps). The precoders are designed as MRT

precoders and the IRS is not deployed to assist the communication system, i.e., $\boldsymbol{\Theta} = \mathbf{0}_N$. The wideband receiving filters $\mathbf{W}_k[\ell], \forall \ell, k$ are designed according to the MMSE criterion.

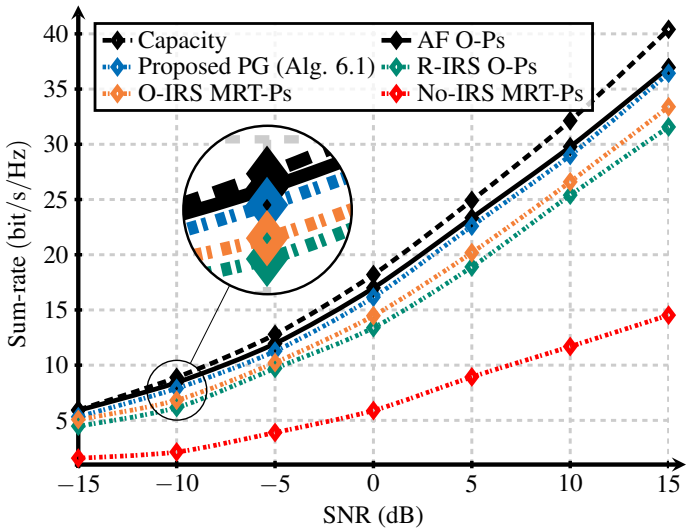

Figure 6.6: Sum-rate (bit/s/Hz) versus SNR (dB) for $K = 3$ users, $N_\mathrm{r} = 4$, $N_\mathrm{t} = 9$, $N = 25$, $\sigma_\mathrm{e}^2 = 0$, and $N_{\mathrm{s},k}[\ell] = 2, \forall k, \ell$.

Figure 6.6 plots the achievable sum-rate obtained with the above mentioned approaches. As shown, AF O-Ps provides the highest achievable sum-rate since the wideband precoders are optimized via Algorithm 6.1 and the diagonal IRS phase-shift matrix has no magnitude constraint in its entries. The proposed PG approach leads to a performance higher than that obtained with the R-IRS O-Ps and the O-IRS MRT-Ps baseline approaches. Recall that R-IRS O-Ps does not optimize the phases of the IRS while O-IRS MRT-Ps does not control the interference when designing the wideband precoders at the BS. The No-IRS MRT-Ps strategy provides the lowest performance because only the direct channel is available. Thus, the system has a reduced capacity and the wideband precoder design does not take into account the MU interference. It is also observed that the proposed Algorithm 6.1 does not lead to a significant gap w.r.t. the unconstrained AF O-Ps strategy and comes close to the maximum system capacity.

Figure 6.7 plots the average MSE obtained with the aforementioned approaches. As shown, AF O-Ps provides the lowest MSE. The proposed approach leads to a MSE lower than those obtained with R-IRS O-Ps and O-IRS MRT-Ps. The No-IRS MRT-Ps strategy provides the highest MSE since it neglects the inter-users interference control in the precoder design and disables the IRS-aided channels.

Figure 6.8 plots the capacity obtained according to [161] for the AF O-Ps, R-IRS O-Ps, R-IRS O-Ps and proposed approaches. As shown, the same behavior exhibited in Figure 6.6 with the same approaches is corroborated by considering the system capacity determined with [161, Algorithm 2]. This constitutes an interesting result since the proper configuration of the IRS phase shift matrix leads to a system improvement not only in terms of the sum-rate but also in terms of system capacity.

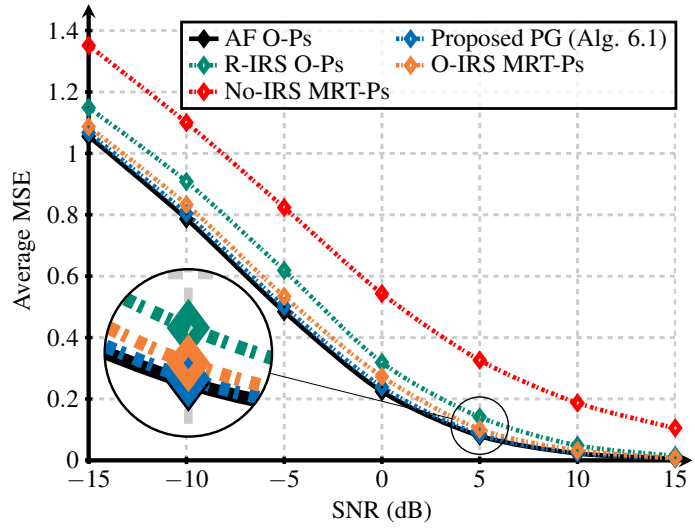

Figure 6.7: MSE versus SNR (dB) for $K = 3$ users, $N_{\mathrm{r}} = 4$, $N_{\mathrm{t}} = 9$, $N = 25$, $\sigma_{\mathrm{e}}^2 = 0$, and $N_{\mathrm{s},k}[\ell] = 2, \forall k, \ell$.

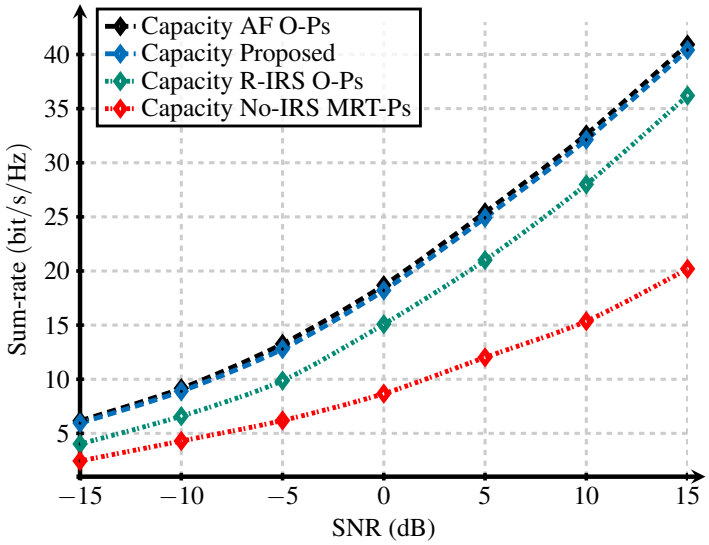

Figure 6.8: Sum-rate (bit/s/Hz) versus SNR (dB) for $K = 3$ users, $N_{\mathrm{r}} = 4$, $N_{\mathrm{t}} = 9$, $L = 32$, $N = 25$, $\sigma_{\mathrm{e}}^2 = 0$, and $N_{\mathrm{s},k}[\ell] = 2, \forall k, \ell$.

In the following, we quantify the performance improvement obtained when optimizing the IRS phase-shift matrix with Algorithm 6.1. We measure the impact of the phase shift optimization at the IRS and evaluate the performance gains obtained when increasing the number of IRS elements N. For that, we define the achievable sum-rate increase ΔR (bit/s/Hz) as the difference between the achievable sum-rate obtained with Algorithm 6.1 and that obtained with R-IRS O-Ps. Figure 6.9 plots the achievable sum-rate increase with respect to N, the number of passive elements at the IRS. As expected, the larger the size of the IRS is, the higher the resulting gains are. Figure 6.9 also shows how ΔR (bit/s/Hz) increases with SNR (dB). This effect is because the optimization of the IRS phase shift matrix, and therefore the control

of the MU interference, has a larger impact on the system performance in the high SNR regime.

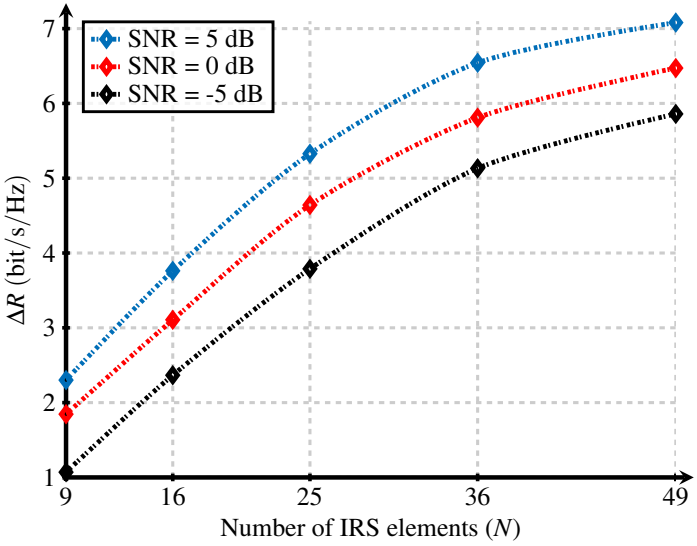

Figure 6.9: Sum-rate increase ΔR (bit/s/Hz) versus N for $K = 3$ users, $N_{\mathrm{r}} = 4$, $N_{\mathrm{t}} = 9$, SNR (dB) $\in \{-5, 0, 5\}$, $L = 32$, $N \in \{9, 16, 25, 36, 49\}$, $\sigma_{\mathrm{e}}^2 = 0$, and $N_{\mathrm{s},k}[\ell] = 2, \forall k, \ell$.

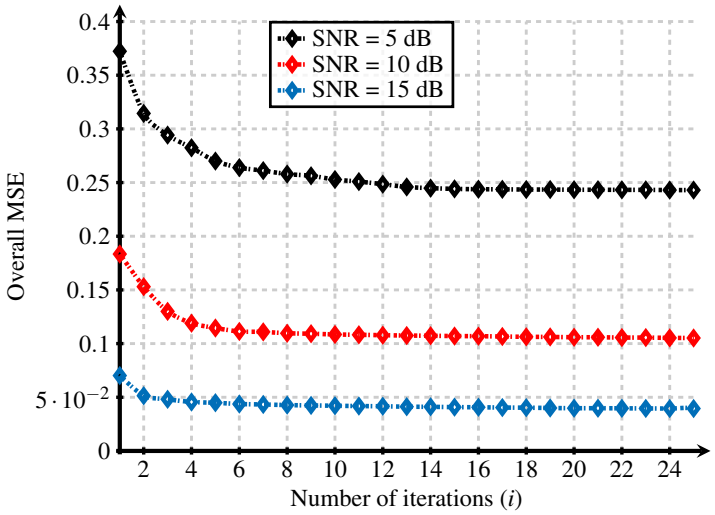

Figure 6.10: MSE versus number of iterations ℓ for $K = 3$ users, $N_{\mathrm{r}} = 4$, $N_{\mathrm{t}} = 9$, $N = 25$, SNR (dB) $\in \{5, 10, 15\}$, $\sigma_{\mathrm{e}}^2 = 0$, and $N_{\mathrm{s},k}[\ell] = 2, \forall k, \ell$.

In the next experiment, we empirically evaluate the convergence of Algorithm 6.1. Figure 6.10 plots the evolution of the average MSE versus the number of iterations performed in the alternating procedure. We considered three SNR levels, namely SNR (dB) $\in \{5, 10, 15\}$. It can be observed that convergence is reached after about 25 iterations.

In the following, we evaluate (in terms of the achievable sum-rate) the impact of the CSI estimation errors and compare our proposed solution with a baseline (labeled non-robust) that does not account for the imperfect CSI (Algorithm 1 in [45] after applying the MAC-BC

MSE duality). We include an approach where the precoders and the IRS phase-shift matrix are determined with the proposed algorithm with perpect CSI. Finally, we also included the capacity and the AF O-Ps solutions with perfect CSI as benchmarks.

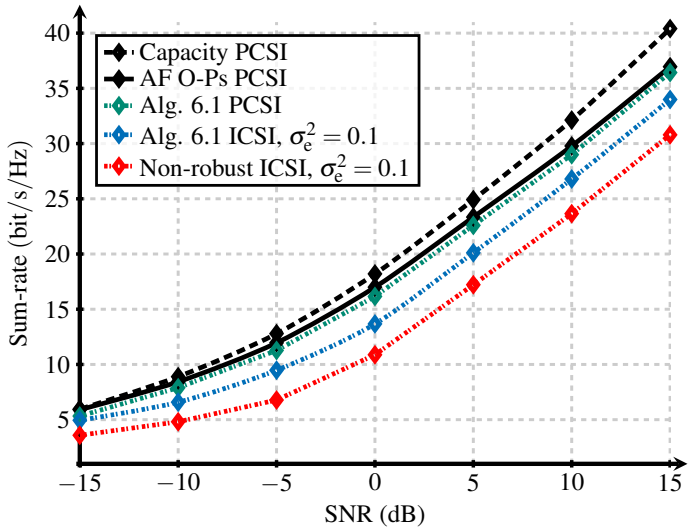

Figure 6.11: Sum-rate (bit/s/Hz) versus SNR (dB) for $K = 3$ users, $N_\mathrm{r} = 4$, $N_\mathrm{t} = 9$, $N = 25$, imperfect CSI with $\sigma_\mathrm{e}^2 = 0.1$, and $N_{\mathrm{s},k}[\ell] = 2, \forall k, \ell$.

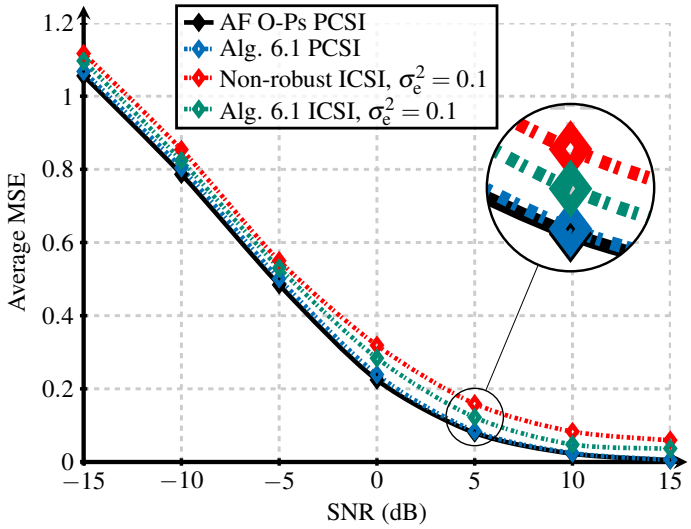

Figure 6.12: Average MSE versus SNR (dB) for $K = 3$ users, $N_\mathrm{r} = 4$, $N_\mathrm{t} = 9$, $N = 25$, imperfect CSI with $\sigma_\mathrm{e}^2 = 0.1$, and $N_{\mathrm{s},k}[\ell] = 2, \forall k, \ell$.

As shown in Figure 6.11, the non-robust strategy leads to the worst system performance since it does not consider imperfect CSI and does not exploit the error statistics. Conversely, Algorithm 6.1 considers the error statistics in the estimation of the direct and the cascade channels and outperforms the non-robust approach leading to a small gap w.r.t. the perfect CSI approach. In Figure 6.12, we compare the proposed and the non-robust approaches in terms of

the MSE. We also consider a benchmark with perfect CSI, namely the proposed approach and AF O-Ps. As observed, the non-robust approach leads to the worst system performance, i.e., the highest MSE whereas the proposed solution in PG outperforms the non-robust approach and comes close to the considered benchmarks for $\sigma_{\mathrm{e}}^2 = 0.1$.

In Figure 6.13, we measure the performance improvement obtained when optimizing the IRS phase-shift matrix, the filters, and the user precoders with Algorithm 6.1 considering the channel estimation error statistics. We measure the impact of including this statistical information in the design of the transceivers and evaluate the performance gains obtained when σ_{e}^2. In particular, we define the achievable sum-rate increase ΔR_{ICSI} (bit/s/Hz) as the difference between the achievable sum-rate obtained with Algorithm 6.1 when considering the channel estimation errors and that obtained with the non-robust strategy, which neglects this information. Figure 6.13 plots the achievable sum-rate increase while varying σ_{e}^2. As an expected, the larger the errors are, the higher the resulting gains are. Figure 6.13 also shows that ΔR_{ICSI} (bit/s/Hz) increases with the SNR (dB).

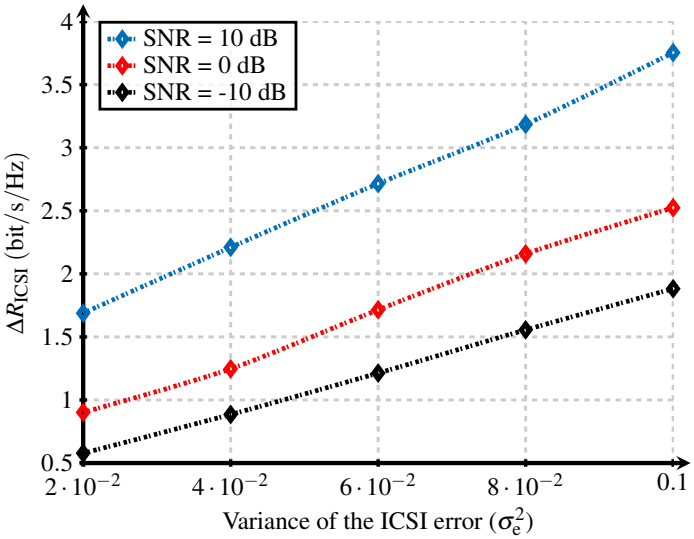

Figure 6.13: Sum-rate increase ΔR_{ICSI} (bit/s/Hz) versus $\sigma_{\mathrm{e}}^2 \in \{0.02, 0.04, 0.06, 0.08, 0.1\}$ for $K = 3$ users, $N_{\mathrm{r}} = 4$, $N_{\mathrm{t}} = 9$, SNR (dB) $\in \{-10, 0, 10\}$, $N = 25$, and $N_{\mathrm{s},k}[\ell] = 2, \forall k, \ell$.

6.7 Conclusions

The design of a wideband MU IRS-aided MIMO system under imperfect CSI has been addressed in this chapter. An innovative alternating minimization algorithm has been proposed to configure the frequency-flat IRS phase-shift matrix as well as the wideband BS precoders and user filters. The algorithm minimizes the MSE between the symbols sent by the users and the symbols received at the BS in the dual MAC. Imperfect CSI is assumed and the available information on CSI errors statistics is incorporated into the system design.

The results show reasonable gains in terms of both the achievable rate and the MSE over baseline strategies. Specifically, the deployment of the IRS and the adequate configuration of the phase shift matrix provides significant performance gains with respect to non-IRS conventional systems with MRT precoding.

Chapter VII

Conclusions and Future Work

7.1 Conclusions

Coding and signal processing are essential when deploying wireless communications systems. In this thesis, we devoted one chapter to analog JSCC mappings and three entire chapters to signal processing techniques for wireless communications in three different scenarios: the uplink of a narrowband mmWave MU MIMO system, the uplink of a wideband mmWave MU MIMO setup, and the downlink of a wideband MU IRS-assisted mmWave MIMO system. In this regard, the fast evolution of nowadays wireless communications systems constitutes a challenge for their versatile and flexible implementation under different scenarios. First of all, we provided a general system model characterization in Chapter 2, where an overall encoded wideband MU MIMO wideband system model is detailed. This system model is then particularized in the different approaches addressed throughout this thesis. The main concepts of the MIMO-OFDM systems are described. The source correlation model, the MAC and BC system models are also analyzed. The relation between the MAC and the BC implementation systems in terms of the MSE are explained through the MAC-BC and the BC-MAC dualities. Finally, the channel models employed for mmWave and the sub-6 GHz systems were also described in Chapter 2.

Chapter 3 was devoted to the analog JSCC issue. Specifically, we approached the transmission of spatially correlated information in a distributed Rayleigh SIMO MAC scenario by using analog JSCC techniques. Blocks of source symbols are individually encoded at each user with an analog lattice-based JSCC mapping. At the central receiver, the estimates of the transmitted symbols are jointly computed by means of a decoding approach that exploits the spatial correlation and the use of codeword sizes larger than one (i.e., non-zero delay). The proposed approach is flexible to work with different codework sizes. Craig's lattices were considered to reduce the computational cost of the encoding operation in the analog JSCC system. The possibility of adjusting the Craig's lattice density allows us to balance the trade-off between the system performance and the computational complexity in the encoding and

decoding operations. The experimental results showed gains by considering certain scenarios where zero-delay mappings found in the literature have shown some performance limitations as non-orthogonal configurations or moderate correlation. In addition, an analysis of the impact of the block size and the lattice density was accomplished thanks to the proposed system design and the use of Craig's lattices.

We addressed in Chapter 4 novel signal processing techniques to deploy a user grouping approach for the uplink of a narrowband MU hybrid mmWave MIMO system. This system based on user grouping is able to handle a high number of sources with a limited number of RF chains through the use of the DQLC mapping. The allocation of the users per group and the hybrid design of the filter at the common BS to serve the gathered users were investigated. For the allocation of the users, we have considered the source correlation and the feasibility of aligning the user channels in order to obtain reasonable performance of the DQLC mapping. Furthermore, a hybrid MMSE filter design was proposed in order to exploit the spatial correlation between the sources in conventional uncoded mmWave uplink systems. We observed considerable performance gains by comparing the proposed MMSE filter with several solutions found in the state-of-the-art for hybrid transceiver implementation. Significant gains were also obtained with the proposed user allocation strategy over a random strategy. The main contribution of this chapter is the considerable reduction of the number of RF chains in MU systems for hybrid architectures by grouping the users via the DQLC mapping.

We provided an extension of the user grouping approach in Chapter 4 for wideband mmWave systems in the face of beam squint in Chapter 5. In particular, we have developed signal processing techniques for the user grouping and the scheduling strategy for wideband scenarios by considering the beam squint effect present in these systems, as well as a novel approach for the interference cancellation at both ends of the communication links for hybrid architectures. The results showed large gains over other strategies found in the state-of-the-art for hybrid implementation in wideband and baselines strategies for the user scheduling that neglect the beam squint effect.

Finally, we approached the paradigm of controlling the propagation environment in wireless communications through IRSs. In particular, we implemented novel signal processing techniques for the design of a downlink wideband MU IRS-aided mmWave MIMO system under imperfect CSI in Chapter 6. We addressed the joint design of the IRS phase-shift matrix, which is frequency flat and common to all the users, and the frequency-dependent precoders at the BS and the receiving filters at the users by considering the statistics of the channel estimation errors. In this case, the simulation results showed that the proposed solution leads to substantial gains with respect to baseline strategies to implement the precoding and the IRS phase shifts, which neglect the imperfect CSI and the interference control.

7.2 Future Work

In this thesis, we have investigated the use of non-zero delay JSCC mappings over fading channels in MU SIMO systems, our main concern was to provide a non-zero delay extension to the existing mappings in the context of wireless communications. Hence, we have considered some assumptions for the JSCC design, such as the channel being perfectly known at both communications ends, i.e., regardless of the error introduced by practical channel estimation methods. For future works, the communications models based on analog JSCC can be further enhanced by including the effects associated to the channel estimation process. In addition, due to the particular properties of analog JSCC mappings, there exist multiple practical scenarios where the application and configuration of this strategy could be very interesting, e.g., in WSNs.

We have also investigated the hybrid architectures for wideband MU mmWave MIMO systems and the wideband IRS-aided communication systems. These communication approaches can complement each other by considering wideband MU IRS-aided hybrid mmWave MIMO systems. These two research lines are also connected in the sense of the characteristics of the signal processing performed at both, the analog part of the hybrid architectures, and the IRS. These components working in the RF domain limit the flexibility of the transceivers, (analog precoder/filter in mmWave and IRS phase shift matrix), which leads to absolute value constraints in the formulations. In this thesis, we assume that these phase shifts are implemented with infinite resolution and not with quantized phase shifting. The implementation through low-resolution quantized phase shifts constitutes a more realistic approach and the particularities that arrive with this consideration for MU IRS-aided hybrid mmWave MIMO systems constitute an interesting research line for the future.

It is evident that the IRSs are receiving intensive attention nowadays and they are envisioned as key technologies for B5G mobile communications, however, the topic is still recent and a large number of ideas in this thesis can be further studied, e.g., near-field considerations for the configuration of IRS-aided systems, channel acquisition, and user scheduling. The development of testbeds for the IRS technology is also timely to judge it in practical scenarios.

By considering the tremendous amount of benefits offered by the IRSs, several application scenarios can be examined by considering this technology. In Figure 7.1, we show some applications, which could benefit from the use of the IRS technology and that constitute scenarios not thoroughly investigated in the literature. The first application illustrated in Figure 7.1(a) focuses on D2D networks [162], where the IRS could be used to cancel the interference, support the required low-power transmission in these systems, and enhance individual data links in these communications systems. Another interesting application illustrated in Figure 7.1(b) is the use of the IRS technology for CR networks (e.g., [163]), where the IRS could be used to increase the degrees of freedom to further improve the CR network performance. Specifically, the IRS could be employed to improve the efficiency of the secondary transmissions.

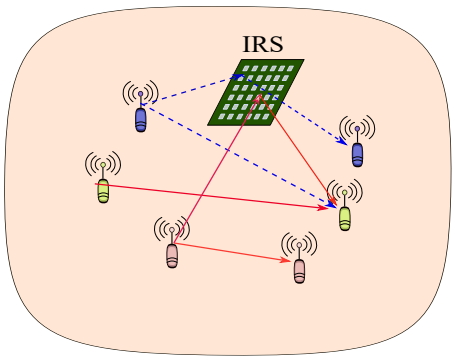

(a) IRSs in D2D communications.

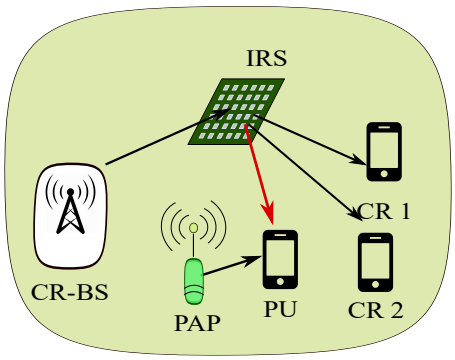

(b) IRSs in CR.

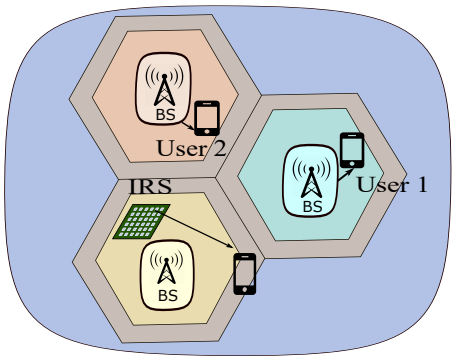

(c) IRSs for cell edge users.

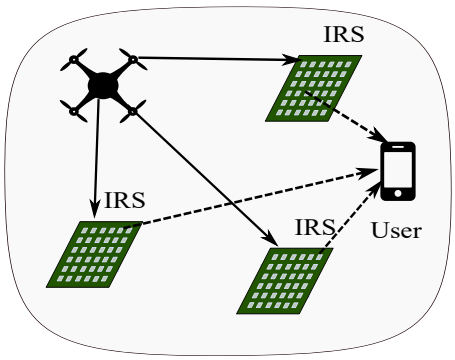

(d) IRSs in UAVs.

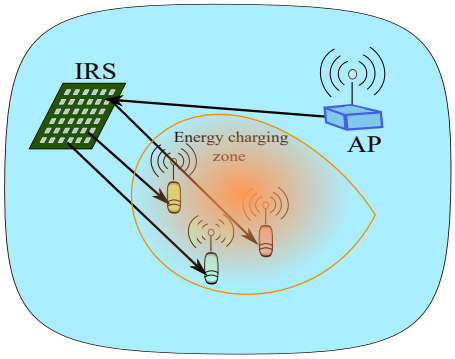

(e) IRSs in energy transfer systems.

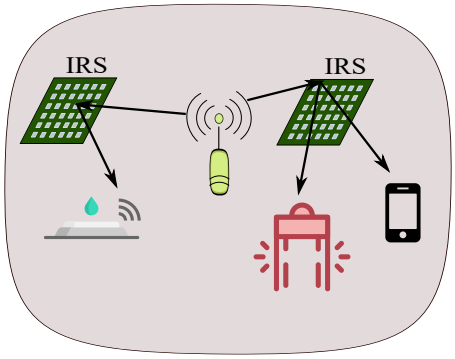

(f) IRSs in IoT networks.

Figure 7.1: Applications of the IRSs.

In the third scenario illustrated in Figure 7.1(c), a cellular network with a cell edge user—which can suffer high signal attenuation from the BS and co-channel interference from near BSs—is considered. In this scenario, the IRS deployment could be helpful to increase the coverage area in the cellular network (see [164]). The use of IRSs is also interesting for UAV networks (Figure 7.1(d)), where the IRS can be used to enhance the quality of the communication between the UAV and the ground users, thus being instrumental for the optimization of the UAV trajectory and the system performance (cf. [132]). The fifth application of the IRS technology illustrated in Figure 7.1(e) is related to the power transfer systems, where the IRS phase-shift matrix is designed to enhance the received signal strength at the energy receivers in the charging zone with the aim of ensuring the energy harvesting requirements

[32]. The last application shown in Figure 7.1(f) is the use of IRSs for IoT systems (e.g., [35]), where a multi-IRS scenario seems to be useful to compensate the power loss over long distances and alleviate the energy budget issue in energy-constrained IoT networks via the passive IRS beamforming.

Next, we summarize the main future research lines to be addressed to complement the work performed in this thesis by considering new case uses and applications of the approached technologies.

7.2.1 Impact of the Imperfect CSI on the Design of Analog JSCC Mappings

In this thesis, we decided to disregard the stage corresponding to the channel estimation process in the design of analog JSCC mappings. Thus, the channel information is assumed to be available at both ends and free of errors. However, small errors introduced by the estimation procedure can be found in practical schemes, which can induce significant distortions after the filtering operation and therefore a degradation of the overall system performance. The study of the impact of the CSI estimation errors on the design of the proposed lattice-based analog mappings represents an interesting complement to this thesis. Moreover, the impact of imperfect CSI has not been widely investigated in the literature related to the design of other analog JSCC.

7.2.2 Low-Resolution Phase Shifts for Hybrid Architectures in mmWave MIMO IRS-Aided Systems

In this work, we have studied the hybrid architectures for mmWave and the IRS-assisted systems separately, however, these two novel communication techniques can be integrated into a MU IRS-aided hybrid mmWave MIMO system. While continuously tuning the phase shift of each of the IRS elements and the RF precoders/filters is certainly advantageous for communication applications, it is costly to implement in practical scenarios because manufacturing such high-precision elements requires sophisticated design and expensive hardware. This may not be a scalable solution for a large number of phase shift elements. Practical deployment considerations such as low-resolution quantized phase shifts can lead to challenging optimization problems to be studied in the future.

7.2.3 Near-Field Region and Spherical Wave-Front Model for MU MIMO IRS-Aided Systems

Throughout this thesis, we have assumed the far-field operation region for the approached communication systems. However, the combination of large-scale antennas with high frequencies often results in communications in the near-field region. The authors in [165]

provide a detailed analysis of the design and use of IRSs by considering both the near-field and far-field radiation characteristics of such surfaces, diverging from the commonly adopted far-field implementation for this technology in the literature. Some important issues are described in that work, which can be considered for the design and for user scheduling in IRS-aided communication systems. The operation of MU MIMO IRS-assisted systems in the near-field regions and the design particularities by considering the spherical wave-front model have not been thoroughly studied in the literature and it constitutes an interesting research area for the future.

7.2.4 User Balancing and Scheduling in MU MIMO Multi-IRS-Aided Systems

Appropriate user scheduling is decisive to perform practical implementations (e.g., in cellular networks and WSNs) able to balance the number of served users according to the power transmission constraints and/or the performance. The schemes of user balancing in MU MIMO multi-IRS-assisted systems have been marginally addressed in the current state-of-the-art. Limited works can be found regarding user scheduling in IRS-assisted systems, e.g., the authors in [166] analyze the optimization of the IRS phase-shift matrix by considering the detection order of the received users by a common BS in a NOMA MIMO system. These ideas can be extended to mobile networks with multiple IRSs by balancing the amount of served users and the overall system performance. The use of the IRS technology together with an efficient scheduling strategy still constitutes a novel and challenging open research line.

7.2.5 Implementation and Testbeds for IRS Technology

We can focus on evaluating the design of the IRS-aided systems over realistic scenarios as future work. To this end, we could make use of an IRS testbed, which would provide us with an idea of the performance of these systems over real-world channels by considering different scenarios and applications. In the last years, a few promising testbeds and experimental activities have been reported [167], and some industrial developments have also been reported [19]. However, these reports are insufficient to practically judge the IRS technology.

Appendix I

Real-Valued Equivalent Model

The complex-valued system models can be transformed into an equivalent real-valued one. For this, the equivalent real-valued matrix $\mathbf{A}_{\text{RV}} \in \mathbb{R}^{2m\times 2n}$ is rearranged from the complex-valued matrix $\mathbf{A}_{\text{CV}} \in \mathbb{C}^{m\times n}$ as

$$\mathbf{A}_{\text{RV}} = \begin{pmatrix} 1 & 0 \\ 0 & 1 \end{pmatrix} \otimes \Re\left(\mathbf{A}_{\text{CV}}\right) + \begin{pmatrix} 0 & -1 \\ 1 & 0 \end{pmatrix} \otimes \Im\left(\mathbf{A}_{\text{CV}}\right) = \begin{pmatrix} \Re\left(\mathbf{A}_{\text{CV}}\right) & -\Im\left(\mathbf{A}_{\text{CV}}\right) \\ \Im\left(\mathbf{A}_{\text{CV}}\right) & \Re\left(\mathbf{A}_{\text{CV}}\right) \end{pmatrix} \in \mathbb{R}^{2m\times 2n}. \tag{A.1}$$

The transformation from a complex-valued vector $\mathbf{x}_{\text{CV}} \in \mathbb{C}^{m}$ into a real-valued vector $\mathbf{x}_{\text{RV}} \in \mathbb{R}^{2m}$ is obtained with

$$\mathbf{x}_{\text{RV}} = \begin{pmatrix} 1 \\ 0 \end{pmatrix} \otimes \Re\left(\mathbf{x}_{\text{CV}}\right) + \begin{pmatrix} 0 \\ 1 \end{pmatrix} \otimes \Im\left(\mathbf{x}_{\text{CV}}\right) = \begin{pmatrix} \Re\left(\mathbf{x}_{\text{CV}}\right) \\ \Im\left(\mathbf{x}_{\text{CV}}\right) \end{pmatrix} \in \mathbb{R}^{2m}. \tag{A.2}$$

By considering a multiple-input multiple-output (MIMO) multiple access channel (MAC) transmission with K users equipped with N_{t} antennas each, the received complex-valued signal at the multi-antenna (N_{r}) centralized node is

$$\mathbf{y}_{\text{CV}} = \mathbf{H}_{\text{CV}}\mathbf{s}_{\text{CV}} + \mathbf{n}_{\text{CV}} \in \mathbb{C}^{N_{\text{r}}}, \tag{A.3}$$

where $\mathbf{H}_{\text{CV}} = [\mathbf{H}_{\text{CV}1}, \ldots, \mathbf{H}_{\text{CV}K}] \in \mathbb{C}^{N_{\text{r}}\times N_{\text{t}}K}$ stacks all the user flat fadng channels $\mathbf{H}_{\text{CV}k}, \forall k \in \mathbb{C}^{N_{\text{r}}\times N_{\text{t}}}$, $\mathbf{s}_{\text{CV}} = \left[s_{\text{CV}_1}^T, \ldots, s_{\text{CV}_K}^T\right]^T \in \mathbb{C}^{N_{\text{t}}K}$ represents all the transmit signals by the K users and $\mathbf{n}_{\text{CV}} \in \mathbb{C}^{N_{\text{r}}}$ is the additive white Gaussian noise (AWGN). Note that the equivalent real-valued model can be obtained as

$$\begin{pmatrix} \Re\left(\mathbf{y}_{\text{CV}}\right) \\ \Im\left(\mathbf{y}_{\text{CV}}\right) \end{pmatrix} = \begin{pmatrix} \Re\left(\mathbf{H}_{\text{CV}}\right) & -\Im\left(\mathbf{H}_{\text{CV}}\right) \\ \Im\left(\mathbf{H}_{\text{CV}}\right) & \Re\left(\mathbf{H}_{\text{CV}}\right) \end{pmatrix} \begin{pmatrix} \Re\left(\mathbf{s}_{\text{CV}}\right) \\ \Im\left(\mathbf{s}_{\text{CV}}\right) \end{pmatrix} + \begin{pmatrix} \Re\left(\mathbf{n}_{\text{CV}}\right) \\ \Im\left(\mathbf{n}_{\text{CV}}\right) \end{pmatrix} \in \mathbb{C}^{2N_{\text{r}}}, \tag{A.4}$$

such that

$$\mathbf{y}_{\text{RV}} = \mathbf{H}_{\text{RV}}\mathbf{s}_{\text{RV}} + \mathbf{n}_{\text{RV}} \in \mathbb{C}^{2N_{\text{r}}}. \tag{A.5}$$

Appendix II

Resumen de la Tesis

Los sistemas de comunicaciones inalámbricas experimentan un crecimiento incesante en la actualidad, y se espera que crezcan aún más en los años venideros, acompañados en su despliegue por novedosas técnicas de codificación y procesamiento de señales. Los servicios multimedia y basados en datos móviles son cada vez más demandados para actividades laborales, de socialización y acceso a los diferentes servicios. Además, las comunicaciones masivas de tipo máquina también están experimentando un aumento considerable (comunicaciones en transporte, redes de sensores, Internet de las cosas (IoT), etc.), y deben ser consideradas para las nuevas generaciones de sistemas de comunicaciones inalámbricas.

Para hacer frente al aumento de los sistemas de comunicaciones se requiere de novedosas técnicas de codificación y procesamiento de señales. Estas técnicas están destinadas a ofrecer mejoras en cuanto a la tasa de datos ofrecida por los sistemas de telecomunicaciones, la eficiencia energética de dichos sistemas, la fiabilidad, etc. La codificación de fuentes está fundamentalmente destinada a la transformación o conversión de las señales para llevar a cabo una transmisión más eficiente, mientras que la codificación de canal está destinada a la detección y corrección de errores de señales transmitidas a través de canales con desvanecimientos, para reducir así la probabilidad de error o la distorsión en la recepción. Por otra parte, el procesamiento de señales está más bien enfocado al tratamiento de las señales (filtrado, modificación, detección de patrones, estimación, etc.), pero tanto las técnicas de codificación como de procesamiento de señales están destinadas a mejorar la transmisión, la recepción y el rendimiento de los sistemas en general.

La aplicación de las técnicas de codificación de señales y de canal siempre ha jugado un papel imprescindible en el despliegue de las redes de comunicaciones inalámbricas. Shannon demostró que un sistema de comunicación es capaz de transmitir con una probabilidad de error arbitrariamente baja siempre que la tasa de transmisión se mantenga por debajo de un cierto límite. Además, postuló que la separación de la codificación de fuente y de los canales constituye la estrategia óptima para alcanzar los límites teóricos. Estas ideas inspiraron el desarrollo de toda una teoría de la comunicación digital centrada en la construcción de esquemas

de codificación cada vez más sofisticados. En la actualidad, la gran mayoría de los sistemas de comunicaciones se diseñan siguiendo una aproximación digital y de acuerdo con el principio de separación. Sin embargo, los sistemas de comunicaciones basados en la optimización conjunta de la codificación de fuente y de canal (JSCC) siguen despertado interés en los investigadores, especialmente para el caso de transmisión de señales analógicas considerando fuentes espacialmente correlacionadas. Las investigaciones se basan en la capacidad de los sistemas de JSCC para aproximarse a los límites teóricos, además de ofrecer ventajas con respecto a los sistemas digitales como, por ejemplo, baja complejidad computacional y mínimo retardo. La mayoría de los trabajos basados en sistemas JSCC consideran una codificación con una configuración de tamaño de palabra de código limitada y asumiendo ruido gaussiano (AWGN), lo cual no constituye un escenario práctico. La aplicación de la estrategia JSCC en canales con desvanecimiento presenta una serie de desafíos importantes a la hora de diseñar estos sistemas analógicos. Por un lado, el sistema JSCC analógico debe adaptarse constantemente a las fluctuaciones del canal, para conseguir un equilibrio entre la distorsión observada y el coste computacional que supone la implementación del sistema. Afortunadamente, en sistemas basados en JSCC no es necesario rediseñar por completo el sistema ante cambios de las respuestas de canal, pues basta con actualizar los parámetros del codificador según las condiciones del canal en cada instante. Sin embargo, es necesaria la implementación de sistemas genéricos con tamaños de palabras arbitrarios, basados en sofisticadas técnicas de codificación, para lograr la implementación práctica de estos sistemas analógicos y compensar las pérdidas de propagación. También es necesario obtener diseños que permitan este tipo de codificación analógica con una complejidad computacional moderada.

La aplicación de novedosas técnicas de procesamiento de señales es cada vez más demandada por las industrias para la implementación de las redes emergentes de comunicaciones inalámbricas. Las comunicaciones desplegadas en el espectro de frecuencias de ondas milimétricas (mmWave) está definiendo una nueva era de las comunicaciones inalámbricas. Esta banda de frecuencias ofrece canales de comunicaciones de mayor ancho de banda en comparación con los que se utilizan actualmente en los sistemas inalámbricos comerciales. Las aplicaciones de mmWave son inmensas: redes inalámbricas de área local, sistemas celulares de generación 5G y posteriores (B5G), las redes de área vehicular, etc. El procesamiento de señales es fundamental para habilitar la próxima generación de comunicaciones en la banda de mmWave, ya que en esta banda de frecuencias las pérdidas de propagación son enormes y es necesario compensarlas. Debido al uso de grandes conjuntos de antenas en el transmisor y en el receptor para compensar las pérdidas de propagación, y combinado con las limitaciones de potencia de señal mixta y de radiofrecuencia (RF), se requiere de nuevas técnicas de procesamiento de señales de comunicación de múltiples entradas y múltiples salidas (MIMO) para diseñar transceptores de bajo costo y consumo, pero con grandes ganancias de precodificación. Específicamente, las arquitecturas híbridas han ofrecido recientemente un enfoque innovador que permite aumentar la eficiencia energética de los

sistemas al desacoplar la precodificación digital de MIMO en una parte analógica o de RF de bajo consumo energético y otra de banda base, a la vez que preserva altas ganancias de precodificación. El diseño de los transceptores híbridos resulta una tarea desafiante, ya que al implementar la parte analógica de precodificación hay restricciones que conducen a problemas de optimización extremadamente complejos.

Otra técnica explorada en la actualidad que permite aumentar la eficiencia energética está basada en el paradigma de control del medio de propagación en redes emergentes de comunicaciones inalámbricas. Tradicionalmente, la optimización de los sistemas de comunicaciones se ha limitado al control de la transmisión en los extremos de la comunicación, es decir, los usuarios finales y la estación base (BS) o el controlador de la red. El canal inalámbrico es incontrolable y se convierte en uno de los principales factores limitantes para la mejora del rendimiento. Las superficies reflectantes inteligentes (IRSs) se componen de una gran variedad de elementos de dispersión, que se pueden configurar individualmente para generar cambios de fase adicionales a las señales. Por lo tanto, de cierto modo se pueden controlar las propiedades de propagación de la señal para favorecer la recepción de esta en su destino y, por lo tanto, crear la noción de un entorno de radio inteligente. El control de los cambios de fase en la IRS, combinado con la precodificación y filtrado convencional, puede generar potencialmente una ganancia de rendimiento en comparación con las redes inalámbricas no equipadas con IRSs. Este paradigma había sido empleado anteriormente para sistemas de radares y satélites mediante el empleo de superficies reflectantes, pero no se consideraba para esquemas con movilidad debido a la incapacidad de implementar superficies reflectantes que hicieran frente al dinamismo de los canales inalámbricos en dichos sistemas. Sin embrago, los avances obtenidos en la actualidad en el estudio de los metamateriales proporcionan garantías de reconfigurabilidad al habilitar el ajuste en tiempo real de los cambios de fase en las IRSs.

Al considerar la gran cantidad de beneficios que ofrecen las IRSs, se pueden examinar varios escenarios de aplicación al considerar esta tecnología, por ejemplo, sistemas de IoT, seguridad en sistemas de comunicaciones, escenarios de radio cognitiva (CR), sistemas en la banda de mmWave, etc. La implementación y diseño de estos sistemas conduce a problemas de optimización desafiantes, ya que las IRSs presentan restricciones de diseño similares a las obtenidas en la implementación del procesado de RF en las arquitecturas híbridas para ondas milimétricas, dado que son empleadas para insertar solo cambios de fase en las señales y no para amplificar o atenuar las mismas. Además, el hecho de emplear IRSs complica en ocasiones la etapa de estimación de canal en escenarios prácticos, ya que la IRS es un elemento pasivo incapaz de llevar a cabo el envío y la recepción de secuencias de entrenamiento.

En este trabajo analizamos e implementamos nuevos métodos de codificación de señales analógicas basados en el principio de optimización de JSCC. En particular, desarrollamos estrategias de codificación de baja complejidad computacional y adaptables a tamaños ajustables de palabras de código. También analizamos e implementamos nuevas técnicas de procesamiento de señales aplicadas a las arquitecturas híbridas en la banda de mmWave, tanto

para sistemas de banda estrecha como de banda ancha. Además, nos centramos en sistemas con múltiples usuarios (MU), los cuales son escenarios muy habituales en la práctica. Finalmente, desarrollamos técnicas de procesamiento de señales para establecer un mejor control del medio de comunicaciones en redes inalámbricas a través del despliegue de las IRSs.

B.1 Retículos para la Codificación de Fuentes Analógicas Correlacionadas

En esta tesis, como primera parte del trabajo realizado, hemos abordamos un esquema de transmisión de información analógica espacialmente correlacionada en un escenario de enlace ascendente de MU en un sistema de entrada única y múltiples salidas (SIMO), usando técnicas de JSCC basadas en retículos. Los retículos son estructuras algebraicas que se pueden emplear para implementar cuantificadores y codificadores, su uso para sistemas de codificación posibilita la implementación de sistemas con palabras de código de gran tamaño y, por ende, la codificación de grandes bloques de símbolos. En nuestro trabajo, los bloques de símbolos fuente se codifican individualmente en cada usuario con un JSCC analógico construido a partir de un retículo dado. En la BS, las estimaciones de los símbolos transmitidos son estimados conjuntamente, por medio de un enfoque de decodificación que explota la correlación espacial y el uso de palabras de código de gran tamaño.

El sistema de JSCC analógico basado en retículos ha sido diseñado y optimizado para la transmisión de bloques de símbolos con un tamaño de palabra de código arbitrario, lo cual representa un resultado novedoso en comparación a los trabajos encontrados en el estado del arte. En estos trabajos, los códigos están diseñados para sistemas de retardo cero, es decir, bloques de solo un símbolo. Esta contribución posibilita ampliar la flexibilidad de las técnicas JSCC analógicas como una alternativa práctica real a los esquemas digitales convencionales. En este sentido, el diseño propuesto es flexible para trabajar con diferentes tamaños de código y explota eficientemente la correlación espacial. Esto ofrece ventajas para la optimización de parámetros y en el procedimiento de decodificación, permitiendo la aplicación en redes de sensores inalámbricas (WSN).

Para bloques de símbolos considerablemente extensos, se han considerado los retículos de Craig, ya que reducen el costo computacional de la operación de codificación en el sistema analógico de JSCC. La posibilidad de ajustar la densidad de los retículos de Craig nos permite también balancear la relación entre el rendimiento del sistema y la complejidad computacional. Se ha realizado una evaluación experimental del esquema propuesto para diferentes configuraciones, obteniendo ganancias en ciertos escenarios donde los codificadores de retardo cero encontrados en la literatura han mostrado algunas limitaciones de rendimiento, como en configuraciones de sistemas no ortogonales o con muy baja correlación entre las fuentes. Además, hemos llevado a cabo un análisis del impacto del tamaño del bloque de

símbolos a codificar y de la densidad del retículo gracias al diseño basado en los retículos de Craig. También analizamos la complejidad en el proceso de decodificación usando diferentes retículos y diferentes tamaños de bloques de símbolos.

B.2 Agrupación de Usuarios en Sistemas de Onda Milimétrica con Arquitecturas Híbridas

Los esquemas híbridos analógicos-digitales para la precodificación y el filtrado han demostrado ser una estrategia de baja complejidad y/o baja potencia para obtener ganancias razonables de precodificación en sistemas MIMO de mmWave. La precodificación híbrida realiza conjuntamente el procesamiento de banda base y el procesamiento analógico en el dominio de RF, lo cual conlleva a una reducción del número de cadenas de RF del sistema, y por tanto, a una reducción del hardware. Sin embargo, en estos sistemas, el número de cadenas de RF limita el número máximo de flujos de datos que pueden manejar simultáneamente los transceptores. Al considerar un escenario de enlace ascendente de un sistema MU mmWave MIMO, la reducción de hardware basada en transceptores híbridos está limitada por la cantidad de flujos de datos que deben ser atendidos simultáneamente por la BS. La mayoría de los trabajos en la literatura científica han abordado el diseño de transceptores híbridos considerando que se despliegan más cadenas de RF que flujos de datos, una suposición poco realista cuando la cantidad de usuarios es muy grande. Por otro lado, convencionalmente se asume independencia estadística en los sistemas de mmWave con MU. Esta suposición no se cumple en escenarios como las WSNs, donde las fuentes producen información correlacionadas.

En esta tesis, como segunda línea de investigación, hemos trabajado en un enfoque de agrupación de usuarios para servir una gran cantidad de fuentes correlacionadas con un número limitado de cadenas de RF, a través del uso de la codificación lineal y analógica de cuantificador distribuido (DQLC), lo cual constituye un esquema de acceso múltiple no ortogonal (NOMA). En el trabajo se analiza la asignación de los grupos a cada usuario en función de su canal inalámbrico y la correlación con los demás usuarios. También se ha analizado el diseño del filtro de arquitectura híbrida desplegado en la BS común para atender conjuntamente a los usuarios agrupados. Además, hemos propuesto un diseño de filtrado híbrido basado en el error cuadrático medio mínimo (MMSE) para explotar la correlación espacial entre las fuentes, para un enlace ascendente de sistemas de mmWave sin agrupación de usuarios ni codificación DQLC.

Como resultados se han obtenido ganancias de rendimiento, en términos de la distorsión de los símbolos recibidos en la BS, sobre los enfoques propuestos en el estado del arte en varias configuraciones de sistemas limitados en hardware de RF para esquemas de MU. Se han observado ganancias también sobre trabajos recientes en la literatura al implementar el diseño de filtro MMSE para sistemas sin agrupación de usuarios. Además, se ha llevado a cabo un análisis de los parámetros considerados para agrupar los usuarios y su impacto en el rendimiento.

B.3 Agrupación de Usuarios en Sistemas de Banda Ancha de Onda Milimétrica con Arquitecturas Híbridas

La implementación de arquitecturas híbridas en mmWave MIMO de banda ancha constituye un desafío aún más complicado que en sistemas de banda estrecha, porque el procesamiento de la señal en el dominio de RF está restringido a ser plano en frecuencia, es decir, común para todas las subportadoras en un sistema que emplea OFDM. Además, si se considera un enlace ascendente con múltiples usuarios y una BS común, el filtro de RF desplegado en la BS será común para todos los usuarios. En esta tesis, hemos abordamos conjuntamente la agrupación de usuarios, el diseño del precodificador de los usuarios y el diseño del filtrado híbrido en la BS para el enlace ascendente de los sistemas MU mmWave MIMO de banda ancha. Por un lado, la precodificación en los usuarios y el filtrado híbrido desplegado en la BS están diseñados conjuntamente para minimizar el impacto de tener componentes de RF de frecuencia plana. Por otro lado, un número de usuarios considerados en el enlace ascendente es superior al número de cadenas de RF, por lo que son servidos por la BS al emplear un esquema de NOMA basado en DQLC que tiene en cuenta el efecto de desviación de los haces de las antenas (beam squint), usualmente encontrado en sistemas de banda ancha. Se aborda una estrategia de asignación de grupos para los usuarios basada en el efecto de beam squint, la correlación entre los usuarios y sus respuestas de canales inalámbricos.

Los resultados obtenidos muestran ganancias notables de rendimiento de los enfoques propuestos sobre los diseños encontrados en la literatura. Específicamente, el diseño propuesto para arquitecturas híbridas en sistemas de banda ancha arroja grandes ganancias sobre los diseños encontrados en la literatura. Además el esquema propuesto para la asignación de usuarios por grupos ofrece beneficios sobre estrategias de referencia de asignación aleatoria.

B.4 Sistemas de Banda Ancha Equipados con IRSs

Una IRS es un reflector controlable en tiempo real que consta de una gran cantidad de elementos pasivos que introducen cambios de fase en las señales provenientes de uno o múltiples transmisores. Las IRSs permiten el control parcial del entorno de radio propagación si se logra configurar adecuadamente los cambios de fase y, por lo tanto, la dirección de salida de las señales reflejadas hacia el receptor. En la última línea de investigación de esta tesis, hemos realizado un estudio acerca de un enlace descendente de MU mmWave MIMO de banda ancha en un sistema asistido por una IRS, donde además se considera que la estimación de canal es imperfecta. Uno de los grandes retos del diseño de este escenario es la implementación de los cambios de fase que se introducen en la IRS, la cual constituye un elemento pasivo que es común para todas las subportadoras y, además, es común para todos los usuarios. También resulta de interés el diseño de los precodificadores y filtros de banda ancha que dependen de la frecuencia de cada subportadora. En nuestro trabajo, la matriz de cambio de fases de la IRS,

los filtros y los precodificadores han sido diseñados para minimizar el error cuadrático medio (MSE), considerando los errores introducidos debido al conocimiento imperfecto del canal. Se ha establecido un problema de minimización del MSE total de los símbolos transmitidos, el cual se ha resuelto mediante el empleo de la dualidad entre los sistemas de radiodifusión (BC) y los sistemas de acceso múltiple al medio (MAC), y siguiendo un enfoque de minimización alternante (AM) combinada con un algoritmo de gradiente proyectado (PG).

Los resultados numéricos muestran que el enfoque de minimización del MSE propuesto conduce a ganancias sustanciales, tanto en términos del propio MSE como de la tasa suma alcanzable del sistema, con respecto a las estrategias de referencia que ignoran los errores de estimación de los canales. Estos errores deben ser tratados para el control de la interferencia entre usuarios, el diseño de los transceptores y los cambios de fase introducidos por la IRS. También se ha observado que las ganancias aumentan a medida que se consideran IRSs con un mayor número de elementos.

Appendix III

List of Acronyms

5G fifth generation
AF O-Ps amplify-and-forward with optimized precoders
AoA angles of arrival
AoD angles of departure
AWGN additive white Gaussian noise
B5G beyond fifth-generation
BC broadcast channel
BS base station
CBTC communications-based train control
CR cognitive radio
CSI channel state information
D2D device-to-device
DPC dirty paper coding
DQLC distributed quantizer linear coding
FCS fully-connected structure
FPGA field programmable gate array
GNU-SVD group null-space directed SVD
H-LISA hybrid-linear successive allocation
IoT Internet of things
IRS intelligent reflecting surface
ISI inter-symbol interference
JCR Journal Citation Reports
JIF Journal Impact Factor
JSCC joint source-channel coding
LISA linear successive allocation
LoS line-of-sight
LS least squares
LTE Long Term Evolution

M2M machine to machine
MAC multiple access channel
MAP maximum a posteriori
MIMO multiple-input multiple-output
MISO multiple-input single-output
ML machine learning
MMSE minimum mean square error
mmWave millimeter-wave
MRC maximum ratio combining
MRT maximum ratio transmitter
MSE mean squared error
MU multiuser
No-IRS MRT-Ps no IRS with MRT precoders
NOMA non-orthogonal multiple access
OFDM orthogonal frequency-division multiplexing
O-IRS MRT-Ps optimized IRS with MRT precoders
OPTA optimum performance theoretically attainable
OTA over-the-air
PCS partially-connected structure
PDF probability density function
PER packet error ratio
PG projected gradient
SC-FDMA single-carrier frequency-division multiple access
PIN positive-intrinsic negative
PS phase shifter
RF radio frequency
R-IRS O-Ps random IRS with optimized precoders
SDR signal-to-distortion ratio
SIMO single-input multiple-output
SINR signal-to-interference-plus-noise ratio
SISO single-input-single-output
SNR signal-to-noise ratio
THz Terahertz
UAV unmanned aerial vehicle
ULA uniform linear array
UPA uniform planar array
URLLC ultra-reliable and low-latency communications
VQ vector quantization
VQLC vector quantizer linear coding

WSN wireless sensor network
ZF zero-forcing

References

[1] Alan V. Oppenheim, John R. Buck, and Ronald W. Schafer, ***Discrete-time signal processing. Vol. 2***. Upper Saddle River, NJ: Prentice Hall, 2001.

[2] Alan V. Oppenheim, Alan S. Willsky, Syed Hamid Nawab, Gloria Mata Hernández, *et al.*, ***Signals & systems***. Pearson Educación, 1997.

[3] Leon W. Couch, Muralidhar Kulkarni, and U. Sripati Acharya, ***Digital and analog communication systems***. Citeseer, 2013, vol. 8.

[4] Robert Gray, "**Vector quantization**", *IEEE Assp Magazine*, vol. 1, no. 2, pp. 4–29, 1984.

[5] T. Goblick, "**Theoretical limitations on the transmission of data from analog sources**", *IEEE Transactions on Information Theory*, vol. 11, no. 4, pp. 558–567, 1965. DOI: 10.1109/TIT.1965.1053821.

[6] Claude Elwood Shannon, "**A mathematical theory of communication**", *The Bell system technical journal*, vol. 27, no. 3, pp. 379–423, 1948.

[7] Theodore S. Rappaport, Robert W. Heath Jr, Robert C. Daniels, and James N. Murdock, "**Millimeter wave wireless communications**", *Prentice-Hall*, 2014.

[8] D.T. Emerson, "**The work of jagadis chandra bose: 100 years of millimeter-wave research**", *IEEE Transactions on Microwave Theory and Techniques*, vol. 45, no. 12, pp. 2267–2273, 1997.
DOI: 10.1109/22.643830.

[9] Mustafa Riza Akdeniz, Yuanpeng Liu, Mathew K. Samimi, Shu Sun, Sundeep Rangan, Theodore S. Rappaport, and Elza Erkip, "**Millimeter wave channel modeling and cellular capacity evaluation**", *IEEE Journal on Selected Areas in Communications*, vol. 32, no. 6, pp. 1164–1179, 2014, ISSN: 0733-8716.
DOI: 10.1109/JSAC.2014.2328154.

[10] Robert W. Heath, Nuria González-Prelcic, Sundeep Rangan, Wonil Roh, and Akbar M. Sayeed, "**An overview of signal processing techniques for millimeter wave MIMO systems**", *IEEE Journal of Selected Topics in Signal Processing*, vol. 10, no. 3, pp. 436–453, 2016.
DOI: 10.1109/JSTSP.2016.2523924.

[11] Roi Méndez-Rial, Cristian Rusu, Nuria González-Prelcic, Ahmed Alkhateeb, and Robert W. Heath, "**Hybrid MIMO architectures for millimeter wave communications: Phase shifters or switches?**" *IEEE Access*, vol. 4, pp. 247–267, 2016.
DOI: 10.1109/ACCESS.2015.2514261.

[12] Shimin Gong, Xiao Lu, Dinh Thai Hoang, Dusit Niyato, Lei Shu, Dong In Kim, and Ying-Chang Liang, "**Toward smart wireless communications via intelligent reflecting surfaces: A contemporary survey**", *IEEE Communications Surveys Tutorials*, vol. 22, no. 4, pp. 2283–2314, 2020.
DOI: 10.1109/COMST.2020.3004197.

[13] Rawan Alghamdi, Reem Alhadrami, Dalia Alhothali, Heba Almorad, Alice Faisal, Sara Helal, Rahaf Shalabi, Rawan Asfour, Noofa Hammad, Asmaa Shams, Nasir Saeed, Hayssam Dahrouj, Tareq Y. Al-Naffouri, and Mohamed-Slim Alouini, "**Intelligent surfaces for 6G wireless networks: A survey of optimization and performance analysis techniques**", *IEEE Access*, vol. 8, pp. 202 795–202 818, 2020.
DOI: 10.1109/ACCESS.2020.3031959.

[14] Emil Björnson, Luca Sanguinetti, Henk Wymeersch, Jakob Hoydis, and Thomas L. Marzetta, "**Massive MIMO is a reality—what is next?: Five promising research directions for antenna arrays**", *Digital Signal Processing*, vol. 94, pp. 3–20, 2019, Special Issue on Source Localization in Massive MIMO, ISSN: 1051-2004.
DOI: https://doi.org/10.1016/j.dsp.2019.06.007. Online access: https://www.sciencedirect.com/science/article/pii/S1051200419300776.

[15] Emil Björnson, Özgecan Özdogan, and Erik G. Larsson, "**Intelligent reflecting surface versus decode-and-forward: How large surfaces are needed to beat relaying?**" *IEEE Wireless Communications Letters*, vol. 9, no. 2, pp. 244–248, 2020.
DOI: 10.1109/LWC.2019.2950624.

[16] Dongfang Xu, Xianghao Yu, Yan Sun, Derrick Wing Kwan Ng, and Robert Schober, "**Resource allocation for secure IRS-assisted multiuser MISO systems**", *Proc. of IEEE Globecom Workshops (GC Wkshps)*, 2019, pp. 1–6.
DOI: 10.1109/GCWkshps45667.2019.9024490.

[17] Ludek Subrt and Pavel Pechac, "**Controlling propagation environments using intelligent walls**", *Proc. of 2012 6th European Conference on Antennas and Propagation (EUCAP)*, 2012, pp. 1–5.
DOI: 10.1109/EuCAP.2012.6206517.

[18] Allen Welkie, Longfei ShangGonzález-Coma, Jeremy Gummeson, Wenjun Hu, and Kyle Jamieson, "**Programmable radio environments for smart spaces**", *Proc. of 16th ACM Workshop on Hot Topics in Networks*, 2017, pp. 36–42.

[19] **NTT DOCOMO and metawave announce successful demonstration of 28GHz-band 5G using world's first meta-structure technology**, https://www.businesswire.com/news/home/20181204005253/en/NTT-DOCOMO-and-Metawave-Announce-Successful-Demonstration-of-28GHz-Band-5G-Using-Worlds-First-Meta-Structure-Technology, Accessed: 2021-09-03, 2018. (visited on 09/03/2021).

[20] P. Suárez-Casal, O. Fresnedo, L. Castedo, and J. García-Frías, "**Analog transmission of correlated sources over fading SIMO multiple access channels**", *IEEE Transactions on Communications*, vol. 65, no. 7, pp. 2999–3011, 2017, ISSN: 0090-6778. DOI: 10.1109/TCOMM.2017.2695197.

[21] Pål Anders Floor, Anna N. Kim, Tor A. Ramstad, and Ilangko Balasingham, "**On transmission of multiple Gaussian sources over a Gaussian MAC using a VQLC mapping**", *Proc. of 2012 IEEE Information Theory Workshop*, 2012, pp. 50–54. DOI: 10.1109/ITW.2012.6404726.

[22] Yichuan Hu, Zhongmin Wang, Javier Garcia-Frias, and Gonzalo R. Arce, "**Non-linear coding for improved performance in compressive sensing**", *Proc. of 2009 43rd Annual Conference on Information Sciences and Systems*, 2009, pp. 18–22. DOI: 10.1109/CISS.2009.5054682.

[23] Tor A. Ramstad, "**Shannon mappings for robust communication**", *Telektronikk*, vol. 98, no. 1, pp. 114–128, 2002.

[24] Jose Balsa, Tomás Domínguez-Bolaño, Óscar Fresnedo, José A. García-Naya, and Luis Castedo, "**Transmission of still images using low-complexity analog joint source-channel coding**", *Sensors*, vol. 19, no. 13, 2019, ISSN: 1424-8220. DOI: 10.3390/s19132932. Online access: https://www.mdpi.com/1424-8220/19/13/2932.

[25] Paal Anders Floor, Anna N. Kim, Niklas Wernersson, Tor A. Ramstad, Mikael Skoglund, and Ilangko Balasingham, "**Zero-delay joint source-channel coding for a bivariate Gaussian on a Gaussian MAC**", *IEEE Transactions on Communications*, vol. 60, no. 10, pp. 3091–3102, 2012. DOI: 10.1109/TCOMM.2012.071912.110456.

[26] Fredrik Hekland, Pal Anders Floor, and Tor A. Ramstad, "**Shannon-kotel-nikov mappings in joint source-channel coding**", *IEEE Transactions on Communications*, vol. 57, no. 1, pp. 94–105, 2009. DOI: 10.1109/TCOMM.2009.0901.070075.

[27] Johannes Kron, Fady Alajaji, and Mikael Skoglund, "**Low-delay joint source-channel mappings for the Gaussian MAC**", *IEEE Communications Letters*, vol. 18, no. 2, pp. 249–252, 2014. DOI: 10.1109/LCOMM.2013.120413.132088.

[28] Xianghao Yu, Jun Zhang, and Khaled B. Letaief, "**Alternating minimization for hybrid precoding in multiuser OFDM mmWave systems**", *Proc. of 2016 50th Asilomar Conference on Signals, Systems and Computers*, 2016, pp. 281–285.
DOI: 10.1109/ACSSC.2016.7869042.

[29] Tadilo Endeshaw Bogale, Long Bao Le, Afshin Haghighat, and Luc Vandendorpe, "**On the number of RF chains and phase shifters, and scheduling design with hybrid analog–digital beamforming**", *IEEE Transactions on Wireless Communications*, vol. 15, no. 5, pp. 3311–3326, 2016.
DOI: 10.1109/TWC.2016.2519883.

[30] Jose P. Gonzalez-Coma, Javier Rodriguez-Fernandez, Nuria Gonzalez-Prelcic, Luis Castedo, and Robert W. Heath, "**Channel estimation and hybrid precoding for frequency selective multiuser mmWave MIMO systems**", *IEEE Journal of Selected Topics in Signal Processing*, vol. 12, no. 2, pp. 353–367, 2018, ISSN: 1932-4553, 1941-0484.
DOI: 10.1109/JSTSP.2018.2819130.

[31] José P. González-Coma, Wolfgang Utschick, and Luis Castedo, "**Hybrid LISA for wideband multiuser millimeter-wave communication systems under beam squint**", *IEEE Transactions on Wireless Communications*, vol. 18, no. 2, pp. 1277–1288, 2019.
DOI: 10.1109/TWC.2018.2890667.

[32] Wenjing Yan, Xiaojun Yuan, Zhen-Qing He, and Xiaoyan Kuai, "**Passive beamforming and information transfer design for reconfigurable intelligent surfaces aided multiuser MIMO systems**", *IEEE Journal on Selected Areas in Communications*, vol. 38, no. 8, pp. 1793–1808, 2020.
DOI: 10.1109/JSAC.2020.3000811.

[33] Min Fu, Yong Zhou, and Yuanming Shi, "**Intelligent reflecting surface for downlink non-orthogonal multiple access networks**", *Proc. of 2019 IEEE Globecom Workshops (GC Wkshps)*, 2019, pp. 1–6.
DOI: 10.1109/GCWkshps45667.2019.9024675.

[34] Özgecan Özdogan, Emil Björnson, and Erik G. Larsson, "**Using intelligent reflecting surfaces for rank improvement in MIMO communications**", *Proc. of ICASSP 2020 - 2020 IEEE International Conference on Acoustics, Speech and Signal Processing (ICASSP)*, 2020, pp. 9160–9164.
DOI: 10.1109/ICASSP40776.2020.9052904.

[35] Minchae Jung, Walid Saad, Mérouane Debbah, and Choong Seon Hong, "**Asymptotic optimality of reconfigurable intelligent surfaces: Passive beamforming and achievable rate**", *Proc. of ICC 2020 - 2020 IEEE International Conference on*

Communications (ICC), 2020, pp. 1–6.
DOI: 10.1109/ICC40277.2020.9148640.

[36] Darian Pérez-Adán, Óscar Fresnedo, José P. González-Coma, and Luis Castedo, "**User grouping for the uplink of multiuser hybrid mmWave MIMO**", *IEEE Access*, vol. 8, pp. 55 323–55 341, 2020.
DOI: 10.1109/ACCESS.2020.2981280.

[37] ——, "**Wideband user grouping for uplink multiuser mmWave MIMO systems with hybrid combining**", *IEEE Access*, vol. 9, pp. 41 360–41 372, 2021.
DOI: 10.1109/ACCESS.2021.3065581.

[38] ——, "**Intelligent reflective surfaces for wireless networks: An overview of applications, approached issues, and open problems**", *Electronics*, vol. 10, no. 19, 2021, ISSN: 2079-9292.
DOI: 10.3390/electronics10192345. Online access: https://www.mdpi.com/2079-9292/10/19/2345.

[39] Darian Pérez-Adán, Michael Joham, Óscar Fresnedo, José P. González-Coma, Luis Castedo, and Wolfgang Utschick, "**An alternating minimization approach for wideband downlink multiuser IRS-aided mmWave MIMO systems**", *In Preparation for IEEE Transactions on Signal Processing*, pp. 1–13, 2022.

[40] Pedro Suárez-Casal, Óscar Fresnedo, Darian Pérez-Adán, and Luis Castedo, "**Lattice-based analog mappings for low latency wireless sensor networks**", *Submitted to IEEE Internet of Things Journal*, pp. 1–15, 2022.

[41] Darian Pérez-Adán, José P. González-Coma, Óscar Fresnedo, and Luis Castedo, "**Hybrid mmWave MIMO transceivers for the uplink of multiple correlated users**", *Proc. of 2019 IEEE 20th International Workshop on Signal Processing Advances in Wireless Communications (SPAWC)*, 2019, pp. 1–5.
DOI: 10.1109/SPAWC.2019.8815403.

[42] ——, "**Low-complexity hybrid transceivers for uplink multiuser mmWave MIMO by user clustering**", *Proc. of 2019 27th European Signal Processing Conference (EUSIPCO)*, 2019, pp. 1–5.
DOI: 10.23919/EUSIPCO.2019.8902982.

[43] Pedro Suárez-Casal, Óscar Fresnedo, José P. González-Coma, Darian Pérez-Adán, and Luis Castedo, "**Analog transmission of correlated sources in SIMO MAC using hexagonal lattices**", *Proc. of WSA 2020; 24th International ITG Workshop on Smart Antennas*, 2020, pp. 1–6.

[44] Darian Pérez-Adán, Óscar Fresnedo, José P. González-Coma, and Luis Castedo, "**Hybrid combining design for user clustering in mmWave MIMO systems**", *Proc. of 2020 IEEE Workshop on Signal Processing Systems (SiPS)*, 2020, pp. 1–6.
DOI: 10.1109/SiPS50750.2020.9195228.

[45] ——, "**Alternating minimization algorithm for multiuser RIS-assisted MIMO systems**", *Proc. of 2022 IEEE International Symposium on Broadband Multimedia Systems and Broadcasting (BMSB)*, 2022, pp. 1–6.
DOI: 10.1109/BMSB55706.2022.9828734.

[46] Darian Pérez-Adán, Michael Joham, Óscar Fresnedo, José P. González-Coma, Wolfgang Utschick, and Luis Castedo, "**Alternating minimization for the downlink of wideband IRS-aided mmWave MIMO systems**", *Submitted to 2023 International ITG 26th Workshop on Smart Antennas and 13th Conference on Systems, Communications, and Coding*, pp. 1–6.

[47] Dariel Pereira-Ruisánchez, Óscar Fresnedo, Darian Pérez-Adán, and Luis Castedo, "**Deep contextual bandit and reinforcement learning for IRS-assisted MU-MIMO systems**", *Submitted to IEEE Transactions on Vehicular Technology (2nd round of reviews)*, pp. 1–12.

[48] ——, "**Joint optimization of IRS-assisted MU-MIMO communication systems through a DRL-based twin delayed DDPG approach**", *Proc. of 2022 IEEE International Symposium on Broadband Multimedia Systems and Broadcasting (BMSB)*, 2022, pp. 1–6.
DOI: 10.1109/BMSB55706.2022.9828652.

[49] Dariel Pereira Ruisánchez, Dalila Garrido Mirabal, Ernesto Fontes Pupo, Claudia Carballo González, Darian Pérez-Adán, and Flavia Alvarez Cesar, "**Prediction of signal quality and SFN interference metrics using machine learning models**", *Proc. of 2021 IEEE International Symposium on Broadband Multimedia Systems and Broadcasting (BMSB)*, 2021, pp. 1–6.
DOI: 10.1109/BMSB53066.2021.9547111.

[50] Dariel Pereira-Ruisánchez, Darian Pérez-Adán, and Luis Castedo, "**A deep learning-based strategy to predict self-interference in SFN DTT**", *Proc. of The 4th XoveTIC Conference, Engineering Proceedings*, vol. 7, no. 1, pp. 1–4, 2021.

[51] Dariel Pereira-Ruisánchez, Óscar Fresnedo, Darian Pérez-Adán, and Luis Castedo, "**Joint optimization of IRS-assisted MIMO communications through a deep contextual bandit approach**", *Proc. of The 5th XoveTIC Conference, Engineering Proceedings*, pp. 1–4, 2022.

[52] Andrea Goldsmith, ***Wireless communications***. Cambridge university press, 2005.

[53] Jerry R. Hampton, ***Introduction to MIMO communications***. Cambridge university press, 2013.

[54] David Tse and Pramod Viswanath, ***Fundamentals of Wireless Communication***. Cambridge University Press, 2005.

[55] Henrik Schulze and Christian Lüders, ***Theory and applications of OFDM and CDMA: Wideband wireless communications***. John Wiley & Sons, 2005.

[56] Ali Zaidi, Fredrik Athley, Jonas Medbo, Ulf Gustavsson, Giuseppe Durisi, and Xiaoming Chen, ***5G Physical Layer: Principles, models and technology components***. Academic Press, 2018.

[57] Helmut Bolcskei, "**MIMO-OFDM wireless systems: Basics, perspectives, and challenges**", *IEEE wireless communications*, vol. 13, no. 4, pp. 31–37, 2006.

[58] T.M. Schmidl and D.C. Cox, "**Robust frequency and timing synchronization for OFDM**", *IEEE Transactions on Communications*, vol. 45, no. 12, pp. 1613–1621, 1997. DOI: 10.1109/26.650240.

[59] B. Le Floch, R. Halbert-Lassalle, and D. Castelain, "**Digital sound broadcasting to mobile receivers**", *IEEE Transactions on Consumer Electronics*, vol. 35, no. 3, pp. 493–503, 1989.
DOI: 10.1109/30.44309.

[60] Claude Elwood Shannon, "**Communication in the presence of noise**", *Proceedings of the IRE*, vol. 37, no. 1, pp. 10–21, 1949.

[61] Daniel Persson, Johannes Kron, Mikael Skoglund, and Erik G. Larsson, "**Joint source-channel coding for the MIMO broadcast channel**", *IEEE Transactions on Signal Processing*, vol. 60, no. 4, pp. 2085–2090, 2012.
DOI: 10.1109/TSP.2011.2180716.

[62] Steven M. Kay, ***Fundamentals of Statistical Signal Processing***. Prentice Hall, 1993.

[63] Q.H. Spencer, A.L. Swindlehurst, and M. Haardt, "**Zero-forcing methods for downlink spatial multiplexing in multiuser MIMO channels**", *IEEE Transactions on Signal Processing*, vol. 52, no. 2, pp. 461–471, 2004, ISSN: 1053-587X.
DOI: 10.1109/TSP.2003.821107.

[64] M. Schubert and H. Boche, "**Solution of the multiuser downlink beamforming problem with individual SINR constraints**", *IEEE Transactions on Vehicular Technology*, vol. 53, no. 1, pp. 18–28, 2004.
DOI: 10.1109/TVT.2003.819629.

[65] S. Vishwanath, N. Jindal, and A. Goldsmith, "**Duality, achievable rates, and sum-rate capacity of Gaussian MIMO broadcast channels**", *IEEE Transactions on Information Theory*, vol. 49, no. 10, pp. 2658–2668, 2003.
DOI: 10.1109/TIT.2003.817421.

[66] Raphael Hunger, Michael Joham, and Wolfgang Utschick, "**On the MSE-duality of the broadcast channel and the multiple access channel**", *IEEE Transactions on Signal Processing*, vol. 57, no. 2, pp. 698–713, 2009.
DOI: 10.1109/TSP.2008.2008253.

[67] Michael Joham, Michael Vonbun, and Wolfgang Utschick, "**MIMO BC/MAC MSE duality with imperfect transmitter and perfect receiver CSI**", *Proc. of 2010 IEEE 11th International Workshop on Signal Processing Advances in Wireless Communications (SPAWC)*, 2010, pp. 1–5.
DOI: 10.1109/SPAWC.2010.5670866.

[68] A.M. Sayeed, "**Deconstructing multiantenna fading channels**", *IEEE Transactions on Signal Processing*, vol. 50, no. 10, pp. 2563–2579, 2002, ISSN: 1053-587X.
DOI: 10.1109/TSP.2002.803324.

[69] L.M. Correia and P.F.M. Smulders, "**Characterisation of propagation in 60 GHz radio channels**", *Electronics & Communication Engineering Journal*, vol. 9, no. 2, pp. 73–80, 1997, ISSN: 0954-0695.
DOI: 10.1049/ecej:19970204.

[70] Zhiqiang Wang, Long Cheng, Jun Wang, and González-Comagrong Yue, "**Digital compensation wideband analog beamforming for millimeter-wave communication**", *Proc. of 2018 IEEE 87th Vehicular Technology Conference (VTC Spring)*, 2018, pp. 1–5.
DOI: 10.1109/VTCSpring.2018.8417590.

[71] José P. González-Coma and Luis Castedo, "**Wideband hybrid precoding using time modulated arrays**", *IEEE Access*, vol. 8, pp. 144 638–144 653, 2020.
DOI: 10.1109/ACCESS.2020.3014471.

[72] Kiran Venugopal, Nuria González-Prelcic, and Robert W. Heath, "**Optimal frequency-flat precoding for frequency-selective millimeter wave channels**", *IEEE Transactions on Wireless Communications*, vol. 18, no. 11, pp. 5098–5112, 2019.
DOI: 10.1109/TWC.2019.2932932.

[73] Bolei Wang, Feifei Gao, Shi Jin, Hai Lin, and Geoffrey Ye Li, "**Spatial- and frequency-wideband effects in millimeter-wave massive MIMO systems**", *IEEE Transactions on Signal Processing*, vol. 66, no. 13, pp. 3393–3406, 2018.
DOI: 10.1109/TSP.2018.2831628.

[74] Constantine A. Balanis, ***Antenna theory: analysis and design***, 3rd ed. Hoboken, NJ, John Wiley, 2005, ISBN: 978-0-471-66782-7.

[75] Y. Chen, Y. Xiong, D. Chen, T. Jiang, S. X. Ng, and L. Hanzo, "**Hybrid precoding for wideband millimeter wave MIMO systems in the face of beam squint**", *IEEE Transactions on Wireless Communications*, pp. 1–1, 2020.
DOI: 10.1109/TWC.2020.3036945.

[76] Amos Lapidoth and Stephan Tinguely, "**Sending a bivariate Gaussian source over a Gaussian MAC with feedback**", *IEEE Transactions on Information Theory*, vol. 56, no. 4, pp. 1852–1864, 2010.
DOI: 10.1109/TIT.2010.2040870.

[77] Sae-Young Chung, "On the construction of some capacity-approaching coding schemes," Ph.D. dissertation, Massachusetts Institute of Technology, 2000.

[78] T. A. Ramstad, "**Shannon mappings for robust communication**", *Telektronikk*, vol. 98, no. 1, pp. 114–128, 2002.

[79] O. Fresnedo, F. J. Vazquez-Araujo, L. Castedo, and J. Garcia-Frias, "**Low-complexity near-optimal decoding for analog joint source channel coding using space-filling curves**", *IEEE Communications Letters*, vol. 17, no. 4, pp. 745–748, 2013.
DOI: 10.1109/LCOMM.2013.021913.122782.

[80] Oscar Fresnedo, José P. González-Coma, Mohamed Hassanin, Luis Castedo, and Javier García-Frías, "**Evaluation of analog joint source-channel coding systems for multiple access channels**", *IEEE Transactions on Communications*, vol. 63, no. 6, pp. 2312–2324, 2015.
DOI: 10.1109/TCOMM.2015.2427164.

[81] Amos Lapidoth and Stephan Tinguely, "**Sending a bivariate Gaussian over a Gaussian MAC**", *IEEE Transactions on Information Theory*, vol. 56, no. 6, pp. 2714–2752, 2010.
DOI: 10.1109/TIT.2010.2044058.

[82] Michael Gastpar, "**Uncoded transmission is exactly optimal for a simple Gaussian "sensor" network**", *IEEE Transactions on Information Theory*, vol. 54, no. 11, pp. 5247–5251, 2008.
DOI: 10.1109/TIT.2008.929967.

[83] Xiaodong Cai and James W. Modestino, "**Bandwidth expansion shannon mapping for analog error-control coding**", *Proc. of 2006 40th Annual Conference on Information Sciences and Systems*, 2006, pp. 1709–1712.
DOI: 10.1109/CISS.2006.286411.

[84] V.A. Vaishampayan and S.I.R. Costa, "**Curves on a sphere, shift-map dynamics, and error control for continuous alphabet sources**", *IEEE Transactions on Information Theory*, vol. 49, no. 7, pp. 1658–1672, 2003.
DOI: 10.1109/TIT.2003.813561.

[85] Pål Anders Floor, Anna N. Kim, Tor A. Ramstad, Ilangko Balasingham, Niklas Wernersson, and Mikael Skoglund, "**On joint source-channel coding for a multivariate Gaussian on a Gaussian MAC**", *IEEE Transactions on Communications*, vol. 63, no. 5, pp. 1824–1836, 2015.
DOI: 10.1109/TCOMM.2015.2410774.

[86] Niklas Wernersson and Mikael Skoglund, "**Nonlinear coding and estimation for correlated data in wireless sensor networks**", *IEEE Transactions on Communications*, vol. 57, no. 10, pp. 2932–2939, 2009.
DOI: 10.1109/TCOMM.2009.10.080230.

[87] M. S. Mehmetoglu, E. Akyol, and K. Rose, "**Deterministic annealing-based optimization for zero-delay source-channel coding in networks**", *IEEE Transactions on Communications*, vol. 63, no. 12, pp. 5089–5100, 2015, ISSN: 0090-6778.
DOI: 10.1109/TCOMM.2015.2494004.

[88] Johannes Karlsson and Mikael Skoglund, "**Lattice-based source-channel coding in wireless sensor networks**", *Proc. of 2011 IEEE International Conference on Communications (ICC)*, 2011, pp. 1–5.
DOI: 10.1109/icc.2011.5962670.

[89] John Horton Conway and Neil James Alexander Sloane, ***Sphere packings, lattices and groups***. Springer Science & Business Media, 2013, vol. 290.

[90] G.Nebe and N.J.A. Sloane, **A catalogue of lattices**, http://www.math.rwth-aachen.de/~Gabriele.Nebe/LATTICES/.

[91] John Leech, "**Notes on sphere packings**", *Canadian Journal of Mathematics*, vol. 19, pp. 251–267, 1967.

[92] Henry Cohn and Abhinav Kumar, "**Optimality and uniqueness of the leech lattice among lattices**", *Annals of mathematics*, pp. 1003–1050, 2009.

[93] E. Agrell, T. Eriksson, A. Vardy, and K. Zeger, "**Closest point search in lattices**", *IEEE Transactions on Information Theory*, vol. 48, no. 8, pp. 2201–2214, 2002.
DOI: 10.1109/TIT.2002.800499.

[94] Maurice Craig, "**Extreme forms and cyclotomy**", *Mathematika*, vol. 25, no. 1, pp. 44–56, 1978.

[95] Ravi Kannan, "**Improved algorithms for integer programming and related lattice problems**", *Proc. of fifteenth annual ACM symposium on Theory of computing*, 1983, pp. 193–206.

[96] Michael Pohst, "**On the computation of lattice vectors of minimal length, successive minima and reduced bases with applications**", *ACM Sigsam Bulletin*, vol. 15, no. 1, pp. 37–44, 1981.

[97] Maurice Craig, "**A cyclotomic construction for leech's lattice**", *Mathematika*, vol. 25, no. 2, pp. 236–241, 1978.

[98] B.M. Hochwald and S. ten Brink, "**Achieving near-capacity on a multiple-antenna channel**", *IEEE Transactions on Communications*, vol. 51, no. 3, pp. 389–399, 2003.
DOI: 10.1109/TCOMM.2003.809789.

[99] B. Hassibi and H. Vikalo, "**On the sphere-decoding algorithm I. expected complexity**", *IEEE Transactions on Signal Processing*, vol. 53, no. 8, pp. 2806–2818, 2005.
DOI: 10.1109/TSP.2005.850352.

[100] Pedro Suárez-Casal, Jose P. González-Coma, Óscar Fresnedo, and Luis Castedo, "**Design of linear precoders for correlated sources in MIMO multiple access channels**", *IEEE Transactions on Communications*, vol. 66, no. 12, pp. 6110–6122, 2018.
DOI: 10.1109/TCOMM.2018.2863362.

[101] Theodore S. Rappaport, Shu Sun, Rimma Mayzus, Hang Zhao, Yaniv Azar, Kevin Wang, George N. Wong, Jocelyn K. Schulz, Mathew Samimi, and Felix Gutierrez, "**Millimeter wave mobile communications for 5G cellular: It will work!**" *IEEE Access*, vol. 1, pp. 335–349, 2013.
DOI: 10.1109/ACCESS.2013.2260813.

[102] Erik G. Larsson, Ove Edfors, Fredrik Tufvesson, and Thomas L. Marzetta, "**Massive MIMO for next generation wireless systems**", *IEEE Communications Magazine*, vol. 52, no. 2, pp. 186–195, 2014.
DOI: 10.1109/MCOM.2014.6736761.

[103] Pallav Sudarshan, Neelesh B. Mehta, Andreas F. Molisch, and Jin Zhang, "**Channel statistics-based RF pre-processing with antenna selection**", *IEEE Transactions on Wireless Communications*, vol. 5, no. 12, pp. 3501–3511, 2006.
DOI: 10.1109/TWC.2006.256973.

[104] Edin Zhang and Chiachi Huang, "**On achieving optimal rate of digital precoder by RF-baseband codesign for MIMO systems**", *Proc. of 2014 IEEE 80th Vehicular Technology Conference (VTC2014-Fall)*, 2014, pp. 1–5.
DOI: 10.1109/VTCFall.2014.6966076.

[105] Ahmed Alkhateeb, Jianhua Mo, Nuria Gonzalez-Prelcic, and Robert W. Heath, "**MIMO precoding and combining solutions for millimeter-wave systems**", *IEEE Communications Magazine*, vol. 52, no. 12, pp. 122–131, 2014.
DOI: 10.1109/MCOM.2014.6979963.

[106] Shu Sun, Theodore S. Rappaport, Robert W. Heath, Andrew Nix, and Sundeep Rangan, "**MIMO for millimeter-wave wireless communications: Beamforming, spatial multiplexing, or both?**" *IEEE Communications Magazine*, vol. 52, no. 12, pp. 110–121, 2014.
DOI: 10.1109/MCOM.2014.6979962.

[107] Shuangfeng Han, Chih-lin I, Zhikun Xu, and Corbett Rowell, "**Large-scale antenna systems with hybrid analog and digital beamforming for millimeter wave 5G**", *IEEE Communications Magazine*, vol. 53, no. 1, pp. 186–194, 2015.
DOI: 10.1109/MCOM.2015.7010533.

[108] Wolfgang Utschick, Christoph Stöckle, Michael Joham, and Jian Luo, "**Hybrid LISA precoding for multiuser millimeter-wave communications**", *IEEE Transactions on Wireless Communications*, vol. 17, no. 2, pp. 752–765, 2018.
DOI: 10.1109/TWC.2017.2770125.

[109] Cristian Rusu, Roi Mèndez-Rial, Nuria González-Prelcic, and Robert W. Heath, "**Low complexity hybrid precoding strategies for millimeter wave communication systems**", *IEEE Transactions on Wireless Communications*, vol. 15, no. 12, pp. 8380–8393, 2016.
DOI: 10.1109/TWC.2016.2614495.

[110] Nanxi Li, Zaixue Wei, Hongwen Yang, Xin Zhang, and Dacheng Yang, "**Hybrid precoding for mmWave massive MIMO systems with partially connected structure**", *IEEE Access*, vol. 5, pp. 15 142–15 151, 2017.
DOI: 10.1109/ACCESS.2017.2720163.

[111] Xianghao Yu, Juei-Chin Shen, Jun Zhang, and Khaled B. Letaief, "**Alternating minimization algorithms for hybrid precoding in millimeter wave MIMO systems**", *IEEE Journal of Selected Topics in Signal Processing*, vol. 10, no. 3, pp. 485–500, 2016.
DOI: 10.1109/JSTSP.2016.2523903.

[112] Jaspreet Singh and Sudhir Ramakrishna, "**On the feasibility of codebook-based beamforming in millimeter wave systems with multiple antenna arrays**", *IEEE Transactions on Wireless Communications*, vol. 14, no. 5, pp. 2670–2683, 2015.
DOI: 10.1109/TWC.2015.2390637.

[113] Jian A. Zhang, Xiaojing Huang, Val Dyadyuk, and Y. Jay Guo, "**Massive hybrid antenna array for millimeter-wave cellular communications**", *IEEE Wireless Communications*, vol. 22, no. 1, pp. 79–87, 2015.
DOI: 10.1109/MWC.2015.7054722.

[114] Xinying Zhang, A.F. Molisch, and Sun-Yuan Kung, "**Variable-phase-shift-based RF-baseband codesign for MIMO antenna selection**", *IEEE Transactions on Signal Processing*, vol. 53, no. 11, pp. 4091–4103, 2005, ISSN: 1053-587X.
DOI: 10.1109/TSP.2005.857024.

[115] Ahmed Alkhateeb, Geert Leus, and Robert W. Heath, "**Limited feedback hybrid precoding for multi-user millimeter wave systems**", *IEEE Transactions on Wireless Communications*, vol. 14, no. 11, pp. 6481–6494, 2015.
DOI: 10.1109/TWC.2015.2455980.

[116] Tadilo Endeshaw Bogale and Luc Vandendorpe, "**Robust sum MSE optimization for downlink multiuser MIMO systems with arbitrary power constraint: Generalized duality approach**", *IEEE Transactions on Signal Processing*, vol. 60, no. 4, pp. 1862–1875, 2012.
DOI: 10.1109/TSP.2011.2180899.

[117] P. Suárez-Casal, O. Fresnedo, and L. Castedo, "**DQLC optimization for joint source channel coding of correlated sources over fading MAC**", *Proc. of 2018 26th European Signal Processing Conference (EUSIPCO)*, 2018, pp. 1292–1296.
DOI: 10.23919/EUSIPCO.2018.8553256.

[118] O. Fresnedo, P. Suárez-Casal, and L. Castedo, "**Transmission of spatio-temporal correlated sources over fading multiple access channels with DQLC mappings**", *IEEE Transactions on Communications*, vol. 67, no. 8, pp. 5604–5617, 2019, ISSN: 1558-0857.
DOI: 10.1109/TCOMM.2019.2912571.

[119] Kyong-Hwa Lee and D Petersen, "**Optimal linear coding for vector channels**", *IEEE Transactions on Communications*, vol. 24, no. 12, pp. 1283–1290, 1976.

[120] Duy H. N. Nguyen, Long Bao Le, Tho Le-Ngoc, and Robert W. Heath, "**Hybrid MMSE precoding and combining designs for mmWave multiuser systems**", *IEEE Access*, vol. 5, pp. 19 167–19 181, 2017.
DOI: 10.1109/ACCESS.2017.2754979.

[121] Mingming Cai, Kang Gao, Ding Nie, Bertrand Hochwald, J. Nicholas Laneman, Huang Huang, and Kunpeng Liu, "**Effect of wideband beam squint on codebook design in phased-array wireless systems**", *Proc. of 2016 IEEE Global Communications Conference (GLOBECOM)*, 2016, pp. 1–6.
DOI: 10.1109/GLOCOM.2016.7841766.

[122] Hongyu Li, Ming Li, Qian Liu, and A. Lee Swindlehurst, "**Dynamic hybrid beamforming with low-resolution PSs for wideband mmWave MIMO-OFDM systems**", *IEEE Journal on Selected Areas in Communications*, vol. 38, no. 9, pp. 2168–

2181, 2020.
DOI: 10.1109/JSAC.2020.3000878.

[123] Yun Chen, Da Chen, and Tao Jiang, "**Non-uniform quantization codebook-based hybrid precoding to reduce feedback overhead in millimeter wave MIMO systems**", *IEEE Transactions on Communications*, vol. 67, no. 4, pp. 2779–2791, 2019.
DOI: 10.1109/TCOMM.2018.2890227.

[124] Jianjun Zhang, Yongming Huang, Jiaheng Wang, and Luxi Yang, "**Hybrid precoding for wideband millimeter-wave systems with finite resolution phase shifters**", *IEEE Transactions on Vehicular Technology*, vol. 67, no. 11, pp. 11 285–11 290, 2018.
DOI: 10.1109/TVT.2018.2869308.

[125] Yun Chen, Da Chen, Yuan Tian, and Tao Jiang, "**Spatial lobes division-based low complexity hybrid precoding and diversity combining for mmWave IoT systems**", *IEEE Internet of Things Journal*, vol. 6, no. 2, pp. 3228–3239, 2019.
DOI: 10.1109/JIOT.2018.2881171.

[126] Roberto Magueta, Daniel Castanheira, Adão Silva, Rui Dinis, and Atílio Gameiro, "**Hybrid multi-user equalizer for massive mimo millimeter-wave dynamic subconnected architecture**", *IEEE Access*, vol. 7, pp. 79 017–79 029, 2019.
DOI: 10.1109/ACCESS.2019.2921530.

[127] Yun Chen, Da Chen, Tao Jiang, and Lajos Hanzo, "**Channel-covariance and angle-of-departure aided hybrid precoding for wideband multiuser millimeter wave MIMO systems**", *IEEE Transactions on Communications*, vol. 67, no. 12, pp. 8315–8328, 2019.
DOI: 10.1109/TCOMM.2019.2942307.

[128] Anthony Ngozichukwuka Uwaechia and Nor Muzlifah Mahyuddin, "**A comprehensive survey on millimeter wave communications for fifth-generation wireless networks: Feasibility and challenges**", *IEEE Access*, vol. 8, pp. 62 367–62 414, 2020.
DOI: 10.1109/ACCESS.2020.2984204.

[129] Sungwoo Park, Ahmed Alkhateeb, and Robert W. Heath, "**Dynamic subarrays for hybrid precoding in wideband mmWave MIMO systems**", *IEEE Transactions on Wireless Communications*, vol. 16, no. 5, pp. 2907–2920, 2017.
DOI: 10.1109/TWC.2017.2671869.

[130] Christos Liaskos, Shuai Nie, Ageliki Tsioliaridou, Andreas Pitsillides, Sotiris Ioannidis, and Ian Akyildiz, "**A new wireless communication paradigm through software-controlled metasurfaces**", *IEEE Communications Magazine*, vol. 56, no. 9, pp. 162–169, 2018.
DOI: 10.1109/MCOM.2018.1700659.

[131] Ertugrul Basar, Marco Di Renzo, Julien De Rosny, Merouane Debbah, Mohamed-Slim Alouini, and Rui Zhang, "**Wireless communications through reconfigurable intelligent surfaces**", *IEEE Access*, vol. 7, pp. 116 753–116 773, 2019.
DOI: 10.1109/ACCESS.2019.2935192.

[132] Xufeng Guo, Yuanbin Chen, and Ying Wang, "**Learning-based robust and secure transmission for reconfigurable intelligent surface aided millimeter wave UAV communications**", *IEEE Wireless Communications Letters*, vol. 10, no. 8, pp. 1795–1799, 2021.
DOI: 10.1109/LWC.2021.3081464.

[133] Qingqing Wu and Rui Zhang, "**Towards smart and reconfigurable environment: Intelligent reflecting surface aided wireless network**", *IEEE Communications Magazine*, vol. 58, no. 1, pp. 106–112, 2020.
DOI: 10.1109/MCOM.001.1900107.

[134] Ludek Subrt and Pavel Pechac, "**Intelligent walls as autonomous parts of smart indoor environments**", *IET communications*, vol. 6, no. 8, pp. 1004–1010, 2012.

[135] Tie Jun Cui, Mei Qing Qi, Xiang Wan, Jie Zhao, and Qiang Cheng, "**Coding metamaterials, digital metamaterials and programmable metamaterials**", *Light: Science & Applications*, vol. 3, no. 10, e218–e218, 2014.

[136] Qingqing Wu and Rui Zhang, "**Intelligent reflecting surface enhanced wireless network via joint active and passive beamforming**", *IEEE Transactions on Wireless Communications*, vol. 18, no. 11, pp. 5394–5409, 2019.
DOI: 10.1109/TWC.2019.2936025.

[137] Jun Zhao, "**A survey of intelligent reflecting surfaces (IRSs): Towards 6G wireless communication networks**", *arXiv preprint arXiv:1907.04789*, 2019.

[138] Haris Gacanin and Marco Di Renzo, "**Wireless 2.0: Toward an intelligent radio environment empowered by reconfigurable meta-surfaces and artificial intelligence**", *IEEE Vehicular Technology Magazine*, vol. 15, no. 4, pp. 74–82, 2020.

[139] Jiezhi Zhang, Yu Zhang, Caijun Zhong, and Zhaoyang Zhang, "**Robust design for intelligent reflecting surfaces assisted MISO systems**", *IEEE Communications Letters*, vol. 24, no. 10, pp. 2353–2357, 2020.
DOI: 10.1109/LCOMM.2020.3002557.

[140] Gui Zhou, Cunhua Pan, Hong Ren, Kezhi Wang, Marco Di Renzo, and Arumugam Nallanathan, "**Robust beamforming design for intelligent reflecting surface aided MISO communication systems**", *IEEE Wireless Communications Letters*, vol. 9, no. 10, pp. 1658–1662, 2020.
DOI: 10.1109/LWC.2020.3000490.

[141] Jafar Shaker, Mohammad Reza Chaharmir, and Jonathan Ethier, ***Reflectarray antennas: analysis, design, fabrication, and measurement***. Artech House, 2013.

[142] Nicolas Bonod, "**Large-scale dielectric metasurfaces**", *Nature materials*, vol. 14, no. 7, pp. 664–665, 2015.

[143] Xiangang Luo, "**Subwavelength artificial structures: Opening a new era for engineering optics**", *Advanced Materials*, vol. 31, no. 4, p. 1 804 680, 2019.

[144] Huanhuan Yang, Xiangyu Cao, Fan Yang, Jun Gao, Shenheng Xu, Maokun Li, Xibi Chen, Yi Zhao, Yuejun Zheng, and Sijia Li, "**A programmable metasurface with dynamic polarization, scattering and focusing control**", *Scientific reports*, vol. 6, no. 1, pp. 1–11, 2016.

[145] Eduardo Carrasco, Mariano Barba, and José A. Encinar, "**X-band reflectarray antenna with switching-beam using pin diodes and gathered elements**", *IEEE Transactions on Antennas and Propagation*, vol. 60, no. 12, pp. 5700–5708, 2012.
DOI: 10.1109/TAP.2012.2208612.

[146] Jonathan Y. Lau and Sean V. Hum, "**Reconfigurable transmitarray design approaches for beamforming applications**", *IEEE Transactions on Antennas and Propagation*, vol. 60, no. 12, pp. 5679–5689, 2012.
DOI: 10.1109/TAP.2012.2213054.

[147] Xin Tan, Zhi Sun, Dimitrios Koutsonikolas, and Josep M. Jornet, "**Enabling indoor mobile millimeter-wave networks based on smart reflect-arrays**", *Proc. of IEEE INFOCOM 2018 - IEEE Conference on Computer Communications*, 2018, pp. 270–278.
DOI: 10.1109/INFOCOM.2018.8485924.

[148] Samith Abeywickrama, Rui Zhang, Qingqing Wu, and Chau Yuen, "**Intelligent reflecting surface: Practical phase shift model and beamforming optimization**", *IEEE Transactions on Communications*, vol. 68, no. 9, pp. 5849–5863, 2020.
DOI: 10.1109/TCOMM.2020.3001125.

[149] Özdogan, Özgecan and Björnson, Emil and Larsson, Erik G., "**Intelligent reflecting surfaces: Physics, propagation, and pathloss modeling**", *IEEE Wireless Communications Letters*, vol. 9, no. 5, pp. 581–585, 2020.
DOI: 10.1109/LWC.2019.2960779.

[150] Christopher L. Holloway, Edward F. Kuester, Joshua A. Gordon, John O'Hara, Jim Booth, and David R. Smith, "**An overview of the theory and applications of metasurfaces: The two-dimensional equivalents of metamaterials**", *IEEE Antennas and Propagation Magazine*, vol. 54, no. 2, pp. 10–35, 2012.
DOI: 10.1109/MAP.2012.6230714.

[151] Fei Ding, Anders Pors, and Sergey I Bozhevolnyi, "**Gradient metasurfaces: A review of fundamentals and applications**", *Reports on Progress in Physics*, vol. 81, no. 2, p. 026 401, 2017.

[152] Lei Zhang, Xiao Qing Chen, Shuo Liu, Qian Zhang, Jie Zhao, Jun Yan Dai, Guo Dong Bai, Xiang Wan, Qiang Cheng, Giuseppe Castaldi, *et al.*, "**Space-time-coding digital metasurfaces**", *Nature communications*, vol. 9, no. 1, pp. 1–11, 2018.

[153] Cheng Huang, Changlei Zhang, Jianing Yang, Bo Sun, Bo Zhao, and Xiangang Luo, "**Reconfigurable metasurface for multifunctional control of electromagnetic waves**", *Advanced Optical Materials*, vol. 5, no. 22, p. 1 700 485, 2017.

[154] Ying-Chang Liang, Ruizhe Long, Qianqian Zhang, Jie Chen, Hei Victor Cheng, and Huayan Guo, "**Large intelligent surface/antennas (LISA): Making reflective radios smart**", *Journal of Communications and Information Networks*, vol. 4, no. 2, pp. 40–50, 2019.
DOI: 10.23919/JCIN.2019.8917871.

[155] Kouvaros, Panagiotis, Dimitrios Kouzapas, Anna Philippou, Julius Georgiou, Loukas Petrou, and Andreas Pitsillides, "**Formal verification of a programmable hypersurface**", *Proc. of Formal Methods for Industrial Critical Systems*, Falk Howar and Jiří Barnat, Eds., Cham, Springer International Publishing, 2018, pp. 83–97, ISBN: 978-3-030-00244-2.

[156] Anna C. Tasolamprou, Mohammad Sajjad Mirmoosa, Odysseas Tsilipakos, Alexandros Pitilakis, Fu Liu, Sergi Abadal, Albert Cabellos-Aparicio, Eduard Alarcón, Christos Liaskos, Nikolaos V. Kantartzis, Sergei Tretyakov, Maria Kafesaki, Eleftherios N. Economou, and Costas M. Soukoulis, "**Intercell wireless communication in software-defined metasurfaces**", *Proc. of International Symposium on Circuits and Systems (ISCAS)*, 2018, pp. 1–5.
DOI: 10.1109/ISCAS.2018.8351865.

[157] J. Brewer, "**Kronecker products and matrix calculus in system theory**", *IEEE Transactions on Circuits and Systems*, vol. 25, no. 9, pp. 772–781, 1978.
DOI: 10.1109/TCS.1978.1084534.

[158] Michael Joham, Hangze Gao, and Wolfgang Utschick, "**Estimation of channels in systems with intelligent reflecting surfaces**", *Proc. of ICASSP 2022 - 2022 IEEE International Conference on Acoustics, Speech and Signal Processing (ICASSP)*, 2022, pp. 5368–5372.
DOI: 10.1109/ICASSP43922.2022.9747624.

[159] Tadilo Endeshaw, Batu K. Chalise, and Luc Vandendorpe, "**MSE uplink-downlink duality of MIMO systems under imperfect CSI**", *Proc. of 2009 3rd IEEE International Workshop on Computational Advances in Multi-Sensor Adaptive Processing (CAMSAP)*, 2009, pp. 384–387.
DOI: 10.1109/CAMSAP.2009.5413251.

[160] S. S. Christensen, R. Agarwal, E. de Carvalho, and J. M. Cioffi, "**Weighted sum-rate maximization using weighted MMSE for MIMO-BC beamforming design**", *Proc. of 2009 IEEE International Conference on Communications*, 2009, pp. 1–6.
DOI: 10.1109/ICC.2009.5199574.

[161] N. Jindal, Wonjong Rhee, S. Vishwanath, S.A. Jafar, and A. Goldsmith, "**Sum power iterative water-filling for multi-antenna Gaussian broadcast channels**", *IEEE Transactions on Information Theory*, vol. 51, no. 4, pp. 1570–1580, 2005.
DOI: 10.1109/TIT.2005.844082.

[162] Hafiz Atta Ul Mustafa, Muhammad Ali Imran, Muhammad Zeeshan Shakir, Ali Imran, and Rahim Tafazolli, "**Separation framework: An enabler for cooperative and D2D communication for future 5G networks**", *IEEE Communications Surveys & Tutorials*, vol. 18, no. 1, pp. 419–445, 2016.
DOI: 10.1109/COMST.2015.2459596.

[163] Jie Yuan, Ying-Chang Liang, Jingon Joung, Gang Feng, and Erik G. Larsson, "**Intelligent reflecting surface-assisted cognitive radio system**", *IEEE Transactions on Communications*, vol. 69, no. 1, pp. 675–687, 2021.
DOI: 10.1109/TCOMM.2020.3033006.

[164] Zhiguo Ding and H. Vincent Poor, "**A simple design of IRS-NOMA transmission**", *IEEE Communications Letters*, vol. 24, no. 5, pp. 1119–1123, 2020.
DOI: 10.1109/LCOMM.2020.2974196.

[165] Okan Yurduseven, Stylianos D. Assimonis, and Michail Matthaiou, "**Intelligent reflecting surfaces with spatial modulation: An electromagnetic perspective**", *IEEE Open Journal of the Communications Society*, vol. 1, pp. 1256–1266, 2020.
DOI: 10.1109/OJCOMS.2020.3017237.

[166] Bashar Tahir, Stefan Schwarz, and Markus Rupp, "**RIS-assisted code-domain MIMO-NOMA**", *Proc. of 29th European Signal Processing Conference (EUSIPCO)*, 2021, pp. 821–825.
DOI: 10.23919/EUSIPCO54536.2021.9616076.

[167] Kaina, Nadège and Dupré, Matthieu and Lerosey, Geoffroy and Mathias Fink, "**Shaping complex microwave fields in reverberating media with binary tunable metasurfaces**", *Scientific reports*, vol. 4, no. 1, pp. 1–8, 2014.